Gems & Gemology

Spring 2018
Volume LIV

The Quarterly Journal of the Gemological Institute of America

Characteristics of Natural-Color Green Diamonds

Iridescence in "Rainbow" Hematite

DNA Identification of Japanese *P. Fucata* Pearls

Tucson Report 2018

2018 GIA SYMPOSIUM

New Challenges. Creating Opportunities.

Harvard Business Track

Authentic Leadership, Disruptive Innovation and Customer Centricity

GIA Research Track

Scientific Findings and Industry Analysis

GIA® is accepting abstract submissions for oral and poster presentations through June 1.

Join us October 7 – 9, 2018 in Carlsbad, California

GIA®

Seats are Limited. Register Now.

symposium.GIA.edu

GEMS & GEMOLOGY

Spring 2018
VOLUME 54, No. 1


pg. 9


pg. 45


pg. 59

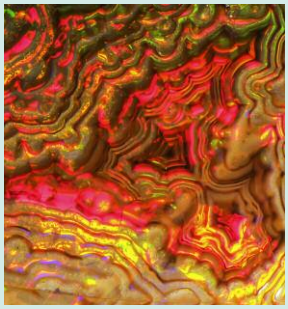
pg. 68


pg. 92

Editorial

Feature Articles

Regular Features

GEMS & GEMOLOGY

gia.edu/gems-gemology

Subscriptions
Copies of the current issue may be purchased for $29.95 plus shipping. Subscriptions are $79.99 for one year (4 issues) in the U.S. and $99.99 elsewhere. Canadian subscribers should add GST. Discounts are available for renewals, group subscriptions, GIA alumni, and current GIA students. To purchase print subscriptions, visit store.gia.edu or contact Customer Service. For institutional rates, contact Customer Service.

Database Coverage
G&G is abstracted in Thomson Reuters products (Current Contents: Physical, Chemical & Earth Sciences and Science Citation Index—Expanded, including the Web of Knowledge) and other databases. For a complete list of sources abstracting *G&G*, go to gia.edu/gems-gemology, and click on "Publication Information."

Manuscript Submissions
Gems & Gemology, a peer-reviewed journal, welcomes the submission of articles on all aspects of the field. Please see the Author Guidelines at gia.edu/gems-gemology or contact the Managing Editor. Letters on articles published in *G&G* are also welcome. Please note that Field Reports, Lab Notes, Gem News International, Micro-World, and Charts are not peer-reviewed sections but do undergo technical and editorial review.

Gems & Gemology is published quarterly by the Gemological Institute of America, a nonprofit educational organization for the gem and jewelry industry.

Postmaster: Return undeliverable copies of *Gems & Gemology* to GIA, The Robert Mouawad Campus, 5345 Armada Drive, Carlsbad, CA 92008.

Our Canadian goods and service registration number is 126142892RT.

About the Cover

Colored by atomic-level defect arrangments, natural-color green diamonds are among the rarest gemstones found on Earth. The cover photo showcases diamonds that display a range of green hues. The diamonds in the rings (clockwise from top) are a 4.17 ct Fancy Vivid yellowish green, a 10.18 ct Fancy Intense yellow-green, and a 3.88 ct Fancy Vivid green, respectively. The unmounted diamonds in the top row are a 1.42 ct Fancy Vivid bluish green, a 1.01 ct Fancy Vivid yellowish green, and a 2.06 ct Fancy Vivid green-blue. In the bottom row are a 0.55 ct Fancy Vivid green and a 0.55 ct Fancy Vivid bluish green. Photo by Robert Weldon/GIA, courtesy of Optimum Diamonds.

Printing is by L+L Printers, Carlsbad, CA.
GIA World Headquarters The Robert Mouawad Campus 5345 Armada Drive Carlsbad, CA 92008 USA

ISSN 0016-626X

The Beauty of **Natural Green Diamonds**

Naturally colored green diamonds are among the most rare and enigmatic of gems, and those with saturated hues—like the stunning examples on our spring issue cover—are highly coveted. Their color origin remains extremely challenging for gemological laboratories to determine.

In our lead paper, Drs. Christopher Breeding, Sally Eaton-Magaña, and James Shigley review these extraordinary gems, identifying four distinct causes of their green colors—radiation damage defects, luminescence from H3 defects, and absorptions by hydrogen- and nickel-related defects—and discuss the difficulties of separating these gems from those colored by manmade irradiation treatments. Using data and observations based on thousands of samples from GIA's research database, the authors offer an unrivaled gemological characterization of these remarkable gems. We're delighted to present this article, which is the first in a series on colored diamonds by the same authors.

"Determining origin of color in green diamonds is a major challenge for gemological laboratories."

Our second paper, by Xiayang Lin, Peter Heaney, and Jeffrey Post, investigates the cause of iridescence in metamorphic "rainbow" hematite from Brazil. The authors use electron microscopy, atomic force microscopy, and X-ray diffraction to identify the repeating microstructures responsible for the material's intense iridescence: oriented arrays of spindle-shaped hematite nanocrystals that form diffraction grating.

In our final feature article, pearl specialists Kazuko Saruwatari, Michio Suzuki, Chunhui Zhou, Promlikit Kessraprong, and Nicholas Sturman apply DNA identification techniques to determine mollusk species by sampling tiny amounts of pearl powder. Their study—using akoya pearls from Ehime Prefecture, Japan—was able to amplify genetic material from this powder and successfully match it with the same gene in mantle tissue from the local *Pinctada fucata* oyster.

Among the standout topics in our spring issue Lab Notes are entries on CVD synthetic diamonds above three carats, a new Kyocera plastic imitation opal, and a real curio: an extraordinary natural blister "pearl" that formed around a pearlfish. Please explore the inner world of gems with our Micro-World column—this issue we feature a type IIa natural diamond with extraordinary etch channels, an opal with agate-like bands, and a pink tourmaline with spodumene inclusions.

In addition to aquamarine from Pakistan's Shigar Valley and natural freshwater pearls from Texas, our GNI section showcases the 2018 Tucson gem shows. It summarizes market trends from this year's show and includes entries on leading jewelry designers, gem artists, and materials such as Russian and Namibian demantoid garnet, fine opal, Oregon sunstone, and turquoise from Arkansas.

Congratulations to the winners of our Dr. Edward J. Gübelin Most Valuable Article Award, announced in this issue. We offer a big "thank you" to all of the readers who voted. Don't forget to take this year's *G&G* Challenge, our annual multiple-choice quiz.

Lastly, please join us for the 2018 GIA Symposium, which takes place October 7–9 in Carlsbad, California. We encourage you to register to attend or submit an abstract for an oral or poster presentation at symposium.gia.edu.

Duncan Pay | Editor-in-Chief | dpay@gia.edu

Natural-Color Green Diamonds: A Beautiful Conundrum

Christopher M. Breeding, Sally Eaton-Magaña, and James E. Shigley

Among fancy-color diamonds, natural-color green stones with saturated hues are some of the rarest and most sought after. These diamonds are colored either by simple structural defects produced by radiation exposure or by more complex defects involving nitrogen, hydrogen, or nickel impurities. Most of the world's current production of fine natural green diamonds comes from South America or Africa. Laboratory irradiation treatments have been used commercially since the late 1940s to create green color in diamond and closely mimic the effects of natural radiation exposure, causing tremendous difficulty in gemological identification. Compounding that problem is a distinct paucity of published information on these diamonds due to their rarity. Four different coloring mechanisms—absorption by GR1 defects due to radiation damage, green luminescence from H3 defects, and absorptions caused by hydrogen- and nickel-related defects—can be identified in green diamonds. Careful microscopic observation, gemological testing, and spectroscopy performed at GIA over the last decade allows an unprecedented characterization of these beautiful natural stones. By leveraging GIA's vast database of diamond information, we have compiled data representative of tens of thousands of samples to offer a look at natural green diamonds that has never before been possible.

Fancy-color diamonds are among the most highly valued of gemstones due to their beauty and rarity. Interestingly, the rarest of diamond colors correlate with the three most popular choices for favorite color, in general—green, blue, and pink to red. The unique set of conditions in nature that produce the structural imperfections (defects in the lattice of carbon atoms; see Shigley and Breeding, 2013) responsible for the most vibrant hues of green, blue, and pink/red diamonds are so uncommon that many people are not even aware these stones exist. Over the last ten years, diamonds with these natural color components comprised less than 0.4% of all diamonds submitted to GIA's laboratories worldwide (including both fancy-color and those on the D–Z scale). Pure hues of green, blue, or red are even rarer, accounting for less than 0.07% of all diamonds examined.

Many articles published over the last 20 years in the scientific and gemological literature have looked at specific properties of colored diamonds, quality grading characteristics, or particular treatments. Few researchers, however, have had the opportunity to examine large quantities of similarly colored natural diamonds and report on their distinctive characteristics. Colored diamonds are extremely rare and, consequently, highly valued. This value factor means that laboratory reports are requested for most colored diamonds prior to being sold. As the creator of the diamond color grading system and the largest provider of these grading reports, GIA is uniquely positioned to examine more colored diamonds than anyone else in the world.

In Brief

- Among natural-color diamonds, those that have a pure green hue are rare and often highly valued.
- While many green diamonds owe their color to natural radiation exposure, three other color causes are often observed.
- These four categories of green diamonds exhibit some distinctive gemological properties and spectral features.
- Separation of some natural- and treated-color green diamonds continues to present a challenge for gem-testing laboratories.

See end of article for About the Authors and Acknowledgments.
Gems & Gemology, Vol. 54, No. 1, pp. 2–27,
http://dx.doi.org/10.5741/GEMS.54.1.2

Figure 1. Natural-color green diamonds such as these rough (0.85–1.07 ct) and faceted (0.68–1.66 ct) stones submitted to GIA by clients or for scientific study are extremely rare and generally found in South America or Africa. Photos by various GIA staff.

Over the last ten years, scientists at GIA have examined more than half a million natural, fancy-color diamonds and systematically documented their gemological and spectroscopic properties. Through a series of articles, we will discuss the major hue groups of natural-color diamonds in detail that has never before been revealed from such a large sampling of stones. The series will include gemological observations, spectroscopy, and statistical compilations from colored diamonds examined over the last decade at GIA. For more information on data collection methods, please see supplemental table 1 at https://www.gia.edu/gems-gemology/spring-2018-natural-color-green-diamonds-beautiful-conundrum.

This first article looks at green diamonds, a beautiful yet enigmatic hue (figure 1). During the last decade, GIA has examined well over 50,000 natural-color diamonds with a green hue component, including more than 9,000 with a pure green hue. While there are a few different causes of green color, the most common cause—accounting for nearly half of the natural green diamonds submitted to GIA—is exposure to radioactive minerals and fluids in the earth's crust. Over thousands to millions of years, radiation produced by the decay of isotopes of elements such as uranium and thorium (present in minerals or dissolved in geological fluids) physically damages the diamond structure by removing carbon atoms to cre-

TABLE 1. Categories of green diamond.

Cause of green color	Defect responsible	Most common colors	Geological formation	Key gemological observations
Radiation damage	GR1	Green to blue-green	Exposure to radiation (minerals or fluids)	Green and/or brown spots or stains in fractures; color zones
Green luminescence	H3	Green to yellow-green	Natural annealing	Localized or dispersed green fluorescence with focused lighting
H-related absorption	Unknown H-related	Gray-green to brownish green	Crystallization in mantle	Fine particulate clouds, often patterned
Ni-related absorption	Unknown Ni-related	Yellow-green to green-yellow	Crystallization in mantle	No distinctive features

ate vacant atomic positions (Meyer et al., 1965; Vance and Milledge, 1972; Mendelssohn et al., 1979; Raal and Robinson, 1981; Titkov et al., 1995; Nasdala et al., 2013). These vacancies (sometimes in combination with other defects) cause the diamond to absorb the blue and red parts of incident visible light, allowing primarily green light to be seen when one observes the stone. This natural irradiation process, however, is easily replicated in a laboratory with electrons, neutrons, or gamma rays, and many green diamonds in the trade have been the product of artificial irradiation treatments (where the radiation exposure times are rapid and controllable) since the late 1940s (Ehrmann, 1950).

The similarity of the natural and laboratory irradiation processes has made it very difficult in many cases for gemologists and laboratories to separate natural- and treated-color green diamonds. Indeed, there have been fewer publications about green diamonds than any other color. The purpose of this article is to provide a detailed account of the gemological and spectroscopic characteristics of natural green diamonds colored by several different mechanisms in order to help the trade better understand these gems.

CAUSE OF COLOR

Green color in gem diamonds can span a wide range of color descriptions. For the purposes of this article, we include all natural fancy-color diamonds that display a primary green color component under standard grading conditions. In the GIA fancy-color grading system, this includes stones with a pure green color as well as a dominant green color mixed with blue, brown, gray, or yellow. Of the green diamonds seen at GIA over the last decade, most have been yellow-green or pure green, followed by those with gray or brown modifiers and blue components. These different color groupings correlate, to some extent, to four significant atomic-level defect arrangements in natural diamond: GR1, H3, hydrogen, and nickel defects (figures 2 and 3). Table 1 summarizes the characteristics of these four groups.

GR1 (General Radiation 1). GR1 defects are empty lattice positions in the diamond structure and serve as the most common mechanism for green color in gem diamonds (Shigley and Fritsch, 1990; Collins, 2001; Shigley and Breeding, 2013). Irradiation, both natural and laboratory-induced, provides sufficient energy to displace carbon atoms from their normal positions in the diamond lattice, leaving vacancies (figure 4; see Koptil and Zinchuk, 2000). The displaced carbon atoms then become what scientists call *interstitials*: atoms that are out of their normal place and "stuck" between other carbon atoms. GR1 vacancies (figure 2A) cause the diamond to absorb light in the red part of the visible spectrum (zero phonon line[1], or ZPL, at 741 nm), with associated broad absorption extending from approximately 550 to 750 nm.

Depending on the amount of vacancies and the other impurities and defects present, green diamonds colored by GR1 typically have pure green or blue-green hues (figure 3); irradiation of a light yellow diamond produces a greener color, while irradiation of a colorless diamond causes a bluer color. Most naturally irradiated diamonds have shallow green "skins" or spots on the crystal surface that produce most of the green appearance (Vance and Milledge, 1972; Vance et al., 1973; Kane, 1979b; Fritsch and Shigley, 1991; Roskin, 2000; Eaton-Magaña and Moe, 2016). Upon faceting, these shallow areas of radiation damage are typically removed and the apparently green rough diamond shows little to

[1]See Luo and Breeding (2011) for diagram and description of the zero phonon line.

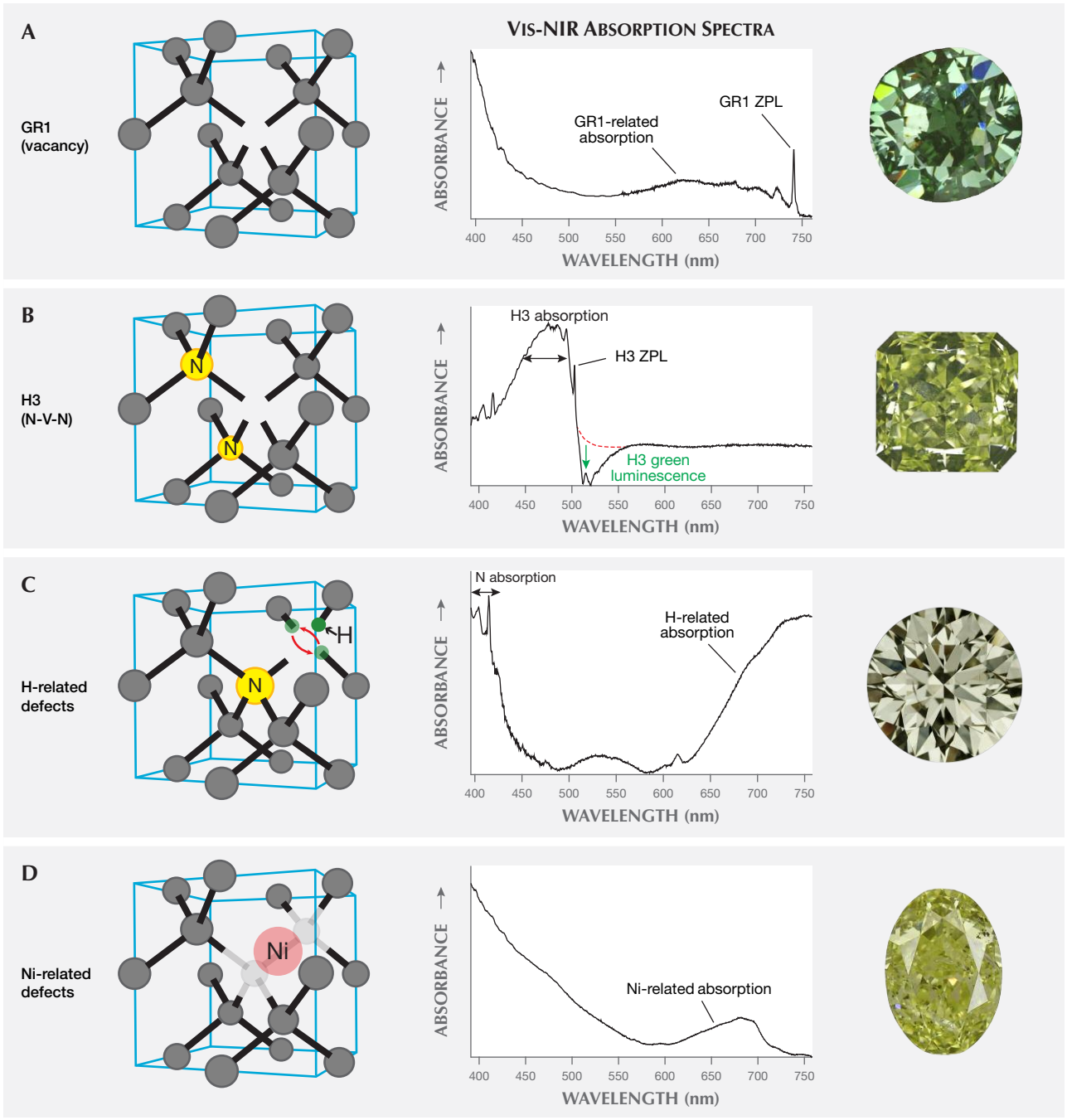

Figure 2. The four main causes of green color in diamond are GR1, H3, H-related, and Ni-related defects. Each absorbs light differently to produce a green color. H3 defects emit green luminescence, seen as the dip in the spectrum below the red dashed line, to cause visible green color.

no color as a finished cut stone (figure 5, bottom row). In some cases, irradiation brings about a deeper green bodycolor that is retained by the diamond after fashioning (figure 5, top row). Vacancies become mobile at temperatures above 600°C and start to move around and create new defects in the diamond lattice that can change the stone's color (Collins et al., 2000; Collins, 2001; Eaton-Magaña

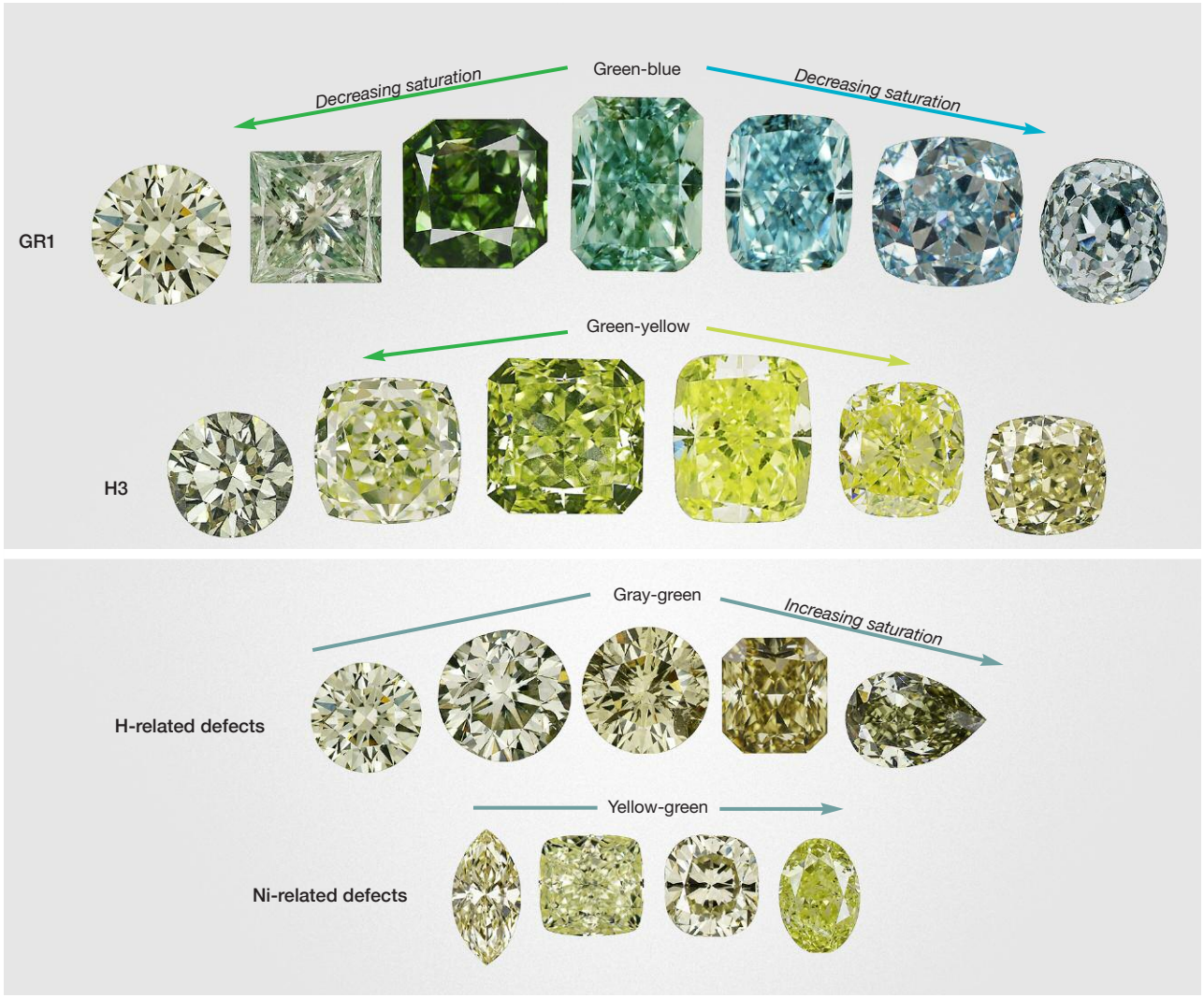

Figure 3. Different causes of color in green diamonds produce slightly different hue ranges, depending on the other impurities and defects present.

and Moe, 2016). During jewelry repair processes, when heating green diamonds colored by this mechanism, jewelers must take great care to avoid destroying the GR1 defects and losing the green color. Heat generated from the friction of polishing can have a similar effect.

The remaining three causes produce less-saturated pure green colors, or green hues with yellow or gray modifiers (figure 3).

Nitrogen-Related Defects: H3. Two nitrogen atoms adjacent to a vacancy in the diamond lattice comprise the H3 defect, the second most common mechanism for green color in diamond (figure 2B; see Collins, 2001; Breeding and Shigley, 2009; Shigley and Breeding, 2013). This uncharged defect is usually produced when diamonds containing pairs of nitrogen impurity atoms (A-centers) are exposed to radiation and subsequent heating above 600°C, either at depth in the earth or in a laboratory (Collins, 2001; Zaitsev, 2003). The vacancies introduced by radiation damage are mobilized during the heating, and they combine with the paired nitrogen impurities to create H3. Unlike GR1, H3 produces green color through emission of light (luminescence), rather than absorption (Collins, 2001; Shigley and Breeding, 2013). H3 absorbs light in the blue part of the visible spectrum (ZPL at 503.2 nm, with associated broad absorption from 420 to 500 nm), generating a yellow bodycolor in diamond. When H3 absorbs visible light, it simultaneously emits green fluorescence. High concentrations of nitrogen in the A form se-

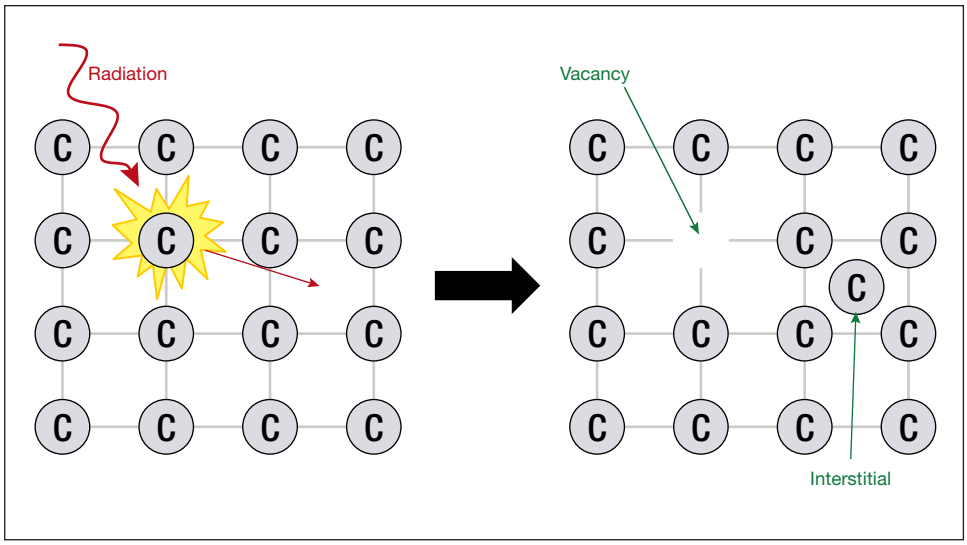

Figure 4. When the carbon atoms that make up the diamond lattice are exposed to high-energy radiation, they can be displaced from their lattice positions to create vacancies. The displaced carbon atoms are called interstitials.

verely quench the H3 fluorescence (Collins, 2001; Luo and Breeding, 2013), but occasionally a diamond with abundant H3 defects and a low concentration of nitrogen will emit sufficient fluorescence to bring about a combined yellow-green appearance (figures 2B and 3) (Collins, 2001; Luo and Breeding, 2013). H3 defects are very stable to temperatures exceeding 2000°C.

Hydrogen-Related Defects. The presence of hydrogen defects in the diamond structure has been known and studied for decades, but very little is known about how H impurities affect color (figure 2C). The best-known hydrogen-related defect in natural diamond is the 3107 cm^{-1} infrared (IR) absorption (Wang and Mayerson, 2002; Goss et al., 2014). This feature is attributed to three nitrogen atoms adjacent to a vacancy

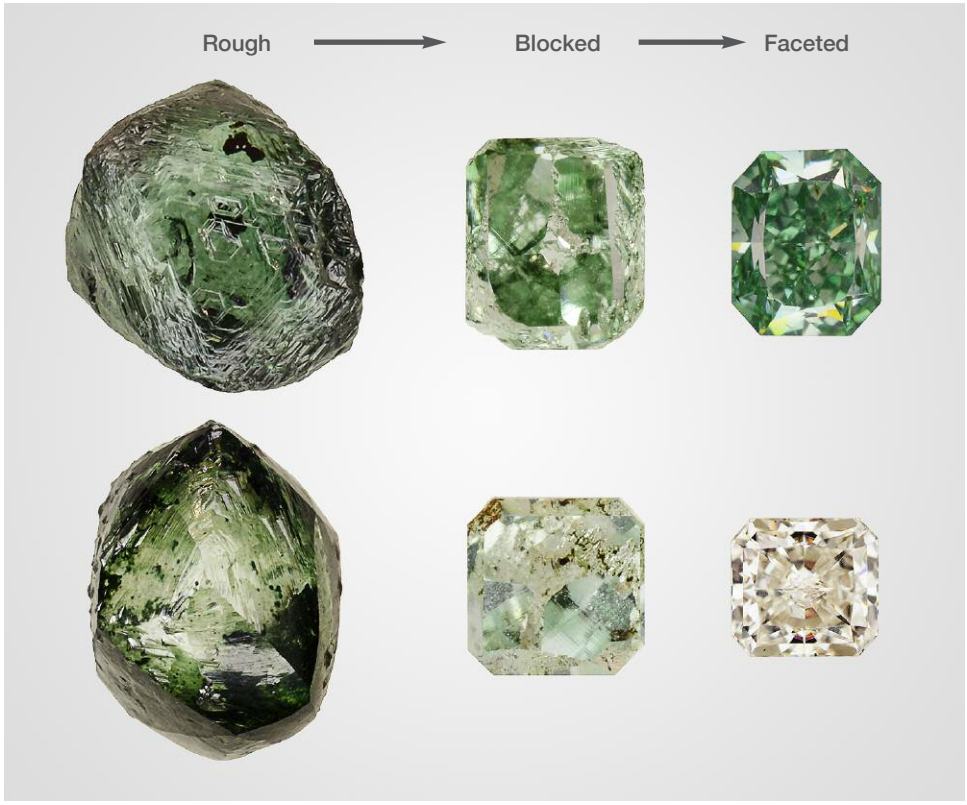

Figure 5. A green diamond's color may be confined to the surface or penetrate deeper into the stone. Upon preforming and faceting, the final product may be green or colorless, depending on the depth of the green coloration. The representative samples shown here are for illustrative purposes and should not be considered a progression of the same stone.

(N3 defect) that hosts an H atom (Goss et al., 2014), showing the intimate association of hydrogen and nitrogen impurities in diamond. Several other infrared absorption peaks are thought to be associated with this defect, including those at 1405, 2786, 3235, and 4498 cm^{-1}. Unfortunately, the intensity of these IR absorptions does not directly correlate with color-causing absorptions seen in the visible to near-infrared part of the spectrum. Two primary broad absorption bands spanning the 620–860 nm range (centered at approximately 730 and 835 nm), combined with nitrogen absorption at the blue end of the spectrum, often produce a green color component in H-rich diamonds (figure 2C). The nature of these broad bands is unclear, as they do not occur in all diamonds showing high concentrations of 3107 cm^{-1} defects, but they also do not occur in diamonds without H-related defects. It is possible that the broad absorptions are related to clouds of hitherto unidentified fine particles (or tiny fluid inclusions) that are relatively common in H-rich diamonds. Green stones colored by H-related defects commonly have brown or gray modifiers (figure 3). While the 3107 cm^{-1} defect is known to withstand temperatures above 2000°C (Goss et al., 2014 and references therein), the stability of the color-producing H-related defects is unknown.

Nickel-Related Defects. Nickel is an uncommon impurity in natural diamonds, considering the large size of the nickel atom that must be accommodated in the tightly packed array of carbon atoms in the diamond lattice. Concentrations of defects related to nickel impurities high enough to produce a green color are less common than other causes, accounting for less than 1% of all green diamonds seen at GIA over the last decade. Many Ni defects are known from natural and synthetic diamonds (based on observed features in spectra), with the most prominent one in natural diamonds consisting of a complex arrangement of nickel atoms (possibly charged interstitials) and vacancies (1.4 eV center; ZPL doublet at 883 and 885 nm; Zaitsev, 2003; Dischler, 2012). Ni defects occur concurrently with nitrogen impurities or other defects in diamond, and the visible absorptions that give rise to green color in these rare stones reflect that pairing. Aggregated N, isolated N, or vacancy-cluster defects may absorb the blue end of the spectrum, and color-affecting Ni absorption occurs as a broad asymmetrical band from approximately 620 to 710 nm, centered near 690 nm (figure 2D; see Wang et al., 2007; Ardon, 2013). Typically, the nitrogen-related absorption is stronger than that of Ni, producing an overall yellow-green bodycolor (figure 3). The origin of the color-causing Ni band is not known, but it is very similar in structure to the absorption sidebands associated with other defects such as N3 and H3. The thermal stability of the broad Ni-related absorption at 685 nm is not known, but studies of synthetic Ni-bearing diamonds suggest it could be stable to temperatures of 2000°C or higher (Zaitsev, 2003).

OCCURRENCE AND FORMATION

Green diamonds have been reported from both kimberlite-hosted and secondary alluvial sediments in nearly every country that produces diamonds, but some localities consistently produce more of these valuable stones. Green diamonds colored by H3, hydrogen, or nickel defects occur in many localities. For decades the largest producers of green diamonds colored by GR1 defects have been alluvial deposits in Brazil, Guyana, Venezuela, Zimbabwe, the Central African Republic, and India (Draper, 1951; Themelis, 1987; Coenraads et al., 1994; Chaves et al., 1996; Chaves et al., 2001).

The largest and most famous green diamond is the 41 ct Dresden Green (figure 6), sourced from the Golconda mines in India sometime before its earliest historical record in 1722 (Hough, 1913; Rosch, 1957; Bosshart, 1989, 1994; Kane et al., 1990; Astric et al., 1994; Morel, 1994). Several other famous green diamonds have been sold in recent years, including the 5.51 ct blue-green Ocean Dream (mined in the Central African Republic), the 25 ct Gruosi Green (South Africa and never graded by GIA), and the 5.03 ct Aurora Green (Brazil), which sold at auction in 2016 for more than US $3.3 million per carat (DeMarco, 2016).

Recent mining in South America has yielded a number of green diamonds from Brazil and Guyana (figure 7). Most show extensive surficial radiation damage with variable amounts of internal GR1-related green coloration. Another recent source is Zimbabwe. Rough diamonds from the Marange region of Zimbabwe (figure 7) are well known to have very dark green or brown coatings of radiation-damaged areas and often show internal green coloration as well (Breeding, 2011). Stones from this source are distinctive in that they also contain high concentrations of hydrogen defects that can enhance the green color from GR1 defects (e.g., a combination of figure 2A and figure 2C contributes to green color). Production from Zimbabwe has been very high in the last decade, but controversy engulfs these goods, as the

Figure 6. Several famous large diamonds have green color in varying hues. Left to right: the 5.03 ct Aurora Green, the 41 ct Dresden Green, and the 5.51 ct Ocean Dream. The Aurora Green photo is courtesy of Christie's. The Dresden Green photo is by Shane F. McClure, and the Ocean Dream photo is by Jian Xin (Jae) Liao.

United States and other countries still have an embargo on the import of Zimbabwe diamonds due to human rights concerns (Miller, 2011).

The formation mechanism for green diamonds in the earth varies significantly depending on the defects responsible for the color. Stones colored by hydrogen- or nickel-related defects incorporate these impurities, along with nitrogen, when they crystallize in the earth's mantle. Long residence times at high temperatures and pressures contribute to the final arrangement of the complex defects that produce green color in these diamonds, but their inherent color centers are imparted at "birth." Diamonds colored by H3 defects have a somewhat more complex history. Nitrogen impurities, incorporated during crystal growth, aggregate into A-centers over millions to billions of years at elevated temperatures deep in the earth. Vacancies associated with H3 defects are most commonly created by plastic deformation as the diamonds are violently transported via erupting kimberlite magmas to shallower depths in the earth. The H3 defects are then created by mobilization of the vacancies to combine with A-centers as the diamonds reside at elevated temperatures. In most scenarios, the color centers in H3-based green diamonds form during magma transport (Fisher,

Figure 7. Modern production of green diamonds has come from mines in Guyana and Brazil (left) as well as Zimbabwe (right). The dark brown to greenish "skins" seen on the surfaces of the rough diamonds are due to radiation damage.

2009). The final, and largest, category of green diamonds—those colored by GR1 defects—are generally thought to obtain their color due to late-stage interactions with radioactive minerals or fluids in the earth's crust over thousands to millions of years. Areas of radiation damage in these diamonds range from green to brownish spots caused by direct contact with radioactive minerals (most likely uraninite) to zones of green- to brown-colored "skin" on the surface or within surface-reaching fractures caused by radioactive fluids (figure 8; see Vance and Milledge, 1972; Vance et al., 1973; Mendelssohn et al., 1979). The shallow nature (approximately 20 µm thick) of the green spots and zones indicates that the radiation damage is primarily caused by alpha particles (see box A for radiation types and sources), most likely from uranium decay (Vance et al., 1973; Nasdala et al., 2013). These spots have been experimentally shown to rapidly turn from green to brown at temperatures of 550–600°C (Nasdala et al., 2013; Eaton-Magaña and Moe, 2016), indicating that diamonds with green radiation damage must have resided at depths less than about 24 km (assuming average geothermal gradient of 25°C/km).

Some green diamonds, however, show color zones that penetrate much deeper than 20 µm, sometimes even throughout the stones. In these cases, it is likely that some form of beta particle decay (or possibly gamma radiation) is contributing to the irradiation (box A). Some beta decay occurs as part of the same U-Th-Pb decay chain that is likely responsible for the stain-producing alpha damage described above. The overall doses of beta particles possible from these later parts of the decay chain are unknown and the subject of ongoing research. Another viable source for beta decay in the earth's crust with a half-life on

the order of millions of years appears to be potassium (^{40}K), but its natural abundance is very low (box A), leaving the complete story of radiation-related green color zoning unclear—in part because so few diamonds with green bodycolor have been available for scientific study.

GEMOLOGICAL OBSERVATIONS

Green diamonds have many interesting natural features that can be observed using a gemological microscope. These properties are quite variable, however, depending on the nature of the green color. In this section, we will review the major observations on green diamonds colored by each group of defects. Keep in mind that it is not uncommon for color to be affected by more than one of these color causes simultaneously. For example, many hydrogen-rich diamonds from Zimbabwe also show signs of radiation damage.

Primarily Colored by GR1. The most distinctive and important gemological features of green diamonds colored by radiation damage are surficial radiation spots or coatings (commonly referred to as "stains" if localized and "skin" if generally distributed) and internal color zonation (figure 9, A–E). Radiation stains occur as either green or brown patches of color on the surface of a rough diamond or within fractures. The radiation damage initially has a forest green color (often very dark green, depending on the dosage of the exposure) and then turns olive green at temperatures between 500 and 600°C and a reddish brown to dark brown at higher temperatures (Vance et al., 1973; Nasdala et al., 2013; Eaton-Magaña and Moe, 2016). Some experiments have shown that the brown stains disappear at temperatures above 1400°C (Eaton-Magaña and Moe, 2016). Radiation stains are thought to be a product of alpha particle bombardment, and structural damage increases to-

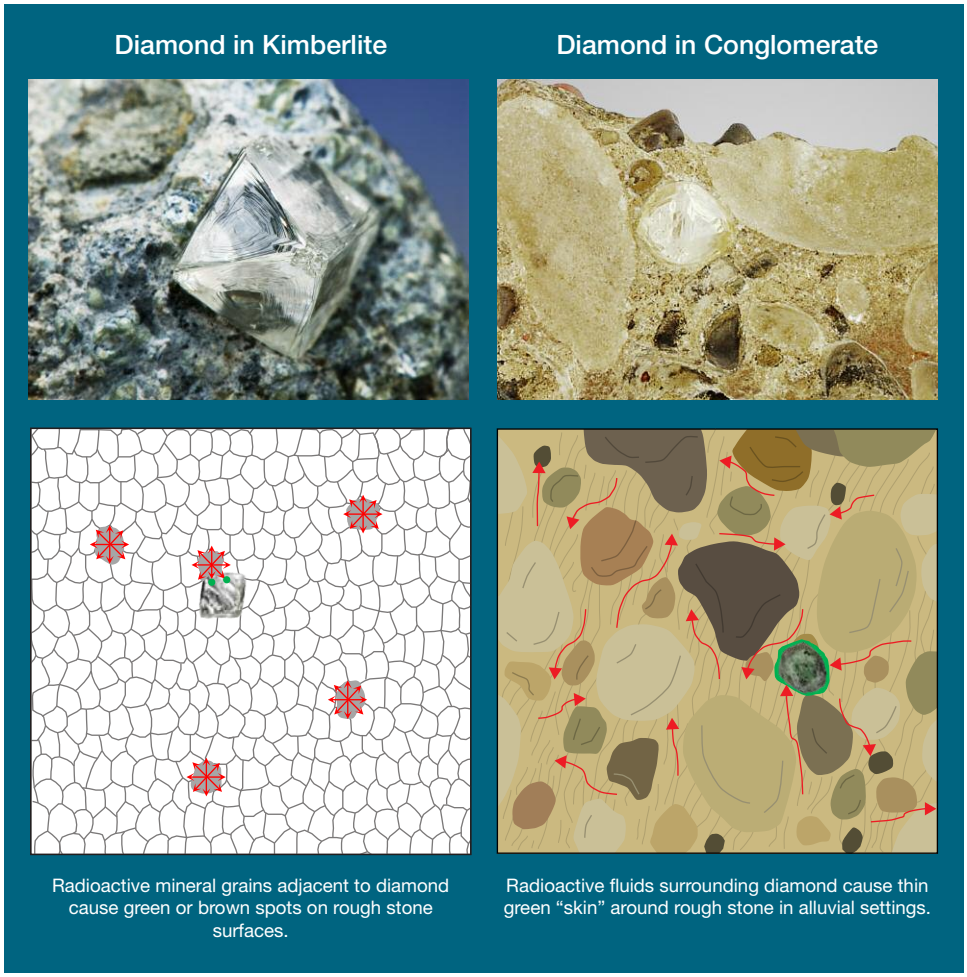

Figure 8. In the earth, diamonds may be exposed to radiation emitted from tiny radioactive mineral grains adjacent to the stones or through interaction with radioactive fluids. The radiation produces either isolated circular radiation "stains" (often from adjacent minerals in the kimberlite host rock, left) or radioactive fluids (usually in alluvial environments) that surround a stone and penetrate into fractures. Photo on the top left courtesy of William F. Larson. Photo on the top right by Robison McMurtry.

BOX A: SUMMARY OF RADIOACTIVE DECAY

Radioactivity primarily occurs by three mechanisms: alpha decay, beta decay, and gamma emission (figure A-1, top left). Alpha decay involves the expulsion of an alpha particle (two protons and two neutrons—equivalent to a helium atom nucleus) as the parent isotope decays to the daughter. Alpha particles are relatively large and slow, causing them to have low penetration depths (stopped by a sheet of paper, skin, or even air; figure A-1, top right). In natural-color green diamonds, alpha particles produce very thin green spots or skins on the stone's surface due to their shallow penetration depth. Beta decay involves ejection of a beta particle (an electron) as parent converts to daughter. Beta particles are small, high-energy, and high-speed, with moderate penetration depths (stopped by a sheet of aluminum). This type of radiation produces internal color zones in diamond at varying depths and is the most common type of radiation used for diamond treatment. In gamma emission, a parent isotope in an excited nuclear state decays to a daughter isotope by release of gamma rays. These extremely small forms of electromagnetic radiation are the fastest, highest-energy, and most penetrative radioactive decay product. They can fully penetrate a large gem diamond to impart uniform coloration and require a sheet of lead to stop their progress.

As shown in figure A-1 (bottom), the most likely sources of alpha decay in the earth are the radioactive isotopes of uranium (^{238}U and ^{235}U) and thorium (^{232}Th). Radiogenic thorium is three times more abundant than uranium in the earth's crust, but its decay is very slow, with a half-life (the time it takes for half of the parent isotope to decay to the daughter) of 14 billion years. ^{238}U is the most abundant radiogenic uranium isotope and has a half-life of 4.5 billion years, making it a more feasible source of radiation damage for diamond. Most uranium is found in the minerals uraninite and zircon. The best sources of beta decay to create green bodycolor in diamond include late-stage radiogenic decay within the uranium-lead decay chain and potassium. ^{40}K, the only significant radiogenic isotope of potassium, has a similar abundance in the earth's crust and a much shorter half-life of 1.3 billion years (figure A-1, bottom). ^{40}K is hosted in common crustal minerals such as micas and feldspars. Because these radioactive isotopes are extremely scarce in the earth's mantle, most green diamonds are thought to obtain their color from radiation exposure in alluvial deposits, where crustal minerals are more abundant, rather than in their kimberlite host rocks. In addition, the elevated temperatures of the mantle cause vacancies in the diamond lattice to be extremely mobile, and thus unstable.

Decay type	Radiation emitted	Model		
Alpha decay	$^{4}_{2}\alpha$	Parent	Daughter	Alpha particle
Beta decay	$^{0}_{-1}\beta$	Parent	Daughter	Beta particle
Gamma emission	$^{0}_{0}\gamma$	Parent (excited nuclear state)	Daughter	Gamma ray

Modified from scienceabc.com

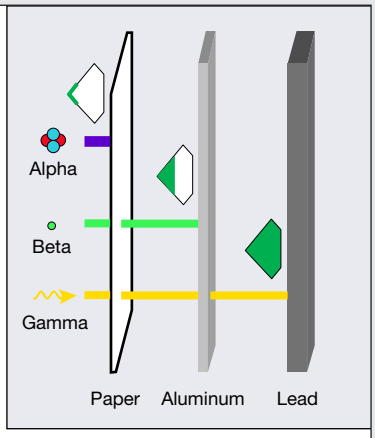

Figure A-1. Radioactive decay usually involves emission of alpha or beta particles or gamma rays. Each type of radiation has a different penetration depth in diamond, with alpha particles only affecting the surface and gamma rays penetrating throughout. Isotopes of uranium, thorium, and potassium are the most likely to affect diamonds in natural settings. These isotopes vary in abundance in the earth.

Radioactive isotope	Main decay type	Half-life (billions of years)	Avg. abundance – Earth's mantle (ppm)	Avg. abundance – Earth's crust (ppm)	Common mineral host
^{238}U	Alpha	4.5	0.022	1.787	Zircon, uraninite
^{235}U	Alpha	0.7	0.0002	0.011	Zircon, uraninite
^{232}Th	Alpha	14.0	0.083	5.999	Zircon, titanite, monazite, thorianite
^{40}K	Beta	1.3	0.031	1.800	Micas, clay minerals, K-feldspar

Abundances from wikipedia.org

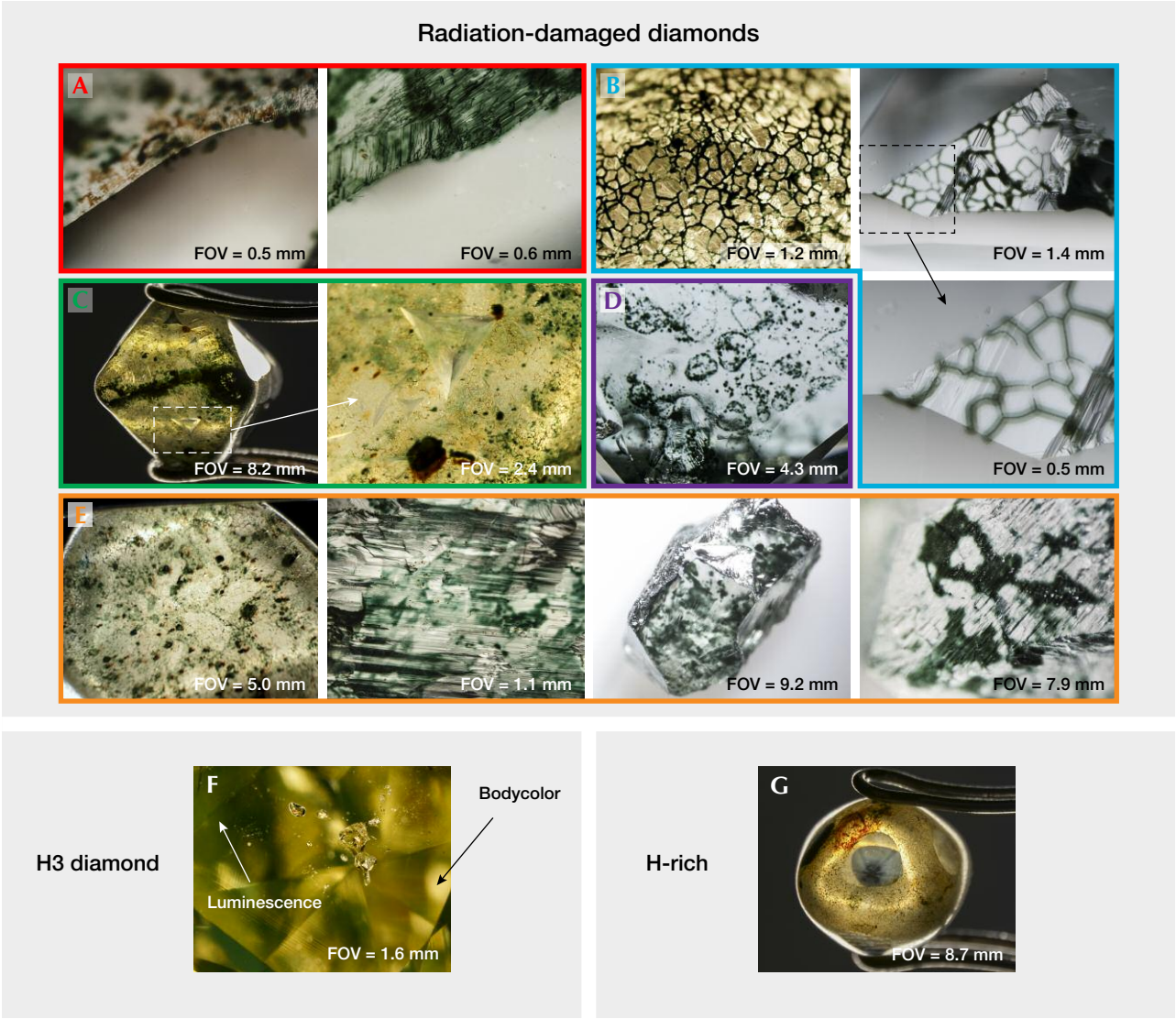

Figure 9. Radiation stains in diamond (A–E) occur initially as green spots that may turn brown with exposure to heat above 500°C (Vance et al., 1973; Nasdala et al., 2013; Eaton-Magaña and Moe, 2016). The stains are caused by alpha decay and occur as spots or thin coatings on the surface (A, C, and E). Green color usually penetrates only a few micrometers deep (A). Natural indentations or fractures allow radioactive fluids to penetrate and leave stains within the features (B). Occasionally, radioactive fluids between grain boundaries of adjacent minerals preserve their positions as green spotted patterns (D). H3-colored green diamonds (F) usually show yellow bodycolor with green luminescence. H-rich diamonds often have distinctively patterned clouds of microinclusions (G). Photomicrographs by various GIA staff.

ward the center of the area. While the stains can occur in any shape or size, depending on the diamond's surface exposure to radioactive material, most take the form of circular spots that likely represent halos extending from multiple point sources (figures 8 and 9A, 9C, and 9E). Damage to the atomic lattice by alpha particles causes a slight volume expansion in the diamond and an elevated surface at the locus of the stain (Nasdala et al., 2013). The green or brown color penetrates to depths of usually not much more than 20 µm (0.02 mm), creating a shallow zone of green color adjacent to the stain(s) (figure 9, A–B; Nasdala et al., 2013; Eaton-Magaña and Moe, 2016).

When many stains are concentrated together, a rough diamond may be covered with large patches of

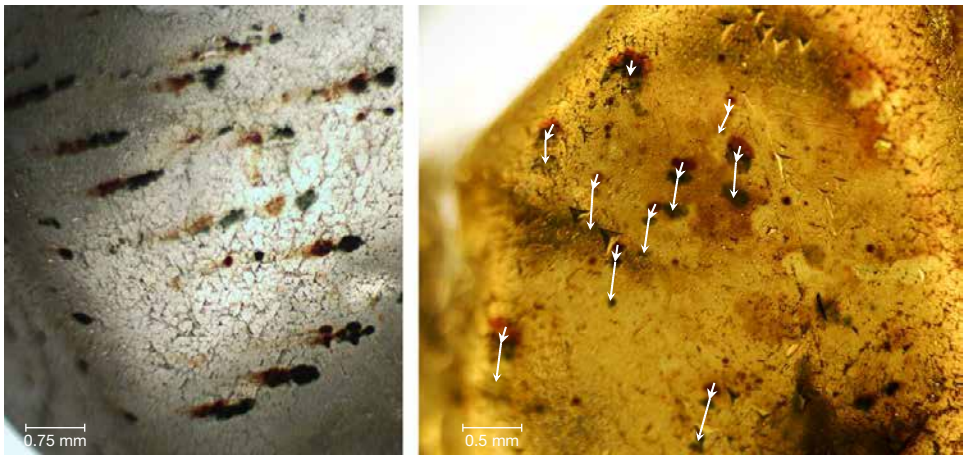

Figure 10. The occurrence of brown and green spots of the same size and shape, but shifted in position, strongly suggests multiple stages of radiation exposure, heating, and movement of the diamond relative to the adjacent radioactive minerals producing alpha particles that cause the damage. Photomicrographs by C.M. Breeding.

green zones. Similarly, very thin skins of relatively uniform green color may coat the surfaces and fractures (figure 9, C and E). These more pervasive areas of radiation damage probably represent radioactive fluids (rather than point sources of particles of radioactive minerals) surrounding a diamond and penetrating into the fractures and crevices (figures 8 and 9B). Patterns of green staining often mimic grain boundaries of minerals that would have surrounded the diamond, suggesting that radioactive fluids were also present between mineral grains in some ancient alluvial environments (figure 9D; see also Mennell, 1915; Guo et al., 1986). Green color zones that extend deeper must be related to beta or gamma radiation (or possibly neutron bombardment). While these zones do occur in some natural diamonds, they are much less common and therefore must represent some unusual radiation exposure conditions. For example, the color of the 41 ct Dresden Green was described by Kane et al. (1990) as "evenly distributed throughout the gem," despite its large size (29.75 × 19.88 × 10.29 mm). This may represent a diffused green color that penetrated uniformly because the diamond was surrounded by radioactive fluids.

Sometimes a complex history of residency in the earth can be gleaned from radiation stain patterns. A number of examples have been observed where green and brown radiation spots with identical shapes are offset from each other in one direction, sometimes with three or more instances of the same radiation spot along the same trajectory (figure 10). Due to the dynamics of how the spots change color with temperature, we know that the farthest brown spot was oldest and that the stone subsequently moved one or more times due to some tectonic or compaction process while the radiation source remained present. Heating episodes exceeding 500°C must have accompanied the shifting process to cause the spot color changes, followed by a cooling and subsequent re-irradiation of a new spot (Vance et al., 1973). The change in diamond position relative to its environment, combined with the unchanged spot shape, suggests that these spots were adjacent to radioactive mineral grains rather than fluid pockets.

Colored by H3. As mentioned earlier, H3 defects primarily cause yellow bodycolor in diamond, with the green component caused by a strong undertone from a luminescence reaction to visible light. Using a fiber-optic or other strongly focused light source, green luminescence (sometimes referred to as "transmission") with a watery appearance is usually seen in green diamonds colored by H3 defects (figure 9F; see also Kane, 1979a). Although the green color may be uniform in the stone, the structure of H3 as a combination of A-centers with vacancies means that if nitrogen aggregate pairs and vacancies are irregularly distributed, the luminescence will show a similar pattern. For example, diamonds with grain lines caused by plastic deformation sometimes have higher concentrations of A-centers along the graining (Massi et al., 2005) and higher amounts of vacancies available (Fisher, 2009). Consequently, fluorescence from H3 defects in these diamonds can often be seen as an alternating banded pattern between green and nonfluorescent regions.

H-Related Green Color. Unlike the two previous groups, direct evidence of the defects related to green color in H-rich diamonds is typically not visible with a microscope. Some features, however, do occur primarily in diamonds with a high concentration of hydrogen defects. The most common features of these stones are milky particulate clouds that have sharp,

angular boundaries with relatively non-included regions. Sometimes these clouds outline a six-rayed star pattern that is well known in hydrogen-rich stones (figure 9G; see also Wang and Mayerson, 2002; Rondeau et al., 2004). When viewed under UV light, H-rich diamonds often fluoresce yellow as well.

Ni-Related Green Color. Gemological observations from Ni-rich green diamonds are generally not distinctive. Some have been reported to show a uniform weak green luminescence to visible light, similar to that from H3, but it has not been directly linked to the Ni impurities.

LABORATORY GRADING

Stones weighing up to 2.0 ct comprised 82% of GIA's intake of natural green diamonds, with those between 1.0 and 2.0 ct accounting for nearly 40% of that amount (figure 11). Rounds were most prevalent (36%), followed by cushions (26%), cut-cornered rectangles (12%), and pears (9%) (figure 11). Color grade distribution, as mentioned earlier, included 54% yellow-green, 28% pure green, and 12% blue-green, with the remainder having gray or brown undertones (figure 12). Many green diamonds are colored by a combination of defects, making it difficult to assign specific percentages to each cause of color. As an estimate, we used a random sample of 250 natural green diamonds colored by the four main defects to determine that 34% were colored by GR1, 21% by H3, 16% by hydrogen defects, and 1% by nickel defects, while the remainder included some combination of these color centers (figure 12). No discernible trends were observed from clarity grades.

ABSORPTION SPECTROSCOPY

Absorption spectroscopy measurements are nondestructive and provide a detailed look at a diamond's atomic structure by passing light of different wavelengths through the stone and measuring what wavelengths (energies) are absorbed by the impurities and defects present. IR absorption gives information about the impurities in the diamond lattice, while ultraviolet-visible (UV-Vis) absorption reveals the color-producing defects. Each group of green color defects has unique spectroscopic features.

IR Absorption. Details of the major impurity present (nitrogen or boron), as well as the configuration of the atoms of those impurities relative to the rest of the carbon lattice in diamond (diamond type), are quickly and directly measured from IR spectroscopy. In addition, information about other impurities such as hydrogen can be inferred through evaluation of IR features created by complex defects involving those atoms. Infrared spectra are typically collected with the stone kept at room temperature conditions (Anderson, 1943a, 1943b, 1943c; Collins, 2001; Zaitsev 2003).

Figure 11. Most of the natural green diamonds submitted to GIA during the last decade have weighed 1–2 ct or less. Fewer than 5% are larger than 4 carats. Rounds were the predominant shape, followed by cushion, cut-cornered rectangle, and pear shapes.

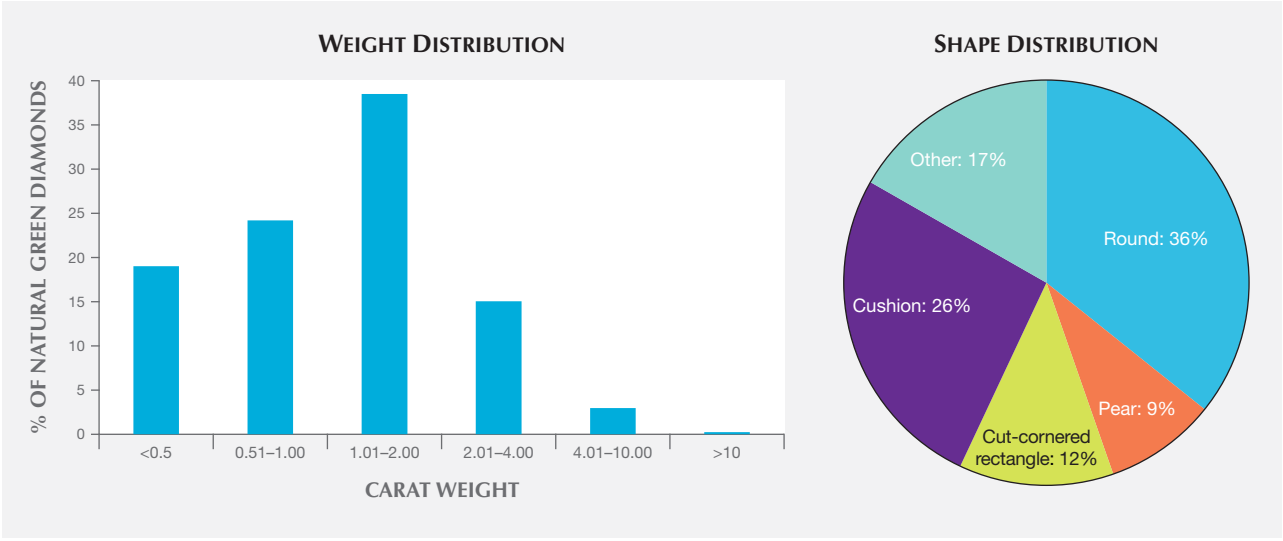

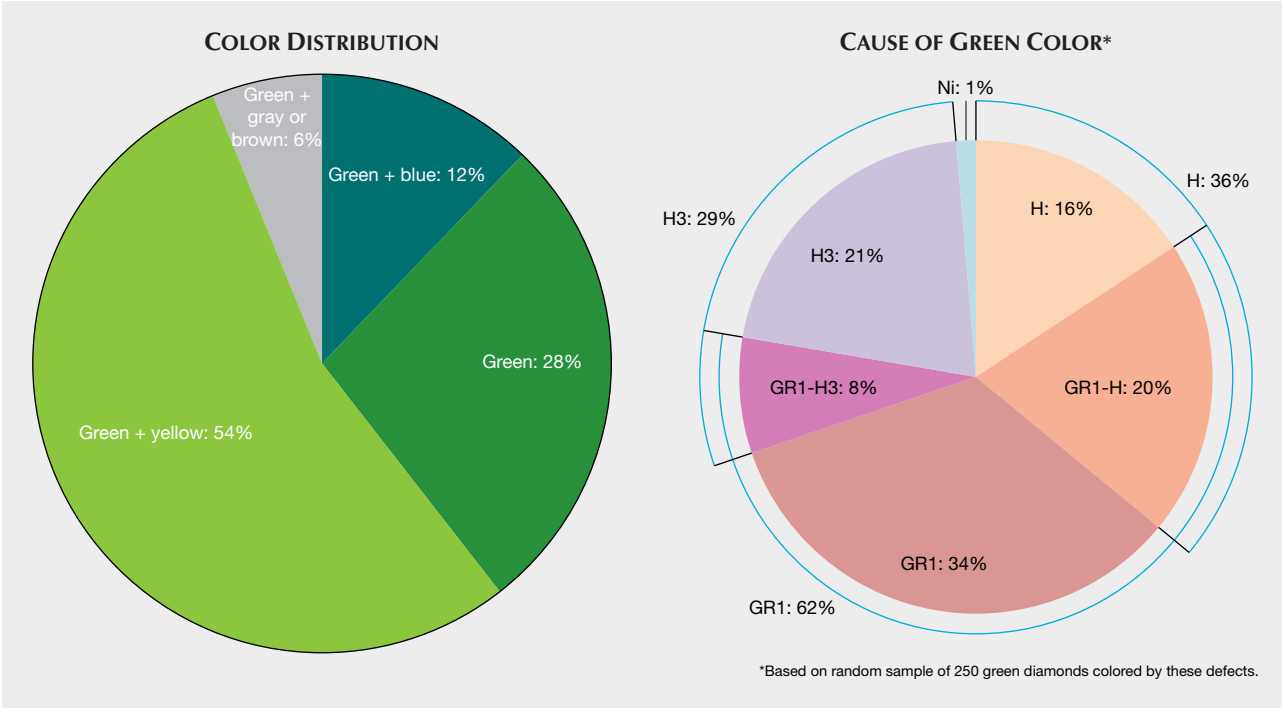

Figure 12. Natural green diamonds submitted to GIA labs over the last decade have been dominated by green + yellow and pure green hues, followed by green + blue color combinations and stones with grayish or brownish undertones. The cause of green color was largely GR1, followed by H3, H, and Ni, with many stones showing combinations of these defects.

Green diamonds colored by H3, H, and Ni defects are all type Ia (containing N impurities). Those with significant H3 defects usually contain low to moderate concentrations of nitrogen, typically both as A-centers (pairs) and B-centers (4N+V) along with associated platelet defects (figure 13; see also Woods, 1986 for platelet defect description). Higher-nitrogen diamonds tend to show very little to no green color from H3 luminescence, even when H3 concentrations are high, because the high levels of A-centers tend to quench the green fluorescence, leaving only the yellow bodycolor due to absorption of H3 (Collins, 2001; Luo and Breeding, 2013). Low concentrations of H-related defects seen at 4496, 3107, and 1405 cm^{-1} are not uncommon. Green diamonds that owe their color to H-related defects have very high concentrations of both H-related defects (4496, 4167, 3236, 3107, 2812, 2785, and 1405 cm^{-1}) and N impurities in the form of A- and B-centers, as well as platelets (1360–1370 cm^{-1}) and related peaks at approximately 1435, 1498, 1525, and 1549 cm^{-1} that shift depending on the A/B center ratio. The concentrations of aggregated N impurities in these stones are so high as to saturate most IR spectrometer detectors (i.e., the peaks extend beyond the upper edge of the infrared spectrum). Green stones colored primarily by Ni-related defects contain very low amounts of nitrogen impurities, predominantly as A-centers (with only occasional traces of B-centers). In many cases, IR spectra also reveal traces of C-centers (i.e., single, substitutional nitrogen) as well as a series of peaks including 3137, 3143, 3180, 3187, 3202, 3242, 3257, and 3272 cm^{-1} that are ascribed to H + C-center defects. Relatively low but variable amounts of the H-related defects seen in H3 diamonds are also present.

Diamonds colored green by GR1 defects from natural radiation span the gamut from high-nitrogen type Ia stones to type IIa diamonds with no measureable nitrogen impurities (figure 13). Likewise, the H content varies widely. The reason for this lack of correlation is the secondary nature of the radiation damage. Any diamond can be exposed to radioactive minerals or fluids after its formation to develop GR1 defects and possibly a green color. The preexisting impurities and other defects will determine whether the green stone resulting from radiation damage has a yellow, gray, or brown undertone, but the green color is entirely introduced secondarily from the original condition of the diamond. One radiation-related defect that occurs as a weak peak in the IR spectrum of some intensely green type Ia natural diamonds is

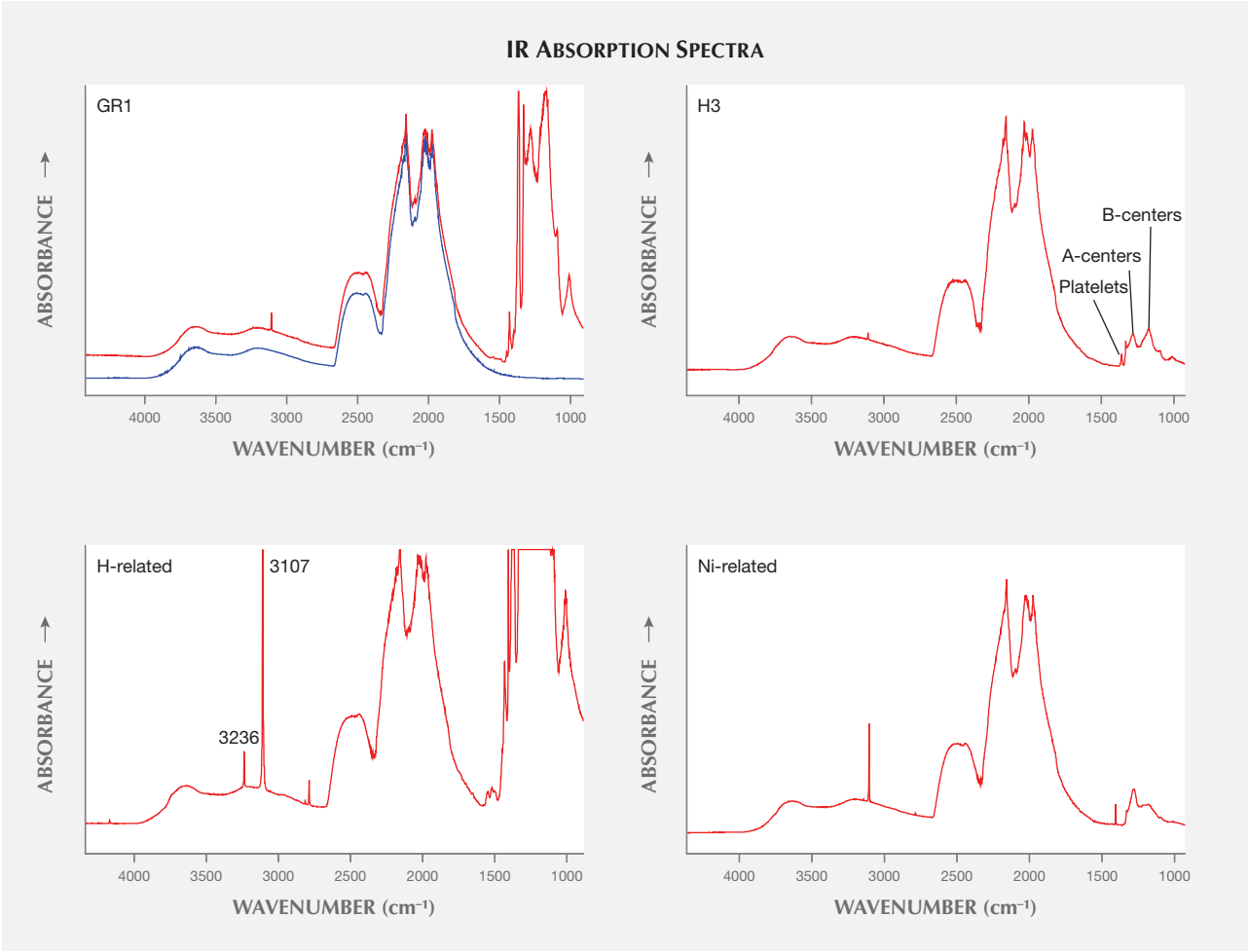

Figure 13. IR absorption spectra from three of the four groups of green diamond defects show generally consistent patterns of nitrogen concentration and aggregation (type Ia). Due to the post-growth nature of radiation damage, GR1-colored diamonds (upper left) tend to span the entire range from type IIa (blue line) to high-nitrogen type Ia stones (red line).

H1a, an interstitial nitrogen defect at 1450 cm^{-1} (Zaitsev, 2003; Dischler, 2012).

UV-Vis-NIR Absorption. Ultraviolet/visible/near-infrared spectroscopy measures the color center absorptions that produce the color we see in a diamond. Although most primary impurity absorptions occur in the IR region, many complex defects (and even some very simple ones) absorb light in the visible part of the spectrum to produce color. These spectra are typically collected at liquid nitrogen temperature (approximately 77 K) to observe narrow peaks from temperature-sensitive defects (Collins, 2001; Shigley and Breeding, 2013).

In the "Causes of Color" section, we discussed the main visible absorption features responsible for color in green diamonds containing GR1, H3, H-related, and Ni-related defects. Here we will detail the less prominent features that tell us more about the nature of the coloring mechanism and how it relates to the color we see. For diamonds colored by H3 or Ni defects alone, UV-Vis-NIR spectra tend to be relatively consistent from stone to stone because both of these defect centers intrinsically coexist with aggregated nitrogen, which always absorbs light toward the blue end of the spectrum and commonly occurs with N3 defects (3N+V) at 415 nm (figure 14). The same is generally true of H-rich diamonds, except that these stones often have accompanying absorptions related to H at 615 nm and more distinctive "cape" absorptions related to nitrogen at 478 nm (N2). Additionally, H-rich green diamonds often have a broad band centered at around 530 nm (figure 14). The combination of this 530 nm band with the N-

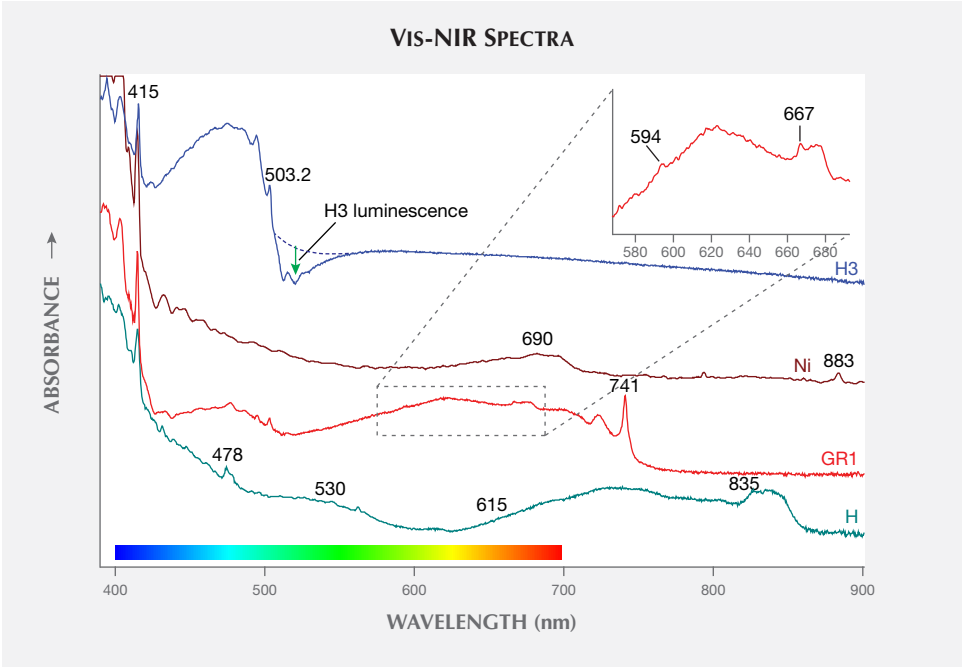

Figure 14. Visible absorption spectra from each of the four green color mechanisms illustrate how different absorptions—and luminescence in the case of H3—can produce green color. In each case, absorption below 450 nm due to nitrogen is important for green coloration.

and H-related visible absorptions causes the lower absorbance part of the spectrum between 500 and 600 nm to be elevated, resulting in the gray undertone that is common in H-rich green diamonds.

Radiation damage in diamond produces a number of defect centers in Vis-NIR spectra in addition to the primary GR1 color center (figure 14). The four most common of these defects occur at 496 (H4), 503.5 (3H), 594, and 667 nm. Natural diamonds remain buried in the near-surface region of the earth for variable amounts of time even after they are exposed to radioactive minerals or fluids. Depending on the depth of residency, green diamonds are commonly exposed to elevated temperatures of a few hundred degrees Celsius that cause a natural annealing effect (Vance et al., 1973). The 667 nm, 594 nm, and 3H defects can all occur from radiation damage alone, without annealing, and are often seen in stones with green radiation stains. The 667 nm center consists of a carbon interstitial that anneals out at 400–500°C (Zaitsev, 2003). The 594 nm center (known to gemologists as the 595 line) is a defect of uncertain structure, possibly consisting of nitrogen atoms and vacancies or interstitials (Collins, 1999; Zaitsev, 2003). It anneals out at approximately 1000°C. The 3H defect is a split carbon interstitial that increases in intensity with annealing and remains stable to at least 600°C (Zaitsev, 2003). The H4 defect at 496 nm is more complex, consisting of four N atoms and two vacancies, and generally forms with radiation damage and subsequent annealing to temperatures above 600°C. H4 is very stable and withstands temperatures of at least 1400°C (Collins, 1997; Zaitsev, 2003).

It is important to remember that radiation damage can also occur simultaneously with any of the other defects that cause green color. It is not uncommon to see H-rich or H3 diamonds with GR1 defects (figure 12, right). We have even observed the occasional Ni-rich diamond with GR1. The combination of multiple causes of green color can dramatically intensify the overall green appearance but often makes identification more difficult, as we will discuss later.

LUMINESCENCE SPECTROSCOPY AND IMAGING

Luminescence spectroscopy measures the light emitted by a diamond in response to stimulation by another source of light, such as a laser or UV lamp. Photoluminescence (PL) uses lasers of different wavelengths to produce emission spectra that reveal the defects present in a stone. DiamondView imaging exposes diamonds to very high-energy UV light (<230 nm) to stimulate fluorescence that can be imaged with great detail (Welbourn et al., 1996). Both techniques are nondestructive and provide important information about the structure of natural green diamonds.

PL Spectroscopy. PL analysis is one of the most useful and sensitive techniques for defect characterization in diamond. Defects occurring at concentrations

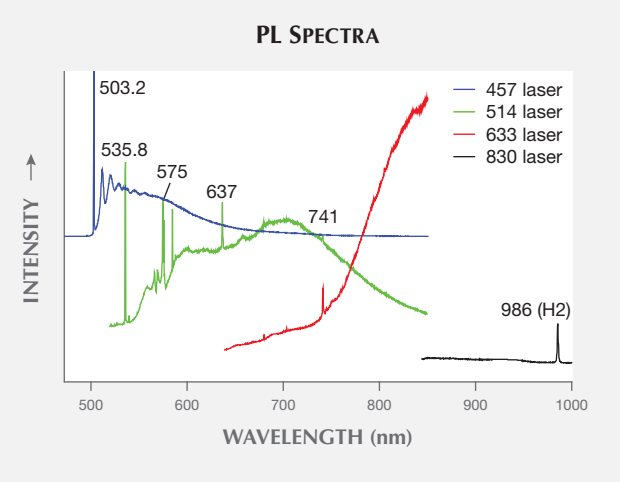

Figure 15. PL spectra of H3-colored green diamonds reveal that H3, H2, and NV defects and a 535.8 nm peak are the main features. Intrinsic diamond Raman lines have been removed for clarity.

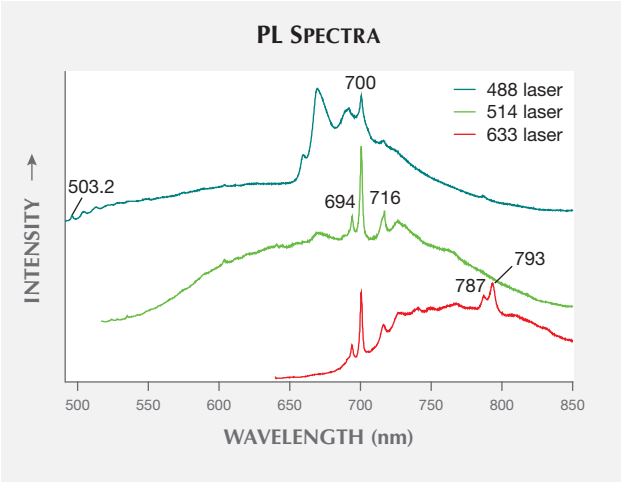

Figure 16. PL spectra from H-rich green diamonds mainly show features attributed to Ni (and possibly H). No features were observed with 830 nm laser excitation (not shown). Intrinsic diamond Raman lines have been removed for clarity.

as low as the ppb (parts per billion) level can easily be detected (Breeding et al., 2010; Eaton-Magaña and Breeding, 2016). Like UV-Vis-NIR absorption, PL measurements of green diamonds are usually focused in the visible range of the electromagnetic spectrum and need to be collected at low temperatures (around 77 K) to resolve many spectral peaks. There are hundreds of PL peaks that might occur in diamond, and some are activated only by certain laser excitation wavelengths since each laser excites luminescence features from diamond in a particular limited range of wavelengths. It would be impossible to characterize every feature—and little is known about many of them—so we have chosen to report representative PL features that are associated with each group of green diamonds.

Green diamonds colored by H3 defects show relatively few prominent PL features. The main peaks are H3 (503.2), 535.8, 575 (NV^0), 637 (NV^-), 741 (GR1), and 986 nm (H2) (figure 15). H2 has the same structure as H3 (N-V-N) but carries a negative electrical charge. Negatively charged defects indicate the presence of trace amounts of single substitutional nitrogen impurities serving as electron donors (Collins et al., 2000; Collins, 2001). The nature of the 535.8 nm feature is unknown, and PL-detectable trace amounts of GR1 are common in many natural diamonds. H-rich green diamonds also contain very few notable PL features. Peaks at 694, 700, 716, 787, and 793 nm are usually encountered with occasional H3 defects (503.2 nm; figure 16). Interestingly, most of these defects (694, 700, 787, and 793 nm) have previously been assigned to complex Ni-N defects (Bokii et al., 1986; Zaitsev, 2003). From our observations, at least two of them, 700 and 793 nm, correlate with A-aggregate concentrations in high-H diamonds. It is possible that these H-rich stones are also high in Ni content but, due to natural annealing and trapping of the Ni impurities by more-abundant aggregated nitrogen, no longer show the 883/885 nm Ni defect. If so, they represent a more N-rich, mature form of Ni-related green diamond. Ni-colored green diamonds show many of the same PL features, including the 700, 787, and 793 nm peaks discussed above that are attributed to Ni-N complexes. Yet these stones also show many other narrow PL features, among which the most consistent and prominent are 603 and 668 nm along with the very strong and well-known Ni doublet at 883/885 nm described earlier (figure 17; see also Zaitsev, 2003; Wang et al., 2007). Little is known about the 603 nm PL feature, but the one at 668 nm has been attributed to a Ni defect (Zaitsev, 2003).

PL spectra collected from diamonds colored by GR1 can vary considerably due to irregular distributions of radiation damage across a stone's surface and interior. PL features related to radiation damage are also dramatically affected by heating, even to relatively low temperatures of a few hundred degrees. In order to represent the PL defects of natural radiation damage, the features below are from Brazilian green diamonds with abundant green radiation stains (meaning they have not been heated to 550–600°C). Similar stones from other localities show the same

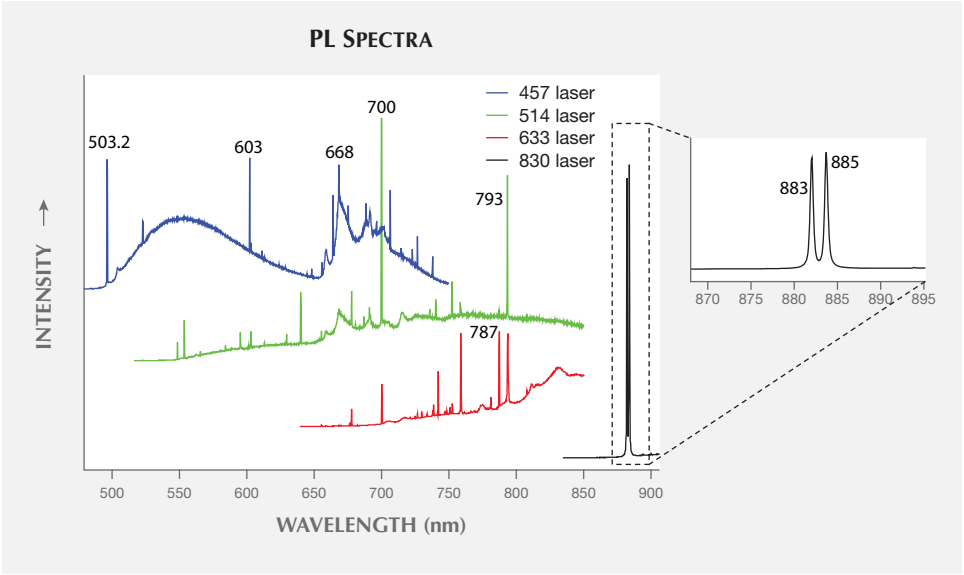

Figure 17. PL spectra from Ni-rich green diamonds contain abundant peaks, including the same Ni-related defects seen in the H-rich stones (though they are much stronger here), as well as the 883, 885 nm Ni-related doublet. Intrinsic diamond Raman lines have been removed for clarity.

features. The strongest PL peaks in these green diamonds are stable defects at 741 and 744 nm (GR1), 503.2 nm (H3), 637 nm (NV^-), and 986 nm (H2). Weaker, much less stable features at 526, 587.9, 647.2, and 722.5 nm are all related to interstitial atoms produced by radiation damage (figure 18). The 526 nm feature has been assigned as nitrogen bound to carbon interstitials, and the one at 587.9 nm is thought to be an interstitial nitrogen atom (Zaitsev, 2003). Little has been reported in the literature about the 647.2 and 722.5 nm defects, but ongoing work by one of the authors (CMB) has shown that these two are related to each other and likely represent interstitial N atoms. The 647.2 and 722.5 nm PL features are completely destroyed by heating to 500°C, and thus do not occur in natural green diamonds with radiation stains that have turned brown.

DiamondView. While photoluminescence records a semi-quantitative spectrum of the light emitted from a diamond at a single spot, DiamondView imaging records the qualitative fluorescence pattern produced

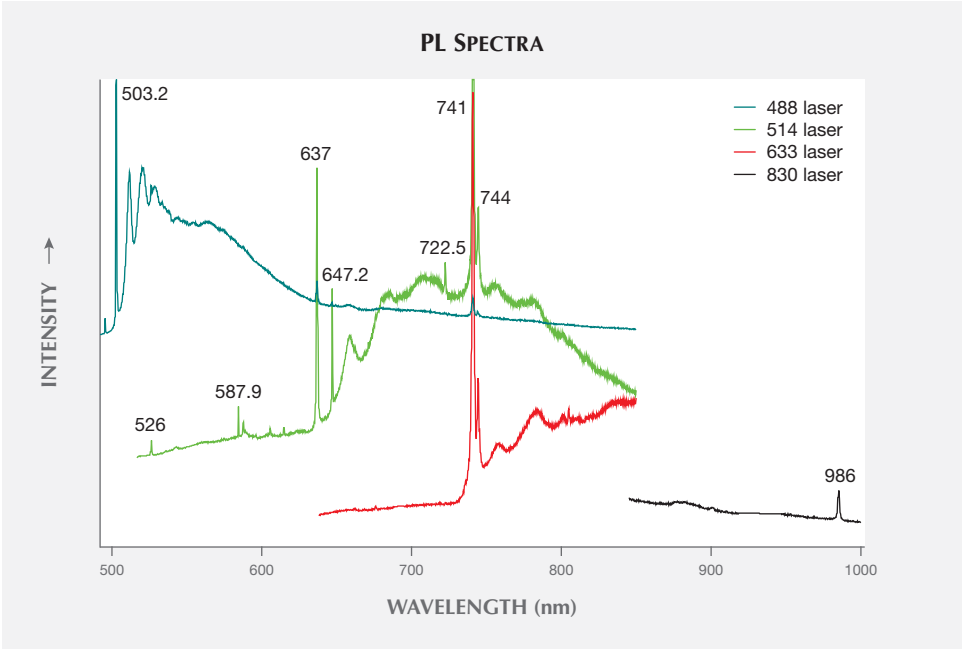

Figure 18. PL spectra from GR1-colored diamonds with green radiation stains reveal relatively stable defects such as GR1, NV^-, and H3, along with unstable interstitial defects at 526, 647.2, and 722.5 nm. Intrinsic diamond Raman lines have been removed for clarity.

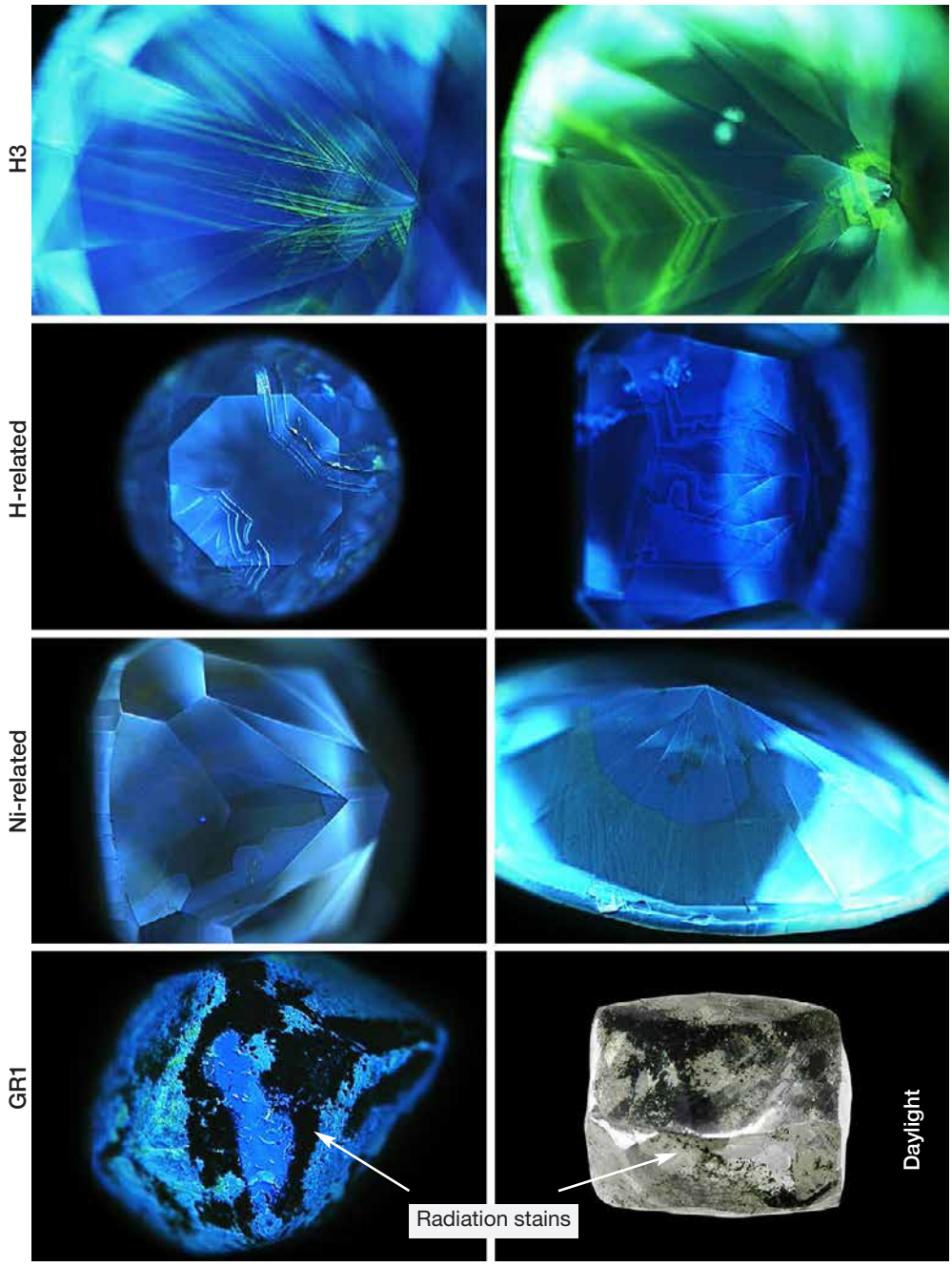

Figure 19. DiamondView fluorescence images from each group show relatively few differences. H3 diamonds mainly show weak to strong isolated green fluorescence, while GR1 diamonds with stains display inert areas due to quenching of fluorescence by strong radiation damage. H- and Ni-related diamonds mainly show patterned blue fluorescence.

over the entire instrument field of view to reveal spatial variations in luminescence. These patterns can be used to separate natural from laboratory-grown diamonds, but also to interpret some of the stone's impurity incorporation and growth history. The DiamondView uses ultra-short-wave UV light (<230 nm) to excite fluorescence from diamonds at room temperature (Welbourn et al., 1996). During UV exposure, the diamond can be rotated to observe fluorescence patterns in several directions.

In green diamonds colored by H3 defects, the most obvious feature shown in the images is green fluorescence from H3 (figure 19), which often follows particular growth zones or plastic deformation structures. Blue fluorescence from N3 defects is also usually visible. The ratio of green to blue fluorescence in the images directly correlates with the total concentration of H3 defects. H-rich diamonds typically show weaker overall fluorescence that is almost always blue from N3 defects. Irregular patterns reflect

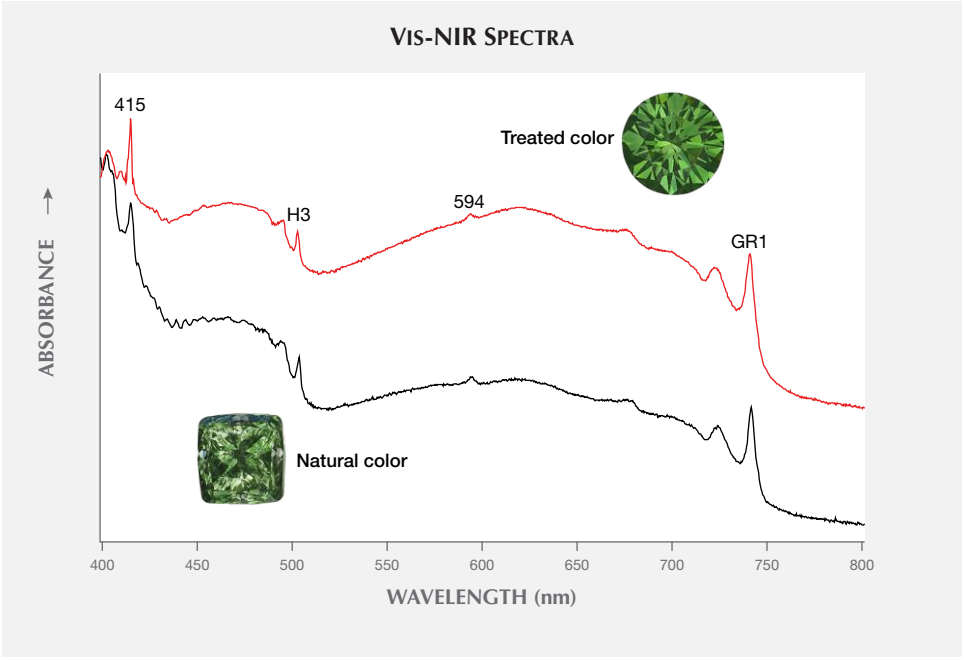

Figure 20. Naturally irradiated and laboratory-irradiated green diamonds show very similar spectra because the same defects are created by both processes. As a result, the color origin of many green diamonds proves very difficult to identify.

cuboid growth, which is often apparent with H diamonds. Isolated green H3 luminescence occurs occasionally at the boundaries between growth zones. Ni diamonds usually contain multiple zones of contrasting fluorescence colors. Blue from N3 is almost always present along with inert zones and/or regions that fluoresce yellowish green (figure 19). The green may be from a Ni-related defect, as there are typically few or no H3 defects seen in these stones. The DiamondView images from green diamonds colored by GR1 are extremely variable because they primarily reflect the defects present in the stones prior to natural irradiation. The observations suggest that high levels of radiation damage tend to quench fluorescence, resulting in areas with radiation staining that appear inert in DiamondView images (figure 19).

IDENTIFICATION CONCERNS

Identification of colored diamonds is a two-step process involving determination of genesis (grown in the earth versus a laboratory) and color origin (a product of natural processes versus treatment). In the case of green diamonds, the first step is relatively easy, but the color origin determination is often problematic. While all the diamonds discussed in this article were identified by GIA as having natural color, green diamonds in general are the single largest group of diamonds that receive "Undetermined" color origin reports from gemological laboratories. Laboratory irradiation using an electron beam takes only a few minutes and can be performed commercially at low cost. This treatment has been performed regularly since the 1950s to create green diamonds, so nearly every green stone in the trade must be regarded with suspicion. Other treatment methods such as embedding diamonds in radioactive compounds, cyclotron and linear accelerators, and gamma ray exposure in nuclear reactors have been employed less frequently to achieve a green color.

As might be expected with the similar processes in nature and the laboratory, the absorption and luminescence spectra from natural- and treated-color green diamonds are virtually identical in many cases (figure 20). Furthermore, almost any kind of diamond can be subjected to irradiation (in nature or the laboratory) to produce a green hue. This means that the preexisting defects, and thus the resulting radiation-related defects, can vary as much as natural heterogeneity in diamond itself. In the absence of obvious color zoning related to laboratory treatment (green culet and a cyclotron "umbrella" pattern), all green diamonds should be sent to a gemological laboratory.

At GIA, we continue to conduct our own irradiation treatment experiments and to examine known natural-color green diamonds from around the world to refine our identification criteria and reduce the number of "Undetermined" reports issued each year. As with all instances of gem testing, the identification of natural- versus treated-color in diamond is based on a variety of features. These identification

Box B: Chameleon Diamonds

Among green diamonds, chameleon diamonds are a fascinating curiosity. They do not directly owe their green color to any of the four major defects discussed in this article. In fact, they span a wide range of color, from predominantly yellow to green hues. What makes these stones particularly interesting is that when heated or left in the dark for an extended period of time (days to weeks), they temporarily lose their green color and change to yellow or orangy hues (figure B-1, top) through energetic shifts in the broad visible absorption bands that cause their color. Within a few seconds to several minutes of being removed from darkness or allowed to cool after heating, chameleon diamonds regain their greenish color. The nature of the color change remains unclear, but these unique diamonds have a cherished niche among collectors (Fritsch et al., 1995; Hainschwang et al., 2005; Fritsch et al., 2007).

Over the last decade, a few thousand chameleon diamonds have been documented within GIA's laboratories; the vast majority had a stable color that included a green contribution (figure B-1, bottom left). Nearly half were grayish yellow-green, and only about 1% had pure green hues; 83% of the chameleons seen at GIA had gray or brown color components as well. Chameleon diamonds were generally smaller than other natural green diamonds (e.g., figure 11), with most weighing less than 1.0 ct (figure B-1, bottom right).

UV fluorescence was a distinctive feature among the chameleon diamonds. Of these, 74% showed yellow fluorescence and another 18% exhibited orange or orangy yellow fluorescence in response to long-wave UV exposure. The intensity of the long-wave fluorescence was predominantly strong (92%). Under short-wave UV illumination, 86% showed yellow fluorescence and another 13% exhibited orange or orangy yellow fluorescence. The intensity of the short-wave UV fluorescence was predominantly medium (85%). Additionally, all the chameleon diamonds exhibited short-wave UV phosphorescence that was usually weak in intensity (54%) and yellow in color (96%).

GIA laboratory reports include a special comment indicating the unique color-change property of a chameleon diamond. To receive this comment on a report, a diamond must have a green color component (either primary or secondary), it must display phosphorescence to short-wave UV light, and it must change color from greenish to yellow or orange upon gentle heating or removal from light. Tremendous caution must be taken when heating green diamonds, as those colored by GR1 defects may permanently lose some or all of their green color. While chameleon diamonds cross the boundary between green and yellow stones, they remain an interesting oddity that accentuates the novelty of green diamonds.

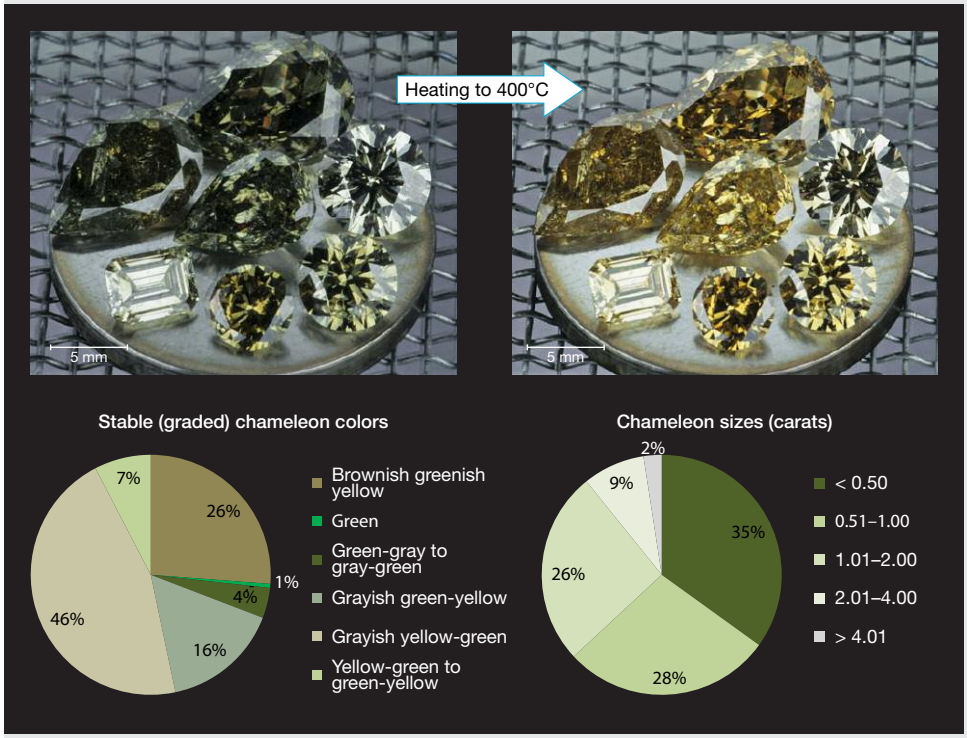

Figure B-1. Chameleon diamonds (top) change from a greenish color to a yellow or orange hue when heated or kept in the dark. Of the chameleon diamonds seen at GIA over the last decade (bottom), most have stable colors of grayish yellow-green and brownish greenish yellow and less than 0.5 ct in size. Photos by C.M. Breeding.

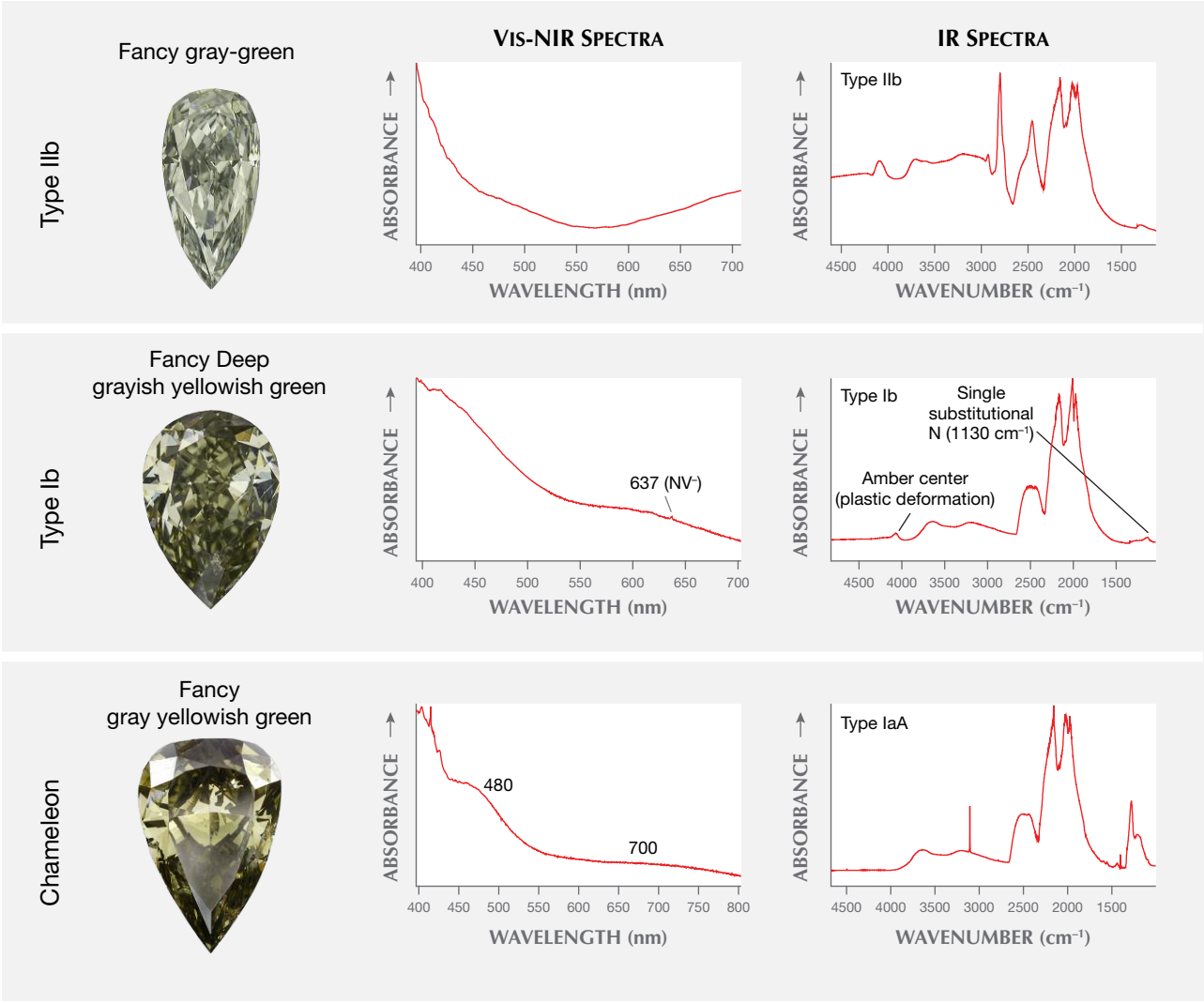

Figure 21. While the vast majority of green diamonds fall into the four categories described in this article, a few very unusual stones with green hues are type IIb, type Ib, or chameleon stones. These very rare diamonds have distinctive spectroscopic features that make them relatively easy to spot.

criteria are considered proprietary information to protect the integrity of GIA's grading report service. To support our conclusion on color origin, dealers sometimes bring an important rough green diamond for us to examine before manufacturing and then during several stages of the process. This allows us to study the progression of the color appearance of the cut stone, and to confirm that it originated from the starting piece of rough.

UNUSUAL EXAMPLES

We have discussed the four major causes of green color in gem diamonds. These are responsible for some 95% of the naturally green diamonds seen at GIA's laboratories in the last decade. As with anything natural, there are a few unusual diamonds with green color components that do not fall within the aforementioned groups. These include type IIb and Ib stones as well as chameleon diamonds (figure 21 and box B). Type IIb diamonds are typically blue due to boron impurities that absorb light from the infrared all the way through the visible spectrum, with the absorption higher at the red end of the spectrum than the blue end. In a few extremely rare cases, a type IIb diamond also has strong absorption from 400 to 500 nm, resulting in a green hue (Crowningshield, 1965; Scarratt, 1989). The cause of the higher-energy absorption is unclear, but it might be elevated trace

Figure 22. Natural-color green diamonds such as these beautiful gems span a range of colors. From left to right: Fancy Vivid green-blue (2.06 ct), Fancy Vivid yellow-green (1.01 ct), Fancy Dark gray-greenish yellow (3.08 ct), and Fancy Intense yellow-green (2.01 ct). Each of the four main color-causing mechanisms usually produces slightly different green hues. Photo by Robert Weldon/GIA, courtesy of Optimum Diamonds.

concentrations of nitrogen impurities that are masked in the IR by the excessive boron. Type Ib diamonds contain single substitutional nitrogen impurities that absorb strongly in the UV to blue part of the spectrum, generating a strong yellow color. If a type Ib diamond is plastically deformed and has enough vacancies to increase the NV^- (637 nm) defect concentration significantly enough to absorb light in the red region, the stone has a greenish hue (usually also grayish or brown from the plastic deformation vacancy cluster absorption, causing a rise to higher energies). The last and perhaps most abundant and interesting oddity is the chameleon diamond (box B). Chameleons are type IaA diamonds (usually with moderate N content) that exhibit broad 480 nm (unknown structure) and 700 nm (H- or Ni- related) bands in the visible spectrum that often give rise to a greenish hue (usually brownish or grayish and termed "brackish"). These popular color-changing collectors' stones occupy their own niche in the diamond trade.

CONCLUSIONS

Natural-color green diamonds (figure 22) are rare and beautiful, with a variety of defects that can be responsible for their color. Today, most are discovered in South American or African mines. The main causes of green color in gem diamonds, either as the sole mechanism or in combination, are vacancies produced by radiation damage (GR1), H3 defects, H-related defects, or Ni impurities. Each of these gives rise to a slightly different green hue. GR1-colored green diamonds are most abundant, followed by those colored by H3 green luminescence. H- and Ni-related green stones are less common. Each group of green color centers displays gemological clues as well as absorption and luminescence spectra that aid in their identification. Both GR1 and H3 defects can be easily induced in diamond by laboratory irradiation and annealing, a process that has been applied since the 1950s. GIA has made significant progress in determining the origin of color of green diamonds since the 1950s and '60s, when the vast majority were described as undetermined. Today, most green diamonds have a definitive origin determination. Due to the similarities between natural radiation damage and laboratory treatment effects, color origin determinations of green diamonds are not always possible and have turned these rare and exquisite gemstones into the beautiful conundrum they are.

ABOUT THE AUTHORS
Dr. Breeding and Dr. Eaton-Magaña are senior research scientists, and Dr. Shigley is a distinguished research fellow, at GIA in Carlsbad, California.

ACKNOWLEDGMENTS
The authors wish to thank the Natural History Museum of Los Angeles County and Optimum Diamonds (New York) for allowing us to photograph pieces from the Gamma Collection for this article.

REFERENCES

Anderson B.W. (1943a) Absorption and luminescence in diamond – I. *The Gemmologist*, Vol. 12, No. 138, pp. 21–22.
——— (1943b) Absorption and luminescence in diamond – II. *The Gemmologist*, Vol. 12, No. 139, pp. 25–27.
——— (1943c) Absorption and luminescence in diamond – III. *The Gemmologist*, Vol. 12, No. 141, pp. 33–35.
Ardon T. (2013) Lab Notes: Diamond with high concentration of nickel. *G&G*, Vol. 49, No. 3, pp. 173–174.
Astric H., Astric B., Merigoux H., Zecchini P. (1994) Evaluation de la masse de Dresde Vert par calcul. *Revue de Gemmologie a.f.g.*, No. 120, pp. 13–14.
Bokii G.B., Bezrukov G.N., Klyuev Y.A., Naletov A.M., Nepsha V.I. (1986) *Natural and Synthetic Diamonds*. Nauka, Moscow, p. 31 [in Russian].
Bosshart G. (1989) The Dresden Green. *Journal of Gemmology*, Vol. 21, No. 6, pp. 351–362, http://dx.doi.org/10.15506/JoG.1989.21.6.351
——— (1994) Investigations modernes du diamant vert de Dresden et interpretation des resultats. *Revue de Gemmologie a.f.g.*, No. 121, pp. 5–12.
Breeding C.M. (2011) Hydrogen-rich diamonds from Zimbabwe with natural radiation features. *G&G*, Vol. 47, No. 2, pp. 129–130.
Breeding C.M., Shigley J.E. (2009) The "type" classification system of diamonds and its importance in gemology. *G&G*, Vol. 45, No. 2, pp. 96–111, http://dx.doi.org/10.5741/GEMS.45.2.96
Breeding C.M., Shen A.H., Eaton-Magaña S., Rossman G.R., Shigley J.E., Gilbertson A. (2010) Developments in gemstone analysis techniques and instrumentation during the 2000s. *G&G*, Vol. 46, No. 3, pp. 241–257, http://dx.doi.org/10.5741/GEMS.46.3.241
Chaves M.L.S.C., Karfunkel J., Banko A., Stasiulevicius R., Svisero D.P. (1996) Diamantes de capa verde: Freqüência, distribuição e possível origem nos depósitos diamantiferos de Minas Gerais. Boletim Instituto de Geociências - Universidade de São Paulo, Vol. 27, pp. 51–60.
Chaves M.L.S.C., Karfunkel J., Stasiulevicius R., Brandao P.R.G., Chambel L. (2001) Discussão sobre a natureza das cores verde e marrom (em "capas" ou "verdadeiras") em diamantes do SE-Brasil (Minas Gerais) e NE-Angola (Lunda). *Revista Brasileira de Geociencias*, Vol. 31, No. 4, pp. 575–582.
Coenraads R.R., Webb G., Sechos B. (1994) Alluvial diamond deposits of the Guaniamo Region, Bolivar State, Venezuela. *Australian Gemmologist*, Vol. 18, No. 9, pp. 287–294.
Collins A.T. (1997) The electronic and optical properties of diamond. In A. Paoletti and A. Tucciarone, Eds., *The Physics of Diamond*. Course 135, Proceedings of the International School of Physics, IOS Press, Amsterdam, p. 273.
——— (1999) Things we still don't know about optical centres in diamond. *Diamond and Related Materials*, Vol. 8, No. 8-9, pp. 1455–1462, http://dx.doi.org/10.1016/S0925-9635(99)00013-8
——— (2001) The colour of diamond and how it may be changed. *Journal of Gemmology*, Vol. 27, No. 6, pp. 341–359, http://dx.doi.org/10.15506/JoG.2001.27.6.341
Collins A.T., Kanda H., Kitawaki H. (2000) Colour changes produced in natural brown diamonds by high-pressure, high-temperature treatment. *Diamond and Related Materials*, Vol. 9, No. 2, pp. 113–122, http://dx.doi.org/10.1016/S0925-9635(00)00249-1
Crowningshield R. (1965) Developments and highlights at the Gem Trade Lab in New York. *G&G*, Vol. 11, No. 11, pp. 331–338.
DeMarco A. (2016) "Aurora Green" diamond sells for record breaking $16.8 million. Forbes.com, https://www.forbes.com/sites/anthonydemarco/2016/05/31/aurora-green-diamond-sells-for-record-breaking-16-8-million/
Dischler B. (2012) *Handbook of Spectral Lines in Diamond, Volume 1: Tables and Interpretations*. Springer-Verlag, Berlin.
Draper T. (1951) The diamond mines of Diamantina – Past and present. *G&G*, Vol. 7, No. 2, pp. 49–57.
Eaton-Magaña S.C., Breeding C.M. (2016) An introduction to photoluminescence spectroscopy for diamond and its applications in gemology. *G&G*, Vol. 52, No. 1, pp. 2–17, http://dx.doi.org/10.5741/GEMS.52.1.2
Eaton-Magaña S.C., Moe K.S. (2016) Temperature effects on radiation stains in natural diamonds. *Diamond and Related Materials*, Vol. 64, pp. 130–142, http://dx.doi.org/10.1016/j.diamond.2016.02.009
Ehrmann M. (1950) Bombarded diamonds. *G&G*, Vol. 6, No. 10, pp. 295–297.
Fisher D. (2009) Brown diamonds and high pressure high temperature treatment. *Lithos*, Vol. 112S, pp. 619–624, http://dx.doi.org/10.1016/j.lithos.2009.03.005
Fritsch E., Shigley J.E. (1991) Optical properties of some natural-color and laboratory-irradiated green to blue diamonds. In R. Messier, J.T. Glass, J.E. Butler, and R. Roy, Eds., *Proceedings of the Second International Conference—New Diamond Science and Technology*, Washington DC, September 23–27, 1990. Materials Research Society, Pittsburgh, Pennsylvania, pp. 677–681.
Fritsch E., Shigley J.E., Moses T., Rossman G.R., Zucker B., Balfour I. (1995) Examination of the twenty-two carat green chameleon diamond. In D.J. Content, Ed., *A Green Diamond: A Study of Chameleonism*. W.S. Maney & Son, Leeds, England, 42 pp.
Fritsch E., Massi L., Rossman G.R., Hainschwang T., Jobic S., Dessapt R. (2007) Thermochromic and photochromic behavior of "chameleon" diamonds. *Diamond and Related Materials*, Vol. 16, No. 2, pp. 401–408, https://doi.org/10.1016/j.diamond.2006.08.014
Goss J.P., Briddon P.R., Hill V., Jones R., Rayson M.J. (2014) Identification of the structure of the 3107 cm^{-1} H-related defect in diamond. *Journal of Physics: Condensed Matter*, Vol. 26, No. 14, pp. 1–6, http://dx.doi.org/10.1088/0953-8984/26/14/145801
Guo J.Q., Chen F., Den H.X., Tan Y.M., Rong Z.Q., Den E. (1986) The colour of placer diamonds in Hunan. *Acta Mineralogica Sinica*, Vol. 6, No. 2, pp. 132–138.
Hainschwang T., Simic D., Fritsch E., Deljanin B., Woodring S., DelRe N. (2005) A gemological study of a collection of chameleon diamonds. *G&G*, Vol. 41, No. 1, pp. 20–35, http://dx.doi.org/10.5741/GEMS.41.1.20
Hough E. (1913) The great green diamond. *Metropolitan Magazine*, Vol. 38, No. 1, pp. 9–13, 69.

Kane R.E. (1979a) Developments and Highlights at GIA's Lab in Los Angeles: Green graining. *G&G*, Vol. 16, No. 7, p. 210.
——— (1979b) Developments and Highlights at GIA's Lab in Los Angeles: Radiation stains. *G&G*, Vol. 16, No. 7, p. 211.
Kane R.E., McClure S.F., Menzhausen J. (1990) The legendary Dresden Green diamond. *G&G*, Vol. 26, No. 4, pp. 248–266, http://dx.doi.org/10.5741/GEMS.26.4.248
Koptil V.I., Zinchuk N.N. (2000) A change in diamond properties induced by natural radioactive irradiation. *Journal of Superhard Materials*, Vol. 22, No. 2, pp. 56–57.
Luo Y., Breeding C.M. (2013) Fluorescence produced by optical defects in diamond: Measurement, characterization, and challenges. *G&G*, Vol. 49, No. 2, pp. 82–97, http://dx.doi.org/10.5741/GEMS.49.2.82
Massi L., Fritsch, E., Collins A.T., Hainschwang T., Notari F. (2005) The "amber centres" and their relation to the brown colour in diamond. *Diamond and Related Materials*, Vol. 14, No. 10, pp. 1623–1629, http://dx.doi.org/10.1016/j.diamond.2005.05.003
Mendelssohn M.J., Milledge H.J., Vance E.R., Nave E., Woods P.A. (1979) Internal radioactive haloes in diamond. *Diamond Research*, Vol. 17, No. 2, pp. 21–26.
Mennell F.P. (1915) Note on the colours of some alluvial diamonds. *Mineralogical Magazine*, Vol. 17, No. 81, pp. 202–204, http://dx.doi.org/10.1180/minmag.1915.017.81.07
Meyer H.O.A., Milledge H.J., Nave E. (1965) Natural irradiation damage in Ivory Coast diamonds. *Nature*, Vol. 206, No. 4982, p. 392, http://dx.doi.org/10.1038/206392a0
Miller J. (2011) U.S. sanctions prohibit trade with Zimbabwe's diamond entities. Diamonds.net, Nov. 2, http://www.diamonds.net/News/NewsItem.aspx?ArticleID=37681
Morel B. (1994) La veritable histoire du diamant vert de Dresden. *Revue de Gemmologie a.f.g.*, No. 121, pp. 2–3.
Nasdala L., Grambole D., Wildner M., Gigler A.M., Hainschwang T., Zaitsev A.M., Harris J.W., Milledge J., Schulze D., Hofmeister W., Balmer W.A. (2013) Radio-colouration of diamond: A spectroscopic study. *Contributions to Mineralogy and Petrology*, Vol. 165, No. 5, pp. 843–861, http://dx.doi.org/10.1007/s00410-012-0838-1
Raal F.A., Robinson D.N. (1981) Research into green diamonds. *Diamond News and S.A. Jeweller*, Vol. 44, No. 6, pp. 47–53.
Rondeau B., Fritsch E., Guiraud M., Chalain J.-P., Notari F. (2004) Three historical 'asteriated' hydrogen-rich diamonds: Growth history and sector-dependent impurity incorporation. *Diamond and Related Materials*, Vol. 13, No. 9, pp. 1658–1673, http://dx.doi.org/10.1016/j.diamond.2004.02.002
Rosch S. (1957) Das Grune Gewölbe in Dresden. *Zeitschrift der Deutschen Gesellschaft fur Edelsteinkunde, Sonderheft*, pp. 79–84.
Roskin G. (2000) Provenance of a green diamond. *Jewelers' Circular Keystone*, Vol. 171, No. 9, pp. 158–169.
Scarratt K. (1989) Naturally coloured green type IIb diamond. *Journal of Gemmology*, Vol. 21, No. 6, p. 346.
Shigley J.E., Breeding C.M. (2013) Optical defects in diamond: A quick reference chart. *G&G*, Vol. 49, No. 2, pp. 107–111, http://dx.doi.org/10.5741/GEMS.49.2.107
Shigley J.E., Fritsch E. (1990) Optical properties of some greenish blue to green diamonds. *SPIE Proceedings*, Vol. 1325, pp. 315–324.
Themelis T. (1987) Diamonds from Venezuela. *Lapidary Journal*, Vol. 41, No. 4, pp. 59–64.
Titkov S.V., Ivanov A.I., Marfunin A.S., Bershov L.V., Kulakov V.M., Chukichev M.V. (1995) Irradiation as the cause of the bulk green color in natural diamonds. *Doklady Earth Sciences*, Vol. 337, No. 5, pp. 133–138.
Vance E.R., Milledge H.J. (1972) Natural and laboratory α-particle irradiation of diamond. *Mineralogical Magazine*, Vol. 38, No. 299, pp. 878–881, http://dx.doi.org/10.1180/minmag.1972.038.299.11
Vance E.R., Harris J.W., Milledge H.J. (1973) Possible origins of α-damage in diamonds from kimberlite and alluvial sources. *Mineralogical Magazine*, Vol. 39, No. 303, pp. 349–360, http://dx.doi.org/10.1180/minmag.1973.039.303.12
Wang W., Mayerson W. (2002) Symmetrical clouds in diamond – the hydrogen connection. *Journal of Gemmology*, Vol. 28, No. 3, pp. 143–152, http://dx.doi.org/10.15506/JoG.2002.28.3.143
Wang W., Hall M., Breeding C.M. (2007) Natural type Ia diamond with green-yellow color due to Ni-related defects. *G&G*, Vol. 43, No. 3, pp. 240–243, http://dx.doi.org/10.5741/GEMS.43.3.240
Welbourn C.M., Cooper M., Spear P.M. (1996) De Beers natural versus synthetic diamond verification instruments. *G&G*, Vol. 32, No. 3, pp. 156–169, http://dx.doi.org/10.5741/GEMS.32.3.156
Woods G.S. (1986) Platelets and the infrared absorption of type Ia diamonds. *Proceedings of the Royal Society A*, Vol. 407, No. 1832, pp. 219–238, http://dx.doi.org/10.1098/rspa.1986.0094
Zaitsev A.M. (2003) *Optical Properties of Diamond: A Data Handbook*. Springer-Verlag, Berlin.

Iridescence in Metamorphic "Rainbow" Hematite

Xiayang Lin, Peter J. Heaney, and Jeffrey E. Post

The authors investigated "rainbow" hematite from Minas Gerais, Brazil, using electron microscopy, atomic force microscopy, and synchrotron X-ray diffraction to determine the cause of its intense wide-angle iridescence. The study revealed that the interference is produced by a highly periodic microstructure consisting of spindle-shaped hematite nanocrystals containing minor Al and P impurities. The nanorods are 200–300 nm in length and 50–60 nm in width. They are arranged in three orientations at 120° angles with respect to each other and stacked layer by layer to form the bulk crystal. The distances between adjacent parallel spindle-shaped particles within the same layer fall in the range of 280–400 nm, generating a diffraction grating for visible light. The organized substructure is apparent on all freshly fractured surfaces, suggesting that it represents more than an exterior surface coating. The authors propose that this periodic substructure results from arrested crystal growth by the oriented aggregation of hematite nanorods.

Hematite specimens that frequently display iridescence are described as "rainbow hematite" and "turgite" (figure 1). The latter term originated with the German mineralogist Rudolph Hermann, who coined it in 1844 to describe iron hydroxide specimens found near the Turginsk River in the Ural Mountains (Hermann, 1844). "Turgite" was discredited as a distinct mineral name in the 1920s, however, based on thermogravimetric (Posnjak and Merwin, 1919) and X-ray diffraction (Böhm, 1928; Palache et al., 1944) studies that identified such specimens as mixtures of microcrystalline hematite (Fe_2O_3) and either goethite (FeOOH) or amorphous Fe hydroxide. Nevertheless, "turgite" has been retained by the mineral collecting and gem community as a catch-all term for naturally iridescent iron (hydr)oxide minerals.

Mineral dealer Rock Currier (1940–2015) was largely responsible for introducing rainbow hematite to the U.S. market. According to notes he published on Mindat.org, Currier first visited an outcrop of what he called "color rock" from the Andrade mine in João Monlevade, Minas Gerais, Brazil, in 1991 (figure 2; Currier, 2012). Shortly after, he shipped a truckload of 55-gallon barrels filled with an estimated 15 tons of the material to the United States. Initially he attempted to sell the rainbow hematite "by the barrel for $3 per pound without very much luck." At a subsequent Tucson Gem and Mineral Show, however, he "arrived to find some guy had rented a big billboard and was selling the stuff as the latest and greatest metaphysical jewelry item. One guy was backing little pieces of the stuff with obsidian and selling earrings…for $90 a pair." Fortunately, Currier had kept enough of the rainbow hematite to select higher-grade samples, and he saw brisk sales of individual pieces.

Bulk samples of this Brazilian rainbow hematite are still sold at major mineral and gem shows, but our discussions with dealers indicate a growing

In Brief

- Iridescent hematite schists from Brazil were analyzed by high-resolution imaging and spectroscopy techniques.
- Rainbow colors arise from the interference of light waves reflecting off arrays of spindle-shaped hematite nanocrystals.
- These nanocrystals assembled through "oriented aggregation" as controlled by hematite's threefold symmetry.

See end of article for About the Authors and Acknowledgments.
Gems & Gemology, Vol. 54, No. 1, pp. 28–39,
http://dx.doi.org/10.5741/GEMS.54.1.28

Figure 1. Rainbow hematite from the Andrade mine in João Monlevade, Minas Gerais, Brazil. Photo © Rock Currier, Mindat.org.

scarcity. Currier attempted to purchase more material from the mine, but apparently the major seam of rainbow hematite at Andrade underlies the primary mine haul road, and excavation would have destabilized this conduit to the open pit. Nevertheless, exquisite pieces of rainbow hematite jewelry are still sold online, with accent stones such as amethyst, apatite, sapphire, tourmaline, and tsavorite (figure 3). Moreover, rainbow hematite plays an important role in the local culture. Villages neighboring the city of Belo Horizonte traditionally sprinkle the streets with truckloads of powdered material for festivals, creating an effect that Currier (2012) likened to "standing in a pile of peacock feathers."

To our knowledge, Ma and Rossman (2003a,b) have performed the only scientific investigation into the cause of iridescence in rainbow hematite, analyzing specimens from Brazil, Mexico, Italy, and several sites in the United States. Their results are also briefly highlighted in Nadin (2007). Using field-emission scanning electron microscopy (FESEM), Ma and Rossman (2003b) reported that their rainbow hematite specimens were coated with a "thin film" of rod-shaped nanocrystals, each measuring 5 to 35 nm in thickness and hundreds of nm in length. These nanocrystals were oriented in three directions, at 120º angles with respect to each other, and formed a grid-like network.

Figure 2. Rock Currier (left) and colleague survey a seam of rainbow hematite at the Andrade mine. Photo © Rock Currier, Mindat.org.

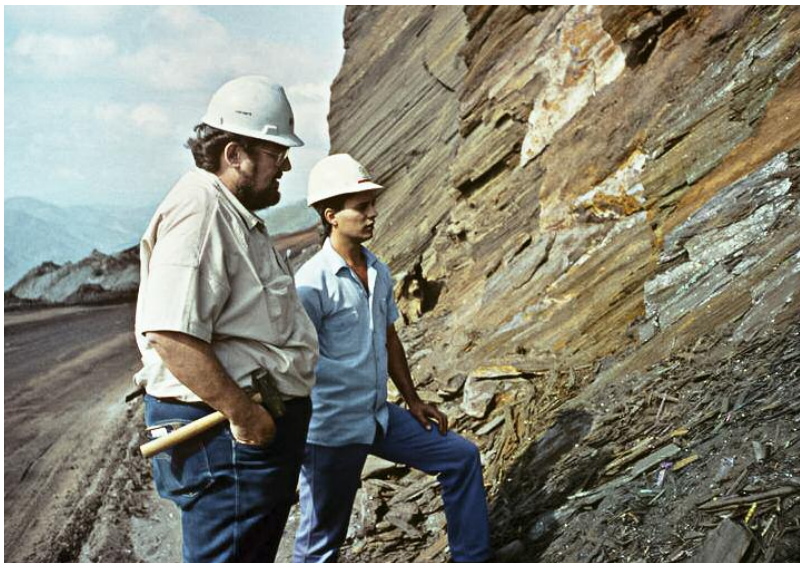

Figure 3. Left: An 18K gold pendant featuring rainbow hematite from Minas Gerais, Brazil, accented with amethyst and apatite. Right: Rainbow Rapture ring in 18K gold with tourmaline, sapphire, and tsavorite. Designs by Judith Anderson. Photos by The Jewelry Experts, Bijoux Extraordinaire, Ltd.

The nanocrystals were too small to determine precise chemical compositions, but energy-dispersive spectroscopy (EDS) revealed high concentrations of Al and P in a ratio that varied from 2.2 to 3.8. Ma and Rossman (2003b) noted that "the minute crystals have failed to produce either an X-ray powder diffraction pattern, an electron back-scatter diffraction pattern, or a Raman spectrum." The study interpreted the rod-like nanocrystals as a new mineral, but a full characterization was not possible with the resolution of the instrumentation.

Over the 15 years since these results were published online, more sophisticated analytical techniques have become available. For the present study, we sought to determine whether iridescence in rainbow hematite arises from thin-film effects involving Al phosphate phases, as earlier researchers hypothesized, or whether a different mechanism is involved. Rainbow effects in minerals are commonly attributed to nanoscale coatings, as in bornite (Buckley and Woods, 1983; Vaughan et al., 1987) and fire obsidian (Ma et al., 2001, 2007). Yet many gem materials (e.g., opal, labradorite, iris agate, and iris quartz) contain modular substructures that create a diffraction grating for visible light and generate rainbow effects (Darragh et al., 1966; Miura and Tomisako, 1978; Heaney and Davis, 1995; Lin and Heaney, 2017). These substructures often yield insights into exotic crystal growth processes that can inspire pathways for the self-assembly of synthetic materials. For the present investigation, we examined rainbow hematite from the Andrade mine using a combination of light optical microscopy, X-ray diffraction (XRD) and Rietveld analysis, FESEM, and atomic force microscopy (AFM).

MATERIALS AND METHODS

Specimen Description. We purchased the iridescent hematite samples used in this study at the 2014 Tucson Gem and Mineral Show from Cinderhill Gems (Meadow Vista, California), who traced the material to Rock Currier's bulk shipment from Brazil in the 1990s. The specimens we studied appeared identical in macroscopic physical character to those described by Currier (2012). As noted below, the microstructures matched the descriptions for Andrade hematite in Rosière et al. (2001) and Ma and Rossman (2003b). Thus, we concluded that the rainbow hematite in this study indeed derives from the Andrade mine.

The Andrade iron ore deposit is located in the eastern high-strain domain of the Quadrilátero Ferrífero district (figure 4) in the southern part of the São Francisco Craton of Brazil (de Almeida, 1977). The Quadrilátero Ferrífero (or "Iron Quadrangle") is so called because the Paleoproterozoic metasediments in the Minas Supergroup exhibit a rectangular arrangement of synclines (Rosière et al., 2001; Rosière and Chemale, 2008). The Caraça, Itabira, Piracicaba, and Sabará groups are four sequences of the Minas Supergroup rocks (Dorr, 1969; Mendes et al., 2017; see figure 5). The iron ore deposits are located within metamorphosed banded-iron formations in the Cauê Formation of the Itabira Group; the Andrade mine is in a contact-metamorphic zone within this formation. The rainbow hematite occurs as iridescent, specular seams oriented parallel to bedding. The material is brittle and fractures into lath-like splinters, but the crystals within the laths have a *granoblastic* texture, a term used to describe equigranular minerals without sharp crystal faces in metamorphic rocks. Rosière et al. (2001) attribute these textures to post-tectonic deformation and recrystallization.

The Andrade rainbow hematite seam occurs within a banded-iron formation (BIF) in the Itabira Group (again, see figure 5), which has lent its name to a broad class of metamorphic rocks called *itabirites*. These are hematitic (rather than mica) schists that formed when the original jasper bands in the BIF recrystallized into distinct layers of macroscopic quartz and hematite (or sometimes magnetite). The hematite schists, from which we infer the rainbow hematite derives, are intergrown within itabirites (Barbour, 1973).

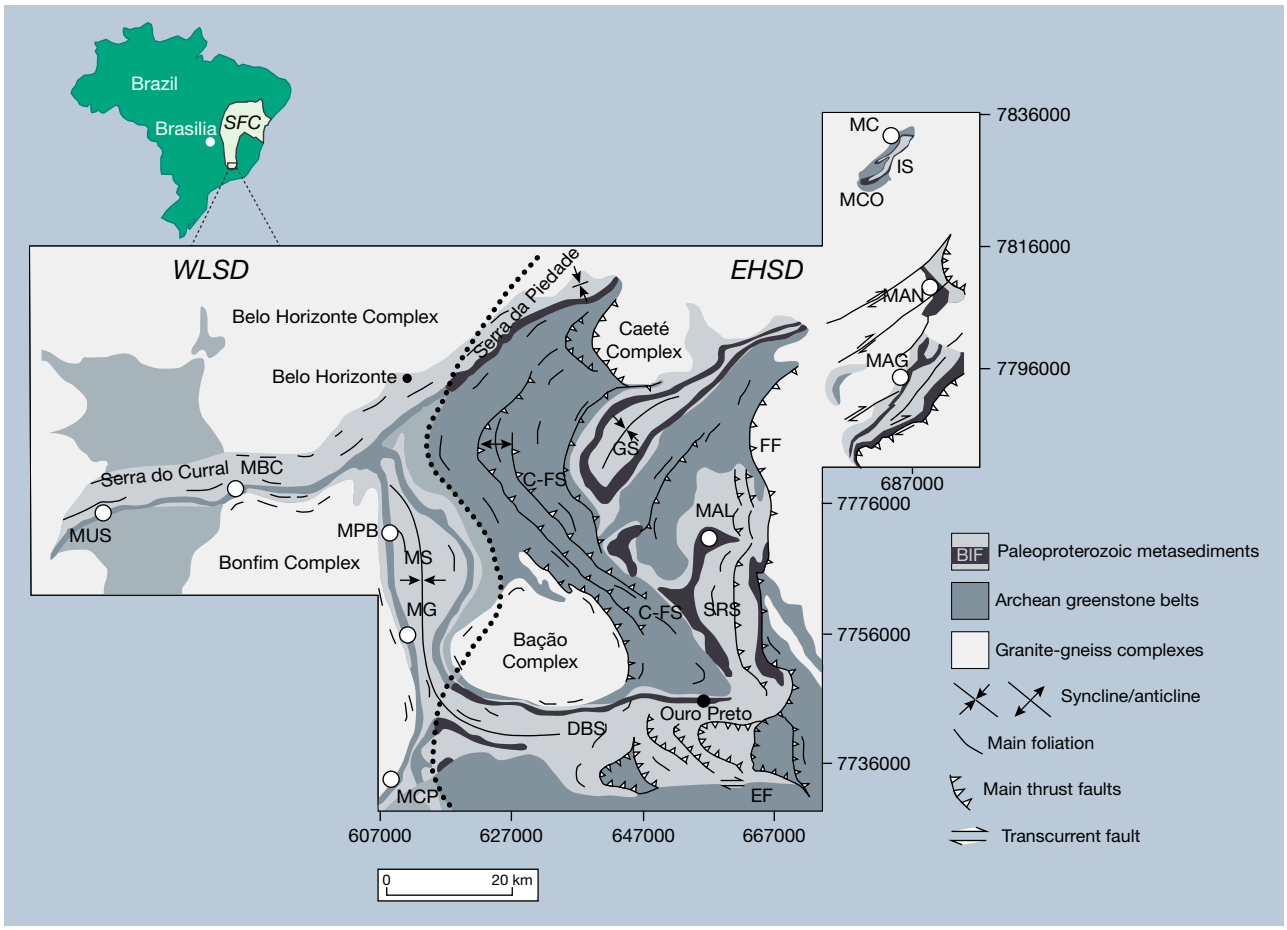

Figure 4. (A) Geologic map of the Quadrilátero Ferrífero in the southern portion of the São Francisco Craton (SFC), Brazil. Iridescent hematite derives from the Andrade mine, denoted toward the upper right as MAN. WLSD: Western Low-Strain Domain; EHSD: Eastern High-Strain Domain. IS: Itabira Syncline. From Mendes et al. (2017), as modified from Dorr (1969).

Scanning Electron Microscopy and Energy-Dispersive Spectroscopy. SEM and EDS were used to characterize surface topography and compositional information for the specimen. As iridescence was evident even from freshly fractured surfaces of the Andrade specimen, we removed a flake from one of our specimens and affixed the flake to an SEM mount using carbon fiber tape so that the flat iridescent surface was parallel to the surface of the SEM mount. We used an FEI Nova NanoSEM 600 field emission scanning electron microscope, outfitted with an Oxford Instruments X-Max (Model 51-XMX1105) silicon drift detector used for EDS analysis, in the Materials Characterization Laboratory (MCL) at Pennsylvania State University to examine the iridescent hematite. Nanoscale secondary electron images were obtained at an acceleration voltage of 5 kV and a current of 9 pA. EDS data were processed using the Oxford Instruments NanoAnalysis AZtec software (version 2.4). We chose three different accelerating voltages (20, 10, and 5 kV) to acquire spectra for the same sites.

Atomic Force Microscopy. To obtain high-resolution surface topography, we used a Bruker Icon I AFM (MCL, Pennsylvania State University) in PeakForce Tapping (PFT) mode with the ScanAsyst image optimization technique. In PFT mode, the cantilever is brought in and out of contact with the surface. PFT algorithms can precisely control the instantaneous force interaction, allowing the use of reduced forces in the imaging process. In this way, both fragile probes and samples can be protected without compromising image resolution. ScanAsyst automatically adjusts the appropriate parameters (such as set points, feedback grains, and scan rates) during the scan and continuously monitors image quality. The AFM probe for this analysis was a Bruker ScanAsyst-Air probe, which has a silicon tip on a nitride lever. The front angle of the

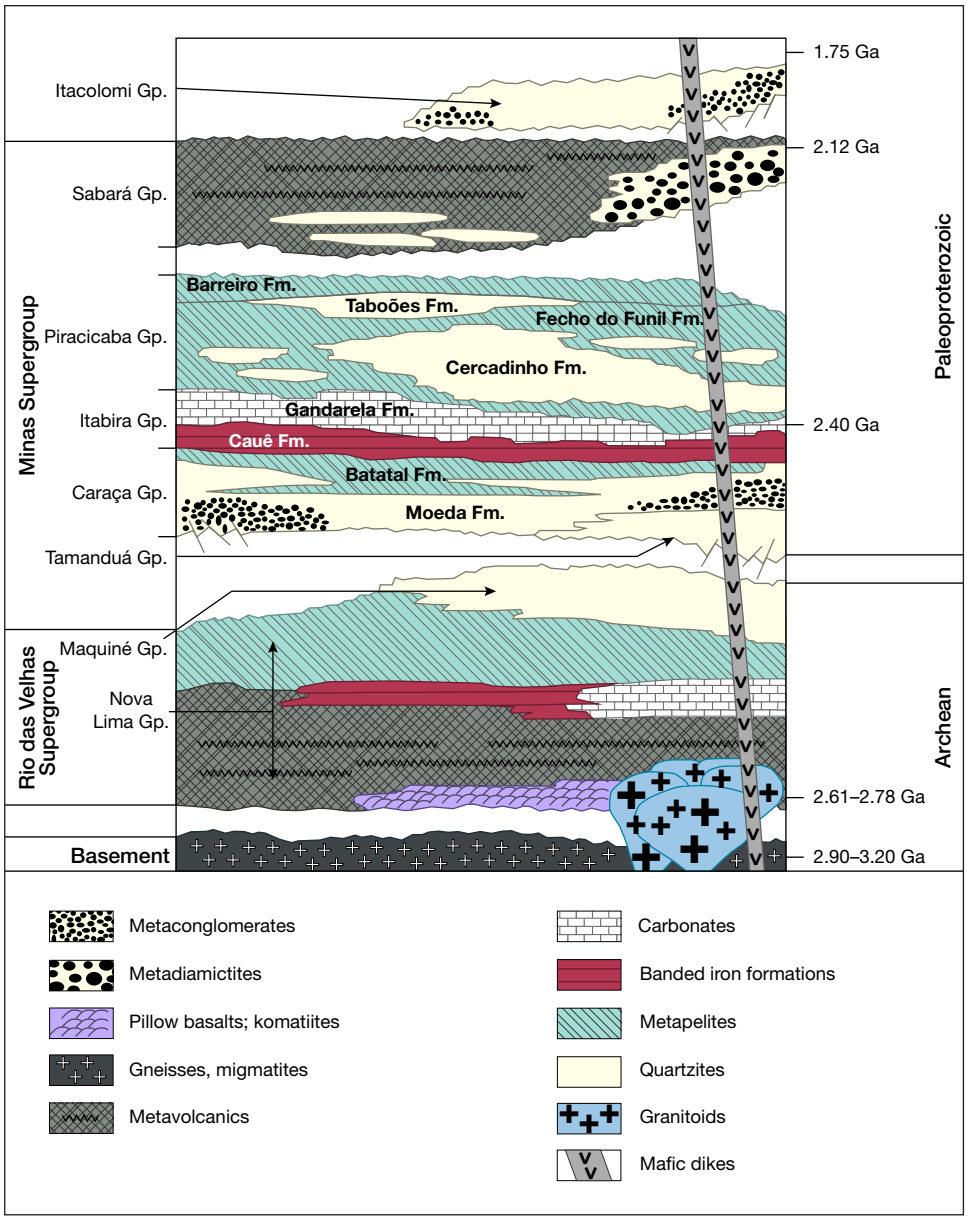

Figure 5. Stratigraphic column of the Quadrilátero Ferrífero. Rainbow hematite is found within the Cauê banded-iron formation. From Carlos et al. (2014).

tip was 15° and the back angle was 25°. For AFM imaging, the peak force set point ranged from 1 to 4 nN and the scan rate was 1 to 0.5 Hz, with 512 data points per line in each scan. NanoScope Analysis software (version 1.50) was used to process the AFM data.

X-Ray Diffraction. Hematite was powdered in an agate mortar and pestle under acetone. Upon drying, the powder was loaded into a 0.7 ID polyimide capillary for X-ray diffraction. Synchrotron X-ray diffraction data were collected at the GeoSoilEnviroCARS (GSECARS) 13-BM-C beamline at the Advanced Photon Source (APS), Argonne National Laboratory (Argonne, Illinois). The X-ray wavelength was 0.8315(4) Å, and the detector-sample distance was 100.469(1) mm. XRD data were collected with a MAR165 CCD camera. The diffraction pattern was integrated into intensity vs. 2θ plots using the Fit2D program with a polarization factor of 0.99 (Hammersley et al., 1996).

Structure Refinement. Rietveld refinement is a technique for determining atomic structures by comparing the misfit between an observed powder X-ray diffraction pattern and a diffraction pattern calculated on the basis of a model crystal structure (Rietveld, 1969). Factors such as unit-cell parameters and atom positions are allowed to refine until the misfit between the observed and calculated patterns

is minimized. Because we suspected that the atomic structure of the iridescent hematite from the Andrade mine might deviate from ideal hematite, we applied Rietveld analysis of the synchrotron XRD data to refine the crystal structure. The Rietveld software employed was the EXPGUI interface (Toby, 2001) of the general structure analysis system (GSAS) (Larson and Von Dreele, 1994). To obtain instrumental broadening parameters, we refined the structure of a LaB_6 standard using starting parameters from Ning and Flemming (2005). For the hematite refinement, we incorporated the peak profile parameters refined for LaB_6, and the initial structure parameters for hematite came from Blake et al. (1966). Using a 2θ range of 11.5° to 37.5° (d_{hkl} = 4.1 Å to 1.3 Å), we refined the background using a cosine Fourier series polynomial with eight profile terms. After the scale factor, background, unit-cell parameter, zero position, and additional profile terms had converged, the atom positions and the Fe occupancy were refined.

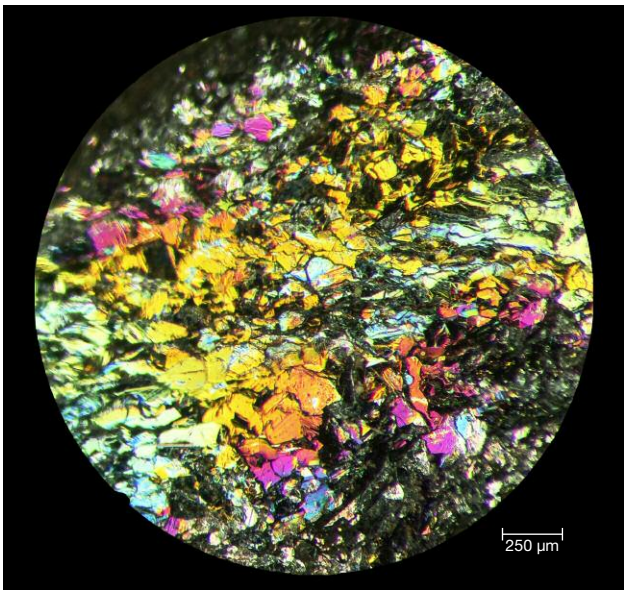

Figure 6. Reflected light microscope image of iridescent hematite revealing the granoblastic texture and strong iridescence of a freshly fractured surface. Photo by Xiayang Lin.

RESULTS

Reflected Light Microscopy. Viewed using reflected light optical microscopy at low magnification, the rainbow hematite sample appeared as a composite of gray hematite platelets with a strong silvery luster, and the platelets varied in diameter from 150 to 250 µm (figure 6). The lenticular to equidimensional texture was consistent with the mosaic granoblastic fabric reported by Rosière et al. (2001). Even when the iridescent Andrade hematite was freshly fractured, all surfaces exhibited intense rainbow colors (figure 6), leading us to interpret the iridescence as a bulk character, or at least as a pervasive character, rather than as the result of a single surface coating.

Scanning Electron Microscopy and Atomic Force Microscopy. When the iridescent surfaces of the Andrade hematite platelets from a freshly fractured surface were analyzed at low magnification using SEM, the surface appeared flat and smooth (figure 7). As first described by Ma and Rossman (2003a), however, sub-micron resolution revealed spindle- and rod-shaped nanocrystals arranged with threefold symmetry. The spindle-shaped particles were 200–300 nm in length and 50–60 nm in width. These oriented nanoparticles were reproducibly observable on freshly fractured surfaces, where they occurred as stacked sheets.

Figure 7. FESEM images of a freshly fractured iridescent hematite surface, shown with increasing magnification from left to right, reveal that the granoblastic texture of a single hematite grain (left) comprises individual nanocrystals oriented at 120° angles (center and right).

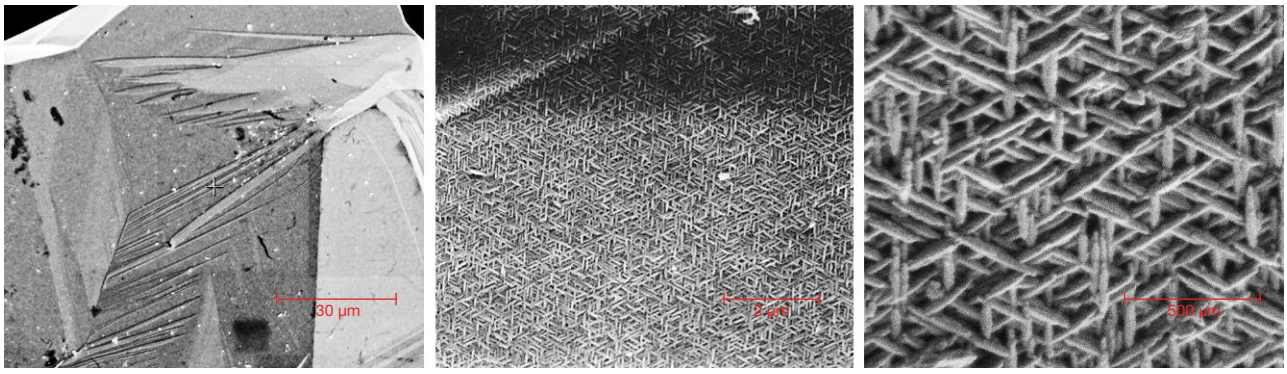

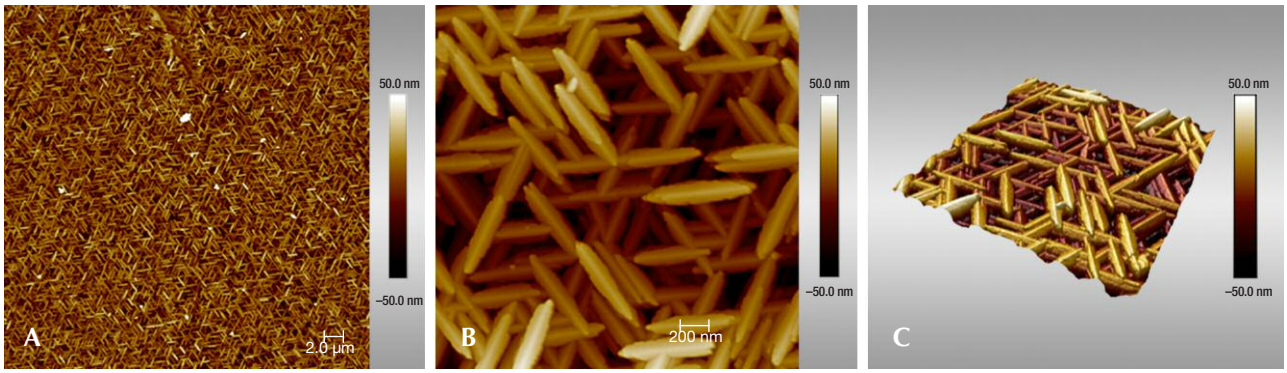

Figure 8. AFM images of iridescent hematite from the Andrade mine at low (A) and high (B) magnifications. The scale bar to the right of each image denotes the height relative to a zero-plane on the surface, with lighter colors representing higher elevations. (C) 3D reconstruction of the image in (B) as calculated by NanoScope Analysis software.

The threefold trellis network generated by the hematite nanoparticles was illustrated even more clearly by AFM imaging of fracture surfaces (figure 8). In particular, the scanning probe technique allowed for a three-dimensional reconstruction of the hematite surface (figure 8C), revealing a ridge-and-valley structure at the nanometer scale along three directions. Moreover, these images exposed a high concentration of nanopores approximately 10 nm in length.

Chemical Composition. We measured the elemental composition of the iridescent surface using EDS from a fractured face with nanoSEM (figure 9). Consistent with the results reported by Ma and Rossman (2003b), our EDS measurements detected Al and P in addition to Fe and O. Al is known to substitute for Fe in natural hematite (Tardy and Nahon, 1985; Cornell and Schwertmann, 2003, p. 51). Moreover, synthetic hematite with variable concentrations of substitutional Al has been studied extensively (Schwertmann et al., 1979; De Grave et al., 1985; Stanjek and Schwertmann, 1992; Gialanella et al., 2010; Liu et al., 2011). Likewise, P has been reported as a common impurity within natural hematite. Indeed, dephosphorization of iron ores to improve the efficiency of iron extraction is a global focus in the mining industry (Li et al., 2014; Lovel et al., 2015), including the Itabira deposits (Barbour, 1973). P-containing hematite also can be synthesized, and studies have revealed that P preferentially attaches to the prismatic (100) and (110) faces of hematite rather than the (001) and (104) basal faces (Colombo et al., 1994; Torrent et al., 1994; Gálvez et al., 1999), inducing particle morphologies to change from rhombohedral to spindle-shaped.

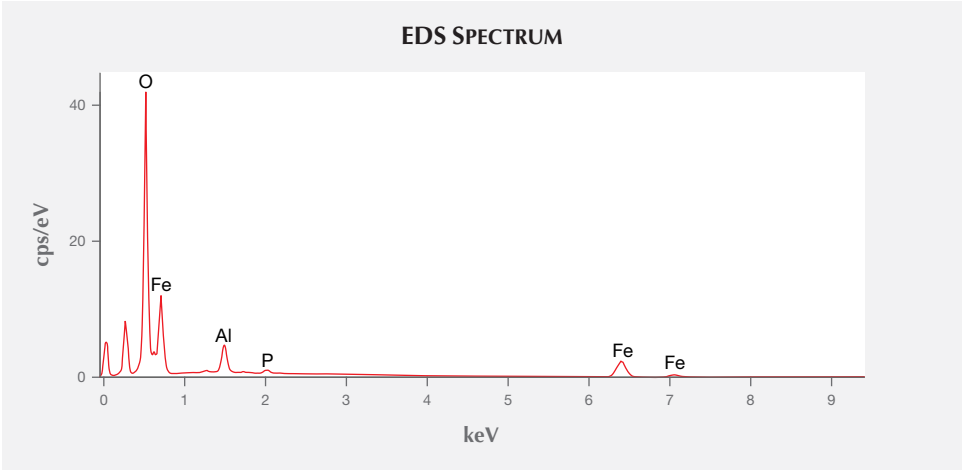

Figure 9. The EDS spectrum for iridescent hematite reveals the presence of Al and P in addition to Fe and O.

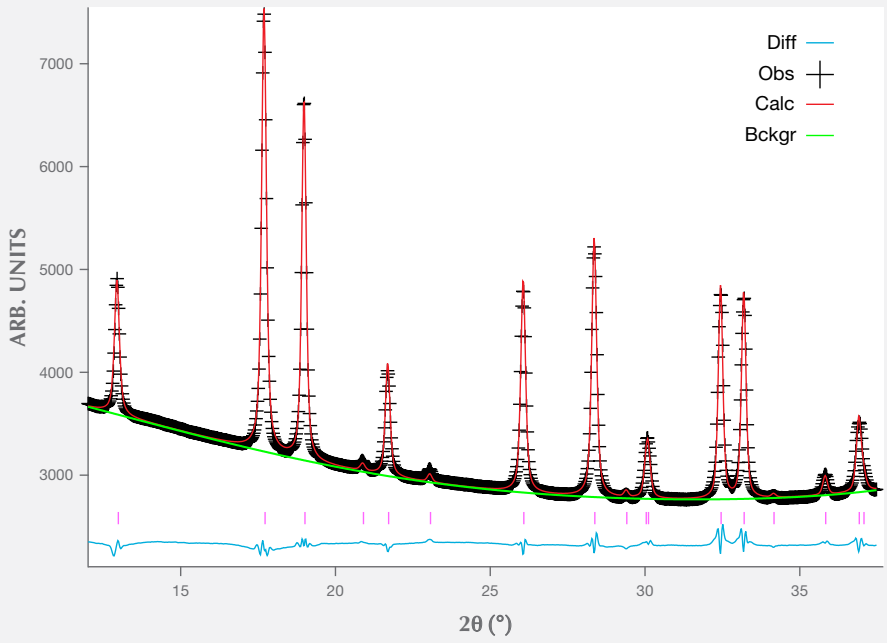

Figure 10. The close correspondence between the observed and calculated XRD patterns in this Rietveld refinement of iridescent hematite from the Andrade mine indicates a strong match between our model structure and the actual atomic structure. The black crosses represent the observed data. The red line is the calculated pattern based on the final refined structure. The green line models the background intensity. The blue line represents the difference between the observed and calculated patterns. The pink vertical lines mark the X-ray diffraction peaks of hematite.

Consequently, we calculated a formula for the iridescent hematite from the Andrade mine using the data in table 3 and assuming the presence of Al and P as impurities. Our EDS results yielded a formula of $Fe_{1.81}Al_{0.23}P_{0.03}O_3$, when normalized to three oxygen atoms. The absence of charge balance may indicate the P is not incorporated within the structure (see below), and it also may arise from the semi-quantitative nature of EDS when performed on a fractured rather than polished surface. Nevertheless, the ratio of Fe to Al suggests occupancies of 89% for Fe and 11% for Al, in good agreement with the results of our Rietveld analysis of XRD data, as described below.

XRD and Rietveld Refinement. Our X-ray diffraction analysis indicated that the Andrade mine hematites were phase pure within the detection limits of synchrotron diffraction (optimally about 0.1 wt.%). The final Rietveld refinement results based on our synchrotron XRD are presented in figure 10, and the unit-cell and refinement parameters are presented in table 1. Atom positions and occupancies are included in table 2.

Although the match between the calculated and observed patterns was excellent, we noted a discrepancy between our refined structure and ideal stoichiometric hematite. When we refined the structure using only Fe in the octahedral site, the occupancy converged to 93.9(4)% rather than 100%. Since our EDS results revealed the presence of Al, we postulated that Al was incorporated into the crystal structure of hematite rather than in the distinct phosphate phase suggested by Ma and Rossman (2003a). To test this hypothesis, we included Al on the same crystallographic site as Fe, with the constraint that the occupancies for Al and Fe would sum to 100%.

The accuracy of a Rietveld refinement is gauged using several goodness-of-fit (GOF) measurements. These include a factor that compares observed and calculated waveforms of the diffracted X-rays (R_{Bragg}) as well as factors that compare intensities of ob-

TABLE 1. Final Rietveld refinement parameters for iridescent hematite.

Space group	$R\bar{3}c$	Refinement parameters	
Unit cell		No. of diffraction points	1,062
a (Å)	5.0500(2)	No. of reflections	29
b (Å)	5.0500(2)	Diffraction range (2θ)	11.5–37.5
c (Å)	13.7903(6)	No. of variables	16
α (°)	90	$R(F^2)$	0.1136
β (°)	90	R_{WP}	0.0079
γ (°)	120	χ^2	0.2020

TABLE 2. Atomic coordinates and occupancy of iridescent hematite after Rietveld refinement.

Atom	*x*	*y*	*z*	Occupancy	U_{iso}
Fe	0	0	0.35530(6)	0.879(7)	0.004
Al	0	0	0.35530(6)	0.121(7)	0.004
O	0.2996(5)	0	0.25	1	0.004

served and calculated diffraction data as a function of scattering angle (χ^2 and R_{wp}). The partial substitution of Al for Fe improved the GOF by all of these measures, with R_{Bragg} decreasing from 0.1369 to 0.1136. Other GOF parameters indicated an excellent match between the calculated and observed diffraction patterns when Al substitution was allowed, with the final $\chi^2 = 0.2020$ and $R_{wp} = 0.0079$. Our final Rietveld refinement of the Andrade hematite yielded an occupancy for Fe of 87.9(7)%, with Al occupying the remaining 12.1(7)% of the sites. That value compares very well with the 11% occupancy for Al calculated from the EDS data.

Our efforts to incorporate P into the crystal structure did not yield a satisfactory structure refinement, which was not surprising since our EDS data suggested much lower concentrations of P than Al, consistent with the analyses of Ma and Rossman (2003b). Thus, P occurs as a minor impurity, either interstitially within the hematite structure, as a substitute for octahedral Fe, or perhaps as atoms attached to the surfaces of individual nanocrystals.

DISCUSSION

A Natural Diffraction Grating of Hematite Nanocrystals. Modulated structures with periodicities on the order of the wavelength of visible light (380–700 nm) can lead to diffraction effects if the structures are physically displaced relative to each other (such as ridges on a crystal surface) or if the nanostructure boundaries exhibit a change in refractive index (as with the alternating Na- and Ca-rich layers that characterize labradorite; reviewed in Lin and Heaney, 2017). Our observations indicate that the iridescence in metamorphic specular hematite from the Andrade mine results from the interference of visible light rays reflected from the stacked nanorods that constitute the bulk minerals. Consequently, the iridescence should not be attributed to a thin film of Al phosphate, as previously suggested by Ma and Rossman (2003a). Instead, the diffraction behavior is analogous to that generated by the modulated substructure in opal. Whereas opal consists of transparent, amorphous nanospheres that are closely packed to form a "photonic crystal" (Gaillou et al., 2008), the nanorods in iridescent hematite are crystalline, opaque, and primarily reflective of visible light.

The individual particles in the rainbow hematite were less than 100 nm wide, approaching the Rayleigh scattering domain (less than one-tenth the wavelength of light) and thus seemingly too small to diffract visible light. However, the average distances observed between parallel nanorods within the same layer were consistently in the range of 280–400 nm, the same order of magnitude as the wavelength of visible light. Consequently, the grating traced by the hematite nanoparticles was of a dimension suitable for scattering visible light.

Our inspection of many fragments of rainbow hematite revealed that the diffraction colors were independent of the angle of incidence. In other words, unlike play-of-color opal, which changes color as the sample is tilted with respect to the light source, the blue, green, and red patches of Andrade mine hematite did not change color as the specimens were rotated. This phenomenon is well known in biological materials with structural rather than pigmented coloration (e.g., the wings of the *Morpho* butterfly), and it appears to violate basic laws of light interference from periodic structures. For example, Bragg's law ($\lambda = 2d \sin \theta$) explicitly states that the wavelength of light (λ) is dependent on the spacing of the periodic substructure (d) and the incident light angle (θ). The apparent paradox embodied in this wide-angle diffraction behavior has been attributed to the combination of regular lamellar nanostructures (which create a strong interference effect) and irregular lamellar ridge heights (which diffuse the diffraction) (Kinoshita et al., 2002; Song et al., 2014). The hematitic substructures seen in figure 8C reveal regular lamellar features with variable topography, perhaps accounting for the angle-independent iridescence.

TABLE 3. EDS analysis using elemental *K*-lines for iridescent hematite.

Element	Wt.%	Wt.% sigma	Atomic %
O	30.78	0.21	59.23 ± 0.2
Al	4.01	0.06	4.58 ± 0.1
P	0.54	0.04	0.54 ± 0.1
Fe	64.67	0.24	35.65 ± 0.2
Total	100		100

Ordered Substructures from Oriented Aggregation. The periodic substructure of specular hematite from the Andrade mine consists of nanorods oriented at 120° angles with respect to each other and stacked layer by layer. This texture strongly suggests crystal growth by oriented aggregation of nanohematite (Niederberger and Cölfen, 2006). In this crystal growth mechanism, individual primary crystallites nucleate and grow to a specific length, followed by the assembly of mineral grains in a crystallographically controlled fashion (Penn and Banfield, 1998; Banfield et al., 2000). Hematite has a particular tendency to form through aggregation-based processes. Oriented aggregation of pseudocubic, ellipsoidal, and disc-shaped crystals has been described in a variety of hematite synthesis studies (Sugimoto et al., 1993; Ocaña et al., 1995; Niederberger et al., 2002).

We propose that the iridescent hematite found at the Andrade mine formed in two stages (figure 11). During the first stage, ultrafine crystallites grew as spindle-shaped rather than rhombohedral nanoparticles. The rod-like morphology may have resulted from the incorporation of Al and/or P within the crystal structure (Schwertmann et al., 1979; Barron et al., 1988; Reeves and Mann, 1991; Stanjek and Schwertmann, 1992; Sugimoto et al., 1993, 1998; Colombo et al., 1994; Galvez et al., 1999). It has been suggested that these ions poison surface sites and induce the growth of non-equant crystals.

In the second stage of growth, the nanorods assembled such that their crystallographic c-axes were parallel. Because hematite has trigonal (threefold) symmetry along the c-axis, two crystals can align in one of three orientations with equivalent energetics of attachment (energy of structural assembly), giving rise to the threefold rotational orientations seen in figures 7 and 8. This interpretation suggests that the particles are elongated perpendicular to the c-axis, in contrast to an earlier finding that ellipsoidal hematite is lengthened along the c-axis (Colombo et al., 1994). Whereas most crystals that form by oriented aggregation eventually fill all spaces, the iridescent hematite from the Andrade mine records an arrested growth, with significant retention of void space. Researchers have attributed the occurrence of hematite in the Cauê Formation to the hydrothermal recrystallization of magnetite (Rosière and Rios, 2004). The density of hematite (5.26 gm/cm^3) is greater than that of magnetite (5.18 gm/cm^3). Thus, the replacement of magnetite by hematite will generate porosity if the volume of the rock unit is unchanged (Putnis, 2002).

Ma and Rossman (2003a) deserve credit for their initial SEM observations of the periodic surface textures, and their online images reveal very similar microstructures in specimens from other localities.

Figure 11. Our model for the formation of the texture observed in iridescent hematite from the Andrade mine. Rod-like nanocrystals of hematite grow to a critical size and population density before assembling with crystallographic control to generate the threefold trellis network observed.

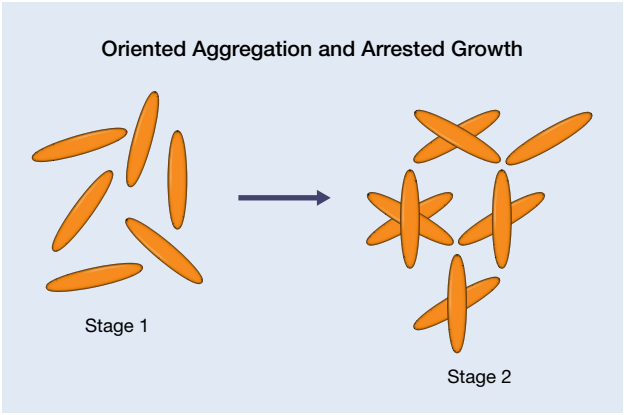

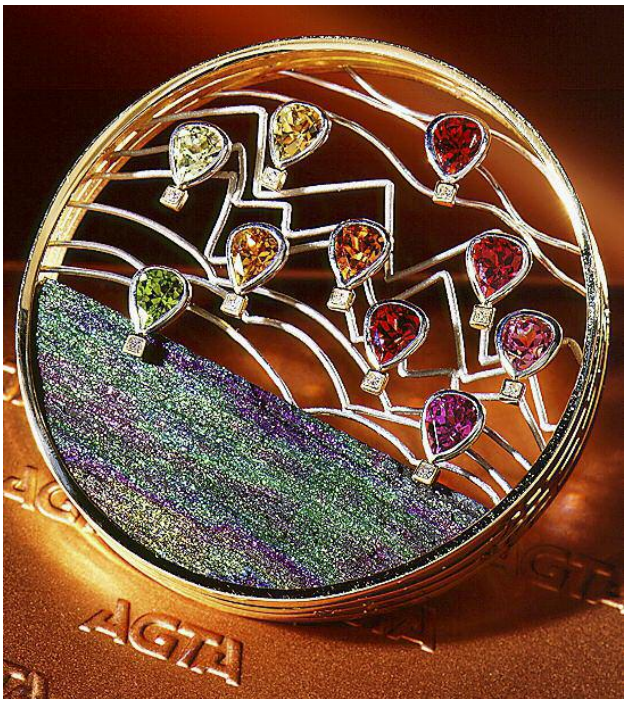

Figure 12. "Flying Free," designed by Llyn Strelau, features Brazilian rainbow hematite and mixed colored garnets set in yellow gold and platinum. The brooch received an AGTA Spectrum Award in 1995. Photo courtesy of Jewels by Design.

In particular, iridescent hematite specimens from the El Salvador mine in Mexico (labeled GRR 1960), Quartz Mountain, Oregon (GRR 2380), and Alaska (CIT 11952) exhibit stacked, oriented aggregates of what we propose are hematite nanocrystals. We conclude that the hydrothermal recrystallization of precursor magnetite, which commonly occurs when banded-iron formations are metamorphosed, may favor porous hematite with crystallographically oriented nanocrystals, giving rise to iridescent specular hematite (figure 12) in many localities around the world.

ABOUT THE AUTHORS

Ms. Lin received her M.S. in geosciences at Pennsylvania State University in 2015. After two years with the Rapaport Diamond Corporation, she is starting her own gem trading firm in China. Dr. Heaney is a professor in the Department of Geosciences at Pennsylvania State University. Dr. Post is the curator of the National Gem and Mineral Collection in the National Museum of Natural History, Smithsonian Institution, in Washington, DC.

ACKNOWLEDGMENTS

This research was made possible through funding from the National Science Foundation (NSF-EAR11-47728 and EAR-1552211). SEM and AFM work were performed at the Materials Characterization Laboratory at Pennsylvania State University with the assistance of Dr. Trevor Clark, Julie Anderson, Joshua Maier, and Timothy Tighe. Special thanks are due to Drs. James Kubicki, Maureen Feineman, and Phil Kong for their useful suggestions and assistance.

REFERENCES

de Almeida F.F.M. (1977) O cráton do São Francisco. *Brazilian Journal of Geology*, Vol. 7, No. 4, pp. 349–364.

Banfield J.F., Welch S.A., Zhang H., Ebert T.T., Penn R.L. (2000) Aggregation-based crystal growth and microstructure development in natural iron oxyhydroxide biomineralization products. *Science*, Vol. 289, No. 5480, pp. 751–754, http://dx.doi.org/10.1126/science.289.5480.751

Barbour A.P. (1973) Distribution of phosphorus in the iron ore deposits of Itabira, Minas Gerais, Brazil. *Economic Geology*, Vol. 68, No. 1, pp. 52–64, http://dx.doi.org/10.2113/gsecongeo.68.1.52

Barron V., Herruzo M., Torrent J. (1988) Phosphate adsorption by aluminous hematites of different shapes. *Soil Science Society of America Journal*, Vol. 52, No. 3, pp. 647–651, http://dx.doi.org/10.2136/sssaj1988.03615995005200030009x

Blake R.L., Hessevick R.E., Zoltai T., Finger L.W. (1966) Refinement of the hematite structure. *American Mineralogist*, Vol. 51, No. 1-2, pp. 123–129.

Böhm J. (1928) Röntgenographische Untersuchung der mikrokristallinen Eisenhydroxydminerale. *Zeitschrift für Kristallographie*, Vol. 68, No. 1-6, pp. 567–585, http://dx.doi.org/10.1524/zkri.1928.68.1.567

Buckley A.N., Woods R. (1983) X-ray photoelectron spectroscopic investigation of the tarnishing of bornite. *Australian Journal of Chemistry*, Vol. 36, No. 9, pp. 1793–1804, http://dx.doi.org/10.1071/CH9831793

Carlos D.U., Uieda L., Barbosa V.C.F. (2014) Imaging iron ore from the Quadrilátero Ferrífero (Brazil) using geophysical inversion and drill hole data. *Ore Geology Reviews*, Vol. 61, pp. 268–285, http://dx.doi.org/10.1016/j.oregeorev.2014.02.011

Colombo C., Barrón V., Torrent J. (1994) Phosphate adsorption and desorption in relation to morphology and crystal properties of synthetic hematites. *Geochimica et Cosmochimica Acta*, Vol. 58, No. 4, pp. 1261–1269, http://dx.doi.org/10.1016/0016-7037(94)90380-8

Cornell R.M., Schwertmann U. (2003) *The Iron Oxides: Structure, Properties, Reactions, Occurrences and Uses*. John Wiley & Sons, New York.

Currier R. (2012) A story about color rock. Mindat.org, https://www.mindat.org/article.php/1481//A+story+about+color+rock

Darragh P.J., Gaskin A.J., Terrell B.C., Sanders J.V. (1966) Origin of precious opal. *Nature*, Vol. 209, No. 5018, pp. 13–16, http://dx.doi.org/10.1038/209013a0

De Grave E., Verbeeck A.E., Chambaere D.G. (1985) Influence of small aluminum substitutions on the hematite lattice. *Physics Letters A*, Vol. 107, No. 4, pp. 181–184, http://dx.doi.org/10.1016/0375-9601(85)90837-0

Dorr J.V.N. (1969) Physiographic, stratigraphic, and structural development of the Quadrilátero Ferrífero, Minas Gerais, Brazil. *U.S. Geological Survey Professional Paper*, No. 641-A.

Gaillou E., Fritsch E., Aguilar-Reyes B., Rondeau B., Post J., Barreau A., Ostrooumov M. (2008) Common gem opal: An investigation of micro-to nano-structure. *American Mineralogist*, Vol. 93, No. 11-12, pp. 1865–1873. https://doi.org/10.2138/am.2008.2518

Gálvez N., Barrón V., Torrent J. (1999) Preparation and properties of hematite with structural phosphorus. *Clays and Clay Minerals*, Vol. 47, No. 3, pp. 375–385, http://dx.doi.org/10.1346/CCMN.1999.0470314

Gialanella S., Girardi F., Ischia G., Lonardelli I., Mattarelli M., Montagna M. (2010) On the goethite to hematite phase transformation. *Journal of Thermal Analysis and Calorimetry*, Vol. 102, No. 3, pp. 867–873, http://dx.doi.org/10.1007/s10973-010-0756-2

Hammersley A.P., Svensson S.O., Hanfland M., Fitch A.N., Hausermann D. (1996) Two-dimensional detector software: From real detector to idealised image or two-theta scan. *High Pressure Research*, Vol. 14, No. 4-6, pp. 235–248, http://dx.doi.org/10.1080/08957959608201408

Heaney P.J., Davis A.M. (1995) Observation and origin of self-organized textures in agates. *Science*, Vol. 269, No. 5230, pp. 1562–1565, http://dx.doi.org/10.1126/science.269.5230.1562

Hermann R. (1844) Untersuchungen russischer Mineralien. *Journal für Praktische Chemie*, Vol. 33, No. 1, pp. 282–300, http://dx.doi.org/10.1002/prac.18440330139

Kinoshita S., Yoshioka S., Kawagoe K. (2002) Mechanisms of structural colour in the *Morpho* butterfly: Cooperation of regularity and irregularity in an iridescent scale. *Proceedings of the Royal Society of London B: Biological Sciences*, Vol. 269, No. 1499, pp. 1417–1421, http://dx.doi.org/10.1098/rspb.2002.2019

Larson A.C., Von Dreele R.B. (1994) GSAS: General Structure Analysis System. *Los Alamos National Laboratory Report*, LAUR 86-748.

Li Y., Sun T., Kou J., Guo Q., Xu C. (2014) Study on phosphorus removal of high-phosphorus oolitic hematite by coal-based direct reduction and magnetic separation. *Mineral Processing and Extractive Metallurgy Review*, Vol. 35, No. 1, pp. 66–73, http://dx.doi.org/10.1080/08827508.2012.723648

Lin X., Heaney P.J. (2017) Causes of iridescence in natural quartz. *G&G*, Vol. 53, No. 1, pp. 68–81, http://dx.doi.org/10.5741/GEMS.53.1.68

Liu Q.S., Torrent J., Barrón V., Duan Z.Q., Bloemendal J. (2011) Quantification of hematite from the visible diffuse reflectance spectrum: effects of aluminium substitution and grain morphology. *Clay Minerals*, Vol. 46, No. 1, pp. 137–147, http://dx.doi.org/10.1180/claymin.2011.046.1.137

Lovel R.R., Sparrow G.J., Fisher-White M.J. (2015) Developments in chemical separation of iron ore. In L. Lu, Ed., *Iron Ore: Mineralogy, Processing and Environmental Sustainability*, Woodhead, Amsterdam, pp. 357–372.

Ma C., Rossman G. (2003a) Low voltage FESEM of geological materials. *Microscopy and Microanalysis*, Vol. 9, No. S2, pp. 990–991.

Ma C., Rossman G.R. (2003b) Iridescent hematite. http://minerals.gps.caltech.edu/manuscripts/in-prep/Submitted/Rainbow_hematite/

Ma C., Gresh J., Rossman G.R., Ulmer G.C., Vicenzi E.P. (2001) Micro-analytical study of the optical properties of rainbow and sheen obsidians. *The Canadian Mineralogist*, Vol. 39, No. 1, pp. 57–71, http://dx.doi.org/10.2113/gscanmin.39.1.57

Ma C., Rossman G.R., Miller J.A. (2007) The origin of color in "fire" obsidian. *The Canadian Mineralogist*, Vol. 45, No. 3, pp. 551–557, http://dx.doi.org/10.2113/gscanmin.45.3.551

Mendes M., Lobato L.M., Kunzmann M., Halverson G.P., Rosière C.A. (2017) Iron isotope and REE+Y composition of the Cauê banded iron formation and related iron ores of the Quadrilátero Ferrífero, Brazil. *Mineralium Deposita*, Vol. 52, No. 2, pp. 159–180, http://dx.doi.org/10.1007/s00126-016-0649-9

Miura Y., Tomisako T. (1978) Ion microprobe mass analysis of exsolution lamellae in labradorite feldspar. *American Mineralogist*, Vol. 63, No. 5-6, pp. 584–590.

Nadin E.S. (2007) The secret lives of minerals. *Engineering and Science*, Vol. 70, No. 1, pp. 10–20.

Niederberger M., Cölfen H. (2006) Oriented attachment and mesocrystals: non-classical crystallization mechanisms based on nanoparticle assembly. *Physical Chemistry Chemical Physics*, Vol. 8, No. 28, pp. 3271–3287, http://dx.doi.org/10.1039/B604589H

Niederberger M., Krumeich F., Hegetschweiler K., Nesper R. (2002) An iron polyolate complex as a precursor for the controlled synthesis of monodispersed iron oxide colloids. *Chemistry of Materials*, Vol. 14, No. 1, pp. 78–82, http://dx.doi.org/10.1021/cm0110472

Ning G., Flemming R.L. (2005) Rietveld refinement of LaB_6: Data from μXRD. *Journal of Applied Crystallography*, Vol. 38, pp. 757–759, http://dx.doi.org/10.1107/S0021889805023344

Ocaña M., Morales M.P., Serna C.J. (1995) The growth mechanism of α-Fe_2O_3 ellipsoidal particles in solution. *Journal of Colloid and Interface Science*, Vol. 171, No. 1, pp. 85–91, http://dx.doi.org/10.1006/jcis.1995.1153

Palache C., Berman H.M., Frondel C. (1944) *The System of Mineralogy of James Dwight Dana and Edward Salisbury Dana*, 7th ed. Wiley, New York.

Penn R.L., Banfield J.F. (1998) Imperfect oriented attachment: dislocation generation in defect-free nanocrystals. *Science*, Vol. 281, No. 5379, pp. 969–971, http://dx.doi.org/10.1126/science.281.5379.969

Posnjak E., Merwin H.E. (1919) The hydrated ferric oxides. *American Journal of Science*, Vol. 47, No. 281, pp. 311–348, http://dx.doi.org/10.2475/ajs.s4-47.281.311

Putnis A. (2002) Mineral replacement reactions: from macroscopic observations to microscopic mechanisms. *Mineralogical Magazine*, Vol. 66, No. 5, pp. 689–708, http://dx.doi.org/10.1180/0026461026650056

Reeves N.J., Mann S. (1991) Influence of inorganic and organic additives on the tailored synthesis of iron oxides. *Journal of the Chemical Society, Faraday Transactions*, Vol. 87, No. 24, pp. 3875–3880, http://dx.doi.org/10.1039/ft9918703875

Rietveld H. (1969) A profile refinement method for nuclear and magnetic structures. *Journal of Applied Crystallography*, Vol. 2, No. 2, pp. 65–71, http://dx.doi.org/10.1107/S0021889869006558

Rosière C.A., Chemale Jr. F. (2008) Brazilian iron formations and their geological setting. *Brazilian Journal of Geology*, Vol. 30, No. 2, pp. 274–278.

Rosière C.A., Rios F.J. (2004) The origin of hematite in high-grade iron ores based on infrared microscopy and fluid inclusion studies: the example of the Conceição mine, Quadrilátero Ferrífero, Brazil. *Economic Geology*, Vol. 99, No. 3, pp. 611–624, http://dx.doi.org/10.2113/gsecongeo.99.3.611

Rosière C.A., Siemes H., Quade H., Brokmeier H.-G., Jansen E.M. (2001) Microstructures, textures and deformation mechanisms in hematite. *Journal of Structural Geology*, Vol. 23, No. 9, pp. 1429–1440, http://dx.doi.org/10.1016/S0191-8141(01)00009-8

Schwertmann U., Fitzpatrick R.W., Taylor R.M., Lewis D.G. (1979) The influence of aluminum on iron oxides. Part II. Preparation and properties of Al-substituted hematites. *Clays and Clay Minerals*, Vol. 27, No. 2, pp. 105–112, http://dx.doi.org/10.1346/CCMN.1979.0270205

Song B., Eom S.C., Shin J.H. (2014) Disorder and broad-angle iridescence from *Morpho*-inspired structures. *Optics Express*, Vol. 22, No. 16, pp. 19386–19400, http://dx.doi.org/10.1364/OE.22.019386

Stanjek H., Schwertmann U. (1992) The influence of aluminum on iron oxides. Part XVI: Hydroxyl and aluminum substitution in synthetic hematites. *Clays and Clay Minerals*, Vol. 40, No. 3, pp. 347–354, http://dx.doi.org/10.1346/CCMN.1992.0400316

Sugimoto T., Khan M.M., Muramatsu A. (1993) Preparation of monodisperse peanut-type α-Fe_2O_3 particles from condensed ferric hydroxide gel. *Colloids and Surfaces A: Physicochemical and Engineering Aspects*, Vol. 70, No. 2, pp. 167–169, http://dx.doi.org/10.1016/0927-7757(93)80285-M

Sugimoto T., Wang Y., Itoh H., Muramatsu A. (1998) Systematic control of size, shape and internal structure of monodisperse α-Fe_2O_3 particles. *Colloids and Surfaces A: Physicochemical and Engineering Aspects*, Vol. 134, No. 3, pp. 265–279, http://dx.doi.org/10.1016/S0927-7757(97)00103-9

Tardy Y., Nahon D. (1985) Geochemistry of laterites, stability of Al-goethite, Al-hematite, and Fe^{3+}-kaolinite in bauxites and ferricretes: an approach to the mechanism of concretion formation. *American Journal of Science*, Vol. 285, No. 10, pp. 865–903.

Toby B.H. (2001) EXPGUI, a graphical user interface for GSAS. *Journal of Applied Crystallography*, Vol. 34, pp. 210–213, http://dx.doi.org/10.1107/S0021889801002242

Torrent J., Schwertmann U., Barrón V. (1994) Phosphate sorption by natural hematites. *European Journal of Soil Science*, Vol. 45, No. 1, pp. 45–51, http://dx.doi.org/10.1111/j.1365-2389.1994.tb00485.x

Vaughan D.J., Tossell J.A., Stanley C.J. (1987) The surface properties of bornite. *Mineralogical Magazine*, Vol. 51, No. 360, pp. 285–293, http://dx.doi.org/10.1180/minmag.1987.051.360.11

DNA Techniques Applied to the Identification of *Pinctada Fucata* Pearls from Uwajima, Ehime Prefecture, Japan

Kazuko Saruwatari, Michio Suzuki, Chunhui Zhou, Promlikit Kessrapong, and Nicholas Sturman

The genetic material deoxyribonucleic acid (DNA) is a useful indicator in identifying pearl species, provided the extraction and amplification of a targeted component is possible from amounts of pearl powder small enough to render the technique essentially nondestructive. This study builds on similar work carried out by Meyer et al. (2013) but focuses on akoya cultured pearls from Uwajima in Ehime Prefecture, Japan. Here, we also target the 16S rRNA genes, the mitochondrial component of DNA to code 16S rRNA (ribosomal ribonucleic acid). We successfully amplified the 16S rRNA gene from the mantle tissues of donor and host pearl oysters and from 5–10 mg of pearl powder samples. The results indicate a match with the *Pinctada fucata* 16S rRNA gene.

Modern pearl identification—including the type of pearl and any treatment applied—is performed by applying almost exclusively nondestructive methods. These include macro to microscopic observations, spectroscopy, chemical analysis, fluorescence, and various forms of X-ray imaging (Scarratt, 2011). Surface inspection differentiates nacreous from non-nacreous pearls, while chemical analyses using X-ray fluorescence and luminescence can distinguish between saltwater and freshwater pearls (e.g., Hänni, 2000; Hänni et al., 2005; Kessrapong et al., 2017). Internal inspection using X-radiography, which was introduced to gemology in the 1930s (Dirlam and Weldon, 2013), has evolved into high-tech X-ray computed microtomography (μ-CT). This technology enables more consistent separation of natural, non-bead-cultured, and bead-cultured pearls (e.g., Sturman, 2009; Karampelas et al., 2010).

One of the ongoing challenges is to identify the saltwater mollusk species producing white, cream, or silver nacreous pearls, since these can form in all *Pinctada* species as well as some other species, and can have similar appearances. As pearls are formed by mollusks, a direct identification method would be to find biological evidence such as **DNA** indicators. (For boldfaced terms, please refer to the glossary on pp. 48–49.)

In Brief

- DNA technique was applied to identify saltwater mollusk species of akoya pearl from Uwajima, Ehime, Japan.
- 16S rRNA genes, which are DNA components in mitochondria, were successfully extracted from the tissue of two mollusks and from 5–10 mg of powder from four pearl samples.
- All amplified nucleotide sequences of the 16S rRNA genes matched with those of *Pinctada fucata*.

DNA studies emerged in the biological sciences (e.g., Toro, 1998; Masaoka and Kobayashi, 2004; Freier et al., 2008) after the development during the 1980s of the polymerase chain reaction (PCR) method of duplicating gene fragments (see figure 1A). A number of studies on pearl oysters of the *Pinctada* species (e.g., Masaoka and Kobayashi, 2006; Tëmkin, 2010; Masaoka et al., 2016) have investigated their nuclear and **mitochondrial** ribosomal ribonucleic acid (rRNA) and the **internal**

See end of article for About the Authors and Acknowledgments.
Gems & Gemology, Vol. 54, No. 1, pp. 40–50,
http://dx.doi.org/10.5741/GEMS.54.1.40

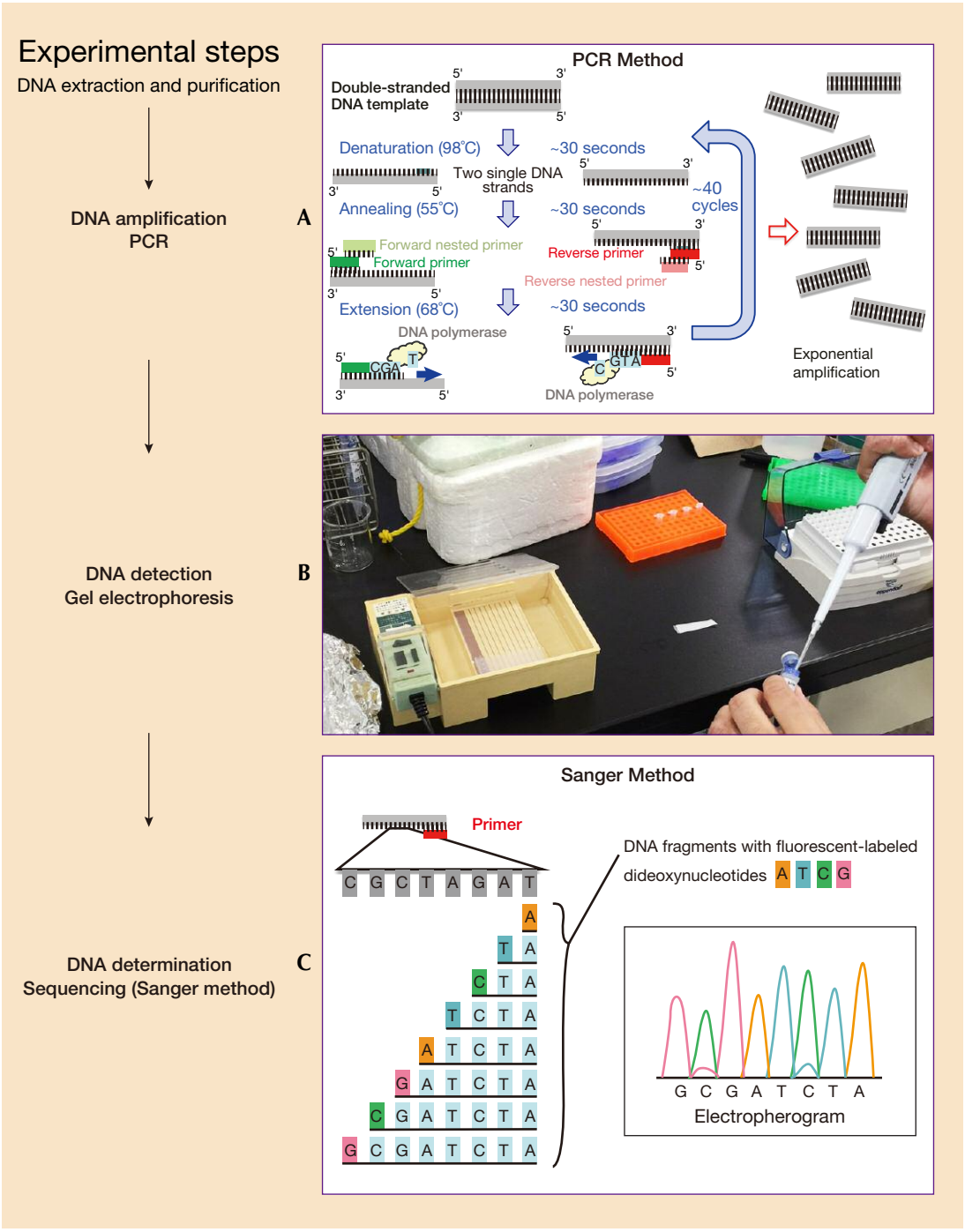

Figure 1. Experimental flow and their images. A: The polymerase chain reaction (PCR) process of denaturation, annealing, and extension. B: The gel electrophoresis step of the polymerase chain reaction (PCR) process is captured here. Four plastic 1.5 µL PCR tubes, which possibly contain amplified target DNA samples, are aligned in the orange container in the middle. The yellow box on the left is a gel electrophoresis well set, with translucent agarose gel at the lower well wall. The researcher is trying to remove 1 µL of loading dye to confirm the mobility of DNA during electrophoresis, and will mix it with 1 µL of PCR product for a total of 2 µL of mixture in the agarose gel for electrophoresis. Photo by K. Saruwatari. C: Schematic figure of the Sanger method. The figure on the left indicates DNA fragments with fluorescent-labeled dideoxynucleotides. The figure on the right is the electropherogram indicating DNA sequence after detecting the fluorescence-labeled dideoxynucleotides using capillary electrophoresis.

BOX A: HISTORY OF PEARL CULTURING AT UWAJIMA

Uwajima, in Ehime Prefecture, is Japan's main pearl culturing area, followed by Mie and Nagasaki prefectures (figure A-1, A and B). The 2014 production was 7,724 kg for Ehime, 6,650 kg for Nagasaki, and 4,375 kg for Mie (Ministry of Agriculture, Forestry, and Fisheries, n.d.). The pearl farms in Uwajima are located along the coast-

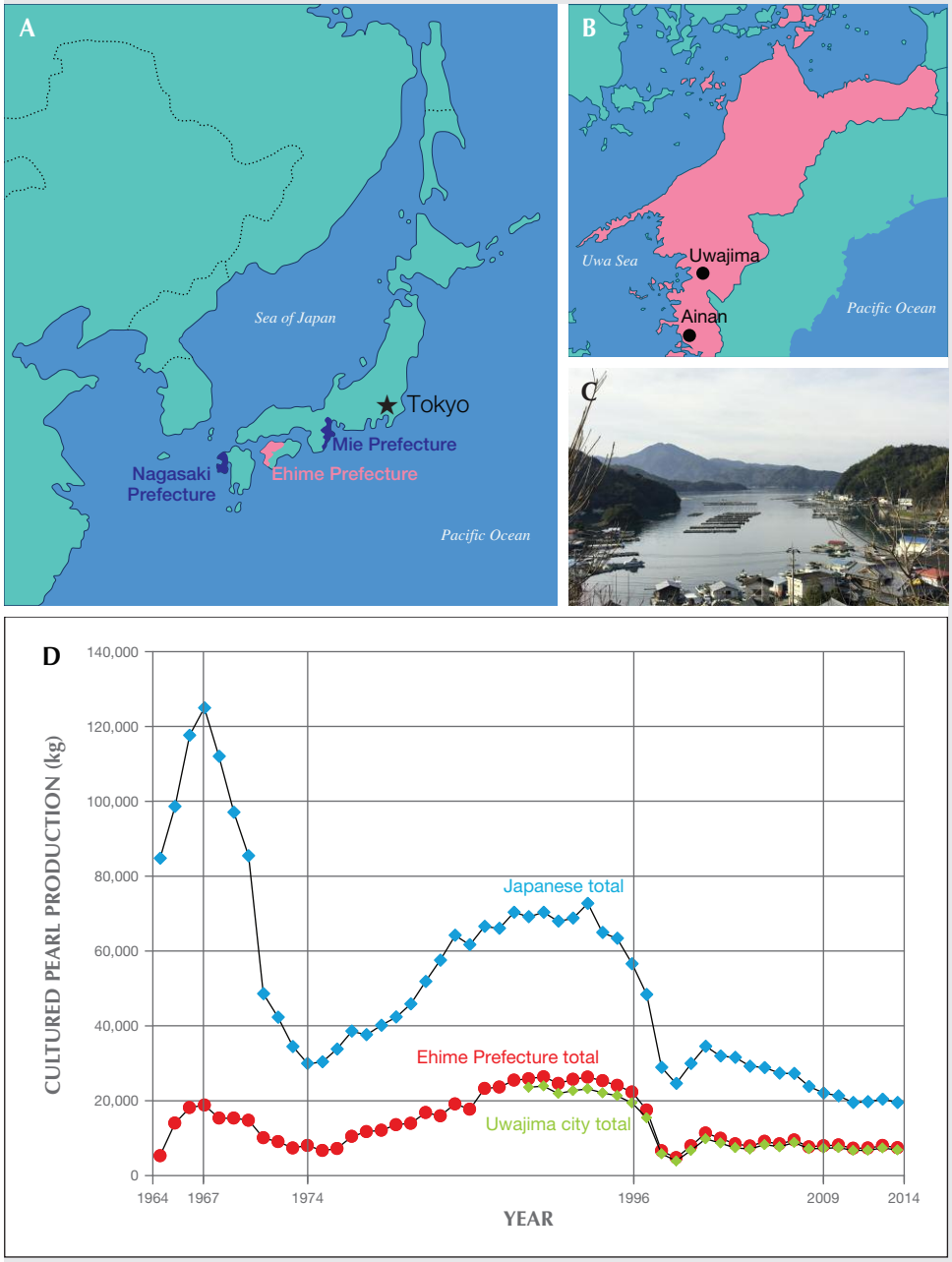

Figure A-1. A: Map of Japan showing the three main prefectures for cultured pearl production: Ehime, Mie, and Nagasaki. B: Expanded view of Ehime (in pink) showing the location of Uwajima and the Uwa-sea region (shaded in blue) along the southwestern coast. C: View of the Uwajima coast, where the floating pearl rafts are visible. Photo by K. Saruwatari. D: A comparison of Ehime's pearl production from 1964 to 2014 with overall Japanese production during those years. Uwajima's pearl production from 1989 to 2014 is also shown. Sources: Ehime Prefectural Government Planning Promotion Division (n.d.) and Ministry of Agriculture, Forestry and Fisheries (n.d.).

transcribed spacer (ITS) regions of nuclear rRNA **genes** while discussing the **phylogeny** and identification of the species.

According to these studies, pearl oysters can be classified into three groups—(1) *P. maxima*, (2) *P. margaritifera*, and (3) akoya-type—that have differ-

line (figure A-1, C), continuing to the south of Ainan. The coastline between the two cities, referred to as Uwa-sea, is known to produce wild akoya oysters. The city has ranked first in Japanese production of akoya bead-cultured pearls in both volume and value for several recent years, according to municipal statistics (figure A-1, D; see also Ministry of Agriculture, Forestry, and Fisheries, n.d.). Most culturing pearl farms in the waters off Uwajima and the surrounding area were established around 1948 (Ehime Prefectural Lifelong Learning Center, 1984 a,b), though the oldest oyster harvesting business listed in Ainan historical records began in 1907.

Since 1957, the prefecture government's policy has been to separate akoya oyster hatcheries and pearl culturing businesses, while permitting only local fisheries to rear mollusks. In 1967, Ehime ranked second in Japanese pearl production (after Mie Prefecture, where Kokichi Mikimoto first cultured pearls). But due to a recession that began that same year, cultured pearl export prices went into a decline that continued until 1971. To overcome the challenging economic situation, pearl-related parties such as farmers and traders attempted to impose controls, remove low-quality pearls from production, reduce storage of overproduced pearls, and apply other measures, but this did not prevent many small businesses across Japan from going bankrupt. However, small businesses in the region around Uwajima were able to survive because the production of medium-size (7 mm) pearls was less severely affected. This was due to several factors, including the relatively short culturing periods; local sourcing of better-quality, less-expensive host akoya oysters; and the area's favorable fishery conditions. By 1972, the Japanese pearl industry had recovered and stabilized.

Ehime Prefecture ranked first nationwide in pearl production and income from 1974 until 1996, when a virus decimated the akoya oysters (Morizane et al., 2001). The Uwa-sea region was unable to escape the effect of the outbreak, resulting in a drastic decrease in akoya production to a mere 20% of the previous high. Since steps were taken to hybridize Japanese with Chinese/Vietnamese akoya oysters that would be resistant to infection, production has recovered (Morizane, 2012) and Ehime has been the top-producing prefecture since 2009 (Ehime Prefectural Government Planning Promotion Division, n.d.).

ent nuclear 28S rRNA and mitochondrial 16S rRNA genes. Akoya-type oysters include *P. fucata* (Indo-Pacific region), *P. radiata* (eastern Indian Ocean to Red Sea), and *P. imbricata* (western Atlantic region), that have the same nuclear 28S rRNA gene but different mitochondrial 16S rRNA genes (Masaoka et al., 2016). Thus, DNA investigation has demonstrated that the members of the akoya pearl oyster group are genetically very closely related species but distinct genealogical units, suggesting subspecies-level differences (Tëmkin, 2010). Tëmkin also pointed out that it might be meaningful to treat the three individual akoya populations as **evolutionary significant units**, because they originated from three different geographic regions. 16S rRNA genes differ in all five of the most abundant pearl oysters (*P. maxima*, *P. margaritifera*, *P. fucata*, *P. imbricata*, and *P. radiata*), making them very useful DNA markers to identify the *Pinctada* species or subspecies.

The targeted component of the DNA, the 16S rRNA gene, is the component necessary to code the 16S rRNA, essential in the process of biological **protein** synthesis. Because the cells of higher-order animals are known to have many copies, the DNA regions have the advantage of developing sensitive PCR-based identification methods (Masaoka and Kobayashi, 2005). Furthermore, 16S rRNA genes are conserved within a *Pinctada* species but contain sufficient variation between species to produce species-specific sequences (Masaoka and Kobayashi, 2004, 2005). These sequences have been registered in GenBank, the genetic sequence database of the National Institutes of Health's National Center for Biotechnology Information (NCBI).

Using a micro-drilling method, Meyer et al. (2013) succeeded in extracting nuclear and mitochondrial DNA samples and identifying the pearl oyster species as *P. margaritifera*, *P. maxima*, or *P. radiata*. For the present study, akoya cultured pearl oysters were sampled during harvesting (*hamaage*) in Uwajima, in Japan's Ehime Prefecture, with the purpose of extracting DNA and the mitochondrial 16S rRNA gene from minute amounts of pearl powder and tissues of *P. fucata*. (For the history of pearl culturing in Uwajima, see box A.) Our goal was to conclusively identify the species and use that as a reference for determining the whole targeted DNA sequence. The Japanese akoya pearl oysters *P. martensii* and *P. fucata martensii* have been distinguished from *P. fucata* based on the classical biological classification such as shell morphologies in most cases (e.g., Hayami, 2000; Masaoka and Kobayashi, 2004). However, their genetic properties are very similar, with the same 16S rRNA genes, indicating that *P. fucata* and *P. martensii* are genetically much closer to other

TABLE 1. List of DNA samples and results.

	Sample	PCR using Ex-Taq[b]	Nested PCR using Ex-Taq[b]	PCR using KOD[b]	PCR data in figure 3	Sequence result (*P. fucata* matching)
Donor oyster 4	Mantle tissue	○	-	-	(a)	524 bp (100%)
Host oyster 14	Mantle tissue	○	-	-	(b)	524 bp (100%)
Pearl 12 cream	9.33 mg (0.046 ct)	X	X	○	(d)	524 bp (100%)
Pearl 14 cream	7.37 mg (0.037 ct)	X	○	X	(c)	524 bp (100%)
Pearl 19 cream	6.03 mg (0.030 ct)	X	X	○	(e)	524 bp (100%)
Pearl 20 cream[a]	5.27 mg (0.026 ct)	X	X	○	(f)	350 bp (100%)

[a]*Only forward sequence data was obtained for pearl no. 20, resulting in a matching sequence molecular weight of 350 bp in total 820 bp (see supplementary figure S-1 at https://www.gia.edu/gems-gemology/spring-2018-DNA-identification-pinctada-fucata-pearls-data-supplement). ○ and X indicate PCR success and failure respectively.*
[b]*An enzyme*
[c]*bp = base pairs*

akoya-type species such as *P. radiata* and *P. imbricata* (Masaoka and Kobayashi, 2004; Wada and Tëmkin, 2008). This study treats *P. martensii* as a subspecies of *P. fucata*, as their 16S rRNA genes have the same DNA sequence alignments.

MATERIALS AND METHODS

The shells sampled for this project were collected from live pearl oysters in January 2016 at Uwajima (see the harvesting details in figure 2). Thirty-seven pearl oysters, consisting of 28 host oysters used to grow pearls and nine donor oysters bred for tissue grafting, were collected after they were confirmed to be alive and immediately transported to the University of Tokyo. The shells were dissected, and both the mantle and pearl samples were frozen and stored at –80°C until analysis was possible. For DNA extraction experiments, the mantle tissue of a host oyster and a donor oyster were selected together with four pearls (see table 1).

Our strategy was to use a simple direct sequence method consisting of three experimental steps: (1) DNA extraction and subsequent purification, (2) amplification and detection, and (3) sequencing. For the first steps of DNA extraction and purification, 16S rRNA gene extraction from mantle tissues was performed using a general phenol-chloroform extraction process (see Suzuki et al., 2004), whereas 16S rRNA genes were obtained from pearl powder samples using a method similar to that described in Meyer et al. (2013). The second step of DNA amplification consists of the PCR and nested PCR methods (figure 1A). The PCR method consists of three repeating processes: denaturation, annealing, and extension using the PCR machine. Denaturation is separating the targeted DNA double strands, called "DNA templates," into two single strands. Annealing is a connecting process of the single DNA strands with forward or reverse primers, which are artificially aligned short nucleotides (about 10–15 nucleotides). Extension is extending the double chain of the single DNA strands with available nucleotides, called deoxynucleotides (see figure 1B). These three processes are repeated for 30–40 cycles, and targeted DNA (the 16S rRNA gene) should be amplified exponentially. The nested PCR method is known to improve PCR sensitivity for specific DNA amplification and is often used for complementary DNA cloning (e.g., Suzuki et al., 2004; Liu et al., 2007), as well as to recover ancient DNA (e.g., Salo et al., 1994; Yang et al., 1997). Meyer et al. (2013) also applied the nested PCR method after drilling pearl samples to obtain as little as 10 mg of powder and succeeded in amplifying nuclear ITS2 regions (refer to glossary for the definition of ITS). The determination of whether DNA was amplified was performed using a gel electrophoresis method (figure 1B). Negatively charged DNA molecules migrate though the gel when an electric field is applied and are separated based on their size. Thus this method produces the quantity and approximate molecule size of amplified DNA necessary for the third step of sequencing. We applied the Sanger method to determine the nucleotide arrangement (figure 1C), added fluorescent-labeled **dideoxynucleotides** to amplify the DNA template, and subsequently generated DNA fragments as the dideoxynucleotides terminated the DNA extension process (figure 1C, left). The DNA fragments were separated by capillary electrophoresis on the basis of the size, producing the **electropherogram** as the final sequence result (figure 1C, right). The detailed DNA extraction to detection methods are described in box B.

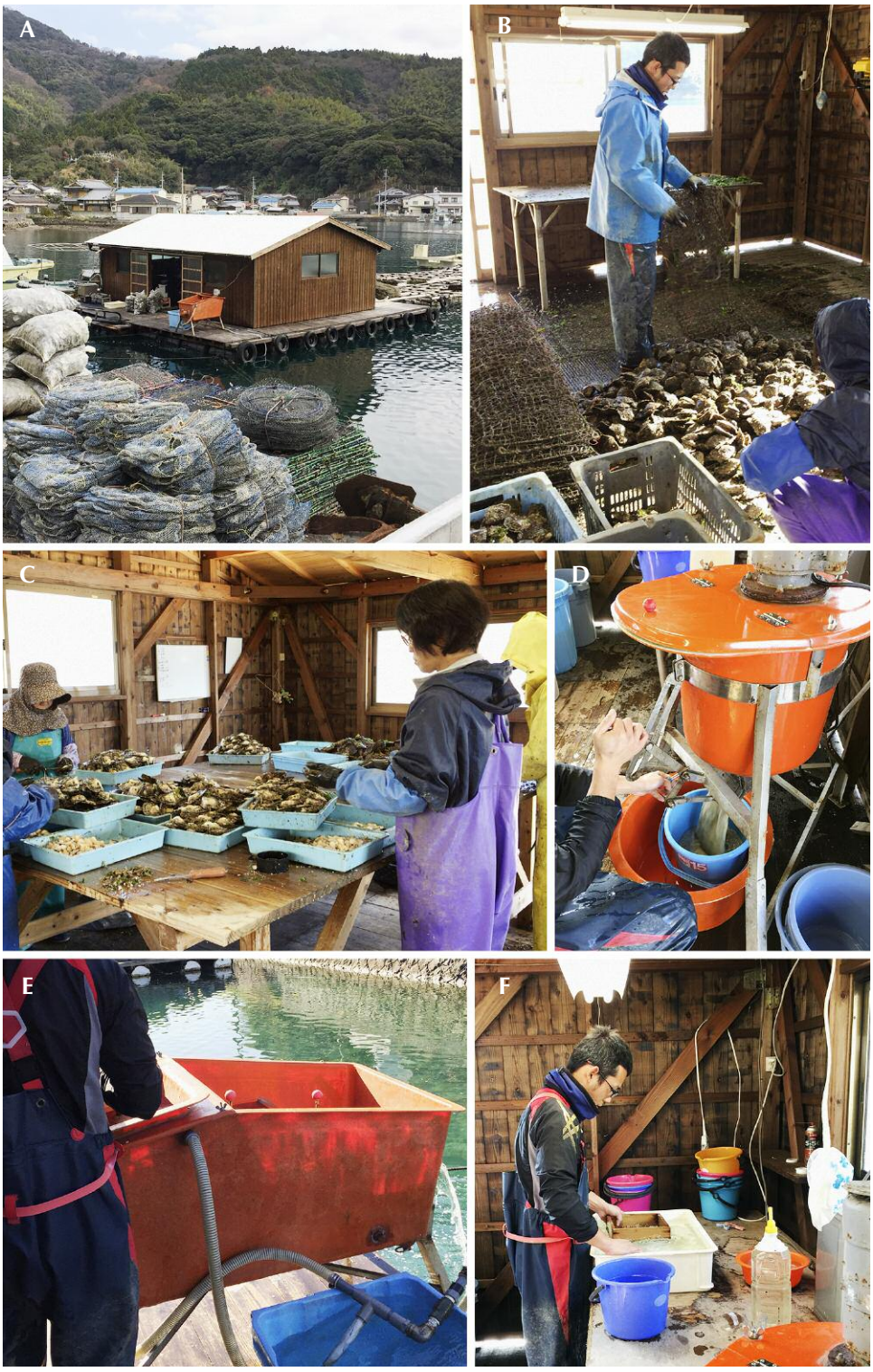

Figure 2. Between November and January of each year, pearls are harvested at Uwajima from akoya shells operated on either six months prior (classified by the Japanese as tonen-mono*) or 18 months prior (*koshi-mono*). A: An Uwajima pearl farmer's work hut. B–F: Various scenes from harvesting in a shed on one of the floating rafts. B: Oysters are removed from a net on the floor to separate the living mollusks from the dead ones. C: After the shells are opened on a table, the adductor muscles are removed and the other soft tissues are separated. D: The liquefied soft tissues containing the bead-cultured pearls are collected in a blue plastic bucket. E: The remaining organic matter containing smaller "keshi" pearls is poured into a separator to remove the keshi pearls. F: The bead-cultured pearls are placed into a wooden box for cleaning and subsequent inspection. Photos by K. Saruwatari.*

RESULTS AND DISCUSSION

Figure 3 shows the PCR and nested PCR products of the 16S rRNA gene obtained from the gel electrophoresis process. All the bands appeared at approximately 500 **base pairs (bp)** of molecular weight markers, and the resulting forward and reverse sequences mostly matched with 524 bp of *P. fucata* (see table 1 and supplementary figure S-1 at

BOX B: PEARL DNA EXTRACTION TO DETECTION—EXPERIMENTAL DETAILS

To prepare the samples for testing, we cleaned the pearls in 4% sodium hypochlorite solution for 20 minutes with no obvious change of appearance, and then peeled the nacreous layers using a drill to obtain minute samples of pearl powder (5.27–9.33 mg, or 0.026–0.047 ct; see table 1 and figure B-1). The pearls were severely damaged since they were only in the mollusks for around six months (**tonen-mono**) and possessed very thin nacreous overgrowths. The effect of the bead nucleus is considered insignificant because the nuclei are mostly produced from Mississippi River mussels—i.e., *Fusconia flava*, *Potamilis alatus*, and *Quadrula quadrula*—belonging to the Unionidae family (Dirlam and Weldon, 2013).

The 16S rRNA genes of the three Mississippi River mussels mentioned above are registered in GenBank; their homologies (shared ancestries) with the 16S rRNA gene of *P. fucata* are only 52–53%. This indicates that the PCR primers for *Pinctada* species will not amplify the 16S rRNA genes present within bead nuclei.

The powder samples from each pearl were dissolved in 500 microliters (µL) of 0.5 M EDTA (pH 8) and vigorously vortexed for two minutes and subsequently incubated overnight at 56°C in a water bath in accordance with the procedures of Meyer et al. (2013). For DNA extraction we used the commercial FastDNA SPIN Kit for Soil (MP Biomedicals) in accordance with the manufacturer's recommendations, with two exceptions:

1) Rather than using the Lysing Matrix E tubes provided in the kit, the 978 µL sodium phosphate buffer was added directly to the microfuge tube of pearl-EDTA solution.
2) Instead of performing the fourth step of homogenization with the FastPrep instrument, the samples were vortexed vigorously for two minutes.

The extracted DNA samples underwent PCR amplification using a Takara TP600 PCR Thermal Cycler Dice Gradient). PCR was carried out with a mixture of 0.25–0.50 µL of DNA template, 0.05 µL Takara Bio's Ex-Taq PCR enzyme, 1 µL of PCR enzyme buffer, 1 µL of dNTP mixture (2.5 mM), 0.5 µL of each forward and reverse primer (10 mM; forward 5'-CGCCTGGTTGATTAAAAACATTGCTGC-3' and reverse: 5'-CCGGTTTGAACTCAGATCACGTA-3') according to Meyer et al. (2013), and 7 µL of Milli-Q water. The total amount was 10.30–10.55 µL for the PCR process. The PCR cycle involved a pre-reaction step at 96°C for three minutes, followed by 35 cycles of denaturation at 96°C for 30 seconds, annealing at 55°C for 30 seconds, and elongation at 72°C for 30 seconds. Nested PCR followed the same procedure as the first PCR process but used inner primers (forward: 5'-AAAAACATTGCTGCACGGA-3' and reverse: 5'-ACTCAGATCACGTAGGGCTT-3').

Initial attempts at amplifying DNA from three pearl samples using the Ex-Taq enzyme did not succeed; another attempt, using a different PCR enzyme, KOD FX Neo (Toyobo Co., Ltd.), was successful (see table 1). PCR using KOD FX Neo enzyme was carried out with a mixture of 0.5 µL of DNA template, 0.5 µL of PCR enzyme, KOD FX Neo, 12.5 µL of PCR enzyme buffer, 5 µL of dNTP mixture (2 mM), 0.5 µL of each forward and reverse primer, and 5.5 µL of Milli-Q water. The total amount was 25 µL for the PCR process. After detecting the amplified DNA using the gel electrophoresis method, the amplified DNA samples were concentrated by ethanol precipitation and diluted using 10 µL distilled water. The samples were then divided into two 5 µL batches. The forward and reverse sequencing were prepared by adding 0.5 µL of primer (10 mM) to each batch and diluting that into 13 µL for the next sequencing process. While all the samples were prepared by authors KS and MS, the 16S rRNA sequencing was outsourced to the Japan Food Analysis and Biotechnology Company (FASMAC), where the Sanger sequencing method was applied.

www.gia.edu/gems-gemology/spring-2018-DNA-identification-pinctada-fucata-pearls-data-supplement). For one pearl sample (no. 20) we only obtained the forward sequence with 820 bp in total. However, the part of the sequence with 350 bp is perfectly matched within the part of the 524 bp range expected for *P. fucata* and not with sequences of the other *Pinctada* species on record, including *P. radiata* and *P. imbricata* (see supplementary figure S-2 at https://www.gia.edu/gems-gemology/spring-

Figure B-1. The akoya pearl samples used in this study. The photos on the left show the specimens in plastic bags (along with the host oysters) before the powder samples were obtained. Photos by K. Saruwatari. The photos on the right, taken after the powder samples were obtained, show severely damaged pearls and exposed inner nuclei. Photos by S. Nagai.

2018-DNA-identification-pinctada-fucata-pearls-data-supplement). Thus, all the 16S rRNA gene samples obtained matched *P. fucata*.

In this study, it was possible to extract DNA from 5 to 10 mg of pearl powder, but the pearls were severely damaged in the process (see figure B-1, right column). To apply the DNA methods effectively within the pearl industry, further improvements to the extraction step are clearly needed. Reducing the sample size required to approximately 0.01 mg

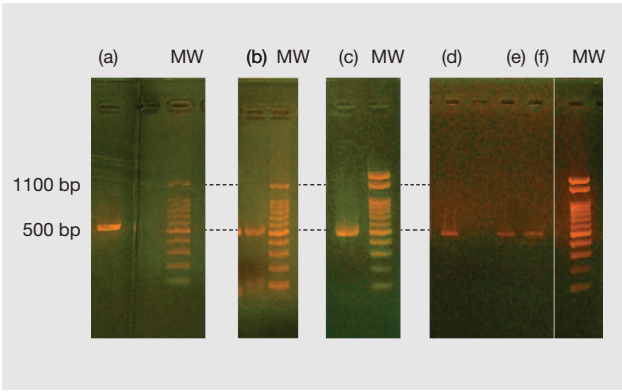

Figure 3. Experimental results of the gel electrophoresis process; letters (a)–(f) correspond with those in table 1. MW (molecular weight) markers for (a) and (d) were obtained from two separate gels during each electrophoresis experiment. The sequence data results are given in table 1. Photo by K. Saruwatari

would be one such improvement. This would equate to the approximate amount ablated during laser ablation–inductively coupled plasma–mass spectroscopy (LA-ICP-MS) chemical measurements (Hänni and Cartier, 2013). DNA amplification using PCR was improved by (1) the application of the nested PCR method and (2) the use of two different types of PCR polymerase: Taq-type and KOD-type (summarized in table 1).

A powder sample was obtained from pearl sample no. 14 to successfully amplify the 16S rRNA using the nested PCR method with a Taq-type polymerase similar to that applied by Meyer et al. (2013). The DNA of the other three pearl samples was amplified using only the first (non-nested) PCR with a KOD-type polymerase. The advantage of KOD-type polymerase is that it has 3'→5' **exonuclease activity** (Morikawa et al., 1994), which is an active process mechanism of "proofreading" the polymerase chain reaction. The Taq polymerase does not have this proofreading activity. At present it is not known why different polymerase activities for the pearl samples occurred, but they may help amplify 16S rRNA genes in various pearl powder samples.

Future research needs to address the effects of any treatments, such as *maeshori* or bleaching, on DNA extraction. Although the species and distinction of the akoya-type pearl oysters are still under discussion, the draft genome of *P. fucata* has been provided by Takeuchi et al. (2012) and ongoing DNA studies will continue. Future results will aid in species identification and may also provide evidence of the geographic region where pearls formed, benefiting the pearl industry in matters of traceability.

CONCLUSIONS

The 16S rRNA genes extracted from the mantle tissues of one donor shell and one host shell fully matched the complete sequence of *P. fucata*. The 16S rRNA genes extracted from the powder of the nacreous layers of four bead-cultured pearl samples were also found to match the sequence of *P. fucata*. Thus, the pearl oysters and pearl samples obtained in January 2016 from Uwajima were categorically identified as originating from *P. fucata* species. From a methodology perspective, it was possible to identify the *P. fucata* 16S rRNA gene from only 5 to 10 mg of pearl powder sample weight, compared to the 10 to 100 mg quantity previously reported by Meyer et al. (2013). This reduced sampling is important when analyzing pearls of historical significance and value.

GLOSSARY

Base pair (bp): A pairing of the molecules that comprise DNA, specifically an adenine (A)/thymine (T) or guanine (G)/cytosine (C) pair.

Deoxyribonucleic acid (DNA): The hereditary material in humans and almost all other organisms. Most DNA is located in the cell nucleus, but a small amount can also be found in the mitochondria. Complementary DNA is DNA synthesized by reverse transcription reaction of messenger RNA.

Dideoxynucleotide: A type of nucleotide that terminates the DNA extension process, as it does not contain the OH^- (hydroxyl) groups needed for extending DNA chains.

Electropherogram: Diagram produced by electrophoresis.

Exonuclease activity: An activity of an enzyme to hydrolyze a DNA chain sequentially from the end of a polynucleotide molecule.

Evolutionary significant unit: A population of subspecies organisms that is considered distinct for conservation purposes. Proposed by Ryder (1986).

Gene: The basic physical and functional unit of heredity. A "gene" is encoded by DNA and usually acts as a template to make a protein.

Internal transcribed spacer (ITS): The gene regions between nuclear rRNA genes.

Koshi-mono: The Japanese term for akoya cultured pearls removed from mollusks 12 months or more after seeding.

Mitochondrion: An **organelle** in cells that have a nucleus, as in plants and animals.

Organelle: Small, specialized structures in cells that operate like organs by carrying out specific tasks.

Polymeric: Referring to an aggregate of monomers or combined molecules.

Protein: A molecule consisting of amino acids that carries out functions related to an organism's biology.

Phylogeny: The history of the evolution of a species.

Ribonucleic acid (RNA): A **polymeric** molecule involved in various biological roles for coding, decoding, regulation, and expression of genes. 16S rRNA (16S ribosomal RNA) is a component of ribosomal RNA, and its gene is coded in **mitochondria**.

Tonen-mono: The Japanese term for akoya cultured pearls removed from the mollusks within a year of seeding.

ABOUT THE AUTHORS

Dr. Saruwatari is supervisor of colored stone identification at GIA in Tokyo. Dr. Suzuki is an associate professor in the department of applied biological chemistry at the University of Tokyo. Dr. Zhou is a research scientist and manager of pearl identification at GIA in New York. Mr. Kessrapong is a staff gemologist, and Mr. Sturman is senior manager of identification, at GIA in Bangkok.

ACKNOWLEDGMENTS

The authors appreciate the assistance of Dr. Ahmadjan Abduriyim (Tokyo Gem Science and GSTV Gemological Laboratory) and Matsumoto Pearl Co., Ltd. (Uwajima, Ehime, Japan), on various aspects of this project. Dr. Hirotoshi Endo (Tsukuba University), the three peer reviewers, and Mrs. Artitaya Homkrajae (GIA, Carlsbad) are also thanked for their discussions and constructive suggestions to improve the article.

REFERENCES

Dirlam D.M., Weldon R. (2013) *Splendour and Science of Pearls*. Gemological Institute of America, Carlsbad, CA, 139 pp.

Ehime Prefectural Government Planning Promotion Division (n.d.) Ehime fisheries statistics, http://www.pref.ehime.jp/h37100/toukei/ [in Japanese].

Ehime Prefectural Lifelong Learning Center (1984a) Ehime prefecture history journal II: Seven Uwaumi pearl culture (1985) http://www.i-manabi.jp/system/regionals/regionals/ecode:2/34/view/4928 [in Japanese].

——— (1984b) Ehime prefecture history journal I (General): Fishery cultivation. http://www.i-manabi.jp/system/regionals/regionals/ecode:2/31/view/4389 [in Japanese].

Freier R., Fernández-Tajes J., Méndez J. (2008) Identification of razor clams *Ensis arcuatus* and *Ensis siliqua* by PCR-RFLP analyses of ITS1 region. *Fisheries Science*, Vol. 74, No. 3, pp. 511–515, http://dx.doi.org/10.1111/j.1444-2906.2008.01553.x

Hänni H.A (2000) Freshwater cultured "Kasumiga pearls" with akoya cultured pearl nuclei. *G&G*, Vol. 36, No. 2, pp. 167–168.

Hänni H.A., Cartier L.E. (2013) Tracing cultured pearls from farm to consumer: A review of potential methods and solutions. *Journal of Gemmology*, Vol. 33, No. 7-8, pp. 239–245.

Hänni H.A., Kiefert L., Giese P. (2005) X-ray luminescence, a valuable test in pearl identification. *Journal of Gemmology*, Vol. 29, No. 5/6, pp. 325–329.

Hayami I. (2000) Family Pteriidae order Pterioida. In T. Okutani, Ed., *Marine Mollusks in Japan*. Tokai University Press, Tokyo, pp. 879–883 [In Japanese with English species and descriptions].
Karampelas S., Miche J., Zheng-Cui M., Schwarz J-O., Enzmann F., Fritsch E., Leu L., Krzemnicki M.S. (2010) X-ray computed microtomography applied to pearls: Methodology, advantages, and limitations. *G&G*, Vol. 46, No. 2, pp. 122–127, http://dx.doi.org/10.5741/GEMS.46.2.122
Kessrapong P., Lawanwong K., Sturman N. (2017) *Pinctada maculata* (Pipi) bead-cultured blister pearls attached to their shells, Apr. 25, https://www.gia.edu/gia-news-research/pinctada-maculata-bead-cultured-blister-pearls-shells
Liu H.-L., Liu S.-F., Ge Y.-J., Liu J., Wang X.-Y., Xie L.-P., Zhang R.-Q., Wang Z. (2007) Identification and characterization of a biomineralization related gene PFMG1 highly expressed in the mantle of *Pinctada fucata*. *Biochemistry*, Vol. 46, pp. 844–851, http://dx.doi.org/10.1021/bi061881a
Masaoka T., Kobayashi T. (2004) Polymerase chain reaction-based species identification of pearl oyster using nuclear ribosomal DNA internal transcribed spacer regions. *Fish Genetics and Breeding Science*, Vol. 33, pp. 101–105.
——— (2005) Species identification of *Pinctada imbricata* using intergenic spacer of nuclear ribosomal RNA genes and mitochondrial 16S ribosomal RNA gene regions. *Fisheries Science*, Vol. 71, pp. 837–846, http://dx.doi.org/10.1111/j.1444-2906.2005.01035.x
——— (2006) Species identification of *Pinctada radiata* using intergenic spacer of nuclear ribosomal RNA genes and mitochondrial 16S ribosomal RNA gene regions. *Fish Genetics and Breeding Science*, Vol. 35, pp. 49–59.
Masaoka T., Okamoto H., Araki K., Nagoya H., Fujiwara A., Kobayashi T. (2016) Distinction between *Pinctada* species based on nuclear and mitochondrial ribosomal RNA gene regions. *DNA Testing*, Vol. 8, pp. 9–21.
Meyer J.B., Cartier L.E., Pinto-Figueroa E.A., Krzemnicki M.S., Hänni H.A., McDonald B.A. (2013) DNA fingerprinting of pearls to determine their origins. *PLOS One*, Vol. 8, No. 10, pp. 1–11, http://dx.doi.org/10.1371/journal.pone.0075606
Ministry of Agriculture, Forestry, and Fisheries (n.d.) Sea surface fishery production statistics survey, http://www.maff.go.jp/j/tokei/kouhyou/kaimen_gyosei/index.html [in Japanese].
Morikawa M., Izawa Y., Rashid N., Hoaki T., Imanaka T. (1994) Purification and characterization of a thermostable thiol protease from a newly isolated hyperthermophilic Pyrococcus sp. *Applied and Environmental Microbiology*, Vol. 60, No. 12, pp. 4559–4566.
Morizane T. (2012) Circumstances and current condition of pearl culturing at Ehime prefecture. *JFSTA News*, No. 17, pp. 1–10 [in Japanese].
Morizane T., Takimoto S., Nishikawa S., Matsuyama N., Tyohno K., Uemura S., Fujita Y., Yamashita H., Kawakami H., Koizumi Y., Uchimura Y., Ichikawa M. (2001) Mass mortalities of Japanese pearl oyster in Uwa Sea, Ehime in 1997–1999. *Japanese Society of Fish Pathology*, Vol. 36, No. 4, 207–216, http://dx.doi.org/10.3147/jsfp.36.207 [in Japanese].
Ryder O.A. (1986) Species conservation and systematics: the dilemma of subspecies. *Trends in Ecology & Evolution*, Vol. 1, pp. 9–10, http://dx.doi.org/10.1016/0169-5347(86)90059-5
Salo W.L., Aufderheide A.C., Buikstra J., Holcomb T.A. (1994) Identification of Mycobacterium tuberculosis DNA in a pre-Columbian Peruvian mummy. *Proceedings of the National Academy of Sciences*, Vol. 91, No. 6, pp. 2091–2094, http://dx.doi.org/10.1073/pnas.91.6.2091
Scarratt K. (2011) Pearl identification—A practitioner's perspective. *G&G*, Vol. 47, No. 2, pp. 117–119.
Sturman N. (2009) The microradiographic structures of non-bead cultured pearls. GIA Thailand Lab Notes, http://www.giathai.net/pdf/The_Microradiographic_structures_in_NBCP.pdf
Suzuki M. Murayama E., Inoue H., Ozaki N., Tohse H., Kogure T., Nagasawa H. (2004) Characterization of Prismalin-14, a novel matrix protein from the prismatic layer of the Japanese pearl oyster (*Pinctada fucata*). *Biochemical Journal*, Vol. 382, pp. 205–213, http://dx.doi.org/10.1042/BJ20040319
Takeuchi T., Kawashima T., Koyanagi R., Gyoja F., Tanaka M., Ikuta T., Shoguchi E., Fujiwara M., Shinzaro C., Hisata K., Fujie M., Usami T., Nagai K., Maeyama K., Okamoto K., Aoki H., Ishiwaka T., Masaoka T., Fujiwara A., Endo K., Endo H., Nagasawa H., Kinoshita S., Asakawa S., Watabe S., Satoh N. (2012) Draft genome of the pearl oyster *Pinctada fucata*: A platform for understanding bivalve biology. *DNA Research*, Vol. 19, No. 2, pp. 117–130, http://dx.doi.org/10.1093/dnares/dss005
Tëmkin I. (2010) Molecular phylogeny of pearl oysters and their relatives (Mollusca, Bivalvia, Pterioidea). *BMC Evolutionary Biology*, Vol. 10, p. 342, http://dx.doi.org/10.1186/1471-2148-10-342
Toro J.E. (1998) Molecular identification of four species of mussels from southern Chile by PCR-based nuclear markers: The potential use in studies involving planktonic surveys. *Journal of Shellfish Research*, Vol. 17, No. 4, pp. 1203–1205.
Wada K.T., Tëmkin I. (2008) Taxonomy and phylogeny. In P.C. Southgate and J.S. Lucas, Eds., *The Pearl Oyster*, Elsevier, Oxford, UK, pp. 37–75.
Yang H., Golenberg E.M., Shoshani J. (1997) Proboscidean DNA from museum and fossil specimens: An assessment of ancient DNA extraction and amplification techniques. *Biochemical Genetics*, Vol. 35, pp. 165–179.

Not all gems come from under the ground.

The Gemological Institute of America® supports communities where gems are mined, working with the Nelson Mandela Centre of Memory to build libraries in Africa and helping artisanal miners understand the quality of their discoveries with our Gem Guide. These initiatives help make it possible for regional populations to take a more active role in the industry and ultimately help their community look forward to a brighter future. Our contributions are one of the many reasons why GIA® is the world's foremost authority on diamonds, colored stones and pearls.

Learn more about the many facets of GIA at GIA.edu

GIA®

The World's Foremost Authority in Gemology™

Ensuring the Public Trust Through Nonprofit Service Since 1931

BENEFICIATION EDUCATION INSTRUMENTS LABORATORY RESEARCH

The

Dr. Edward J. Gübelin Most Valuable Article AWARD

Gems & Gemology is pleased to announce the winners of this year's Dr. Edward J. Gübelin Most Valuable Article Award, as voted by the journal's readers. We extend our sincerest thanks to all the subscribers who participated in the voting.

The first-place article was "Big Sky Country Sapphire: Visiting Montana's Alluvial Deposits" (Summer 2017), which documents a visit to the upper Missouri River and Rock Creek sapphire mining areas. Receiving second place was "The Colombian Emerald Industry: Winds of Change" (Fall 2017), a first-hand look at Colombia's emerald mines and the cutting and trading industry in Bogotá. Third place was awarded to "Characterization of Mg and Fe Contents in Nephrite Using Raman Spectroscopy" (Summer 2017), an evaluation of the usefulness of Raman spectroscopy in distinguishing the color varieties of nephrite based on the relative ratio of Mg to Fe concentrations.

The authors of these three articles will share cash prizes of $2,000, $1,000, and $500, respectively. Following are brief biographies of the winning authors.

Most Valuable Article

Tao Hsu

Andrew Lucas

Robert Kane

Shane McClure

Nathan Renfro

First Place

Big Sky Country Sapphire: Visiting Montana's Alluvial Deposits

Summer 2017

Tao Hsu, Andrew Lucas, Robert E. Kane, Shane F. McClure, and Nathan D. Renfro

Tao Hsu is manager of global professional development, gemology; technical editor of *Gems & Gemology*; and a contributor to the Research and News section of GIA's website. Dr. Hsu, who received her PhD in geology from the University of Southern California, is based at GIA in Carlsbad, California. **Andrew Lucas** is a field gemologist in GIA's content strategy department in Carlsbad. Mr. Lucas researches and documents the entire mine-to-market gem and jewelry industry for GIA education. He also presents seminars on colored stones and diamonds. **Robert Kane** is president and CEO of Fine Gems International in Helena, Montana. **Shane McClure** is director of identification services at GIA in Carlsbad. He is well known for his many articles and lectures on gem identification. He is also co-editor of *G&G*'s Lab Notes section. **Nathan Renfro** is the manager of the gem identification department and microscopist in the inclusion research department at GIA in Carlsbad.

Second Place

The Colombian Emerald Industry: Winds of Change

Fall 2017

Darwin Fortaleché, Andrew Lucas, Jonathan Muyal, Tao Hsu, and Pedro Padua

Darwin Fortaleché

Jonathan Muyal

Pedro Padua

Formerly chief gemologist at Centro de Desarrollo Technológico de la Esmeralda Colombiana (CDTEC), **Darwin Fortaleché** is now chief gemologist at Guild Gem Laboratory in Hong Kong. Mr. Fortaleche earned a degree in gemology from Universidad Pedagógica y Tecnológica de Colombia. **Jonathan Muyal** is a staff gemologist at GIA in Carlsbad, California, where he also serves as the librarian for the research reference stone collection. Mr. Muyal specializes in photomicrography of inclusions in gem materials. **Pedro Padua** is the senior video producer at GIA in Carlsbad. He also contributes to GIA website articles and educational course materials. He received his master's degree in communications from Loyola Marymount University. **Andrew Lucas** and **Tao Hsu** were profiled in the first-place entry.

Third Place

Characterization of Mg and Fe Contents in Nephrite Using Raman Spectroscopy

Summer 2017

Xiaoyan Feng, Yong Zhang, Taijin Lu, and Hui Zhang

Xiaoyan Feng

Yong Zhang

Taijin Lu

Hui Zhang

Xiaoyan Feng is a senior engineer at the National Gems & Jewellery Technology Administrative Center (NGTC) in Beijing. She has been active in jewelry testing and research for 14 years. **Yong Zhang** is a research assistant at NGTC in Beijing. He is actively engaged in research on diamonds and colored gemstones, including jade. **Taijin Lu** is chief researcher at NGTC in Beijing. **Hui Zhang** is the dean of Yunnan Land and Resources Vocational College in Kunming, China.

Thank you to all the readers who voted. In addition to our winning authors, we congratulate Adam Hitchin of Shropshire, UK, whose name was randomly drawn from the entries to win a one-year subscription to *G&G*.

The following 25 questions are from the four 2017 issues of *G&G*. Refer to the articles in those issues to find the single best answer for each question.

Mark your choice on the response card provided in this issue or visit gia.edu/gems-gemology to take the Challenge online. Entries must be received no later than **Friday, August 10, 2018**. All entries will be acknowledged with an e-mail, so please remember to include your name and e-mail address (and write clearly).

Score 75% or better, and you will receive a certificate of completion (PDF file). Earn a perfect score, and your name also will be listed in the Fall 2018 issue of *Gems & Gemology*.

1. With regard to diamonds, the term "Old Mine" refers to
   A. diamonds of bluish white color from old diggings in Brazil.
   B. a cutting style.
   C. None of the above
   D. Both A and B

2. Which of the following is true about Russian diamonds from the Lomonosov mine?
   A. They come from Europe's first diamond mine.
   B. 50–60% of the diamonds mined are at or near gem quality.
   C. They have been in the marketplace for more than half a century.
   D. The largest diamond found to date was a gem-quality 106 ct stone.

3. Synthetic star sapphires produced by Wiede's Carbidwerk
   A. in many cases have shorter rutile needles than those found in Linde stars.
   B. were not grown by the Verneuil method.
   C. are always indistinguishable from Linde stars.
   D. were grown using exactly the same process used for Linde stars.

4. CLIPPIR diamonds
   A. do not contain hydrogen.
   B. tend to contain magnetic inclusions.
   C. contain mainly sulfide and oxide inclusions.
   D. form under oxidizing conditions in the mantle.

5. All of the following statements about blue jadeite from Japan are true except:
   A. It can be found in both Tottori Prefecture and Niigata Prefecture.
   B. Ti^{4+}-Fe^{2+} charge transfer pairs produce its blue color.
   C. Only Japan produces blue jadeite.
   D. It contains high TiO_2 levels.

6. Which of the following is true about white nephrite?
   A. It can be much more valuable than the other colors of nephrite.
   B. It shows strong peaks at 3661 and 3645 cm^{-1} with Raman.
   C. It contains more Fe^{2+} than green nephrite.
   D. It is referred to as *biyu*.

7. HPHT-grown synthetic diamonds
   A. are only produced in yellow to orange-yellow hues.
   B. are only used for melee.
   C. Both A and B
   D. None of the above

8. Unlike gem carvers in other regions, Idar's craftsmen
   A. hold the rough steady in two hands against the cutting wheel.
   B. fashion only local material.
   C. have never ventured elsewhere to learn new techniques.
   D. None of the above

9. Vivid blue to green copper-bearing tourmalines are
   A. only found in Paraíba State in northeastern Brazil.
   B. found in Brazil, Mozambique, and Nigeria.
   C. classified in the liddicoatite species.
   D. vivid in color due to manganese.

10. Which characteristic of conventional diamond and carbonado is the most comparable?
    A. Habit or shape of the rough
    B. Composition of inclusions
    C. X-ray diffraction data
    D. Toughness

11. The *R*-lines observed in photoluminescence (PL) spectroscopy of emerald

A. are in the red region of the visible spectrum.
B. appear in absorption spectra for emerald as well.
C. result from the electronic decay of a doublet metastable state.
D. All of the above

12. Which is true regarding Australian akoya cultured pearls?
A. The ratio of blue to yellow bodycolor produced is related to the individual seeders.
B. Bead rejection rates are comparable to farms in India and Micronesia.
C. Most of the pearl growth happens from June to August.
D. Their nacre is less thick than that of Japanese cultured pearls.

13. The presence of silicon in sapphire containing titanium (Ti), iron (Fe), and magnesium (Mg) will
A. result in an absence of blue color as Ti pairs with Mg.
B. permit or augment a blue color by pairing with Mg.
C. impact color if chromium is present.
D. have no impact on the color.

14. PL mapping of optical defects in diamond
A. provides no additional information over standard PL measurements.
B. is well correlated to growth features imaged with DiamondView.
C. cannot identify diamond synthetics.
D. can be done at room temperature.

15. The difference between dalmatian jasper and dalmatian stone is
A. none.
B. the composition of the host rock.
C. the diameter of the spots does not exceed 4 mm in dalmatian jasper.
D. the color of the spots.

16. A flat panel detector (FPD) used with real-time X-ray microradiography has the following advantage over an image intensifier (II) detector:
A. Images produced by the FPD have far less noise.
B. No hazardous liquids are needed.
C. It is approximately 40% less expensive.
D. Images are produced much faster.

17. Pink diamonds from the Lomonosov mine
A. most likely owe their color to deformation.
B. have a similar color origin to Argyle diamonds.
C. occur in a Proterozoic orogenic setting.
D. All of the above

18. The color of by-product synthetic zincite from zinc oxide processing is
A. not distinctly correlated to the chemical composition manganese.
B. due to a single sharp absorption at 480 nm.
C. solely due to the chromophore manganese.
D. clearly attributable to iron.

19. Alluvial sapphire from Montana
A. is never heat-treated.
B. was used for bearings for torpedoes during World War II.
C. is no longer actively mined.
D. only comes in pastel bluish green to greenish blue.

20. Tourmaline from Luc Yen, Vietnam, is known for
A. specimens of liddicoatite and uvite.
B. high transparency and facetable quality.
C. color variety and large sizes suitable for carving.
D. electric blues and greens, rivaling the best Paraíba tourmalines from Brazil.

21. An estimated ___% of Colombia's emeralds have been mined to date.
A. 20
B. 50
C. 70
D. 90

22. A challenge for radiocarbon dating of pearls arises from
A. samples impacted by atomic bomb activity.
B. marine pearls of unknown origin.
C. the geology of the watershed.
D. All of the above

23. The Czochralski crystal growth method was chosen for GIA's new corundum standards because
A. with this method, it is easy to incorporate ideal amounts of iron, chromium, and titanium into corundum.
B. this method produces uniformly "doped" crystals with low variation in the trace elements of interest.
C. it is a very quick and economical method of crystal growth.
D. None of the above

24. "Superdeep" diamonds generally differ from lithospheric diamonds in what way?
A. Diamond type
B. The compositions of their inclusions
C. The shape of the rough
D. All of the above

25. What causes the iridescence in quartz from the Deccan Traps of India?
A. Surface grooves paired with an underlying lamellar structure
B. The presence of silica spheres
C. Dominant *r* {101} faces
D. Thin-film effects

DIAMOND

Fracture-Filled Diamond with "Rainbow" Flash Effect

A loose diamond submitted for a diamond grading report is evaluated and given a grade on a scale relative to each value factor. Clarity, defined as a diamond's relative freedom from inclusions or blemishes, is graded on a scale of Flawless (least included) to I_3 (most included). The most common inclusions in diamond are crystals, which are contained entirely within the stone, and fractures—also known as feathers—which are surface reaching. Various clarity treatments exist to mask or remove undesirable inclusions because high-clarity diamonds are considered more valuable. Some diamond clarity treatments are permanent, while others are not and may change drastically in appearance with time or improper care. For this reason, GIA does not issue grading reports for diamonds that have been treated with unstable, non-permanent treatments. Acceptable treatments such as laser drilling and internal laser drilling are always clearly disclosed on grading reports.

One such unstable treatment is fracture filling. Large, deep fractures in a diamond will often appear white or reflective due to the difference in the refractive index of the diamond and the air within the fracture. In an effort to disguise this, a substance with a refractive index similar to diamond's, such as highly refractive lead glass, is introduced into surface-reaching fractures to reduce the interference of air (figure 1). Several telltale signs, such as the flash effect, typically reveal the presence of a filled fracture. The classic flash effect displays a vivid pink color in darkfield illumination and a complementary green color in brightfield illumination (figure 2). In a different orientation in brightfield lighting, a filled fracture can also appear bright blue.

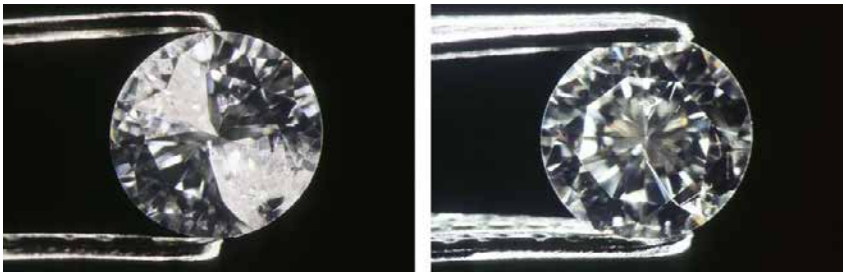

Figure 1. Large fractures in this diamond are exposed in high relief before treatment (left). After the fractures are filled, the same stone has a much improved apparent clarity (right).

A 1.21 ct near-colorless square modified brilliant diamond was recently submitted to GIA's Carlsbad laboratory for a diamond grading report (figure 3). It was rejected for grading after examination revealed a large filled fracture. Interestingly, the flash effect looked noticeably different from the classic appearance described

Figure 2. The classic flash effect appearance: a pink flash in darkfield lighting (left) and a complementary green flash in brightfield lighting (right).

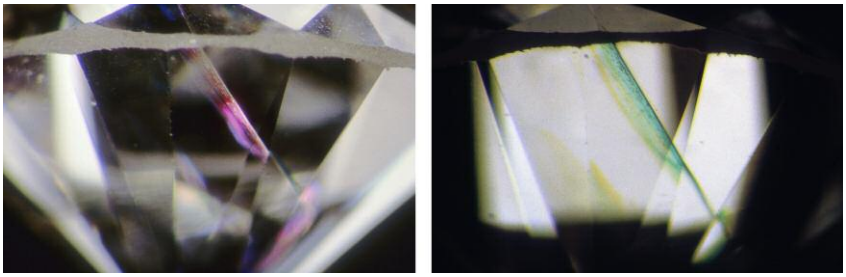

Editors' note: All items were written by staff members of GIA laboratories.

Gems & Gemology, Vol. 54, No. 1, pp. 56–64.

Figure 3. A face-up view of the near-colorless 1.21 ct fracture-filled square modified brilliant cut.

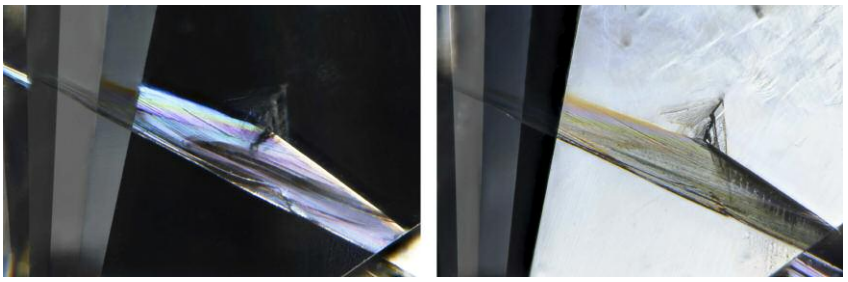

Figure 4. When viewed nearly parallel to the plane of the fracture, this filled fracture exhibits a multicolored "rainbow" flash effect in both darkfield illumination (left) and brightfield illumination (right), as opposed to a classic single-color flash effect. Field of view 2.21 mm.

above. Rather than flashing a single color in darkfield lighting and a single complementary color in brightfield lighting, this filled fracture flashed multiple colors in darkfield and multiple complementary colors in brightfield (figure 4). The unusual effect may be due to a difference in ingredients used to manufacture the filling material. To the untrained eye, it could easily be mistaken for the natural iridescence very commonly seen in unfilled fractures. However, such iridescence typically appears when the viewing angle is nearly perpendicular to the fracture, while the flash effect is most visible when the viewing angle is nearly parallel to the plane of the fracture. In addition to the "rainbow" flash effect, this filled fracture showed a dendritic pattern at the fracture opening that is caused by air pockets in the filling substance (figure 5). This pattern is characteristic of incomplete fracture filling (J.I. Koivula, *The MicroWorld of Diamonds*, Gemworld International, Inc., Northbrook, Illinois, 2000, pp. 106–108) and provides further evidence of the treatment.

Hollie McBride

Figure 5. In addition to a "rainbow" flash effect, this filled fracture displays a dendritic pattern (and its mirror reflection) at the opening of the fracture. This pattern occurs as a result of incomplete fracture filling. Field of view 1.83 mm.

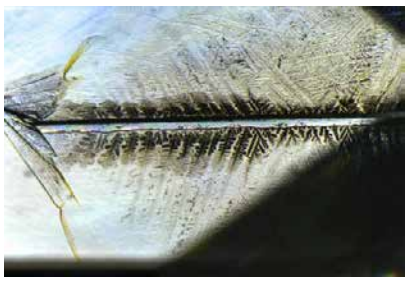

HPHT-Processed Diamond Fraudulently Represented as Untreated

The Hong Kong lab recently encountered another instance of fraud: A natural but HPHT-treated round brilliant diamond (figure 6, left) weighing more than 6 carats submitted for verification service was found to be inconsistent with the claimed GIA report issued a few months prior for an untreated diamond. Moreover, the GIA report number and another inscription on the girdle, both supposedly laser-inscribed by GIA (figure 6, right), looked convincing but were also found to be fraudulent.

The HPHT-processed round brilliant was believed to have been carefully selected to match the original diamond—its color grade (F) matched, and only minor differences were observed in carat weight and measurements. The HPHT-processed diamond weighed 6.30402 ct and measured 11.73–11.82 × 7.32 mm, whereas the original one weighed slightly less (6.30216 ct), and measured 11.72–11.83 × 7.32 mm. Furthermore, the IF

Figure 6. This 6.30 ct round brilliant diamond (left) with a fraudulent inscription of a GIA report number (right) from a similar-looking diamond was confirmed to have been HPHT processed for color improvement.

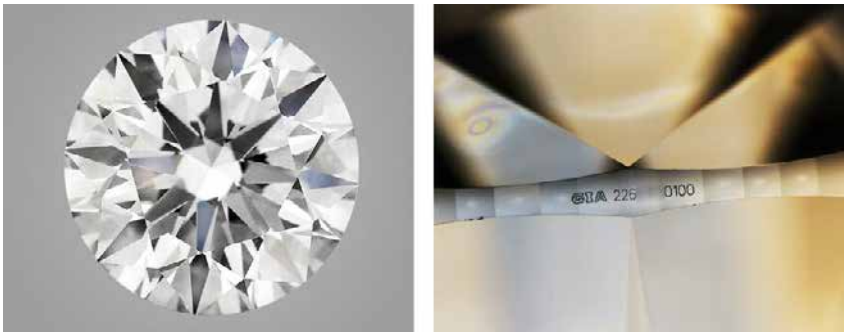

clarity of the HPHT-treated stone was an improvement over the VVS_1 clarity of the natural stone.

Despite all the efforts put into those convincing features and measurements, spectroscopic testing easily revealed the stone's true identity. Infrared absorption spectroscopy showed the HPHT-processed diamond was type IIa, but the original diamond was type Ia. Photoluminescence (PL) spectra were collected at liquid nitrogen temperature with various excitation wavelengths. The slight reversal in the ratio between the 575 and 637 nm peaks (NV centers), together with other spectroscopic features, confirmed the stone had gone through an HPHT treatment process for color improvement. A strain pattern observed under cross-polarized light ruled out the possibility of a synthetic diamond.

This case should raise awareness among the industry and the public that, although rarely encountered in larger stones, this kind of fraud does exist. Verification services at GIA confirm that an item is exactly the same as the one described on a previous report and has not been recut or treated—or, as in this case, replaced with a similar-looking stone. This provides a simple way to check for any type of fraudulent activity if there is doubt about the origin of a diamond.

Billie Law

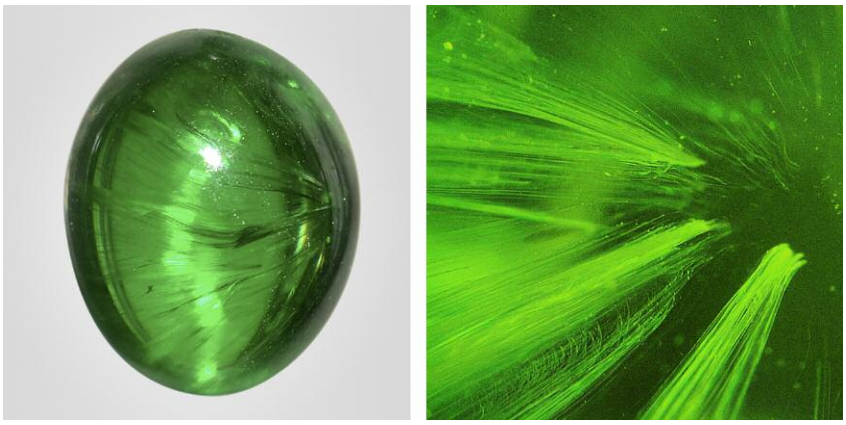

Figure 7. This 2.51 ct green demantoid with chatoyancy (left) contained well-aligned fibers of horsetail inclusions (right, field of view 1.10 mm).

GARNET

Cat's-Eye Demantoid and Brown Andradite with Horsetail Inclusions

Two garnets were recently submitted to the Tokyo lab for identification. One was a green cabochon weighing 2.51 ct; the other was an orangy brown round brilliant weighing 2.47 ct. Both had a refractive index (RI) over the limits of the refractometer and a hydrostatic specific gravity (SG) of 3.84. To confirm the identification, we used Raman spectroscopy. Both stones matched the andradite garnet group from the reference database. The ideal chemical formula of andradite is $Ca_3Fe_2Si_3O_{12}$. The most important feature in both garnets was their horsetail inclusions. The presence of horsetail inclusions, which are thought to consist of chrysotile fibers branching out and radiating toward the surface from a small chromite nodule, has been regarded as diagnostic for natural demantoid.

The 2.51 ct stone was a rare cat's-eye demantoid (figure 7). Demantoid garnet is by definition the green-colored andradite caused by chromium substitution. Chatoyancy is usually caused by closely spaced bands of long, thin parallel needles or fibers in the correct orientation, with a polished rounded surface such as a cabochon to reflect the light off the parallel inclusions. In this stone, the chatoyancy was due to the fibers of the horsetail inclusions. The radiating fibers were not parallel straight lines but parallel curves, so the "eye" was slightly curved.

The 2.47 ct stone was an andradite garnet with classic horsetails (figure 8). The dominant bodycolor was brown. The gemological properties and chemistry were classified as andradite in the garnet solid solution, but it was poorer in calcium and richer in iron and silicon than the ideal andradite composition. The brownish cast was due to

Figure 8. This 2.47 ct orangy brown andradite (left) contained radiating horsetail inclusions regarded as exclusive to demantoid (right, field of view 1.60 mm).

iron. On occasion we encounter stones with a strong yellow component that still have enough green to qualify as demantoid. However, this stone had no green in it and therefore was just andradite, not demantoid.

Consequently, the horsetail inclusions cannot be considered exclusively diagnostic for demantoid. They may also be found in non-green andradite. These two identifications—"cat's-eye demantoid" and normal "andradite" in spite of horsetail inclusions—were issued for the first time in GIA's colored stone report records.

Taku Okada and Philip G. York

Unusual Orange Pyrope-Spessartine-Grossular Garnet

GIA's New York laboratory recently examined an orange pear-shaped faceted stone (figure 9). Standard gemological testing revealed an RI of 1.771 and a hydrostatic SG of 3.89. The fluorescence reaction was inert to long-wave and short-wave UV light. The stone did not show any pleochroism when viewed with a dichroscope. Using a handheld spectroscope, absorption bands located at 410 and 430 nm in the blue and violet sections were clearly observed. All of these gemological properties are consistent with pyrope-spessartine garnet based on the classification system from Stockton and Manson ("A proposed new classification for gem-quality garnets," Winter 1985 *G&G*, pp. 205–218).

Besides standard gemological testing, all garnets submitted to GIA laboratories are routinely analyzed by energy-dispersive X-ray fluorescence (EDXRF) spectroscopy (see column 4 of the supplementary table available at https://www.gia.edu/gems-gemology/spring-2018-labnotes-unusual-orange-pyrope-spessartine-grossular-garnet). EDXRF results showed that the stone was predominantly composed of 15.37 mol.% pyrope, 53.70 mol.% spessartine, and—surprisingly—25.39 mol.% grossular. Unlike normal pyrope-spessartine garnet submitted to GIA that contains a small amount of grossular (less than 10 mol.%), this garnet had a much higher grossular component that had never been reported before in gem-quality garnets, to our knowledge. (Note that "malaia/malaya" is a trade name for yellowish, reddish, or pinkish orange pyrope-spessartine garnets that can potentially contain 2–94% spessartine, 0–83% pyrope, 2–78% almandine, 0–24% grossular, and 0–4% andradite. The garnet we examined falls into this concentration range.)

Figure 9. The unique composition of this 7.97 ct orange pear-shaped garnet was revealed as pyrope-spessartine-grossular.

To validate the accuracy of the chemistry, we performed laser ablation–inductively coupled plasma–mass spectrometry (LA-ICP-MS) analysis using a Thermo Fisher iCAP Qc ICP-MS coupled with a New Wave Research UP-213 laser ablation unit to obtain an additional set of chemical composition. USGS glass standard GSD-1G and GSE-1G were used as external standards. ^{29}Si was used as internal standard. The LA-ICP-MS results showed good agreement with the EDXRF results (see columns 1–3 of the supplementary table at https://www.gia.edu/gems-gemology/spring-2018-labnotes-unusual-orange-pyrope-spessartine-grossular-garnet).

Garnets are a group of isometric nesosilicates with the general chemical formula $X_3Y_2Z_3O_{12}$. Natural rock-forming silicate garnets are commonly divided into the pyralspite (pyrope, almandine, and spessartine) and ugrandite (uvarovite, grossular, and andradite) groups. In pyralspite, Al^{3+} occupies the Y-site and the X-site may contain Mg^{2+}, Fe^{2+}, or Mn^{2+}; these garnets are composed predominantly of pyrope ($Mg_3Al_2Si_3O_{12}$), almandine ($Fe^{2+}{}_3Al_2Si_3O_{12}$), and spessartine ($Mn_3Al_2Si_3O_{12}$) end members. Stockton and Manson (1985) presented a ternary plot (figure 10) to gemologically classify the pyralspite garnet species, and this showed the correlation among refractive index, visible spectroscopic observation, and chemistry. They determined that pyrope-spessartine should have an RI between 1.740 and 1.780 along with clear 410 and 430 nm absorption bands. We concluded that the orange pear-shaped garnet should be classified gemologically as pyrope-spessartine garnet.

To understand why this garnet with a high grossular component still shows the same gemological properties of normal pyrope-spessartine, we plotted the orange garnet chemistry in this ternary plot by combining pyrope with a grossular component. The orange spot representing the orange garnet appeared in the pyrope-spessartine region, because the refractive index of pure pyrope (1.714)

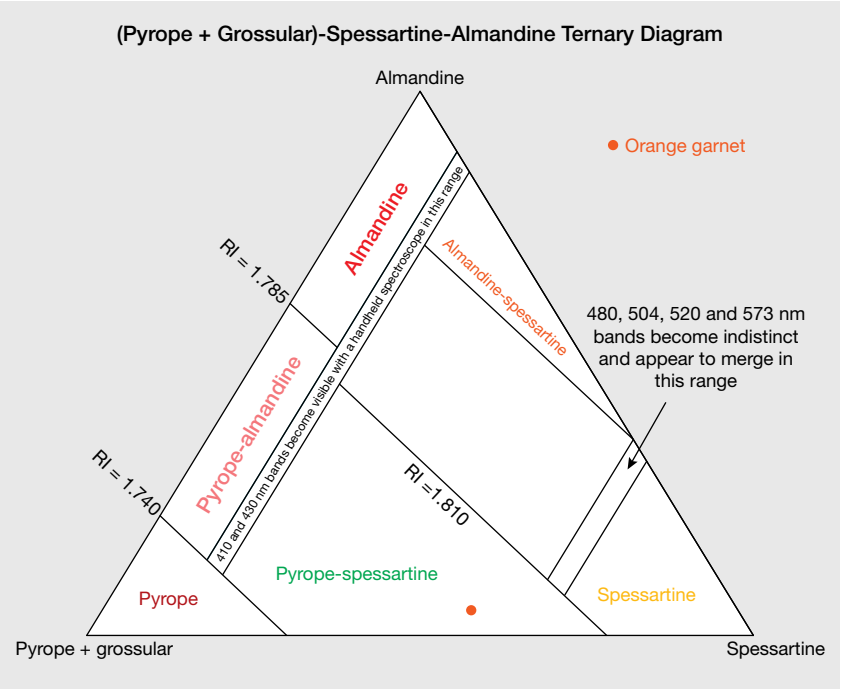

Figure 10. (Pyrope + grossular)-spessartine-almandine ternary diagram with data points based on molecular percentages for pyralspite garnet (modified after Stockton and Manson, 1985). The orange spot is the average of three sets of LA-ICP-MS data (table 1, columns 1–3). Refractive index and spectral boundaries are used to distinguish among the six proposed garnet species labeled in the diagram.

is close to and functions almost the same as the RI of pure grossular (1.734) in contributing to the combined refractive index. Since there is not a specific gemological species name for this orange garnet with higher grossular than pyrope component, the authors suggest that the stone be called *pyrope-spessartine-grossular*. This case demonstrates that sophisticated chemical analysis of garnet should be practiced routinely in gemological laboratories to make sure unique garnets are not misidentified.

Pamela Cevallos and Ziyin Sun

New Plastic IMITATION OPAL From Kyocera

Recently, the Carlsbad laboratory examined an interesting new gem material manufactured by the Japanese company Kyocera that displayed a play-of-color phenomenon. In the trade, this material may be sold as an "opal-like product," because of the play-of-color phenomenon observed (figure 11, left).

Standard gemological testing revealed a hydrostatic SG of 1.35. The refractive index was measured as 1.49. According to GIA, an imitation is defined as a natural or manmade material that mimics the appearance of, and is used as a substitute for, another gem material. Likewise, a synthetic gem is defined by GIA as a laboratory-grown gem material with virtually the same chemical and physical properties as a natural gem. Because the gemological properties for this new

Figure 11. This new plastic opal imitation (left) shows a very pleasing play-of-color that does not have the classic "snakeskin" columnar structure one would expect to see in traditional polymer-impregnated synthetic opal produced by Kyocera (right). The largest sample of plastic imitation opal in the left photo weighs 227 grams, and the largest sample of synthetic opal in the right photo weighs 65 grams. The rectangular black block in the photo on the left is 9.7 cm in length.

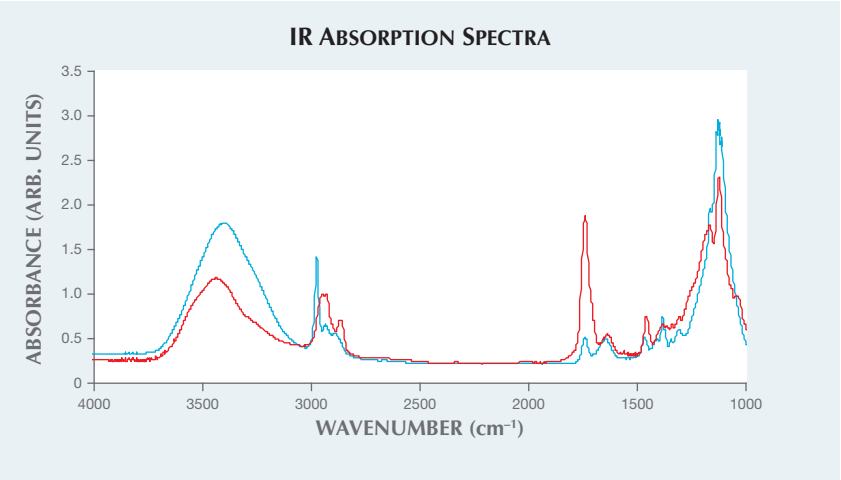

Figure 12. The infrared absorption spectrum of the new plastic imitation opal (red trace) was very similar to that of traditional plastic-impregnated synthetic opal (blue trace) except that the polymer feature at ~1734 cm^{-1} was about five times as strong.

Figure 14. Randomly oriented patches of play-of-color are uniformly distributed throughout this new plastic opal imitation. The imitation looks the same from all different angles. Field of view 13 mm.

material are out of range for natural opal (SG of 2.00 and RI between 1.37 and 1.47), it is best described as an imitation opal.

Further testing revealed that this material readily burns with a hot point and produces a strong acrid odor indicating that a significant amount of plastic is present. Additionally, advanced testing using EDXRF revealed the presence of silicon. Fourier-transform infrared (FTIR) testing revealed a spectrum that was quite similar to traditional polymer-impregnated synthetic opal (figure 11, right) except for a polymer peak that was nearly five times as strong (figure 12). These tests indicate that this material is composed of both plastic resin and silicon. When exposed to ultraviolet light, samples with a white bodycolor fluoresced a weak blue to short-wave and medium blue to long-wave UV. Samples with a black bodycolor fluoresced a weak orange to short-wave UV and were inert to long-wave UV.

Microscopic examination revealed some interesting features. The pattern in the play-of-color was random and unlike traditional synthetic opal did not display any "snakeskin" or "chicken wire" pattern (figure 13, left), but instead showed colored polygonal patches about 2 mm in size uniformly distributed throughout (figure 14). Nor did the plastic imitation opal display the columnar structure one would expect to see in synthetic opal (figure 13, right).

Visually, this new material is a very good imitation of natural opal. Gemologically, it is easy to separate from natural opal due to the comparatively high refractive index and low specific gravity. There are other pos-

Figure 13. Traditional synthetic opal shows a "chicken wire" or "snakeskin" pattern (left) and a columnar structure (right) that are diagnostic of synthetic origin. The new plastic opal imitation does not show these features. Fields of view 7.20 mm (left) and 14.40 mm (right).

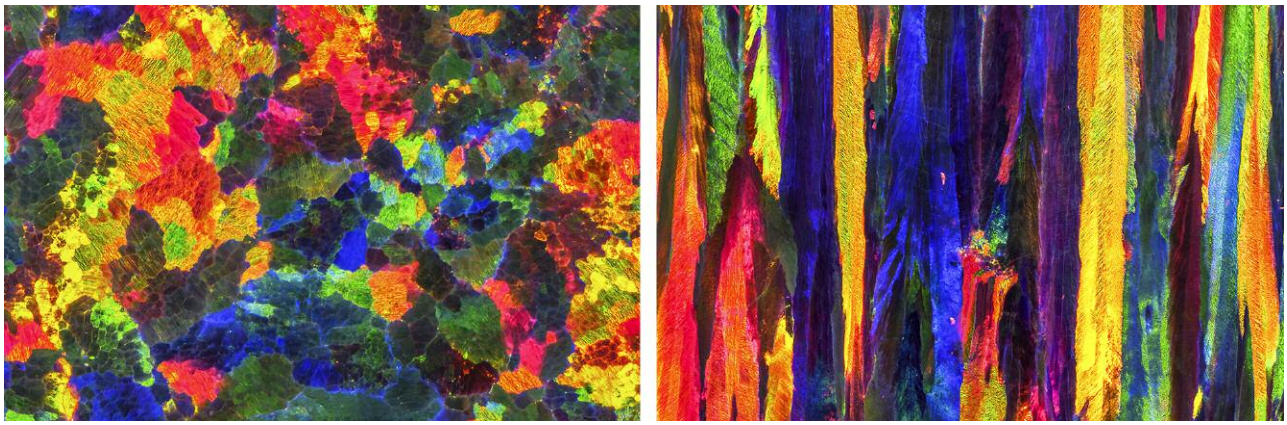

Figure 15. A natural blister that took the form of a pearlfish on the inner surface of one Pinctada maxima *valve. Courtesy of ECIJA.*

sible decorative applications for this plastic opal imitation material due to the large sizes that can be produced. This attractive material is a welcome addition to the gem trade and is easy to separate from natural opal with standard gemological testing.

Nathan Renfro and James E. Shigley

Natural Blister from Entombment of a Pearlfish Within a *Pinctada Maxima* SHELL

Pearlfish are marine fish of the Carapidae family that live symbiotically inside various invertebrate hosts. Occasionally, the remains of these fishes may be found completely covered by mother-of-pearl on the inner surfaces of some bivalve mollusks (J. Ballard, "The pearlfish," *African Wildlife*, Vol. 45, No. 1, 1991, pp. 16–19). The New York laboratory recently had the opportunity to examine a unique *Pinctada maxima* shell with a clear blister that took the form of a fish (figure 15). The shell dimensions were approximately 21 × 19 cm, and the entombed fish measured approximately 10 cm in length.

The *P. maxima* bivalve's soft internal body organs are enclosed and protected by the outer shell that is secreted by the mantle to form the beautiful inner nacreous mother-of-pearl layers and the pearls that are familiar to most (P.C. Southgate and J.S. Lucas, *The Pearl Oyster*, Elsevier, Oxford, UK, 2008, pp. 57–58). The hard surface of the oyster shell and the nooks within the shells provide places where a host of small animals such as pea crabs, shrimp, and fish can live. Pearl gemologists from GIA in Bangkok observed these within numerous *P. maxima* mollusks during a 2013 field expedition 80 miles off the coast of Broome, Western Australia. The shape and size of an example

Figure 16. An example of a living pearlfish with a slender, elongated shape and translucent body, found residing inside a P. maxima *shell during a 2013 GIA field expedition to Broome, Australia.*

recorded from the trip (figure 16) closely resembles the one examined by the lab.

There is a delicate harmony and balance between the mollusk and fish in their cohabitation. The pearlfish has been known to settle in the oyster shell for shelter and live in symbiosis without either one harming the other (E. Parmentier and P. Vandewalle, "Morphological adaptations of Pearlfish (Carapidae) to their various habitats," in A.L. Val and B.G. Kapoor, Eds., *Fish Adaptations*, Science Publishers, Enfield, New Hampshire, 2003, pp. 261–276). When the pearlfish eventually dies, the oyster cannot eject the organism and its self-healing mechanism

Figure 17. Microradiographic image of the pearlfish on the shell revealing the preserved details from head to tail beneath the nacre.

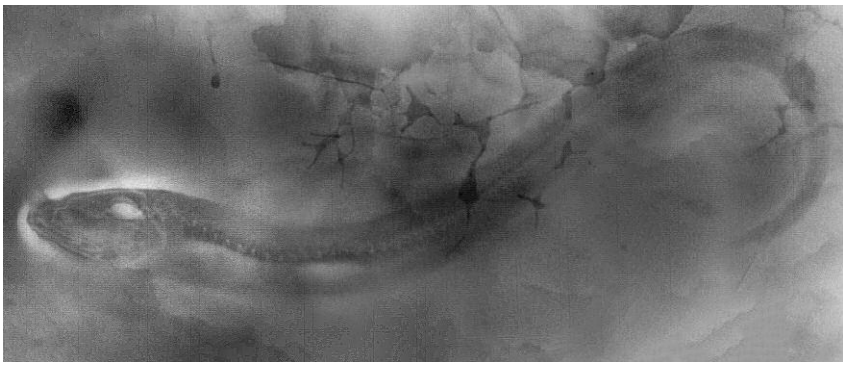

Figure 18. This 3.52 ct sample was the largest of a selection of recently submitted CVD synthetics.

kicks into action. The mollusk begins to deposit layers of nacre over the irritant to ease the likely discomfort experienced. The organism decomposes over time and the skeletal remains are left encased underneath the nacre to form a "blister" (GIA and CIBJO definition) on the inner surface of the shell.

The microradiographic images obtained for this sample examined by the New York laboratory show the fish's skeletal remains very clearly (figure 17). This extraordinary specimen is another prime example of Mother Nature's fascinating manifestations and was something out of the ordinary for everyone who handled and examined it in the laboratory.

Sally Chan and Emiko Yawaza

SYNTHETIC DIAMOND

Five CVD Synthetics Greater Than Three Carats

The quality and carat weight of CVD synthetic gem diamonds has increased dramatically over the last ten years (S. Eaton-Magaña and J.E. Shigley, "Observations on CVD-grown synthetic diamonds: A review," Fall 2016 *G&G*, pp. 222–245). Very recently a 6 ct round CVD synthetic was reported ("US lab creates 6ct. CVD synthetic," *Rapaport News*, Feb. 1, 2018). However, we still only occasionally receive CVD synthetic diamonds for grading reports, and very rarely do these submissions weigh more than three carats. In fact, GIA graded its first CVD synthetic over three carats not long ago, in October 2015 (Winter 2015 Lab Notes, pp. 437–439), and as of January 2018 had only examined a total of eight. So it was quite interesting when, in late January 2018, we received five CVD synthetics simultaneously (four known to be from the same client) that were all above three carats. The quality factors for these five samples submitted for synthetic diamond grading reports are presented in table 1, and the largest of the five is shown in figure 18.

TABLE 1. Summary of equivalent quality factors in five CVD synthetic diamonds.

Weight (ct)	Color	Clarity	Shape	Cut grade
3.02	F	VS_1	Cushion	n/a
3.12	G	VS_1	Round	Excellent
3.26	H	VS_2	Round	Excellent
3.37	H	VS_1	Cushion	n/a
3.52	J	SI_2	Round	Excellent

As table 1 shows, four of the five were in the near-colorless range and the smallest one was in the colorless range. Four had clarity grades equivalent to VS_1 or VS_2, while the largest was equivalent to SI_2. All three round brilliants received Excellent cut grades. These results are consistent with a recent survey (Eaton-Magaña and Shigley, 2016), which found that a majority of D-to-Z CVD synthetics are in the near-colorless range (67%) and that a slight majority have clarity grades equivalent to VVS_2–VS_1.

In keeping with standard GIA procedure, we performed IR absorption and PL spectroscopy on all five samples. As expected for CVD synthetics, all were identified as type IIa, showed pronounced silicon-related peaks in their PL spectra, and displayed striations in DiamondView imaging that are characteristic for CVD synthetics. All except the 3.52 ct sample also showed nickel-related peaks at 883/884 nm in their PL spectra with 830 nm excitation. We expect that submissions of CVD synthetics in this weight range and beyond will become more common in the next few years.

Sally Eaton-Magaña

Fancy Deep Brown-Orange CVD Synthetic Diamond

A 0.56 ct diamond (figure 19) was color graded as Fancy Deep brown-orange. The diamond was found to be a CVD-grown synthetic that had been irradiated and annealed, perhaps multiple times. DiamondView imaging (figure 20) showed the telltale striations of the CVD growth process, and the PL spectrum showed the SiV^- (736/737 nm doublet) commonly found in CVD synthetics. The Vis-NIR spectrum (figure 21) showed a GR1 defect (the neu-

Figure 19. A face-up image showing the deep brown-orange bodycolor of a CVD-grown synthetic that has been irradiated and annealed.

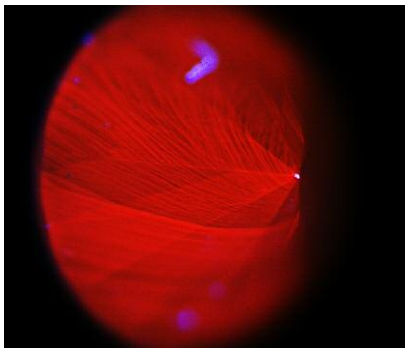

Figure 20. A DiamondView image reveals the characteristic growth striations of a CVD-grown synthetic diamond.

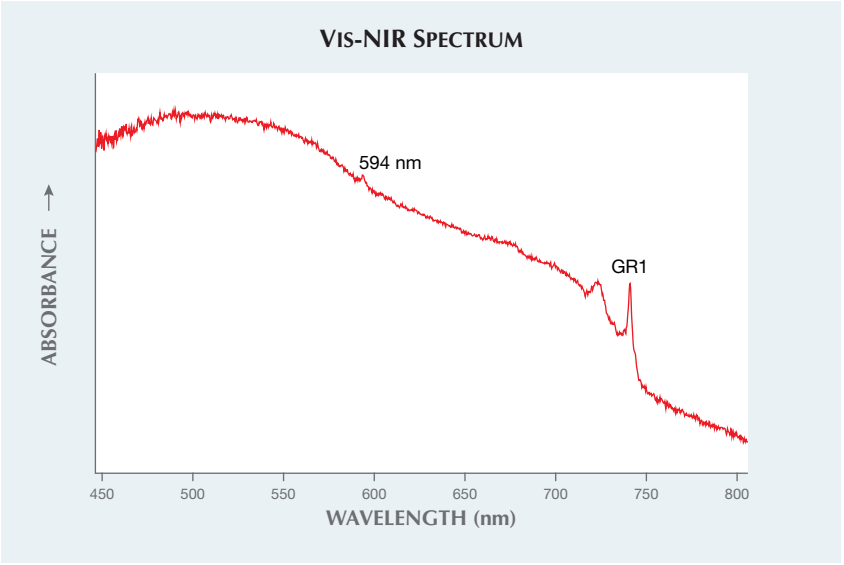

Figure 21. The visible-NIR spectrum of the irradiated and annealed CVD synthetic shows the GR1 and 594 nm defects.

tral vacancy center) and a peak at 594 nm that is commonly seen in diamonds that have been irradiated and annealed. This is in contrast to the normal irradiated and annealed CVD synthetic diamonds that show features related to nitrogen vacancies. The PL spectrum shows the NV^0 (575 nm) and NV^- (637 nm) peaks in relatively high concentrations compared to the diamond Raman line. In the infrared spectrum, a clear band at 1130 cm^{-1} and a peak at 1344 cm^{-1} indicate the presence of single substitutional nitrogen.

CVD-grown synthetic diamonds have been known to be irradiated (Fall 2014 Lab Notes, pp. 240–241; Fall 2015 Lab Notes, pp. 320–321) and also irradiated and annealed (J. Shigley et al., "Lab-grown colored diamonds from Chatham Created Gems," Summer 2004 *G&G*, pp. 128–145). The irradiation and annealing performed on CVD synthetics is generally done on those with isolated nitrogen and produces a pink to red bodycolor. This color is caused by nitrogen-vacancy centers created when the vacancies produced by irradiation combine with the isolated nitrogen during the annealing process. In this case, the diamond showed a brown-orange bodycolor due to the combination of the isolated nitrogen and irradiation features. The stone in question contained isolated nitrogen, so it is possible that the intent was to create a pink to red color, but the treatment did not produce the expected results. Brown-orange color as a result of treatment has not been seen in a CVD synthetic diamond before, so the intentions of the treatment are as yet unknown.

Troy Ardon and Nicole Ahline

PHOTO CREDITS
John I. Koivula—1, 2; Robison McMurtry—3, 9, 18, 19; Nathan Renfro—4, 5, 13, 14; Tony Leung—6 (left); Billie Law—6 (right); Shunsuke Nagai—7 (left), 8 (left); Taku Okada—7 (right), 8 (right); Diego Sanchez—9; Robert Weldon—11; Jian Xin (Jae) Liao—15, 17; Areeya Manustrong—16; Nicole Ahline—20.

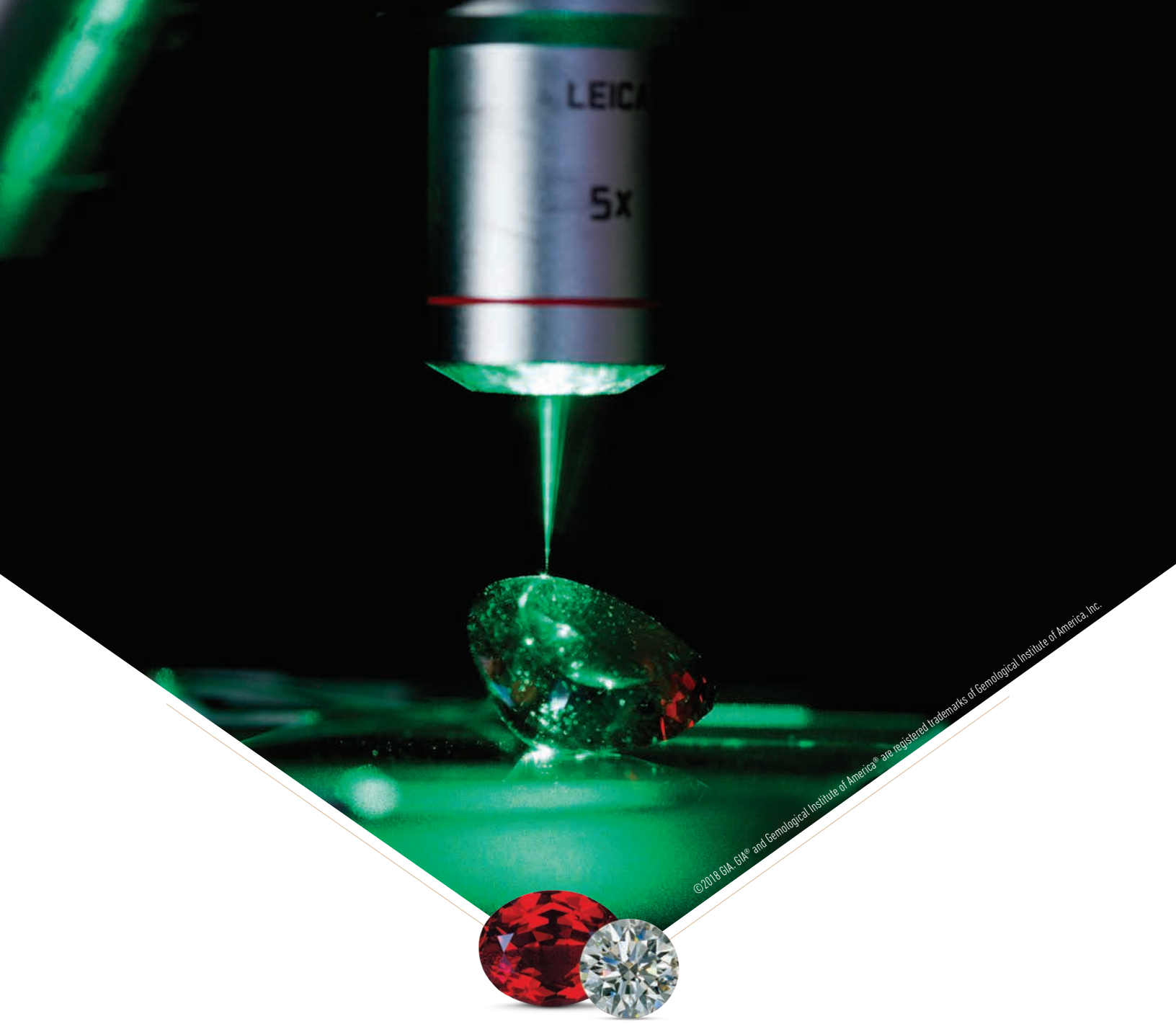

At GIA, gems endure even more pressure.

Science and discovery underpins everything we do. Since 1931, the Gemological Institute of America® has been unearthing the truth about gems and creating industry standards. With unwavering commitment to accurate and unbiased methodologies, our dedicated research staff advances the knowledge the industry and consumers need to protect confidence in gems and jewelry. Our discoveries are one of the many reasons why GIA® is the world's foremost authority on diamonds, colored stones and pearls.

Learn more about the many facets of GIA at GIA.edu

GIA®

The World's Foremost Authority in Gemology™

Ensuring the Public Trust Through Nonprofit Service Since 1931

BENEFICIATION EDUCATION INSTRUMENTS LABORATORY **RESEARCH**

Beryl Crystal in Fluorite

Recently, the authors examined a purple fluorite specimen that contained an elongate hexagonal rod-shaped crystal (figure 1). The crystal host had been collected by Chris Lehmann (Lehmann Minerals, Benton, California) in the Birch Creek area of the White Mountains in Inyo County, California. This area was host to volcanic activity that resulted in granitic dikes cutting across dolomite and other sedimentary rock types. The most abundant minerals found in the area are quartz, calcic oligoclase, microcline, biotite, and muscovite. Smaller amounts of apatite, zircon, tourmaline, magnetite, epidote, purple fluorite, and beryl have also been reported (C.A. Nelson and A.G. Sylvester, "Wall rock decarbonation and forcible emplacement of Birch Creek Pluton, southern White Mountains, California," *Geological Society of America Bulletin*, Vol. 82, No. 10, 1971, pp. 2891–2904). While the morphology of the prismatic inclusion hinted at its identity, the hexagonal crystal was conclusively identified as beryl by laser Raman spectrometry. Also present in the fluorite were numerous veils of fluid inclusions and prominent color zoning (again, see figure 1). This exciting discovery was the authors' first encounter with beryl as an inclusion in fluorite.

Ian Nicastro
San Diego, California

Nathan Renfro
GIA, Carlsbad

Figure 1. A colorless prismatic beryl crystal within a fluorite specimen from the White Mountains in Inyo County, California. Photomicrograph by Nathan Renfro; field of view 8.60 mm.

Type IIa Diamond with Extraordinary Etch Channels

Etch channels are rare inclusions in natural diamonds, both type I and type II (see T. Lu et al., "Observation of etch channels in several natural diamonds," *Diamond and Related Materials*, Vol. 10, No. 1, 2001, pp. 68–75). Recently, the Laboratoire Français de Gemmologie received a 1.77 ct round brilliant-cut diamond containing numerous large etch channels, a feature appreciated by inclusion collectors. The gem had K color and I_1 clarity due to the etch channels and their reflectors (figure 2). Infrared absorption spectroscopy revealed a type IIa diamond.

Dissolution etch channels in diamond are rare but can have various forms (M. Philippe and E. Fritsch, "Dissolved dislocation: Inclusions not always easy to identify, part I," *Revue de Gemmologie*, Vol. 200, 2017, pp. 11–22, in French). They are due to the dissolution of dislocations in-

About the banner: This thin wafer of agatized fossil dinosaur bone from Utah was photographed using diffuse reflected light and transmitted light in conjunction with a blue filter for contrast. Photomicrograph by Nathan Renfro; field of view 9.6 mm.

Editors' note: Interested contributors should contact Nathan Renfro at nrenfro@gia.edu and Jennifer-Lynn Archuleta at jennifer.archuleta@gia.edu for submission information.

Gems & Gemology, Vol. 54, No. 1 pp. 66–73.

Figure 2. A rare 1.77 ct type IIa diamond with significant etch channels caused by dissolution along dislocations. Photo by Aurélien Delaunay.

side the crystal. These dislocations might be growth dislocations or caused by later deformation. One type of etch channel in diamond consists of regular and parallel lines related to diamond's crystallographic structure. The other type, the kind exhibited in this diamond, is a worm-like ribbon due to crystallographic defects. All of the dissolution etch channels have rhombic openings at the surface of the diamond (figure 3); a few have a pyramidal termination and restart in another direction (figure 4). This is a rare occurrence and confirms that dissolution can be stopped—or slowed—by defects in the crystal structure. In addition, the dissolution can start in an easier direction, such as a dislocation.

Etch channels are rarely observed in cut gem diamonds. But when gemologists observe a specimen like this one, it is always a pleasure for the eyes and a curiosity of nature.

Aurélien Delaunay
Laboratoire Français de Gemmologie, Paris
Emmanuel Fritsch
University of Nantes, France

Omphacite and Chromite: A "Bimineralic Inclusion" in Diamond

The micro-world of diamonds is fascinating not only to gemologists interested in inclusions but also to mineral physicists who study the deep earth, arguably one of the last frontiers and one not yet accessible to us. Diamond inclusions offer a window into that world and help us piece together its nature to unravel the mysteries of the earth's very formation (J.I. Koivula and E.A. Skalwold, "The microworld of diamonds: Images from the earth's mantle," *Rocks & Minerals*, Vol. 89, No. 1, 2014, pp. 46–51). Sometimes even relatively common inclusions in diamond present an uncommon sight.

In this case, two minerals identified by Raman microspectroscopy, omphacite and chromite, are in such close association that they appear joined (figure 5). Such a "bimineralic inclusion" poses the question of how they might have ended up that way: Was it just fate or attrac-

Figure 3. Etch channels with rhombic openings at the surface of the diamond. Photomicrograph by Aurélien Delaunay; field of view 2.22 mm.

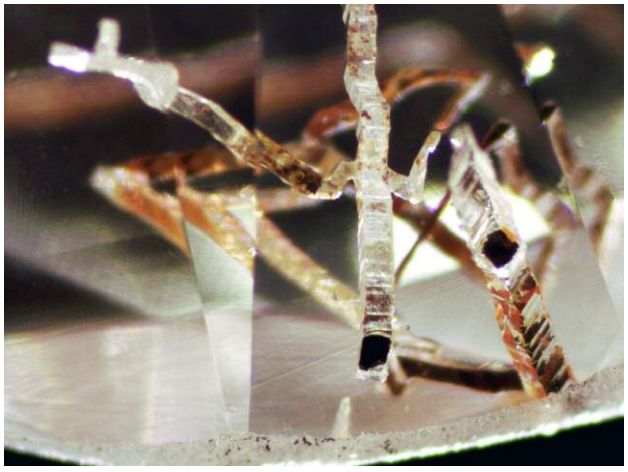

Figure 4. Rare etch channel with a pyramidal termination in a 1.77 ct type IIa diamond. Note the lateral continuation of the dissolution. Photomicrograph by Aurélien Delaunay; field of view 1.39 mm.

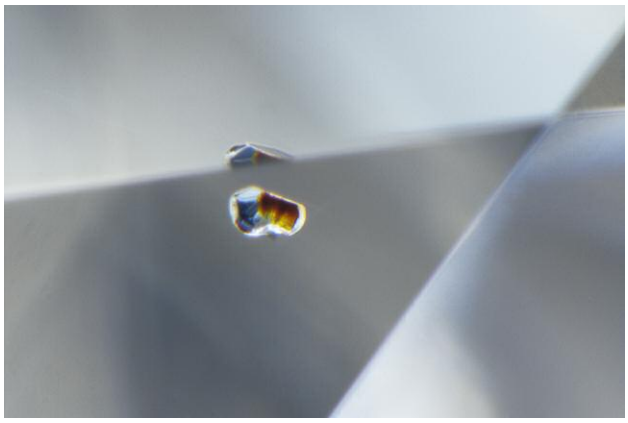

Figure 5. Sometimes a clue to the identity of an inclusion is its color. Diffuse transmitted lighting reveals the colors of the omphacite (left) and chromite (right) crystals composing a "bimineralic inclusion" in a 90-point diamond. Photomicrograph by Nathan Renfro; field of view 0.95 mm.

Figure 6. This opal from the Shewa region of Ethiopia, weighing just over 10 ct, shows areas of agate-like banding. Photo by Diego Sanchez and Robison McMurtry.

tion? There is even the possibility that they were a single mineral at the time of inclusion into the diamond but separated when pressure and temperature dropped as the diamond found its way to the earth's surface. Future detailed chemical analysis of this pair may yield valuable information about the earth's interior, including the compositions, pressures, and temperatures of the host rocks in which the diamonds formed.

Many gemologists are familiar with so-called carbon spots in diamonds. Often these are actually chromite crystals—not carbon at all, but rather a chromium-rich iron oxide mineral of the spinel group. If thin enough, these may appear dark red-brown to yellowish brown in transmitted light, as seen in this specimen. Chromite is classified in both the peridotitic and eclogitic inclusion suites found in diamonds. By contrast, the omphacite crystal next to it is a monoclinic pyroxene mineral (clinopyroxene) that is typically pale to dark grayish green or grayish blue in transmitted light and considered a member of the eclogitic suite of inclusions found in diamonds. This inclusion specimen is not only worthy of the photomicrographer's artistry but also a very valuable portion of the earth's interior puzzle, which is slowly being put together one piece at a time.

Elise A. Skalwold and William A. Bassett
Ithaca, New York
Nathan Renfro

Opal with Agate-Like Banding

Recently, author SC purchased an interesting Ethiopian opal (figure 6) that displayed a most unusual growth structure. A portion of the orangy brown opal displayed a small patch of wavy "varve" banding much like one would expect to see in an agate (figure 7). The banded area was composed of layers of translucent dark brown material alternating with lighter opaque material. It was also evident that the dark layers were much harder than the lighter layers, which had significant undercutting on the polished surface. These lighter areas also showed play-of-color, which made it obvious that they were precious opal layers. The dark areas did not show play-of–color, leaving it unknown if they were also opal or perhaps chalcedony, consistent with their banded pattern. It was also interesting to note that the lighter areas readily absorbed water and became transparent, an indication of hydrophane opal.

To test the composition of the various layers, we polished a flat surface on the back of the stone in order to accu-

Figure 7. Prominent agate-like banding was seen in the opal. Photomicrograph by Nathan Renfro; field of view 8.22 mm.

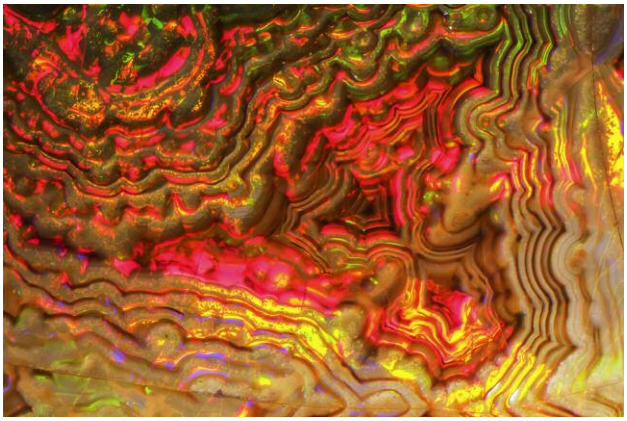

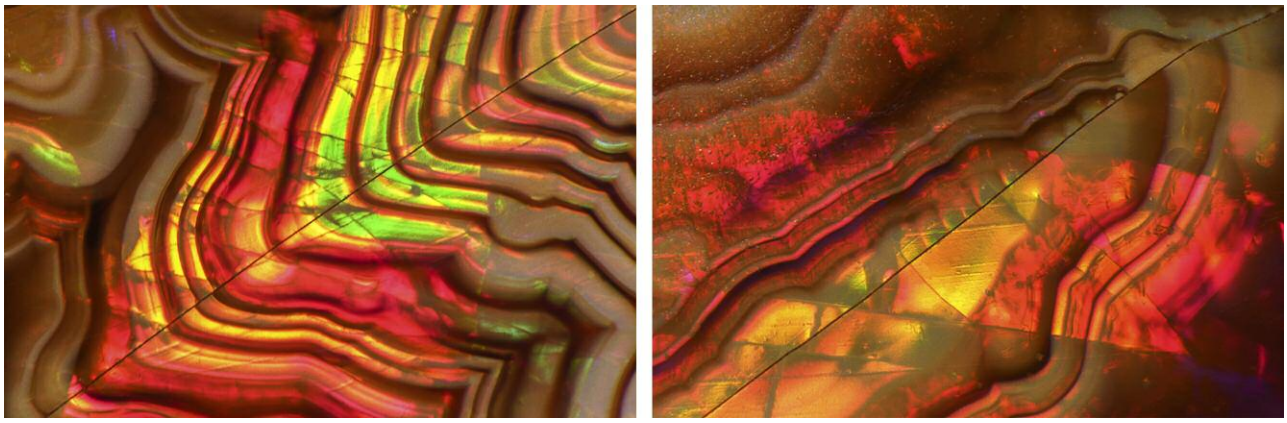

Figure 8. Left: A crack running diagonally across the banding exhibits an offset shifting indicative of a strike-slip type of "microfault." Right: A second area in this stone also shows "micro-faulting" with movement along the banding and no movement across the photonic crystal, indicating that opalization of the chalcedony was a secondary process. Photomicrographs by Diego Sanchez and Robison McMurtry; fields of view 2.50 mm (left) and 2.62 mm (right).

rately measure the refractive index (RI). Two measurements were resolvable with the refractometer, at 1.43 and 1.47. Further testing revealed an extremely low specific gravity measurement of 1.42 (compared to a typical SG of about 2.00 for opal), implying that the hydrophane areas were very porous. Further testing by Raman spectrometry was unable to detect the presence of quartz in either the light or dark brown bands, a finding consistent with the RI measurements.

Careful microscopic observation yielded some interesting conclusions. A few small healed cracks in this stone were naturally repaired with opal infilling. Some of these cracks showed a lateral offset as they cut across the banding (figure 8, left). We also observed that the fractures that showed an offset in the banding showed no offset in the "photonic crystal" (B. Rondeau et al., "On the origin of digit patterns in gem opal," Fall 2013 *G&G*, pp. 138–146), or in the single play-of-color patches (figure 8, right). These observations are important in revealing the order of events that took place to produce such a specimen. First, the deposition of chalcedony had to occur in order to produce the crenulated (wavy) banded pattern. Second, stress cracks were introduced into the agate and then laterally shifted, creating several "micro-faults." These micro-faults were subsequently "healed" with a secondary deposit of opal. This secondary opal deposition also replaced the chalcedony while preserving the original agate-like banding, which was apparent since there was no offset along the micro-faults in the patches of play-of-color.

This is one of the most unusual opals the authors have encountered to date. The microscopic observations tell an interesting story about the formation of a unique gem.

Nathan Renfro
Stephen Challener
Raleigh, North Carolina

Dendritic Inclusions in Cambodian Sapphire

A 0.66 ct piece of blue sapphire rough from the Bo Tang Su mining area of Cambodia's Pailin region displayed dendritic inclusions, commonly found in quartz and chalcedony but rarely seen in corundum.

These epigenetic inclusions occur as a dendritic pattern trapped along surface-reaching fractures and show higher luster than the host under reflected light. Viewed in fiber-optic light, they appear black along the fracture and the trapped unknown fluid phases (figure 9). Raman spectroscopy identified the inclusions as a compound of manganese oxide-hydroxides. The presence of these dendritic

Figure 9. Fiber-optic illumination reveals dendritic inclusions of a manganese oxide-hydroxide compound trapped within a fracture. Photomicrograph by Charuwan Khowpong; field of view 1.05 mm.

Figure 10. The dendritic inclusions were trapped in a triangular fracture. Photomicrograph by Charuwan Khowpong; field of view 1.75 mm.

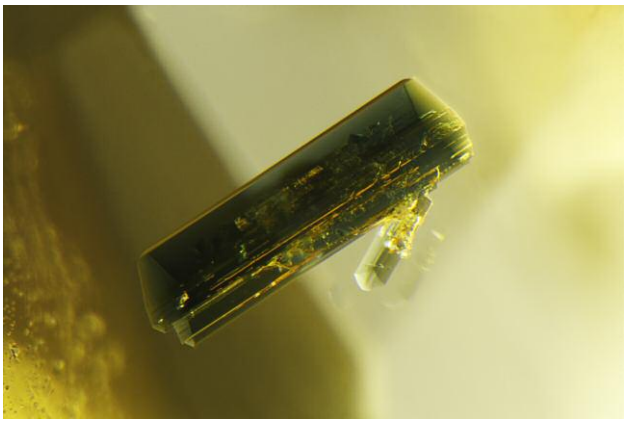

Figure 12. A beautiful euhedral pargasite crystal displaying its monoclinic nature in yellow sapphire. Photomicrograph by Nathan Renfro; field of view 1.43 mm.

inclusions, seen trapped in a triangular fracture in figure 10, is quite unusual in sapphire from Cambodia.

Charuwan Khowpong
GIA, Bangkok

Green Crystals in Yellow Sapphires

Two yellow sapphires recently examined by the authors each contained a green crystal inclusion. Upon analysis, however, the two inclusions turned out to be very different minerals.

A yellow sapphire of Sri Lankan origin hosted a saturated bluish green crystal inclusion. Optically it was singly refractive, and Raman spectroscopy proved it to be a spinel crystal (figure 11). Spinel inclusions of this color have been documented in yellow sapphires before (E.J. Gübelin and J.I. Koivula, *Photoatlas of Inclusions in Gemstones*, Vol. 1, ABC Edition, Zurich, 1986, pp. 353–354), but this crystal was remarkably large and completely enclosed in the stone.

The second yellow sapphire contained a green semitransparent crystal that, unlike the previous inclusion, was doubly refractive and more rectangular in shape (figure 12),

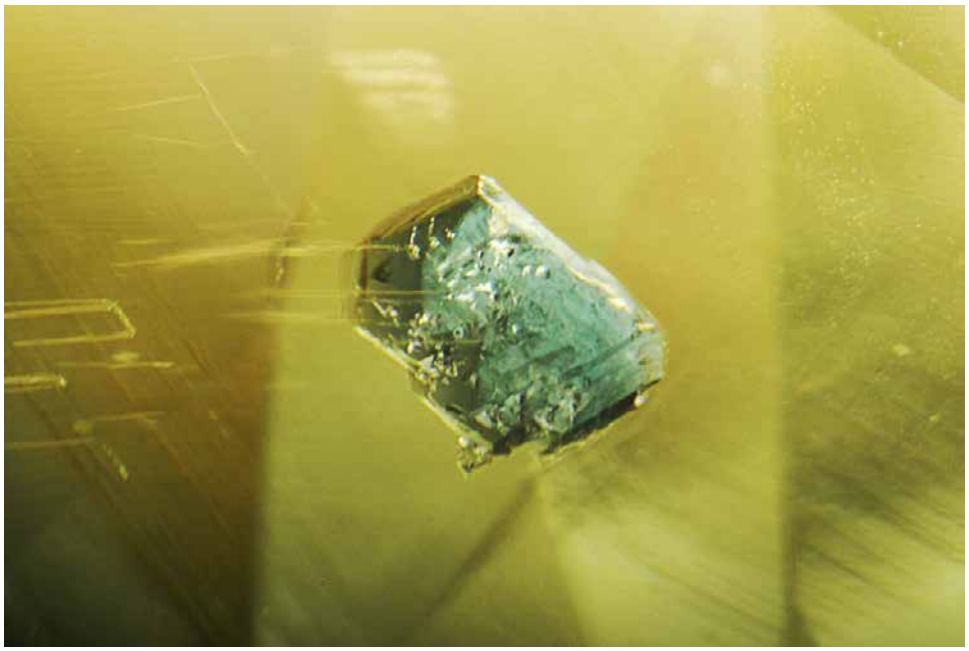

Figure 11. A bluish green spinel crystal found in a Sri Lankan yellow sapphire. Photomicrograph by Tyler Smith; field of view 1.76 mm.

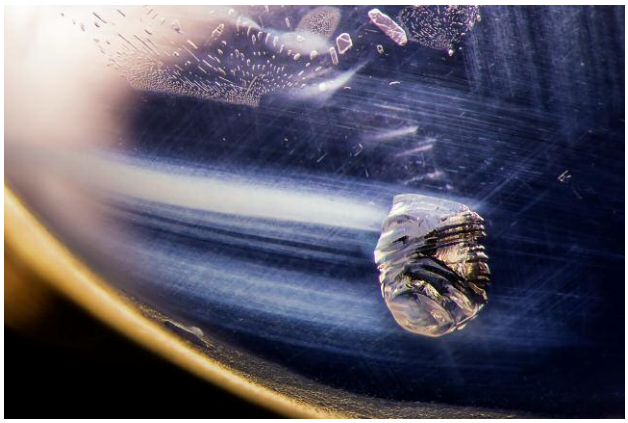

Figure 13. This inclusion scene features an apparent iron sulfide crystal against a midnight blue backdrop. It is reminiscent of the night sky, echoing the surface appearance of the star sapphire host. Photomicrograph by E. Billie Hughes; field of view 2.15 mm.

with sublinear striations and a smaller secondary crystal on the opposite side. With the aid of Raman spectroscopy, the brownish green crystal was identified as pargasite, a metamorphic calcium-dominated amphibole mineral associated with spinel and corundum deposits (J.W. Anthony et al., *Handbook of Mineralogy*, Vol. 2, Mineral Data Publishing, Tucson, Arizona, 1995). As an inclusion, pargasite has been previously documented in corundum—more frequently in rubies from Myanmar, Pakistan, and Tanzania, and in blue sapphires from Kashmir (E.J. Gübelin and J.I. Koivula, *Photoatlas of Inclusions in Gemstones*, Vol. 3, Opinio Verlag, Basel, Switzerland, 2008). The fact that the host sapphire was yellow makes this inclusion a fascinating discovery for the authors.

Nicole Ahline
GIA, Carlsbad

Tyler Smith
GIA, New York

Six-Rayed Star in Sapphire from Myanmar

Gems are renowned for their outward beauty, but their internal world can be just as striking. Lotus Gemology recently came across a Burmese sapphire, cut as a cabochon and measuring 8.92 × 7.10 × 4.75 mm, that displayed a six-rayed star. Once we examined it under the microscope, we were surprised to find that this celestial theme carried through to the inclusion scene inside (figure 13).

The long, undissolved rutile silk needles that form the six-rayed star are evident in angular zones. We could also see other inclusions typical of unheated sapphire, such as the tiny negative crystals forming a "fingerprint" at the top of the image. What was most interesting about this piece was the large, irregularly shaped crystal with a metallic appearance hovering close to the surface of the cabochon dome, which we believe is an iron sulfide crystal based on its appearance. This highly reflective crystal seems to float across a midnight blue backdrop, reminiscent of an asteroid floating in space and making for a fitting inclusion in a star sapphire.

E. Billie Hughes
Lotus Gemology, Bangkok

Pink Tourmaline in Spodumene

The pegmatitic mineral spodumene commonly exhibits fluid inclusions as well as muscovite-mica, feldspar, and clay mineral inclusions (E.J. Gübelin and J.I. Koivula, *Photoatlas of Inclusions in Gemstones*, Vol. 1, ABC Edition, Zurich, 1986). A colorless 7.85 ct emerald-cut spodumene, purportedly from Afghanistan, was of particular interest for the eye-visible pink tourmaline crystal inclusion (figure 14) under

Figure 14. Appearing as if suspended in water, a pink tourmaline inclusion in spodumene is illuminated by diffuse and fiber-optic illumination. Photomicrograph by Jonathan Muyal; field of view 7.19 mm.

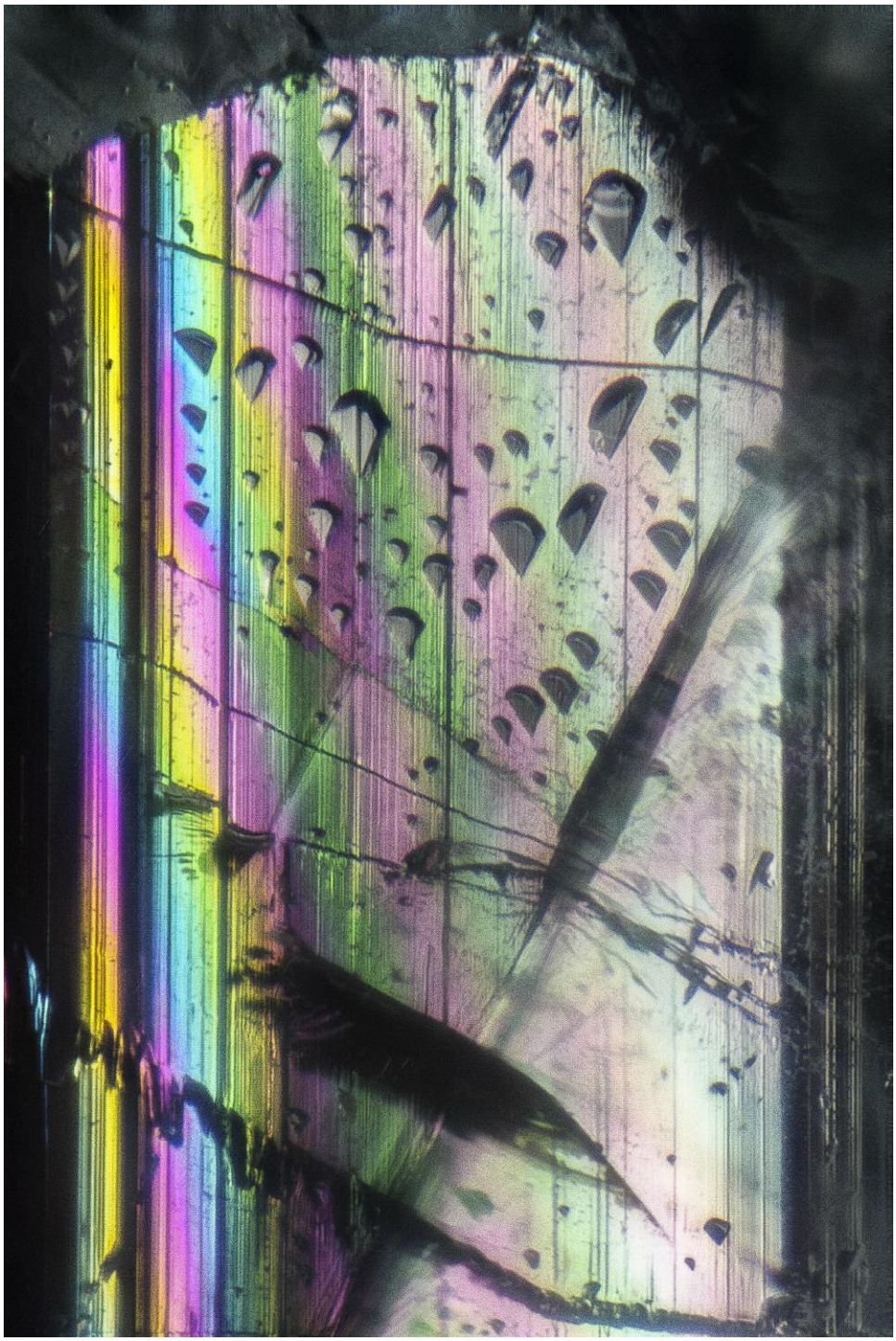

Figure 15. Diffuse and fiber-optic illumination reveal the fine striations common to tourmaline along the length and the shallow triangular etch markings typical of spodumene along the interface, as well as vivid iridescent colors. Photomicrograph by Jonathan Muyal; field of view 1.26 mm.

the table facet. The mineral inclusion's identity was confirmed by Raman microspectrometry analysis.

Although green tourmaline inclusions in spodumene have been documented (E.J. Gübelin and J.I. Koivula, *Photoatlas of Inclusions in Gemstones*, Vol. 3, Opinio Publishers, Basel, Switzerland, 2008, p. 642), very few references are found in the literature, and pink tourmaline in spodumene remains a rare occurrence. The transparent inclusion showed a well-formed trigonal prismatic crystal habit with fine vertical striations along its length (parallel to the c-axis). It exhibited a hemimorphic nature, with a flat termination on one end and a low pyramidal termination on the other.

Figure 16. Measuring 7.59 mm in largest dimension and weighing 1.84 ct, this partially etched diamond octahedron contains a bright green inclusion of chromium diopside. Photo by Robison McMurtry.

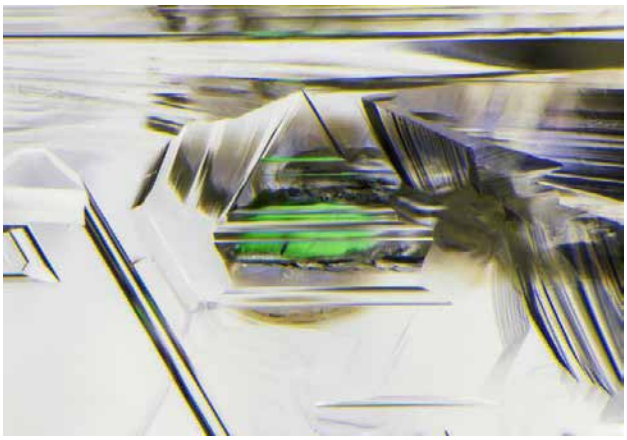

Figure 17. Rich green transparent crystals of chromium diopside are very uncommon inclusions in diamond. The example shown here has a typical rounded, etched habit. Photomicrograph by Nathan Renfro; field of view 1.80 mm.

Abundant uneven wavy fractures, more or less perpendicular to the c-axis, were also visible within the crystal.

Of interest were some triangular etch marks common to spodumene. Although at first they appeared to be on the inclusion's surface, they were actually on the spodumene interface. Additionally, the interface space exhibited vibrant iridescent colors when illuminated with oblique fiber-optic illumination (figure 15). This special guest inclusion thus gives the impression of having been "dressed and embellished" by its host spodumene and is displayed in its best attire.

Such a large tourmaline inclusion specimen in spodumene also provides valuable mineralogical information for the gemologist. The syngenetic inclusion and the host reflect their common pegmatitic geological genesis. The lithium-bearing granitic pegmatitic occurrence of spodumene strongly suggests that the inclusion is a lithia tourmaline variety, with lithium and aluminum substituting for iron and magnesium.

While spodumene is not known and prized for its inclusions, the beautifully highlighted pink tourmaline inclusion makes this gem a rare collector specimen.

Jonathan Muyal
GIA, Carlsbad

Quarterly Crystal: Cr-Diopside in Diamond

Brightly colored mineral inclusions in diamonds are rare. Some examples of these rarities are dark blue kyanite, yellowish orange almandine-pyrope, and deep purplish red pyrope garnet. This year's first Quarterly Crystal offering expands on this bright inclusion theme with a transparent colorless partially etched octahedron from the Kimberley mine in South Africa. Shown in figure 16, the diamond measures 7.59 × 6.59 × 4.79 mm and weighs 1.84 ct.

Situated along the edge of one of the octahedral planes, the diamond crystal plays host to a bright green transparent elongated mineral inclusion. Laser Raman microspectrometry was used to identify this included crystal as diopside, and the bright green color results from a trace amount of chromium.

As a diamond inclusion, chromium diopside is a medium to deep green transparent mineral with a vitreous luster. As shown in figure 17, it typically forms as rounded protogenetic mineral grains. Geologically, the presence of a Cr-diopside inclusion in a diamond is an indicator that the host diamond formed in a rock type known as peridotite.

John I. Koivula
GIA, Carlsbad

G&G

Gem News International

Contributing Editors

Emmanuel Fritsch, *University of Nantes, CNRS, Team 6502, Institut des Matériaux Jean Rouxel (IMN), Nantes, France* (fritsch@cnrs-imn.fr)

Gagan Choudhary, *Gem Testing Laboratory, Jaipur, India* (gagan@gjepcindia.com)

Christopher M. Breeding, *GIA, Carlsbad* (christopher.breeding@gia.edu)

TUCSON 2018

Every February the gem and mineral world descends on Tucson, transforming the downtown convention center and a great many of the city's hotels into a fascinating collage of traders bearing goods from all over the planet (figures 1 and 2).

Many of the exhibitors we spoke with described 2018 as the strongest year since 2008. Although traffic wasn't especially heavy at the AGTA and GJX shows, most dealers there enjoyed brisk sales and healthy demand for high-quality goods. Some of the same trends from last year were evident. Customers still sought out one-of-a-kind pearls and colored gemstone pieces, and the secondary market in the U.S. for exceptional pieces remained highly significant. There was a continuing focus on untreated material and ethically sourced gemstones, a subject articulated for us by Jean Claude Michelou of the International Colored Gemstone Association and officials from the Responsible Jewellery Council. Market realities such as very strong price competition for newly mined gem rough were mentioned as a major challenge by many dealers and cutters.

In addition to strong demand for high-end gems, many dealers at AGTA and GJX reported a surge in more moderately priced goods. Meanwhile, dealers at other locations told us the commercial end of the market remained soft.

Pantone's color of the year for 2018, a shade of purple called Ultra Violet, was well represented at the shows. A couple of dealers had exceptional examples of purple sillimanite. Many dealers posted strong sales of pastel-colored spinel—in pink and lavender hues—in suites and sets as customers found the scarcity and high prices of red spinel prohibitive. In a similar vein, Margit Thorndal of Madagascar Imports reported strong demand for purple-lavender spinel and purple sapphire from Madagascar, as well as teal hues of unheated Montana sapphire.

We noted that electric blues, teals, hot pinks, hot yellow greens, and pastel-colored gems were quite popular. Bill Larson of Pala International pointed to this trend and showed us a number of spectacular examples from his inventory. Fine blue zircon from Cambodia was prominent, as was attractive sphene from Zimbabwe and Madagascar.

Dave Bindra of B&B Fine Gems said his company was very active in scouring the secondary markets for old jewelry items and gemstones that have been out of circulation

Figure 1. Although traffic at the AGTA show was lighter than in some previous years, demand was brisk and most traders were satisfied with their 2018 business. Photo by Kevin Schumacher.

Editors' note: Interested contributors should send information and illustrations to Stuart Overlin at soverlin@gia.edu or GIA, The Robert Mouawad Campus, 5345 Armada Drive, Carlsbad, CA 92008.

Gems & Gemology, Vol. 54, No. 1, pp. 74–110.


Figure 2. Customers in Tucson sought out unique goods, a trend that carried over from last year's shows. Photos by Kevin Schumacher.

for decades. This year's standouts were two incredible red beryls from Utah (a 3 ct emerald cut and a 4 ct round brilliant), a 61.92 ct Imperial topaz (figure 3), and a fine selection of Kashmir sapphires, which were very sought after this year. Fran Mastoloni of Mastoloni Pearls updated us on current trends in the cultured pearl market and showed examples of unique pieces.

Dealers specializing in domestic gems reported strong demand. John Woodmark of Desert Sun Mining & Gems told us the market for Oregon sunstone was the strongest he had seen since the andesine controversy challenged suppliers of the natural Oregon gem a decade ago. As a result, the company has scaled up its mining activities and built new relationships with gem cutters to improve supply to its clients.

As always, the Tucson shows were a rich source for the latest on global colored stone supply. Conversations with Luis Gabriel Angarita and Edwin Molina revealed insights on the mining and branding of Colombian emerald. Marcelo Ribeiro shared details on mining and cutting at the Belmont emerald mine in Brazil. Alexey Burlakov offered his perspective on Russian demantoid production, while Stephan Reif did the same for demantoid from the Green Dragon mine in Namibia. Miriam Kamau shared information on her Kenyan tsavorite mining operation and offered her own inspirational success story. From Jürgen Schütz of Emil Weis Opals we learned about the cutting of opal, both play-of-color and nonphenomenal, from sources around the world. Alexander Arnoldi explained Arnoldi International's strategy in sourcing and cutting high-quality aquamarine and tourmaline. We also saw examples of gem production from unexpected sources: Indonesian opal and turquoise from the state of Arkansas.

Figure 3. Dave Bindra of B&B Gems showed us a selection of standout gems from the secondary market, including this 61.92 ct Imperial topaz. Photo by Kevin Schumacher.

Tucson is also a destination for many leading gem artists and jewelry designers. Award-winning carver Michael Dyber explained the inspiration behind some fantastic one-of-a-kind pieces bearing his signature optical disks. At the intersection of science and art, Rex Guo discussed his approach to recutting gems to optimize light performance and beauty. And designers Paula Crevoshay and Erica Courtney showed us striking and innovative new pieces with unexpected and fascinating gem combinations.

Duncan Pay
GIA, Carlsbad

COLORED STONES AND ORGANIC MATERIALS

Multi-generation cutting family from Idar-Oberstein. Idar-Oberstein, Germany is a historic agate locality that became famous over the last century as a colored stone trading and cutting center. In recent decades, though, much of the lapidary activity has moved from Idar-Oberstein to cutting centers in Asia such as Jaipur and Bangkok. The remaining businesses in Idar are focusing on highly specialized mar-

Figure 4. Aquamarine has long been Arnoldi International's signature stone. Photo by Kevin Schumacher.

Figure 5. More recently, Arnoldi International has begun working with tourmaline from the Democratic Republic of Congo. Photo by Kevin Schumacher.

ket segments, such as precision cutting and unusual stone varieties. Alexander Arnoldi explained to us the strategy of Arnoldi International and provided an update on some new high-quality materials.

The cutting business was founded in 1919, making Alexander Arnoldi a fourth-generation gemstone dealer and cutter. They process all the goods in-house, from rough sorting to final polishing. Lapidary work is still based on the traditional techniques of Idar-Oberstein, where the wheel is turned with the dominant right hand, leaving the left hand free to hold the stone. Laps are motor-driven today, but the stone is still held with the left hand. According to Arnoldi, it takes more than five years to master cutting and learn all the facet placements and correct angles for the different styles and materials.

The company focuses on flawless stones, a challenging segment of the gemstone industry. Prices for these goods have exploded, but supply is extremely low and competition at the source is very high. Finding extremely high-quality rough that yields large clean stones is one of the main challenges they face in the current market. Nowadays, most rough suppliers bring their goods to Bangkok and Jaipur instead of Germany. This forces companies such as Arnoldi to go source their own material on site—for instance, copper-bearing tourmaline from Mozambique.

Idar-Oberstein's first main product more than 500 years ago was agate, polished using hard sandstones found nearby. When Germany's population began moving abroad in the early nineteenth century, Idar's network became more global and gained access to the Brazilian deposits, which produced many quartz varieties. The German cutters became very adept at cutting and polishing the materials sourced in Brazil. Arnoldi focused on aquamarine (figure 4), a stone that remains their strong suit in 2018. Originally they worked with goods from South America, including the fabled Santa Maria deposit in Minas Gerais, Brazil. Much of the rough is now sourced in Central and East Africa, which produces deep blue material similar to Santa Maria aquamarine.

Another stone they are focusing on is tourmaline, including Paraíba, rubellite, and bicolor stones. In December 2017, they traveled to Central Africa to source the new tourmalines from the Democratic Republic of Congo (figure 5). This material comes in different shades of green, often in the same crystal. Pink crystals are occasionally found. Supply is highly irregular, and quality varies greatly.

Arnoldi International is putting their focus on high-quality, flawless goods and excellent cutting standards. This allows them to supply high-end vendors who often ask for unique, customized cutting styles.

Wim Vertriest
GIA, Bangkok

Update on the Green Dragon demantoid mine in Namibia. According to Stephan Reif, Namibia's Green Dragon mine is the largest continuously operating demantoid deposit. Green Dragon has a complete mine-to-market approach, handling everything from mining, ore processing, sorting, cutting, and grading to wholesale. They mainly supply the European market through Vienna and the Asian market through Hong Kong.

The mine was discovered in a remote part of southern Namibia in the 1990s and has been producing since the mid-2000s. In 2017, Green Dragon received a 25-year mining license for the deposit, offering stability as an incentive to invest in the mine. In the near future, mining will be scaled up and production will increase. This will provide a more consistent and attractive supply for buyers in the

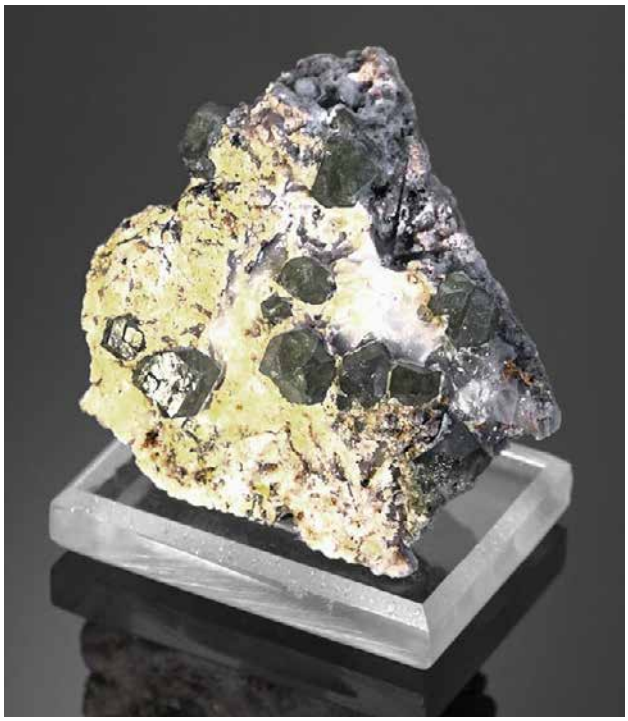

Figure 6. Namibian demantoid retrieved from the Green Dragon mine and preserved in its host rock. Photo by Albert Salvato.

trade. As part of the 25-year mining lease, Green Dragon has committed to supporting the local communities.

Namibian demantoid mining is highly mechanized, using heavy equipment to extract the green garnets from their host rock (see figure 6). Monthly production varies between 15 and 20 kg. Of that, a little over 10% is considered gem quality and goes for faceting.

Color ranges from yellowish green to bluish green, and some darker brownish greens are also found. Demand for certain colors varies, but at the moment the yellowish "golden" colors are in highest demand by designers. For Reif, the ideal Namibian demantoid is a slightly bluish green gem full of fire and brilliance.

The combination of lighter color and very high dispersion sets Namibian demantoid apart from other green garnets. These properties also depend on the quality of cutting and polishing (figure 7), something Green Dragon has focused on in recent years by having their in-house lapidaries and quality control perform to a higher standard. Because clarity, color, and calibration standards are so tight, the yield is only around 9%.

Most of the production is in melee and small calibrated sizes, with fine singles being extremely rare. Fine-quality melee is in very high demand in Europe at the moment, especially in the 4.0–6.5 mm range. In recent years, the demand for very small melee (1–2 mm) has increased substantially. Larger exceptional pieces typically go to Asia.

Wim Vertriest

Figure 7. The cutting and polishing of Namibian demantoid should emphasize the material's lighter color and high dispersion. Photo by Albert Salvato.

Update on Russian demantoid production. Russian demantoids (figure 8) are renowned in the gem community for their pure, vivid colors and spectacular inclusions. Alexey Burlakov, founder of Tsarina Jewels, shared some insights on the current production of Russian demantoids and emeralds. Tsarina Jewels is based out of Bangkok and was co-founded with his father, Dr. Evgeny Burlakov, curator of the Ural Geological Museum in Yekaterinburg.

According to Burlakov, there are currently two mines in the Urals producing demantoid in commercial quantities: Korkodin and Poldnevaya. They are about 7 km apart, located in the same geological massif that also hosts numerous gold and platinum mineralizations. Although the two mines are very close to each other, the material is very different. The Korkodin mine is characterized by a darker color, often with a brownish tint that can be removed by

Figure 8. Russian demantoids are well known for their pure colors and remarkable inclusions. Photo by Kevin Schumacher.

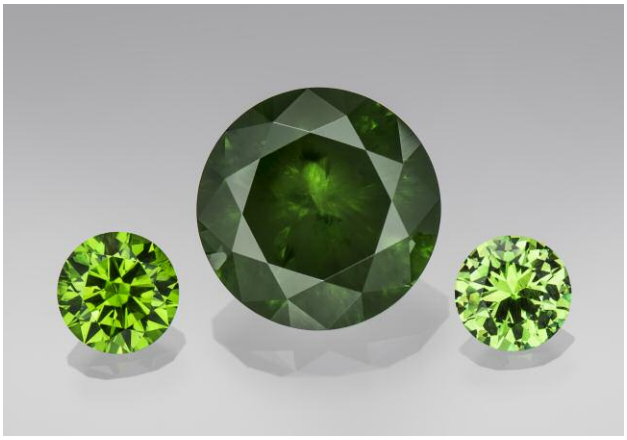

heat treatment. Poldnevaya produces material of lighter, more "open" colors without the secondary brown. Because they are naturally a pure green, these demantoids do not require heating to optimize the color.

A third known deposit is Nizhny, located in the Tagil region about 200 km north of the other two mines. This was the original deposit where Russian demantoid was discovered, but it is currently inactive. The material from this mine typically has a lighter color with a slightly bluish tint, setting it apart from the other two.

Russian demantoid comes in a wide range of colors, covering all shades of green. Much of the material has a brown color that can become dominant. The finest color is considered a pure, vibrant green with no secondary hues. It is estimated that around 80% of the Poldnevaya mine production has a secondary yellow color, while 15% is apple green and around 5% top vibrant green.

A typical feature of Russian demantoids is the horsetail inclusion, a radiating pattern of asbestos fibers. Fully developed horsetails are still rare. This inclusion has been found in demantoids from other localities as well, but none of these deposits match the importance of Russia's.

The main markets for Russian demantoid are the United States, China, and France. The French market demands smaller melee-sized stones, while Chinese and U.S. customers opt for stones over 1 ct. Prices of Russian demantoid have increased, especially for larger sizes. This is due to the limited production. It is estimated that the Poldnevaya mine produces between 300 and 1,000 carats of gem-quality material per month. This means that only a few stones over 3 ct are produced on a yearly basis.

Other important gemstones from the Ural Mountains are emeralds and alexandrites. The Urals produced large volumes of emerald in the beginning of the 20th century. During the Soviet era, the mines were reopened for beryllium mining. In recent years, emerald mining has started again. New production and specimens have already reached the market. The Russian emeralds are generally lighter green but clean compared to other deposits. Alexandrite is not being mined, but a Russian government corporation is actively developing and expanding the alexandrite/emerald mines in the Urals.

Wim Vertriest

Fortieth anniversary of the Belmont mine. This year marks the 40th anniversary of the Belmont emerald mine. Director Marcelo Ribeiro updated us on mining and cutting activities in Brazil and shared his thoughts on today's dynamically changing market.

As in 2017, mining activities are still focused on underground mining below the original Belmont open-pit site and the newly developed Canaan mine about 2 km away. In the near term, underground mining will continue to dominate emerald production. Ribeiro shared some new geological study findings related to multiple deposits in the Belmont area. Detailed geological analysis proved that over the past 40 years, only about one-fifth of the deposit within the Belmont property has been mined. Some exciting mineralogical study results from a mining site nearby hint at even deeper extension of the emerald-bearing rocks. Belmont has better wall rock stability than some other famous emerald sources around the globe. This makes underground mining an ideal option in the foreseeable future.

Figure 9. This 13 ct emerald represents some of the finest production material from Belmont's underground tunnel. Photo by Kevin Schumacher.

Currently, all rough emerald with a value of more than $20 per carat is faceted by Belmont's own cutters, while everything else is transported to Jaipur, India, for processing. The cutting facility at the Belmont mine now handles 1,500 to 2,000 carats of emerald per month. Ribeiro visited the factories in Jaipur in late 2017 and is very satisfied with the quality of goods produced from the rough he exports to India. In terms of adding value to the medium- to low-quality rough stones, cutters in Jaipur have more experience and expertise. According to Ribeiro, the company's sales jumped about 15% each of the past three years. A 13 ct top-quality emerald recovered in 2017 from the underground mine at the original site (figure 9) and a 15.01 ct stone from the Canaan mine (figure 10) were brought in by Ribeiro. The stone from Canaan showed a very special color reminiscent of the electric bluish green color of some copper-bearing tourmalines. This stone also displayed quite strong green and blue pleochroism. Ribeiro informed us that this is a very rare color and only a very limited amount of rough can potentially produce stones of this color.

Belmont has exhibited in Tucson for the past 17 years, and Ribeiro pointed out that the way of doing business has changed dramatically in recent years. The booth at the GJX show once generated about 80% of the company's sales. Now, 80% of the sales happen online. Ribeiro used to stay at the booth to sell stones, but nowadays he needs to spend most of his time walking around the show to talk to different people. When asked about the role of middlemen in the current and future marketplace, Ribeiro shared his opinion. When he first got into the trade, he envisioned that one day middlemen would be removed from the pic-

Figure 10. This 15.01 ct emerald from the Canaan mine had an unusual color, and many customers at the show thought it was a Paraíba tourmaline. Photo by Kevin Schumacher.

ture and he would market his stones directly to end consumers. With the industry experiencing dramatic changes these days, he has started to feel that middlemen will remain but must change their mindset to adapt to new ways of doing business.

The logistics network within the United States allows very fast, safe, and economically viable transportation of gemstones between dealers and jewelers. Overseas suppliers like Belmont do not have access to the same services, which makes it necessary to have an intermediary located in the States who can handle shipping, receiving, and securing stones between the supplier and the buyers. This person also works as a sales representative to connect the supplier and the buyers. Ribeiro pointed out that unlike the traditional middleman, this person does not do business by trying to hide the supplier from the buyers and vice versa. In fact, this representative should ideally make the supply chain even more transparent by letting the two ends easily see and connect with each other to build more solid trust, connections, and inventory in between.

For the past 40 years, the Belmont mine has practiced community building and empowered people through gemstone mining. Ribeiro feels that this is already embedded in the DNA of the company and will continue to guide their good work. He hopes that gemstone purchasing will remind younger buyers of the benefits these stones bring to the local people and their next generation.

Tao Hsu and Andrew Lucas
GIA, Carlsbad

Colombian emerald industry: The new generation. Following author AL's 2015 visit to Colombian emerald mines and cutting operations, we again had the opportunity to interview two representatives from this important source country. As part of the new generation of the Colombian emerald industry, both shared with us their experience and vision for the industry.

Luis Gabriel Angarita, director of the CDTEC gem laboratory in Bogotá, comes from a family that has been heavily involved in the industry for over 40 years. Since 2009, Angarita has been working on branding Colombian emerald. He recently resigned as president of the Association of Colombian Emerald Exporters and is working full-time for the gem lab. Angarita updated us on the large production coming from the Chivor mines. He said that while the production has been low for over 20 years, the quality of extracted stones is quite high.

Even though Angarita no longer heads the exporters association, promoting Colombian emerald as a brand is still at the top of his list of priorities. He sees several challenges in branding the Colombian emerald. First, the Colombian emerald industry lacks a well-accepted standard. This causes inconsistency between different players and makes it extremely hard to face the global market as a unified entity. Effectively educating consumers is another obstacle in branding. Angarita admitted that the Chinese market has the greatest potential for emerald. However, most Chinese consumers only want emeralds with no oiling. Goods with moderate oiling are almost unsellable. This misunderstanding of emerald value factors hinders the stone's promotion. Inconsistent description among major gem laboratories further complicates the situation. Angarita also shared some information about a new emerald treatment being developed in Colombia. Finally, he informed us that the second World Emerald Symposium will be held in Bogotá in October 2018.

Edwin Molina, a fourth-generation Colombian emerald miner, serves on the board of directors of the Cunas mine in Santa Rosa. He also became president of APRECOL (the Association of Emerald Producers of Colombia) in 2017. Molina's family has played a critical role in emerald mining in the Muzo area, and he was partially responsible for the transaction that formed today's Muzo International. The family later switched its interest to the Cunas mine, which has been a joint venture with foreign investors since 2009 and is now one of the biggest in the area. According to Molina, production from Cunas is quite large. Although the mine typically lacks the very high-end stones with large sizes like those from Muzo, the quality is very stable. Compared to other operations in Muzo, Cunas is more controllable because its entrance is located far from the extraction points. There are three emerald-bearing zones in the mining concession, and so far only one is being worked on. Therefore, Cunas still has plenty of potential.

Molina also related his experience during this profound transformation from a family business to a formal mining corporation. He admitted that at the beginning of this journey, building trust with the investors was a challenge due to lack of supporting data from previous miners and operations. When he became involved, a new emphasis was put on formalizing the operation through environmental protection, infrastructure construction, and mining community building. Molina informed us that the mine would focus on increasing production by working on more extraction points

within the 0.6 km^2 concession. This is very important because foreign investment will dry up if the mine has no production for a prolonged period, as has happened before in the Muzo area. Another important factor in attracting and keeping foreign investors is the security of the mine and production. With the support of the national police, a local police department will soon be formed to help with security. Molina has always believed that the only thing investors need to worry about is the production of a mine. As a miner and businessman who grew up in the United States and went back to his motherland of Colombia, Molina wants local miners to go out and see the world. Putting the industry in a global framework will enable them to adapt to a new environment and seize new opportunities.

During the interviews, both Angarita and Molina expressed confidence in the future of the Colombian emerald industry and optimism about global demand for this "Mother Gem" of Colombia.

Tao Hsu and Andrew Lucas

***Zoning In on Liddicoatite* exhibit.** The calcium-rich lithium tourmaline liddicoatite was first recognized as a new mineral species in 1977. It was named by research staff at the Smithsonian Institution after GIA's then-president, Richard T. Liddicoat (1918–2002). In honor of Mr. Liddicoat's centennial birthday, the GIA Museum hosted an exhibit titled *Zoning in on Liddicoatite* at the Tucson Gem and Mineral Show, February 8–11. With highlights from Mr. Liddicoat's career alongside crystals and polished crystal slices showing spectacular color zonation (figure 11), the exhibit was a fitting tribute to GIA's own "Father of Modern Gemology."

Jennifer-Lynn Archuleta
GIA, Carlsbad

Outlook on opals from Mexico and Australia. Emil Weis Opals (Idar-Oberstein, Germany) opened its doors in 1905, making it the oldest opal cutting company in the world. Idar-Oberstein was the only global gem cutting center at the time, and opal buyers from all major gem markets had to send rough there for cutting. Emil Weis catered to this niche market early on and has since branched into mining; the company now owns mines in Australia and Mexico. We sat down with Jürgen Schütz, part of the founding family at Emil Weis, to discuss their activities in the opal market.

Currently the company is cutting 50 different types of opal from all over the world, the majority of it from Australia and Mexico. Emil Weis sells more nonphenomenal opal from these countries than it does play-of-color opal. The Mexican boulder opals they had on display were such an example. These specimens are cut to include both opal and rhyolite matrix, which some jewelry designers like to use in their pieces. According to Schütz, the nonphenomenal "fire" opal from Mexico (figure 12) is the only opal mined in quantity that is clear enough for faceting. It ranges from colorless to a dark red that is comparable with ruby. This type of material is available in large quantities and can even be calibrated.

Figure 11. At the 64th annual Tucson Gem and Mineral Show, the GIA Museum hosted Zoning in on Liddicoatite *in honor of Richard T. Liddicoat's 100th birthday. Photo by McKenzie Santimer.*

Schütz then discussed the shortage of and demand for Australian black opals (see figure 13). In the past, Japanese demand for black opals drove prices up, but when Japan's economy slowed in the early 1990s, prices fell and production slowed. However, recent rumors that Chinese markets are interested in black opal have doubled prices. Schütz showed us a rare black opal suite from Lightning Ridge, Australia, which took years to collect. Emil Weis

Figure 12. Mexican fire opal is clear enough to be faceted, and ranges from colorless to dark red. Photo by Kevin Schumacher.

Figure 13. Jürgen Schütz discussed the current supply and demand dynamics of Australian black opal. Photo by Kevin Schumacher.

has had this suite for about 10 years; today, it would be impossible to assemble this combination of black opals due to low production.

Production of Australian boulder opal (figure 14) is quite low. This is partially due to weather conditions, but Schütz noted that the boulder opal belt of Queensland is about 3,000 km long and 800 km wide, with only about 25 people mining it. This means that medium- to high-quality material is not produced in quantity. Schütz himself has connections with some of the older Queensland miners who have held on to parcels. Over the past two years he has been able to buy a parcel at a time from them. As a result, Emil Weis has a huge stockpile of boulder opal to cut, but does so sparingly.

Figure 14. According to Schütz, the lack of active miners along the Queensland opal belt has led to a shortage of Australian boulder opal. Photo by Albert Salvato.

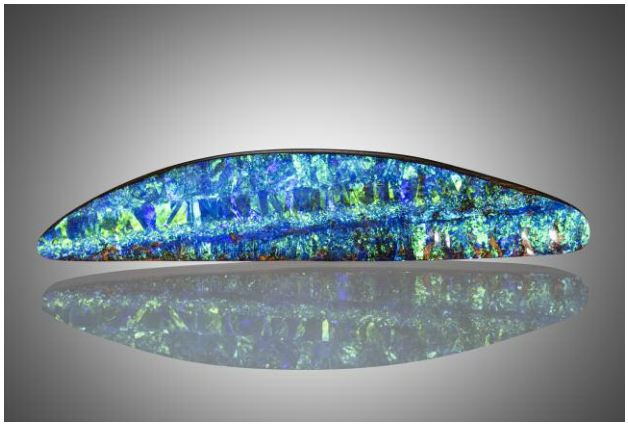

Schütz noted that the supply of South Australian light opals is also severely constrained. When Ethiopian opal came on the market at one-tenth of the price, the demand for Australian opal slowed. By the time buyers regained interest in South Australian opal, the mining population had dropped from several thousand to about 20 in less than a decade. In fact, Schütz said, Australian opal mining has traditionally been such a difficult way of life that many young people are opting for more stable jobs, leaving large gaps in the mining industry. He thinks that it may take another generation or two before mining once again hits its stride Down Under.

Duncan Pay and Jennifer-Lynn Archuleta
GIA, Carlsbad

Opal from West Java, Indonesia. At the AGTA show, Rare Earth Mining Co. (Trumbull, Connecticut) displayed an unexpected material: Indonesian opal reportedly from West Java. Two cabochons (figure 15) yielded a refractive index of 1.45 and a specific gravity of 2.13, consistent with opal. Energy-dispersive X-ray fluorescence (EDXRF) analysis revealed the presence of copper.

According to Rare Earth's Curt Heher, the material was first seen in the spring of 2017. While the opal comes in a wide range of colors, including browns and blues, the greenish blues were of particular interest. Rare Earth displayed cabochons where this was the primary hue, with the accessory colors distributed in an aesthetically pleasing manner.

Jennifer-Lynn Archuleta and Nathan Renfro
GIA, Carlsbad

Cultured pearl update. We had the opportunity to speak with Fran Mastoloni (Mastoloni Pearls, New York) at the AGTA show and hear his thoughts on the current status of the cultured pearl market.

Figure 15. These cabochons, weighing 6.94 ct and 3.79 ct, were among the Indonesian opals at Rare Earth's AGTA booth. Photo by Robison McMurtry.

Figure 16. The pearl market has seen a rise in popularity in pieces with unusual color (left) and size combinations (right). Photos by Kevin Schumacher.

According to Mastoloni, pearls continue to do very well. His company had one of its best fourth quarters in recent history, and he believes that has much to do with the pearl cycle. He noted that pearls tend to be in fashion in seven-year periods. Mastoloni believes this is the second year of a seven-year trend. Last year pearls were making a resurgence, but instead of classic white pearls they were selling unique and fashionable pieces, such as the cocktail necklaces of white South Sea, gold Philippine, and silvery Tahitian pearls seen in figure 16, left. Mastoloni explained that customers are enjoying the organic shapes and colors of these different varieties and how versatile such necklaces and pieces can be. This trend has continued into 2018, but they are selling these unusual combinations to designers and major manufacturers rather than individual stores. These clients are incorporating Tahitian or keshi pearls or stations into necklaces, as well as Mastoloni's colored pearl palette, with their own design elements. Mastoloni also noted a greater use of keshi pearls as stations, with one designer planning to use a bezel-set light sapphire between the stations to create something different, fun, and marketable.

Fine pearls continue to sell, though with a twist. Mastoloni's top sellers include white South Sea, Indonesian, and Australian pearls in classic styles such as long necklaces, but with a more organic appearance. The price point is very important, Mastoloni said, because a number of customers self-purchase for work or to satisfy their own tastes. In fact, he has found that self-purchasing of pearls has become more popular than gift giving. Pearls are versatile and can be worn anywhere, he said, because they communicate that the wearer is confident but not ostentatious.

Mastoloni showed us two graduated Japanese akoya necklaces that appear to date from the 1970s or '80s. The pearls measure 7.5 × 10.5 mm and are perfectly matched, with no imperfections and a nacre coating that is just not seen anymore; he has three other strands that are slightly smaller. These sizes are "almost unheard of" in akoyas and make for an unusual addition to a collection. He also showed his "cloud" necklace (figure 16, right), one of his most popular, created from Chinese tissue-nucleated pearls. Chinese pearls are sold by weight, and the cultivators are using larger nuclei to create larger pearls. Since pearls are no longer grown in the sizes used in this necklace, this material is unlikely to be found on the market despite its popularity.

Duncan Pay and Jennifer-Lynn Archuleta

Finds from the secondary market. During the AGTA show, Dave Bindra of B&B Fine Gems (Los Angeles) showed us some noteworthy pieces from a gem collection he acquired last year and shared his thoughts about the state of the colored stone market.

Bindra noted that B&B is very active in searching the secondary markets for unique material. Last year, they came into a significant collection from a client. Several of the items had previously been in B&B's stock, though the collection contains stones from all over the world. Among them are two incredible red beryls from Utah: a 3.01 ct emerald cut and a 4.08 ct round brilliant (figure 17) that is the world's largest round red beryl. Bindra considers these two of the most important red beryls on the market. Red beryl from Utah has been well out of production in these sizes for decades.

Another highlight was a 61.92 ct Imperial topaz of unknown provenance and free of heat treatment (again, see figure 3). The very rich sherry color in unheated Imperial topaz is extremely rare. That, plus the clarity and size, makes for an impressive stone of museum quality.

Also on display was a collection of 2–3 ct Kashmir sapphires, material that Bindra said customers are seeking, particularly in the Southeast Asian market. Kashmir sapphires have been out of production and even circulation for many years and are often found only at estate sales. Other remarkable stones from the collection included a 76.50 ct sphene with coloring reminiscent of a Christmas tree and a sugarloaf-cut 38.46 ct tanzanite (figure 18).

Bindra sees unprecedented demand for colored gemstones, particularly the high-end and unusual, making

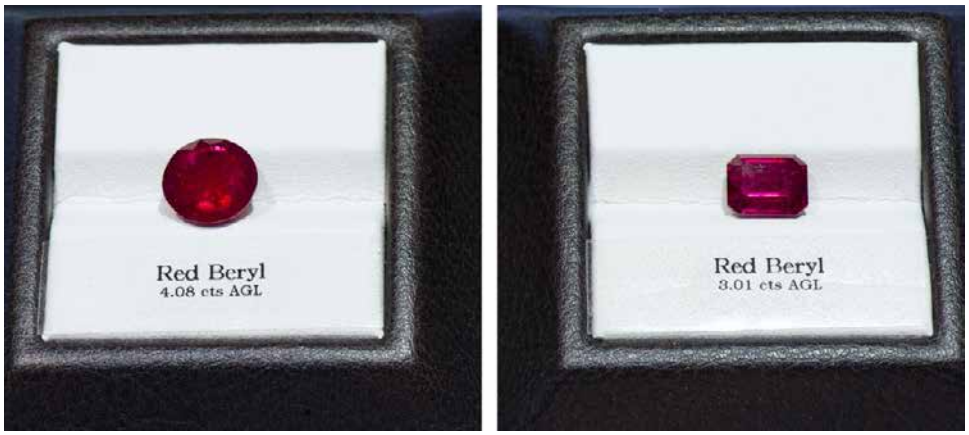

Figure 17. Two of B&B's most spectacular finds on the secondary market were these two red beryls from Utah, which has been out of production for decades. Photo by Kevin Schumacher.

this an exciting time for those who deal in the rare and esoteric. There are a number of factors at play, including the influx of new consumers domestically and abroad, particularly in Southeast Asia, though the Chinese market is less active than in previous years. Record-breaking auction prices are also driving up the value of colored gems. Bindra cited commercial-quality Mozambique ruby as an example; the very finest specimens from that country still command top prices. The highest-quality Mozambique rubies exhibit a subtle fluorescence, giving them a glow reminiscent of Burmese material. B&B has sold some of the extraordinary pieces that were featured in previous *G&G* Tucson reports. Bindra believes that many Americans have generated new wealth and view colored gemstones in the same way they see other tangible and collectible assets, such as luxury cars and fine art. This has been a great boon to the market. As Bindra noted, "The time for color is now."

Duncan Pay and Jennifer-Lynn Archuleta

Figure 18. Also part of a collection purchased from a client was this 38.46 sugarloaf-cut tanzanite. Photo by Albert Salvato.

Ponderosa sunstone update. John Woodmark, president of Desert Sun Mining & Gems (Depoe Bay, Oregon), provided an update on the Ponderosa mine. According to Woodmark, the mine is Oregon's most prolific sunstone source, producing about 95% of all material currently on the market. He explained that the mine's operations have changed to compensate for the characteristically short May-to-October mining season at the Ponderosa, which is at an elevation of 6,000 feet. In September 2015, Woodmark contracted with a sand and gravel company to bring a much larger excavator on site along with a high-capacity screen. This allowed the operators to stockpile a large enough volume of concentrate to sustain production through the entire following season.

In years past, even though the miners had access to the site as soon as the snow cleared in mid-May, they had to wait for the ground to dry out before they could mine. Now they can process the prior year's stockpiled concentrate through a wet trammel—which removes some of the volcanic crust on the rough feldspar—and pickers can start work immediately. The new process ensures more production: During the five-month 2017 season, Ponderosa produced 4,400 kg of rough labradorite feldspar.

In September 2017, the combination of the bigger excavator and the high-capacity screen produced approximately 5,000 cubic yards of concentrate in just under a month. Woodmark estimated that the concentrate contains 5 kg of Oregon sunstone per cubic yard, and the new process has dramatically increased production of Ponderosa sunstone.

Another development has been extensive test digging to determine gem potential over Desert Sun's existing 60-acre claim. Woodmark explained that these test digs located a promising area of approximately one quarter of an acre, which has been developed into an open pit about 50 feet deep. Woodmark's miners are finding larger stones as they go deeper, including one that weighed approximately 1,800 ct (figure 19). In addition, many of these larger gems are red/green dichroic stones, along with approximately 18 kg of extremely rare fine red and orangy red material (figure 20).

Woodmark has streamlined the company's operations in other ways. He now contracts with a cutting house in India that grades the rough gems into categories. This frees

Figure 19. A new test pit on Desert Sun's Ponderosa claim has produced much larger rough, with a high proportion of large dichroic stones. The largest recovered so far was approximately 1,800 ct. Photo by Kevin Schumacher.

Woodmark's team from having to grade and allows them to focus on mining and production. It also allows the cutting company to respond more quickly to customers' requests for a particular color or grade of finished gems. According to Woodmark, this development helps manufacturers use sunstone more effectively. He mentioned that sales have increased year-on-year since the andesine controversy earlier in the decade as trust in the natural-color Oregon gem has increased. He noted that 2017 was the company's most successful year to date.

Woodmark noted that sustained production has been a major factor in this renewed confidence. He also told us that recent interest in North American gemstones, especially among TV merchandisers, has driven sales. He says that when clients see the quality of an untreated red Oregon sunstone and compare the pricing for a one-carat stone to that of an equivalent-color ruby or spinel, they realize the $150-per-carat price tag is an absolute bargain.

Figure 20. Oregon sunstone retains its rich orangy red hues even in smaller sizes. Photo by Kevin Schumacher.

Figure 21. Desert Sun hires Native American teenagers from the local community to separate sunstone from ore. Photo by Duncan Pay.

Woodmark added that consumer concern about the integrity of the gem supply chain has fostered interest in domestic gems. People are looking for gems that can be followed "from the dirt to the finger."

Desert Sun Mining & Gems hires local Native American teenagers to help pick the sunstones from the processed ore (figure 21), which helps the local community. Woodmark explained that each picker can typically produce between 10 and 11 kg per day, but some might pick as much as 17 kg. He mentioned that the company had recently raised the pickers' hourly wage by 20%, citing the community unemployment rate of 87%. He told us, "They're always available…and they're good kids."

Woodmark told us the operation had recently hosted a PhD geoscience student from Washington State University who was studying the volcanism of the area. The student determined that the flow that hosts the sunstone at Pon-

derosa is approximately 18 million years old, and that the mine sits atop a vent, which is why those searching for similar deposits nearby have yet to find anything. As Woodmark said, "It just came up, and we're right on it." He added that the deposit "looks inexhaustible. From the bores that we've done, we have over a trillion carats."

Duncan Pay

Interview with a Kenyan miner and dealer. Miriam Kamau, owner of Mimo Gems Traders Ltd. in Nairobi, transformed from an office assistant to a dealer and miner to a representative of her country on the international stage of the colored gemstone trade. Her career has not only changed her life but also inspired many women in Kenya to pursue their dreams in the gem and jewelry industry.

Born and raised in Nairobi, she entered the trade working for an American gem dealer in her hometown. In the beginning, she greeted the clients and took care of errands for her boss. She gradually realized the big fortune these small stones can carry as she passed the stones and money between the dealer and his clients. Kamau started to pay more attention to trading activities in the office and ask more questions. Luckily enough, her boss generously shared his knowledge of the gems he dealt and did not mind her interacting with his clientele and even doing business with them. When he was away and the rest of the office staff was gone for the day, Kamau visited the mining area to talk to the clients, generally women, who brought stones to the office. She learned a lot from these female miners. She also realized she needed to go back to school for a formal education on gemstones. This led her to enroll in courses in Nairobi and Johannesburg to systematically study diamond and colored gemstone identification.

After returning to Kenya, Kamau started her own gem business in Nairobi, buying from the miners and selling wholesale and retail. During this time, she got to know many important people in the industry, including the late Campbell Bridges. Finally, an opportunity came to represent a Kenyan woman dealer who exported stones to Thailand. Kamau, who wanted to travel overseas, did not let this opportunity go. This trip opened her eyes to the world outside of Africa. Her trade contacts then introduced her to the International Colored Gemstone Association, and she became the ICA ambassador to Kenya. In that role, she gained the trust of Kenyan local miners to represent their interests.

As she seeks to bring added value to the local miners, her own business has expanded. She now has her own tsavorite mine in Kenya. She informed us that the mine's operation tunnel is about 90 feet deep, and the first extractions have been quite exciting (figure 22, left).

Kamau admits that when she started her own business, she experienced prejudice in the Kenyan trade, which has traditionally been dominated by men. Only very recently did Kenya begin to grant mining licenses to women, which allowed her to own an operation. While it is often considered unsafe for women to work in remote mining areas in Africa, Kamau readily adapted to the bush life and built a thriving business. She now works with her brother and other male miners in the mining operation.

As more women in Kenya learn about Miriam Kamau, many of them ask her for career advice. Kamau is now a key member of a Kenyan association dedicated to empowering women in mining. Kamau helped organize the first gem and jewelry show devoted to Kenyan women in the trade. The second show will take place in July 2018. Kamau is very optimistic about Kenya's future as a gem trading hub in Africa. She says the government is very supportive, and she sees a lot of positive changes happening in the mining sector. Kamau also brought with her some

Figure 22. Left: These faceted tsavorites were extracted from Miriam Kamau's mining operation in northern Kenya. Right: Kamau also brought Kenyan red spinel to Tucson. Photos by Kevin Schumacher.

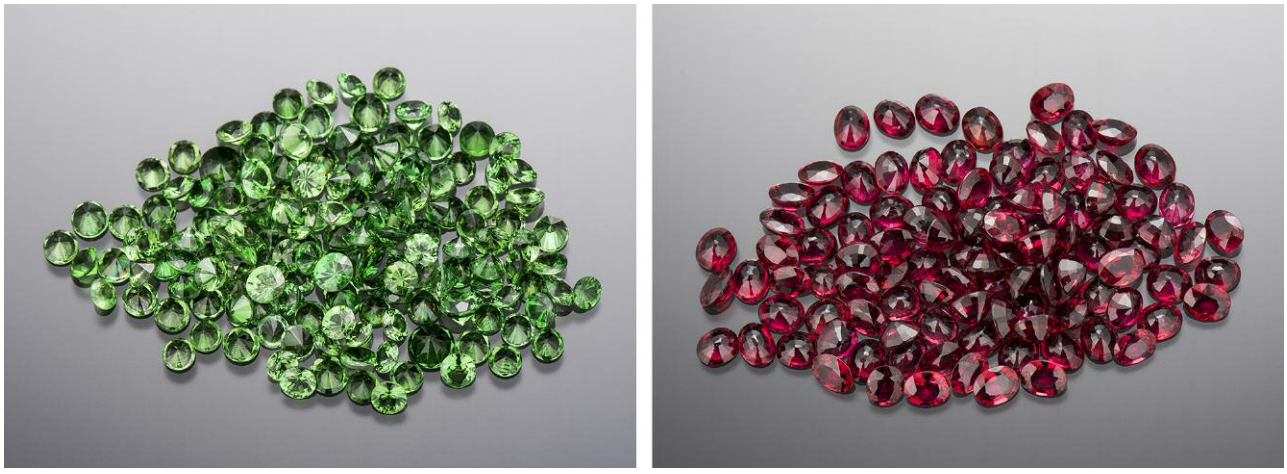

spinel (figure 22, right) and fancy sapphire from the same area where she mines tsavorite.

Tao Hsu and Andrew Lucas

Turquoise from western Arkansas. At their AGTA booth, Avant Mining (Jessieville, Arkansas) displayed an unexpected material: turquoise from Polk County, Arkansas. According to owner James Zigras, this is the only gem-quality turquoise deposit in the U.S. located outside the Southwest. Calibrated goods and specimens ranging from blue-green to greenish blue were on view (figure 23). Also at the booth was a 245 lb. boulder unearthed in 1982 and polished in 2018 by Michael Beck (Copper Canyon Lapidary & Jewelry, Sedona, Arizona). The boulder, shown in figure 24, is the largest known American turquoise nugget.

The source was first mined from 1978 to 1986 under a previous owner, but the material was likely sold as Southwestern turquoise. During these years, there was too much competition in the market for stabilized turquoise, and activity eventually ceased. In 2017, Zigras bought the previous owner's estate, which included two tons of turquoise rough, and restaked a claim on the original mining site. He expected the source to yield planerite and was surprised to find that the material was close to ideal for the turquoise end member of the planerite-turquoise solid solution series. In January 2018, a test trench was worked for seven days. In that time, the deposit produced approximately 1,000 lbs. of turquoise and an old mine shaft was uncovered. Veins are located about 10 feet below the surface (see video at https://www.gia.edu/gems-gemology/spring-2018-gemnews-turquoise-from-western-arkansas). Quartz crystals and wavellite are also found in the deposit.

Figure 23. Recent production from a reactivated turquoise deposit in Polk County, Arkansas. The beads shown here measure up to 25 mm in diameter, while the largest cab weighs 30 ct. Photo by Robert Weldon/GIA.

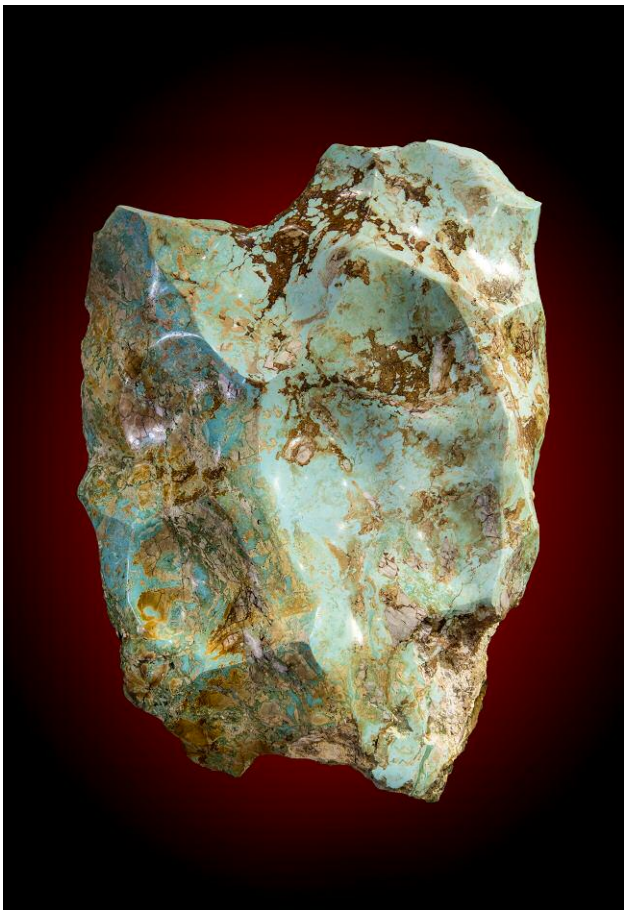

Figure 24. This 245 lb. boulder of turquoise, removed from the Polk County deposit in 1982, is the largest known American turquoise nugget. Photo by Robert Weldon/GIA.

Zigras indicated that the turquoise is impregnated but not dyed. Independent testing at GIA confirmed impregnation; no evidence of dye was detected on the samples. Zigras plans to submit the material for Zachery treatment, a process designed to improve the polish and color of turquoise. It will be interesting to see this source's output in the coming years.

Jennifer-Lynn Archuleta and Nathan Renfro
GIA, Carlsbad

Unheated and unusual colors. Margit Thorndal of Madagascar Imports, Ltd. (Laurel, Montana) was one of several AGTA vendors carrying small stones in today's hottest colors. Thorndal showed two of her most popular stones from Madagascar: lavender spinel from the Bekily region and purple sapphire from Ilakaka (figure 25). Both materials are unheated and represent unique colors, particularly the lavender spinel.

Figure 25. Madagascar Imports exhibited an array of small unheated stones, including 3.3 mm round brilliant lavender spinel from the Bekily region (left), and 2.5 mm round brilliant purple sapphire from Ilakaka (right). Photos by Jennifer Stone-Sundberg.

Thorndal indicated that buyers appreciate the unheated and nontypical colors. Along with purple stones from Madagascar, she has been doing very well with pink and orange Malaya garnet from the Bekily region and bright yellow-green demantoid. The rough from Madagascar is all precision cut by hand into melee at a single facility in Bangkok. The finished stones are used by designers creating one-of-a-kind pieces, jewelers performing custom work, and manufacturers producing higher-end goods. She also showed a suite of 21 unheated Ilakaka sapphires totaling 22 carats that displayed attractive pastel hues (figure 26).

Another item that has been doing very well for Madagascar Imports is unheated Montana sapphire, particularly in teal hues, a sentiment echoed at many other AGTA booths. There is strong demand for American gemstones, particularly untreated ones.

Jennifer Stone-Sundberg
Portland, Oregon

Vibrantly colored gems. Pala International (Fallbrook, California) reported a very strong AGTA show, a common sentiment among vendors there. This was clearly evident to us, as many buyers were actively looking at and purchasing items while we were at the booth. Popular colors on display at Pala matched what we saw elsewhere at the show: electric blues, teals, hot pinks, hot yellow-greens, and pastels.

When asked what was new, Bill Larson showed us a suite of spectacular sphenes mined in 2017 from Zimbabwe, ranging in size from about 5 to 40 ct (figure 27, left). The response to this material was very positive, and one of the pieces had already sold on the first day of the show. Larson also showed us two exceptionally fine purple sillimanites (figure 27, right).

Electric blue stones were popular throughout the show, either loose or in jewelry items. At the Pala booth we noticed many examples such as blue zircon and chrysocolla (figure 28), as well as Paraíba tourmaline and neon apatite.

Figure 26. Suite of 21 unheated Ilakaka sapphires, approximately 1 ct each. Photo by Jennifer Stone-Sundberg.

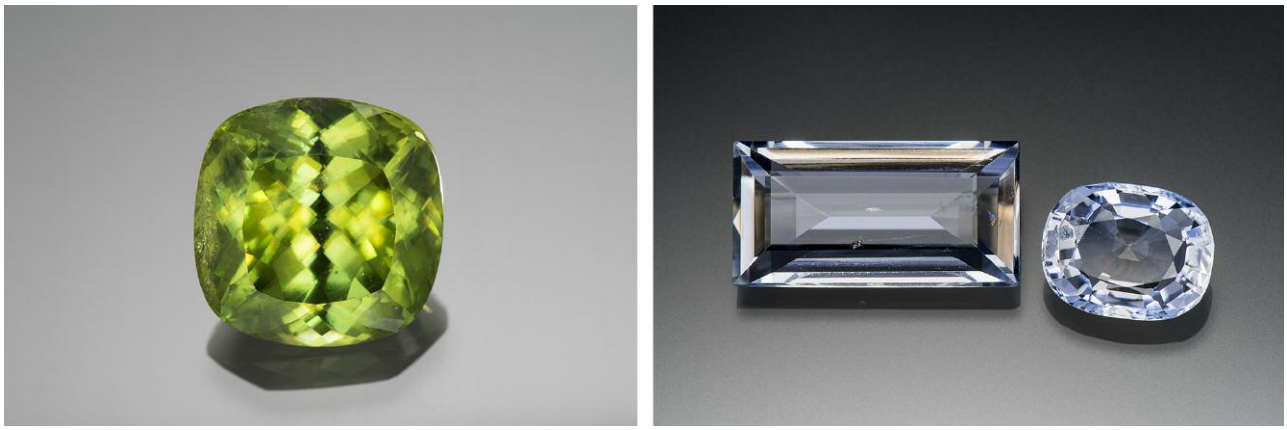

Figure 27. Left: A 24.96 ct cushion-cut sphene from Zimbabwe. Right: Two exceptionally fine sillimanite gems: a 10.39 ct baguette from Sri Lanka and a 4.81 ct cushion cut from Myanmar. Photos by Kevin Schumacher.

Also popular were electric pinks in the forms of rhodochrosite, pezzottaite, sapphire, and spinel.

Non-nacreous pearls were also to be found in both the AGTA and GJX shows, such as the large round Melo pearl offered by Pala (figure 29).

Jennifer Stone-Sundberg and Kevin Schumacher

CUTS AND CUTTING

Michael Dyber's innovative gem carving. Michael Dyber (Rumney, New Hampshire) discussed how 30 years as a gem artist have influenced his techniques and informed the creation of his optically stunning carvings (figure 30). He believes his method is a gift, one from the heart, and knows that his approach would not suit everyone's style.

Dyber prefers to pay premium prices for flawless material, as flaws that cannot be removed during preforming affect the polished piece's entire appearance. He finds sourcing rough to be a challenge and buys select pieces rather than lots of material. He also makes his own tools in his studio. When starting a piece, he chooses the rough by intuition and begins preforming the stone on a large grinding wheel by removing sharp edges and letting the lines and sides join together naturally. After preforming, he sits at the wheel with his handmade diamond tools and looks for inspiration in the piece, which he might find in the shape or an inclusion.

"So instead of trying to force a design into the stone," Dyber explains, "what I end up doing is sitting and looking at it and deciding, 'Let's start here,' and not having to think about where it's going to go. By doing this, and having this open-minded, I'm not confined." Dyber works with the stone in three dimensions—from the front, back, and sides—without any dopping or affixing to a surface. He holds the stone throughout, even during the four-hour process of drilling each one-millimeter hole into a piece (figure 31); this allows for a more continuous workflow. He noted that the pre-polish is the most important step of all. Carving can be finished quickly, but the pre-polish requires a great deal of patience or else the scratches will remain in the piece for good. Over the past three decades, he has managed to reduce pre-polishing from six steps to three. While the work is time consuming, Dyber finds his work emotionally satisfying, because he gets to see the potential of the rough transform into the finished piece.

In the future, Dyber wants to keep refining his techniques so that his pieces stay simple without losing their dynamic. "That's the excitement of the work, what drives

Figure 28. Electric blues were seen, including a 36.11 ct blue zircon from Cambodia (left) and a 23.90 ct chrysocolla mined in the 1950s from the Old Globe mine in Miami, Arizona (right). Photos by Kevin Schumacher.

Figure 29. A large Melo pearl from Vietnam (43.40 ct). Photo by Kevin Schumacher.

me on. Just changing something I've done for years and seeing how it turns out. Sometimes it's that simple."

Duncan Pay and Jennifer-Lynn Archuleta

Rex Guo: The science and art of recutting fine gemstones. Deciding how to cut a gemstone is inevitably one of the most difficult decisions when transforming a piece of rough into a fine faceted gem. The three main factors to consider are final carat weight, color, and light performance (a general term describing the brilliance and scintillation of a faceted stone). In most cases, optimizing one of these factors comes only by sacrificing something else. This is especially true for light performance, which often suffers at the expense of carat weight. The colored stone market has historically demanded that cutters produce goods with the highest possible weight in the finished stone. This often leads to cuts that are not designed to optimize light performance. In recent years, however, there has been an increasing demand in the high-end colored stone market for precision cuts and optimized light performance. This year at Tucson we had the chance to sit down with Rex Guo, whose Singapore-based Sutra Gems focuses on sourcing and systematically recutting faceted stones to unlock their inner beauty.

Guo is a self-taught gem cutter who came into this profession after spending 20 years working with computer graphics and video editing software. In 2015, he decided to take a sabbatical from software to pursue his passion for gemstones. The seed of his passion was planted during childhood, when he discovered an amethyst geode among a pile of sand in his schoolyard. This inspiration stuck with him and was fueled by years of formal engineering studies, which now serve as the backbone of his lapidary art. This technical foundation led to his realization in 2016 that optimizing the interaction of light with a faceted gemstone was exactly the sort of problem he had been working on for 20 years in 3D graphics software. Guo's mathematical mentor, the late Professor Timothy "Geometeer" Poston, was the inspiration for one of his latest creations, currently featured in the *Somewhere In The Rainbow* exhibit at the University of Arizona Gem and Mineral Museum. The Geometeer (figure 32), dedicated to Poston, is a precision-cut synthetic ruby in an innovative hybrid brilliant-Portuguese cut designed with Guo's proprietary gem design and optical simulation software, Axiom.

While Guo enjoys the privilege of cutting from fine gem rough, about 80% of his work is in recuts. Given the ever-increasing price of rough material, recutting provides an opportunity to work with very fine material that would otherwise be difficult to obtain. He starts with excruciat-

Figure 30. For 30 years, Michael Dyber has designed and fashioned gems, such as this aquamarine, in ways that please the eye and amaze the connoisseur. Photo by Albert Salvato.

Figure 31. Each hole Dyber drills into a gem, as in this Brazilian green beryl, can take up to four hours to complete. Photo by Albert Salvato.

Figure 32. The Geometeer, a synthetic ruby cut in a hybrid Portuguese-brilliant design, is dedicated to Rex Guo's mathematics professor and mentor, Dr. Timothy Poston. Photo by Rex Guo.

ingly accurate measurements of the geometry of the original faceted stone. Every angle of every facet must be recorded for input into Axiom. This software allows him to experiment with many possible recut designs to see how changing any single facet will affect the appearance of the final stone. Guo works very closely with his clients in this stage of the process to ensure they are getting what they want out of the recut. There are multiple paths that can be taken. The stone can be recut with an emphasis on saving weight, or a bolder design can be chosen with better light performance to bring out the stone's inner beauty, but with more significant weight loss. At this point Guo finds he has to walk a fine line between presenting himself as a master craftsman and as a scientist. While diagrams from his software are useful to show clients various options, he avoids coming across as overly technical so as not to detract from the emotional and romantic aspect of his craft. He quips, "Machines and software don't understand beauty—humans do."

Figure 33. Guo's light performance–optimized unheated blue sapphire. Photo by Rex Guo.

Guo is very much on a journey through the world of gemstone faceting. He started with round patterns, as most cutters do. Once he understood rounds, he moved on to optimizing trilliant and oval cuts. In the future, he plans to experiment with squares, rectangles, and more. The light performance–optimized cuts in which he specializes are best exhibited in high-RI materials. For this reason, he has set a minimum refractive index of 1.72 for stones he works with, a playing field that includes spinel, zircon, garnet, ruby, and sapphire (figure 33). Test cuts are often used before recutting important stones.

Spinels are one of his favorite stones to cut. The high RI and rich color of fine spinel produce stones that are "just divine." Zircons are another favorite, as they have a much higher RI than most other natural stones. With such a cornucopia of gem materials in front of him, Rex Guo's lapidary journey has just begun.

Aaron C. Palke
GIA, Carlsbad

Wim Vertriest

JEWELRY DESIGN

Designs from Erica Courtney. Erica Courtney has been adorning Hollywood stars for the red carpet for decades. Her eye for color and bringing out a stone's beauty are immediately apparent. In talking to her at the AGTA show, we discovered that she is the only jeweler in her family. She was introduced to jewelry making at the age of 11 through a Catholic Youth Organization class. This multiple AGTA Spectrum Award winner has always done things her own way, not following trends when choosing stones or creating designs. In fact, she confided that she does not plan what stones she will purchase, but lets the gems pick her. She likened the jewelry design process to a movie going through her head—designs start forming and keep changing until she settles on the final one.

Courtney's work pulls the viewer in to study meticulous details—the more you look, the more you see. Her attention to detail does not stop at the outward-facing front of her pieces. You need to turn the pieces around in all directions to appreciate the designs that spill over the edges and cover the sides and backs of her work. Returning to her point about the gems picking her, she stated that once a gem seduces you, "if you buy for love, you can't make a mistake." This is evident in the centerpiece stones in four of her creations. The Victoria pendant (figure 34, left) contains a 114.56 ct colorless topaz accented with a Tanzanian spinel from Mahenge and surrounded by more spinel plus rubellite, Mandarin garnets, and diamonds in an intricate gallery work. In the Autumn pendant (figure 34, right), a 47.16 ct Malaya zircon is surrounded by Tanzanian peach spinel, topaz, yellow sapphire, and diamonds. The Etoile ring's green African Paraíba-type tourmaline is flanked by blue Brazilian Paraíba tourmalines and diamonds (figure


Figure 34. Left: Erica Courtney's Victoria pendant showcases a 114.56 ct colorless topaz with a 2.76 ct Mahenge spinel set above it, surrounded by 86 Mahenge spinels, 20 rubellites, 10 Mandarin garnets, and 558 diamonds. Right: The Autumn pendant contains a 47.16 ct Malaya zircon accented with 3.91 carats of Tanzanian peach spinel, 7.00 carats of peach topaz, 1.31 carats of yellow sapphire, and 1.68 carats of diamond. Photos by Kevin Schumacher.

35, left), while the Imperial earrings (figure 35, right) contain perfectly color-matched Mandarin garnets flanked by pink spinel and diamonds. She confided that the electric orange and pink in the Imperial earrings was her favorite color combination of these four pieces.

Courtney's desire to understand the entire gem cycle from unmined rough to polished stones set in finished jewelry has taken her backpacking across far-flung locations. She described the experience as giving her an appreciation of how difficult it is to find real gems. She also took notice of the passion of the miners, each wanting to be "the one to have found it."

Jennifer Stone-Sundberg and Andrew Lucas

Preview of *Nature Art Science* with Paula Crevoshay. Paula Crevoshay described 2018 as an "opulent year" and showed us several new pieces that celebrate nature. Her remarkable use of color draws in and enchants the viewer.


Figure 35. Left: Courtney's Etoile ring has a 7.71 ct Paraíba-type tourmaline accented with 12 Paraíba tourmalines and 370 diamonds, all set in 18K yellow gold. Right: The Imperial earrings feature a pair of Mandarin garnets (21.25 total carat weight) accented with 1.87 carats of pink spinel and 0.71 carats of diamond in 18K yellow gold. Photos by Kevin Schumacher.

Figure 36. Left: Paula Crevoshay's Siberian tigress Baianai incorporates aquamarine eyes with black diamond pupils, 286 white diamonds, 168 cognac diamonds, and a 1.05 ct pink Oregon opal in 18K gold. Right: The "Morning Glory" brooch contains 272 Yogo sapphires, 90 purple sapphires, 45 pink sapphires (2.75 carats), and a 2.92 ct central moonstone, all in 18K gold. Photos by Kevin Schumacher.

She is working on a museum exhibition concept entitled *Nature Art Science*, with the intent of capturing how art is inspired by nature and how science is essential in the execution of art. Her work illustrates this concept, as the lifelike flora and fauna creations maximize the use of color and light while being solidly engineered and highly versatile.

Crevoshay displayed several realistic pieces depicting endangered animals, including the Siberian tigress Baianai (figure 36, left), whose mesmerizing eyes are composed of aquamarine with black diamond pupils. Baianai's nose is a hand-carved pink Oregon opal, and the rest of the 18K yellow gold jewel contains 286 white and 168 cognac diamonds. The hardware is engineered to allow the piece to be worn in many different ways. There are lush new flowers from Crevoshay such as the Morning Glory brooch (figure 36, right), which draws the observer into its center with an adularescent moonstone surrounded by a sea of 272 blue Yogo sapphires. The hue shifts toward purple and pink with the use of 90 lavender and 45 fuchsia sapphires from the tips of the petals to the center.

Crevoshay's first cuff of 2018 (figure 37, left) is titled Moon Glow and features moonstones as well as blue zircon, iolite, and blue sapphire. She likened it to "painting with light." Another piece that spoke to this concept was a pendant containing a large and exceptionally fine 30.64

Figure 37. Left: Crevoshay's Moon Glow cuff contains 72.28 carats of moonstone, 36.68 carats of blue zircon, 8.58 carats of iolite, and 3.47 carats of blue sapphire in 18K gold. Right: The Gelila pendant features a 30.64 ct Ethiopian opal surrounded by blue zircon, pink tourmaline, tsavorite, apatite, ruby, and diamond melee. Photos by Albert Salvato.

ct Ethiopian opal (figure 37, right). The flanking of the opal's intense play-of-color hues with like-colored surrounding stones such as blue zircon, pink tourmaline, tsavorite garnet, apatite, and ruby made for a stunning and very aesthetically pleasing piece. Both works showcased many of the most popular hues we observed throughout the AGTA show.

Talking with the artist, we learned that her father was an engineer, an exposure that led her to design all of her own mechanisms (such as hinged bales), allowing the pieces to be worn in many ways, such as a pendant or brooch. From an artistic standpoint, Crevoshay has drawn inspiration from Schlumberger, Fabergé, and Lalique. Their influence is evident in her designs that are simultaneously intricate and fluid, while focusing on the use of light with the color of the incorporated materials. From the mesmerizing and magnificent details such as the hand-carved Oregon pink opal nose of her tigress to side stones mimicking the play-of-color of a precious opal, it is easy to understand why her work has attracted such a following.

Jennifer Stone-Sundberg and Andrew Lucas

RESPONSIBLE PRACTICES

Update from the Responsible Jewellery Council. The Responsible Jewellery Council (RJC) has announced plans to include colored stones and silver in the next revision cycle for its Code of Practices, which RJC members are certified against. The organization has begun updating its existing standards, a process that takes place every five years. These plans dovetailed with the release of the United Nations' 2030 Agenda for Sustainable Development, which outlines 17 goals and 169 targets for member nations to meet. The author sat down with Edward Johnson and Anne-Marie Fleury of the RJC during the 2018 Tucson gem shows to discuss the status of these efforts.

The first round of public consultation, which focused on the scope of changes to the standard, took place in 2017. As of February 2018, RJC's Code of Practices were under review prior to a second public consultation phase, which targets industry and non-industry stakeholders, of proposed changes to the Code. These consultation phases are in line with RJC's annual auditing of their standard-setting approach, assurance framework, and measuring impacts program.

Like previous versions, the revised Code will certify business practices rather than products. The certification will cover all the important social, environmental, and health and safety issues in the jewelry supply chain. RJC's priorities for change, which must work for businesses of all sizes, involve several areas, including:

- Due diligence for responsible sourcing: RJC recognizes that traceability does not automatically translate to sustainability. As a standard for alignment with the Organisation for Economic Co-operation and Development, RJC encourages companies to adopt a due diligence approach to managing risks in their supply chain. Traceability remains a powerful tool for making responsible sourcing claims and is a voluntary certification option.
- Gender equality: RJC endorses best practices that promote diversity, including gender equality. To this end, it is partnering with Business for Social Responsibility (BSR), a nonprofit organization dedicated to sustainable business practices, to develop better guidance on gender equality in the gem and jewelry sector. Topics to be covered include working conditions, facilities, and approaches to family leave.
- Updating requirements on responsible mining: Many of the most challenging issues in the industry occur at the mining stage, and RJC continues to evolve its responsible mining provisions to address these challenges.
- Reducing audit duplication: As it continues to work with jewelry industry members of all sizes, RJC continues to harmonize with and cross-recognize other industry initiatives already in place from other organizations so that businesses do not have to duplicate efforts at their own cost.

The consultation phase of the Code of Practices review is scheduled to run from April to July 2018. Announcements about the process can be found at https://www.responsiblejewellery.com/standards-development/code-of-practices-review-2/.

Jennifer-Lynn Archuleta

Supply chain transparency and beneficiation. As the industry sees technology become more involved in daily gem trading and responsible sourcing has become a hot topic, Jean Claude Michelou, the editor-in-chief of *InColor* and a veteran of the industry, shared his perspective about supply chain transparency, beneficiation in source countries, and recent development of a Nigerian sapphire mining project.

While the diamond industry is already applying the blockchain concept, Michelou believes it is also the future of the colored stone counterpart. Blockchain and cryptocurrency both have the potential to increase the transparency of the colored stone supply chain by digitally recording all trading activities between different parties involved in the gem trade. He pointed out why miners, dealers, big brands, and consumers all need more transparency. The big jewelry brands especially need transparency to reinforce brand image and consumer confidence. Therefore, he expects the real changes will start with these companies, and gradually other players will be drawn in.

Michelou also sees the impending shortening of the supply chain, especially as new technologies such as mobile devices become readily available even in the very remote mining areas. Even though many do not welcome

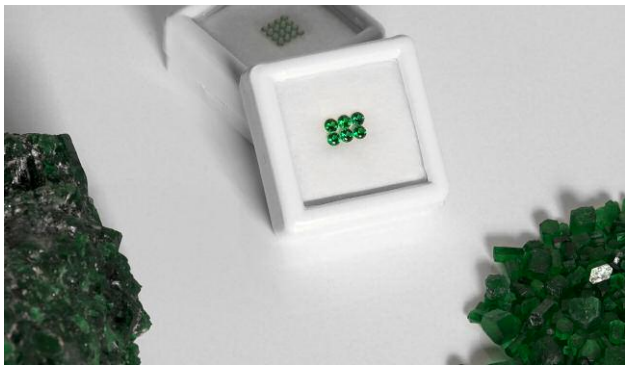

Figure 38. Swat Valley emerald yields fine precision-cut stones in small sizes. Photo by Albert Salvato.

the disappearance of the middleman between the supplier and the end consumers, it is unavoidable if no extra value can be added other than sharing the margin with both ends.

For the past decade, Michelou has taken part in several beneficiation projects initiated by multiple organizations. One project he is highly involved with is in the Swat Valley emerald deposits of Pakistan. Before he joined this project, a partnership between the local miners and a foreign company worked quite well for a three-year period. The company bought all the finished stones that were cut and faceted by local cutters. When this partnership stopped for unknown reasons, Michelou was contacted by locals who knew of his expertise.

There are three mines in Swat Valley. The one that this project is working on has about 80 to 100 individual tunnels. Trained local women, usually the wives of miners, can handle 1.5–3.0 ct round brilliant cuts very well. Michelou became the liaison between them and a luxury jewelry brand in Europe that offered these women training and paid them a $500 per month salary. If these rough emeralds were transported to Jaipur for faceting, the cost would in fact be lower. However, the luxury brands are willing to pay more to guarantee a transparent supply chain since it enhances their brand image for consumers who care about where the stones are from. It also improves their reputation with the local people. Even though many rough stones are still exported to other countries for further processing, at least a portion of them stay in Pakistan for services that benefit the community through employment and added value to the resource (figure 38).

Finally, Michelou talked about his involvement in a Nigerian sapphire mining venture. Although the project was delayed for eight months, it will be a large-scale operation with two washing plants. The first plant will have a washing capacity of 50 tons per hour. From his time spent in Nigeria and Pakistan, Michelou has rich experience working with the people at the source. He said that understanding the local culture is very important for any company or individual wanting to start a gem mining or trading enterprise in these source countries. His personal experience has told him that trying to adapt the local people to the Western way of doing business is a challenge, especially at the beginning stage of the collaboration. One must gradually prove to the locals that a different approach can produce results that will benefit them tremendously, and this will help to change their mindset.

Tao Hsu and Andrew Lucas

ANNOUNCEMENTS

Gianmaria Buccellati Foundation Award for Excellence in Jewelry Design. The first annual Gianmaria Buccellati Foundation Award for Excellence in Jewelry Design was presented on February 2, 2018, to GIA graduate Catherine Zheng (figure 39). The competition, open to students who successfully completed the GIA Jewelry Design course in 2017, recognizes artistic excellence in jewelry design. Zheng received the award for her rendering of an Art Deco–inspired pendant necklace. Zheng, who studied at GIA in Carlsbad, was one of 12 finalists from seven campuses whose hand-rendered designs were judged by a committee comprised of jewelry design, manufacturing, retail, and media experts. The finalists' designs were on display and the recipient of the award was announced at the annual GIA alumni party held during the AGTA Gem Fair in Tucson.

The Gianmaria Buccellati Foundation sponsored the award as a way to inspire beginning jewelry designers and honor the work of the renowned jewelry design house's founder, Gianmaria Buccellati. The 2018 competition is under way and open to students in GIA's Jewelry Design course who meet the eligibility requirements.

Figure 39. Gianmaria Buccellati Foundation Award winner Catherine Zheng (center), with GIA president and CEO Susan Jacques and Gianmaria Buccellati Foundation chief officer of North American strategies Larry French. Photo by Kevin Schumacher.

2018 Tucson Photo Gallery

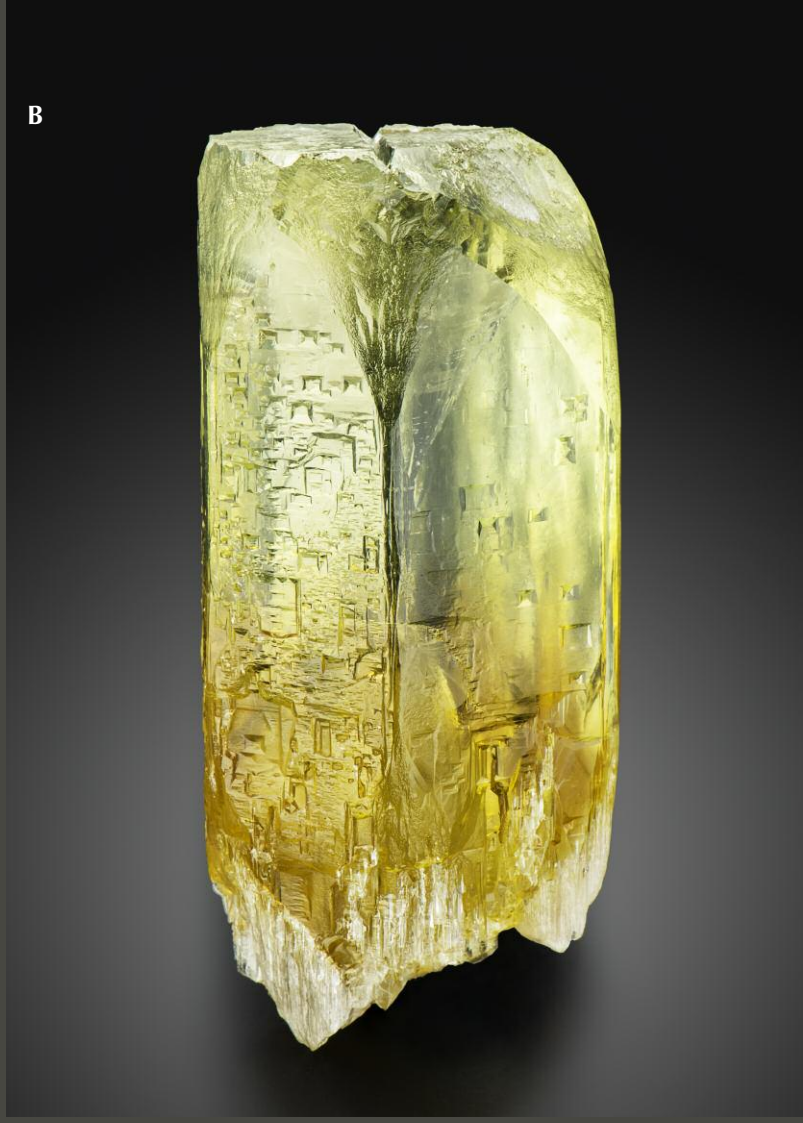

A: Bicolor tourmaline frog carving by Daniela Becker. Photo by Robert Weldon/GIA, courtesy of William Larson. B: Bicolor beryl from Ukraine. Photo by Robert Weldon/GIA, courtesy of Quarts Samocveti. C: Emeralds from Zarajet, Afghanistan, 23.43 ct and 4.46 ct. Photo by Robert Weldon/GIA, courtesy of Himalayan Gems and Jewelry. D: 54.07 ct carved moonstone. Photo by Emily Lane, courtesy of K&K International. E: Ethiopian sapphire. Photo by Emily Lane, courtesy of Michael Couch.

F

G

H

I

J

F: Rough bicolor topaz, 1.907 kg, from Ukraine's Volyn deposit. Photo by Robert Weldon/GIA, courtesy of Quarts Samocveti. G: Lavender jade carving. Photo by Emily Lane, courtesy of Mason-Kay. H: 7.72 ct black opal from Lightning Ridge, Australia. Photo by Robert Weldon, courtesy of Bear Essentials. I: 34.22 ct cushion-cut peacock sapphire from Sri Lanka. Photo by Robert Weldon/GIA, courtesy of Crown Color. J: Green and ice jade ring. Photo by Emily Lane, courtesy of Mason-Kay.

K: 10.8 ct emerald-cut bicolor sapphire. Photo by Robert Weldon/GIA, courtesy of Mayer and Watt. L: Gold-in-quartz from the Red Bank mine in California. Photo by Robert Weldon/GIA, courtesy of Stonetrust. M: 15.69 ct emerald-cut rhodochrosite from Colorado's Climax mine. Photo by Robert Weldon/GIA, courtesy of Beija Flor Gems. N: The beryl variety vorobyevite, from Badakhshan Province, Afghanistan. Photo by Robert Weldon/GIA, courtesy of Stonetrust. O: "Tarugo" rubellite measuring 85 cm and weighing 82 kg (180 lbs.) from the Jonas mine in Minas Gerais, Brazil. Beside it are Richard Freeman (left) and James Elliott (right). Photo by Robert Weldon/GIA, courtesy of E.F. Watermelon and Co.

REGULAR FEATURES

COLORED STONES AND ORGANIC MATERIALS

Aquamarine from Pakistan. In recent decades, a steady supply of aquamarine has come from northern Pakistan, an increasingly important mining locality. The aquamarine was mined mostly from the Gilgit-Baltistan region, including the Shigar Valley, as well as the Hunza and Braldu Valleys (figure 40). The aquamarine occurs in zoned pegmatites formed by hydrothermal fluids in the cavities or veins (M.H. Agheem et al., "Shigar Valley gemstones, their chemical composition and origin, Skardu, Gilgit-Baltistan, Pakistan," *Arabian Journal of Geosciences*, Vol. 7, No. 9, 2014, pp. 3801–3814).

Most aquamarines from northern Pakistan show a long hexagonal prism habit and can reach up to a dozen centimeters in length (figure 41). Albite, muscovite, and tourmaline (schorl) are commonly associated as matrix, and most of these are collected as mineral specimens. Parts of them are gem quality and suitable for jewelry use.

Aquamarine samples from the Shigar Valley were obtained from local merchants who deal with Pakistani material. The samples displayed colors ranging from pale greenish blue and pale blue to nearly colorless, with a translucent to transparent appearance. The samples measured 1–2 cm in length and 0.5–1 cm in diameter. To explore the gemological and other properties of these samples, six of them (figure 42) were investigated by standard gemological methods as well as spectroscopic and chemical analyses at China University of Geosciences (Wuhan).

The following gemological properties were recorded: RI—n_o = 1.574–1.580, n_e = 1.569–1.575; birefringence—0.005–0.006; SG—2.60–2.72; UV fluorescence—weak bluish white to both long- and short-wave UV. The moderate to weak dichroism observed was a relatively saturated blue or greenish blue along the e-ray and very pale blue, greenish blue, or near-colorless along the o-ray.

Microscopic observation revealed abundant 20–300 μm inclusions, either two-phase (fluid, gas) or three-phase (one or two types of fluid, solid, gas) with various shapes. The irregularly shaped multiphase inclusions often gathered together to form a complex "fingerprint" network distributed along healed fissure planes (figure 43, top row). In addition, two-phase inclusions with elongated shapes parallel to the c-axis, and with hexagonal outer profiles perpendicular to the c-axis, were consistent with the crystalline symmetry of beryl (figure 43, bottom row).

These two kinds of multiphase inclusions formed by different crystallization processes. When the beryl crystal-

Figure 40. Map of the Gilgit-Baltistan region in northern Pakistan showing the main aquamarine deposits of the Hunza, Braldu, and Shigar Valleys.

Figure 41. The aquamarine crystal on feldspar from the Shigar Valley in Pakistan measures 17 cm tall. Photo by Joe Budd, courtesy of Arkenstone.

lized out of a hydrothermal fluid, some of the fluid was trapped. With dropping temperature during mineralization, beryl was re-deposited and a gaseous phase was released from the fluid, gradually forming single multiphase inclusions whose shape conformed to beryl's hexagonal symmetry. But the formation of multiphase "fingerprint-like" inclusions with irregular shape occurred later. Fluid was embedded in the fracture of the beryl crystal. Due to the solution and re-deposition of beryl from fluid on the fracture surfaces, a small amount of liquid and released gas were gathered and closed off, just like "fingerprint" or dendritic growth networks along healed fissure planes. For a detailed description of these processes, please refer to E. Roedder, "Ancient fluids in crystals," *Scientific American*, Vol. 207, No. 4, 1962, pp. 38–47.

Large amounts of multiphase inclusions could lead to a misty, translucent, and uneven appearance, such as the aquamarine crystal in figure 41, with a misty translucence toward the bedrock end. Generally, these characteristics can also be seen in aquamarine from other deposits in Brazil, the United States, South Africa, and China (D. Belakovskiy et al., *Beryl and Its Color Varieties: Aquamarine, Heliodor, Morganite, Goshenite, Emerald, and Red Beryl*, Lapis International LLC, East Hampton, Connecticut, 2005).

Multiphase and mineral inclusions were identified by Raman spectroscopy with 532 nm laser excitation. The gaseous phase was identified as a mixture of CO_2 and a small amount of methane (CH_4), and the fluid inclusion consisted of water with dissolved CO_2 or liquid CO_2. Solid phases inside the multiphase inclusions were identified as solid sulfur

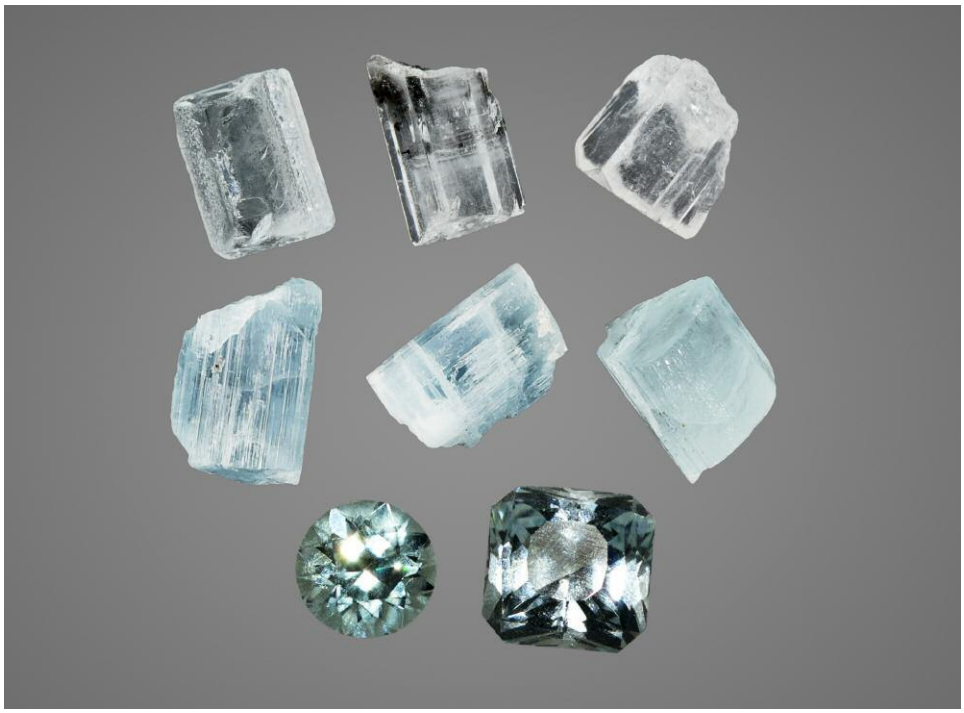

Figure 42. Six rough and two faceted aquamarines from Shigar Valley. The rough samples range from about 5 to 10 ct. The round brilliant cut weighs 3.82 ct, the square cut 7.91 ct. Photo by Yang Hu.

and orpiment. Along with columnar tourmaline, white albite, and flaky muscovite, other mineral inclusions such as orange-red almandine, brown tantalite, and yellow argentojarosite [$AgFe_3(SO_4)_2(OH)_6$] were identified by Raman.

Chemical analysis on aquamarine samples by laser ablation–inductively coupled plasma–mass spectrometry (LA-ICP-MS) showed the following ranges for alkali elements: Li 70–1240 ppmw, Na 830–3970 ppmw, K 54–453

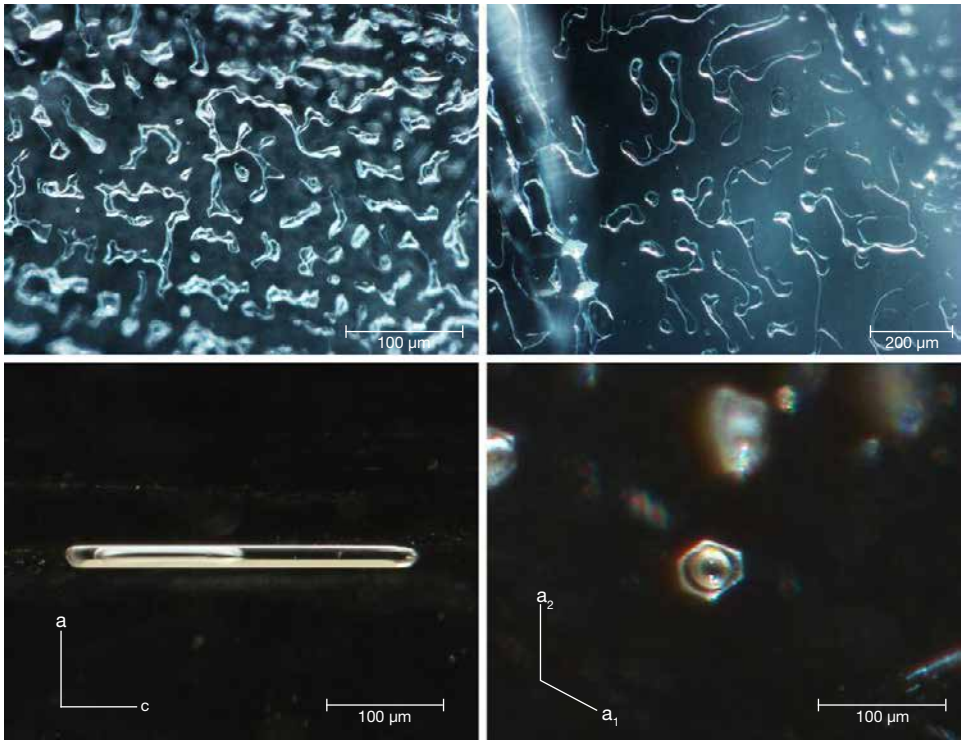

Figure 43. Multiphase inclusions in aquamarines from Shigar Valley. Top: Abundant two-phase and multiphase inclusions with irregular shape showing complex "fingerprint" networks. Bottom left: An elongated two-phase inclusion parallel to the c-axis. Bottom right: The same inclusion (shown in the bottom left image) viewed down the c-axis, presenting a perfect circular gas bubble and hexagonal outer profile consistent with the crystalline symmetry of beryl. Photomicrographs by Yang Hu.

Figure 44. Phenakite with beryl in mica (left) and yellow phenakite (right). Photos by Mikhail Popov; fields of view 5 cm.

ppmw, Rb 10–64 ppmw, and Cs 310–3220 ppmw. The amount of total alkali content including Li, Na, K, Rb, and Cs ranged from 1296 to 6033 ppmw. As alkali ions (mainly for Na) were associated with "type II" water molecules in structural channels (D.L. Wood and K. Nassau, "The characterization of beryl and emerald by visible and infrared absorption spectroscopy," *American Mineralogist*, Vol. 53, No. 5, 1968, pp. 777–800), the relatively low Na content was in agreement with the low peak intensity of "type II" H_2O revealed by Raman and IR spectroscopy. The low concentration of alkali content and lack of "type II" water in our aquamarine samples were similar to that in aquamarine from Italy and Vietnam (R. Bocchio et al., "Aquamarine from the Masino-Bregaglia Massif, Central Alps, Italy," Fall 2009 *G&G*, pp. 204–207; L.T.-T. Huong et al., "Aquamarine from the Thuong Xuan District, Thanh Hoa Province, Vietnam," Spring 2011 *G&G*, pp. 42–48). The chromophore Fe, responsible for blue color, was the richest among all transition elements between 1350 and 5080 ppmw; the samples showed the typical iron absorption at 375, 425, 620, and 820 nm in UV-Vis-NIR spectra. Transition elements V and Mn were present at 1–33 ppmw and 17–56 ppmw, respectively, and the bluish white fluorescence mentioned above may originate from Mn^{2+} or VO_4 centers (M. Gaft et al., *Modern Luminescence Spectroscopy of Minerals and Materials*, 2005, Springer Berlin, pp. 97–99). Chemical and spectral characteristic suggested the Pakistani samples were low-alkali aquamarine colored by Fe ions rather than irradiation (i.e., Maxixe beryl).

Yang Hu and Ren Lu
Gemmological Institute
China University of Geosciences, Wuhan

Color origin of phenakites from the Ural emerald mines. Phenakite (Be_2SiO_4) was first discovered at Russia's Ural emerald mines, and was chemically identified in 1833. The mineral is widely distributed in beryllium deposits, but crystals of gem quality or large size are rare. At the Ural mines, however, there are large transparent crystals that can be used in jewelry. Jewelry-grade phenakite is generally colorless or yellowish brown (figure 44; see M.P. Popov et al., "Features of phenakite mineralization from the Ural emerald mines," *Bulletin of the Ural Branch of the RMS*, No. 13, 2016, pp. 105–111). The main mineral inclusions are chlorite, talc, phlogopite, actinolite, and ilmenite; fluid inclusions with a gas-liquid composition also occur.

The color origin of phenakite using optical absorption spectroscopy has not been studied in detail. Many authors agree that the coloration is associated with electron-hole centers (see A.S. Marfunin, *Spectroscopy, Luminescence and Radiation Centers in Minerals*, 1975, Nedra, Moscow). This is indicated by the disappearance of color when phenakite is exposed to either ultraviolet radiation or high temperatures. According to one theory of absorption, this is related to the oxygen vacancies that have captured electrons (again, see Marfunin, 1975). Other researchers believe that the absorption features are associated with bridging electronic centers such as Al-O-Al, which are formed by isomorphous replacement of silicon by aluminum ions in the crystal lattice, in amounts up to 0.5% (see A.N. Platonov, *Nature of Coloring of Minerals*, 1976, Naukova Dumka, Kiev).

To determine the color origin of yellow-brown phenakites, we obtained optical absorption spectra of colorless and yellow-brown phenakite from the Mariinsky deposit. These spectra were collected in the 185–700 nm wavelength range, at room temperature, on a specialized Shimadzu UV-3600 spectrophotometer. A broad absorption band was noted in the 225–325 nm range of the yellow-brown phenakite spectrum, with a maximum at 268 nm. Absorption in the ultraviolet range of the optical spectrum was not detected in transparent colorless phenakites (figure 45).

To study electron-hole centers and to reveal color centers in phenakite, crystals were examined using electron paramagnetic resonance (EPR). EPR is an informative method for studying dissymmetry of crystals, the role of the symmetry elements of the spatial group, and the distribution of impurity ions and point defects in the bulk of the crystal. Dissymmetry of crystals, as a result of the uneven distribution of point defects in the process of crystal growth, is a widespread phenomenon (see G.R. Bulka et al., "Dissymmetrization of crystals: Theory and experiment," *Physics and Chemistry of Minerals*, Vol. 6, 1980, pp. 283–293; R.A. Khasanov et al., "Derivation of the conditions for equivalent positions in crystals: The dissymmetrization of barite by electron spin resonance," *Crystallography Reports*, Vol. 57, No. 5, 2012, pp. 751–757; J.M. Hughes et al.,

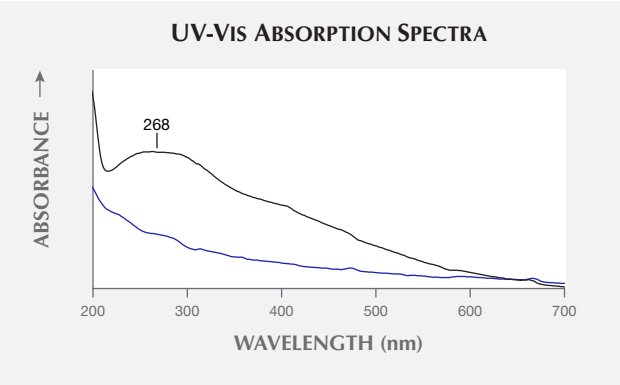

Figure 45. Absorption spectra of colorless phenakites (blue trace) and yellow-brown phenakites (black trace).

"Dissymmetrization in tourmaline: the atomic arrangement of sectorally zoned triclinic Ni-bearing dravite," *The Canadian Mineralogist*, Vol. 49, 2011, pp. 29–40). We used an Adani CMS8400 spectrometer (frequency ν=9, 4 GHz) at room temperature to perform EPR on our samples. During an experiment on the EPR spectra of the impurity radical $[PO_4]^{4-}$ phenakite of deposits in Volynskii (see A.I. Novozhilov et al., "Electron paramagnetic resonance in irradiated phenakite Be_2SiO_4," *Journal of Structural Chemistry*, Vol. 11, 1970, pp. 393–396), we found a difference in intensity of the lines of three magnetically nonequivalent centers for the impurity radical. The paramagnetic center $[PO_4]^{4-}$ was only detected in the yellow-brown crystals (figure 46), and active centers were absent in colorless specimens. From this we concluded that the origin of the yellow-brown color of phenakite is associated with a paramagnetic complex $[PO_4]^{4-}$ that produces absorption bands in the ultraviolet region, which in turn leads to the formation of this color in the mineral.

Figure 46. Phosphorus ions replace silicon ions in a tetrahedral structure to form a $[PO_4]^{4-}$ complex in yellow-brown phenakites. This complex is paramagnetic and gives several signals in the range of 320–340 mT. Splitting of the hyperfine structure of the signal occurs; lines 1, 2, and 3 appear and indicate the existence of the $[PO_4]^{4-}$ radical. When the crystal rotates along its c-axis, it changes the intensity of these lines.

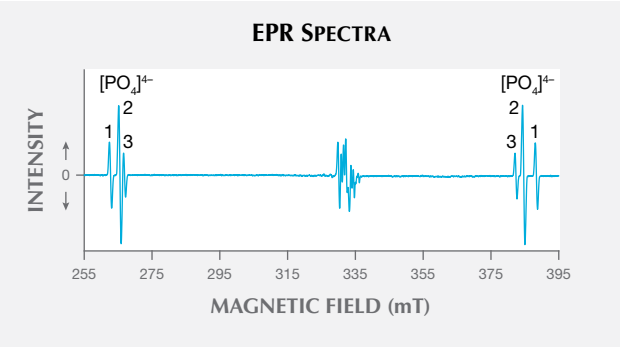

These results can be used in gemological identification of phenakites from the Ural emerald mines.

This study was performed in the context of the Russian Government Program of Competitive Growth of Kazan Federal University, "Paleogeodynamics and evolution of structural-material complexes in the formation of the continental-type crust ...," theme no. 0393-2016-0019.

Anatoliy G. Nikolaev and Nazym M. Nizamutdinov
Kazan (Volga Region) Federal University
Kazan, Russia

Michael P. Popov
Ural State Mining University
Institute of Geology and Geochemistry
Yekaterinburg, Russia

Freshwater natural pearls from the Concho River, Texas. Throughout history, natural pearls have been found in many species of freshwater mollusk in North American lakes and rivers. They are most abundant within the Mississippi River drainage basin, which provides the perfect habitat for these animals because of the large watershed areas with their underlying limestone substrata (J.L. Sweaney and J.R. Latendresse, "Freshwater pearls of North America," Fall 1984 *G&G*, pp. 125–140). Lesser-known sources of natural freshwater pearls are the Colorado River and Brazos River and their tributaries in the state of Texas. However, the best samples are sometimes found in a species named Tampico Pearlymussel (*Cyrtonaias tampicoensis*) that inhabits the Concho River in West Texas.

The mollusk is distributed from northeastern Mexico into the Concho, Colorado, and Brazos Rivers of central Texas and has been collected by licensed harvesters. Mussel harvesting is restricted to hand collection only, and there is a legal minimum shell size requirement. In addition, several areas in Texas have been designated mussel sanctuaries in order to provide protection and species conservation (R.G. Howells, "The Tampico pearlymussel (*Cyrtonaias tampicoensis*), shades of the Old West," http://www.conchologistsofamerica.org/articles/1996/the-tampico-pearlymussel.html). Pearlers find mussels by wading into water that is three to four feet deep and feeling for the shells with their toes. Rattlesnakes on the banks and water moccasins and snapping turtles in the murky water (J. Morthland, "Irregular radiance: The rare beauty of Conch River pearls," *Texas Highways*, April 2015) pose risks to these adventurers searching for gems.

GIA's New York laboratory recently received nine loose pearls from Stone Group Laboratories (Jefferson City, Missouri) for a joint study. The pearls ranged in size from 2.95 × 2.45 mm to 14.76 × 13.55 × 13.13 mm. Reportedly recovered from Tampico pearlymussel shells taken from the Concho River, they exhibited colors ranging from purplish pink to orangy pink. Some of the samples also possessed varying degrees of a brownish hue (figure 47). Most of the

Figure 47. Nine "Concho" pearls examined in this study together with a Tampico pearlymussel shell. The shell measures approximately 12 × 8 cm. Pearls range from 0.12 to 16.59 cts. Photo by Sood Oil (Judy) Chia.

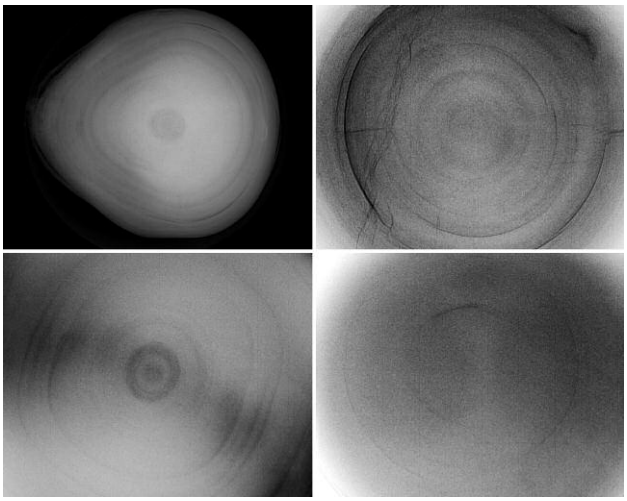

Figure 48. The pearls' internal structures showed typical natural concentric growth arcs, while some also exhibited dark organic-rich centers and natural internal cracks.

small pearls in the group exhibited a dull chalky appearance, with some broken or cracked areas of the nacreous surface. The largest pearl in the group (16.59 ct) showed good nacre condition, a high luster, and noticeable orient on its surface.

The internal structures of the pearls were analyzed by real-time microradiography, and the majority revealed typical concentric natural growth arcs (figure 48). Dark organic-rich centers were also seen in some of the pearls, as well as internal fissures, cracks, or growth boundaries. There were no indications of bead nuclei or non-bead cultured features (irregular linear or void structures). Additional advanced techniques such as X-ray fluorescence imaging and energy-dispersive X-ray fluorescence (EDXRF) spectrometry revealed noticeable X-ray luminescence and high manganese content, confirming the pearls' freshwater origin. Furthermore, Raman spectroscopic analysis of all the pearls detected polyacetylenic compounds (figure 49); these are natural pigments responsible for the colors of many freshwater and some saltwater pearls.

The study provided GIA with a rare opportunity to study this unique group of freshwater natural pearls originating from the southwestern United States. Both gemological and analytical data were consistent with their claimed natural and freshwater origin. Pearls produced from this locality often possess beautiful fancy pink, purple, or lavender colors (Summer 1989 GNI, p. 115; Fall 2005 Lab Notes, pp. 259–260), as demonstrated by these examples.

Figure 49. Raman spectrum of a "Concho" pearl showing polyacetylenic pigment-related peaks at 1130 and 1516 cm^{-1} and peaks at 1086, 704, and 701 cm^{-1} (the latter two a doublet) of structural calcium carbonate in the form of aragonite.

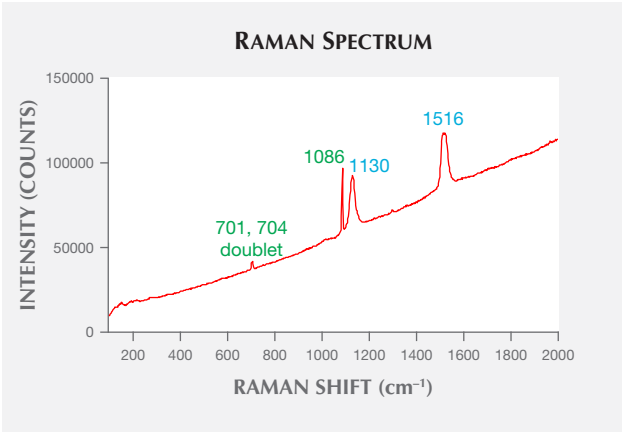

Chunhui Zhou and Emiko Yazawa
GIA, New York

Bear Williams
Stone Group Laboratories, Jefferson City, Missouri

Very small akoya cultured pearls. Akoya cultured pearls are produced by the *Pinctada* genus, specifically *Pinctada fucata* (*martensii*). The mollusk and closely related species are found in the seas off Japan, China, South Korea, and Australia, as well as in the Mediterranean and Arabian Gulf and in the waters of other countries between the Tropic of Cancer and the Tropic of Capricorn such as Vietnam and India.

Akoya pearl farming was first established in the Mie Prefecture in Japan by Kokichi Mikimoto more than a century ago and still exists there to this day. Other suitable lo-

cations in Japan such as the waters off the islands of Shikoku and Kyushu, as well as pearl farms in other parts of the world such as Bai Tu Long and Ha Long Bays in the north of Vietnam and in the waters along the southern coast of China from Leizhou peninsula to the border of Vietnam also produce cultured akoya pearls. The round nuclei are commonly fashioned from freshwater shell imported from the USA (T. Hsu et al., "Freshwater pearling in Tennessee," 2016, https://www.gia.edu/gia-news-research/freshwater-pearling-tennessee). The technicians who insert the nuclei usually surgically maneuver one or two bead nuclei, ranging from 1.5 to 1.7 mm, into position within the gonad using a piece of mantle tissue from a donor mollusk to produce the bead-cultured pearls. Akoya mollusks are typically left in the water for 10 to 14 months. The best harvesting time is in the winter season, when cooler temperatures ensure the mollusks produce nacre slowly and more tightly, yielding the highest luster possible in akoya pearls before any processing is applied. Akoya bead-cultured pearls are typically round and range from 2 to 11 mm in diameter, with the most common sizes between 6 and 8 mm.

During the formation of bead-cultured pearls, the accidental formation of some non-bead cultured pearls (NBC), sometimes referred to as "keshi" pearls, may also take place. Those produced by the akoya mollusk are generally very small (the word "keshi" translates in Japanese to "poppy seed").

GIA's Bangkok laboratory examined a short strand of what were supposedly the smallest commercially produced akoya bead-cultured pearls available today, together with a selection of randomly picked NBC pearls from the same origin (figure 50), all loaned by Orient Pearl Company. The pearls and the shell reportedly came from Vietnam, and the author was informed that the shell used to culture the pearls was *Pinctada fucata* (*martensii*). The graduated strand, consisting of 42 very small bead-cultured pearls, weighed 4.68 ct total, and the pearls ranged from 1.90 to 3.17 mm. Also examined were nine tiny shell bead nuclei between 1.59 and 1.74 mm and weighing 0.30 carats total, as well as 67 loose akoya NBC pearls, ranging from 0.80 mm in diameter to 2.82 × 1.91 × 1.75 mm and weighing 2.31 carats total. The akoya bead-cultured pearls in the strand were round and near-round with a predominantly cream color. The NBC pearls were mostly baroque and predominantly white, with some cream and light gray samples.

Although observation down the drill holes with a loupe indicated bead-cultured pearls, real-time X-ray microradiography (RTX) proved this beyond any doubt. A clear bead nucleus was visible in each pearl (figure 51). Characteristic small voids and/or organic features seen in many bead-cultured pearls were present in some cases between the shell bead nucleus and nacre overgrowth. Banded structure within the beads and/or differences in radio-opacity between the shell bead nuclei and nacre were other characteristic features of bead-cultured pearls noted when the pearls were examined at higher magnification. Measurements of five randomly selected pearls revealed nacre thicknesses from 0.20 to 0.41 mm, within the usual commercially accepted range (0.15–0.50 mm) expected for akoya bead-cultured pearls. The majority of the larger pearls showed very good nacre thickness, and none of them were below the minimum standard that might lead to durability concerns.

Figure 50. The graduated strand of small akoya bead-cultured pearls with nine tiny shell bead nuclei and loose akoya NBC pearls next to a Pinctada fucata (martensii) *akoya shell. Photo by Nuttapol Kitdee.*

Figure 51. RTX analysis revealed the round shell bead nuclei used in the production of the bead-cultured pearls in the strand. A typical-size (7.70 mm) akoya bead-cultured pearl is shown in the center for comparison. Image by Promlikit Kessrapong.

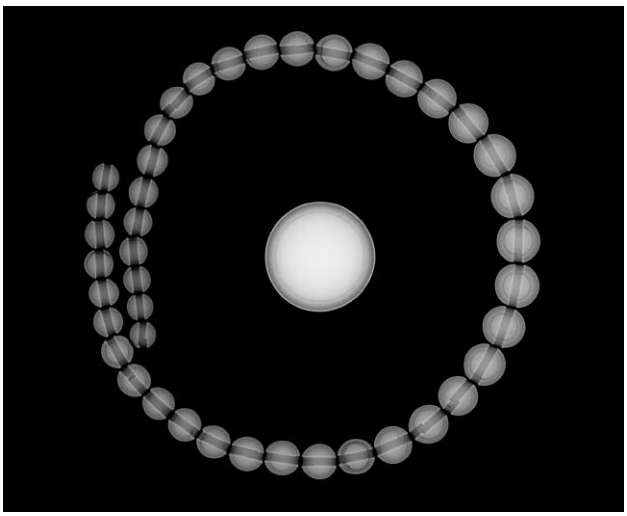

Figure 52. RTX analysis of tiny loose akoya NBC pearls revealed void-like structures in most of them. Image by Promlikit Kessrapong.

RTX analysis of the loose NBC pearls revealed typical void-like structures expected for akoya NBC pearls in most of the samples (H.A. Hänni, "A short review of the use of 'keshi' as a term to describe pearls." *Journal of Gemmology*, 2006, Vol. 30, pp. 51–58; N. Sturman, "The microradiographic structures of non-bead cultured pearls," 2009, https://www.gia.edu/gia-news-research-NR112009). Those with less-defined structures needed further RTX analysis in additional directions to find sufficient evidence of their claimed origin (figure 52).

Figure 53. RTX analysis of some of the smallest pearls, claimed to be NBC, revealed structures more consistent with natural pearls. Image by Kwanreun Lawanwong.

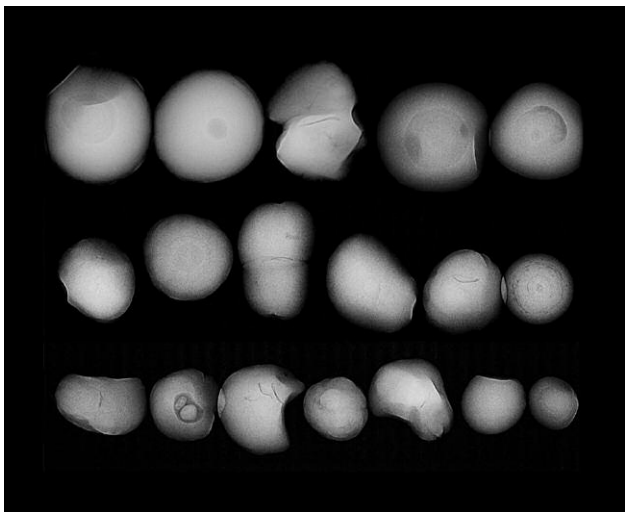

After additional RTX analysis in other directions, some of the more questionable structures showed features that were clear enough to consider as NBC. Most of the smallest pearls from the group revealed structures that were not consistent with those commonly seen in NBC pearls. Their "meaty" structures, central rounded dark organic features, and/or boundary or fold lines (seen in multi-nuclei/part pearls such as twins or aggregates) are in fact more typical of natural saltwater pearls (figure 53). Advanced analysis such as X-ray computed microtomography (μ-CT) may be required in these difficult cases, but owing to their very small sizes, obtaining clearer imagery is impractical. In this case, the lab gemologists did not find enough evidence to identify these pearls as non-bead cultured. Since most pearls are submitted without any information and laboratory gemologists have to go by what they see, such pearls would likely be considered natural, even if they are not such by definition. This clearly shows the challenges faced by gemologists carrying out pearl identification on some client-submitted items.

Areeya Manustrong
GIA, Bangkok

TREATMENTS

Irradiated and annealed blue type Ia diamond. Many diamonds are subjected to artificial radiation, usually with subsequent annealing to create attractive colors. Most blue diamonds in the market are treated by artificial irradiation, yet irradiated blue diamonds with a multi-step treatment process are rarely seen in the lab. The National Center of Supervision and Inspection on Quality of Gold and Silver Products (Nanjing, China) recently examined such an example.

The 0.36 ct round brilliant, graded as fancy deep green-blue (figure 54), had natural mineral inclusions under the table and a fracture near the girdle. The DiamondView image showed a ring-like natural growth pattern (figure 55). The infrared spectrum revealed the diamond was type IaAB, with absorptions at 1282 cm^{-1} and 1175 cm^{-1} (A-aggregated nitrogen and B-aggregated nitrogen, respectively); the spectrum also revealed a radiation-related peak at 1450 cm^{-1} (figure 56). The H1a center reflected by the 1450 cm^{-1} band, involving a single nitrogen atom and two equivalent carbon atoms, was formed by irradiation and annealing above 300°C for diamonds with aggregated nitrogen (type Ia) (I. Kiflawi et al., "Nitrogen interstitials in diamond," *Physical Review B*, Vol. 54, No. 23, 1996, pp. 16719–16726). The UV-Vis-NIR absorption spectrum showed absorption from a GR1 defect at 741.2 nm and revealed weak absorptions from a defect of uncertain structure (594.4 nm), H3 (503.2 nm), and H4 (496.2 nm) centers (figure 57). The GR1 center, believed to be a neutral vacancy (V^0) defect, is a typical radiation-induced defect; the vacancies begin to move at 500°C and the GR1 center begins to decrease until it disappears, at around 800°C (A.T. Collins,

Figure 54. This 0.36 ct Fancy Deep green-blue diamond is a multi-step treated diamond. Photo by Wenqing Huang.

Figure 55. The DiamondView image showed a characteristic ring-like natural growth pattern. Image by Wenqing Huang.

"Investigating artificially coloured diamonds," *Nature*, Vol. 273, No. 5664, 1978, pp. 654–655). The 595 nm center is also a typical radiation-induced center, which appears at temperatures above 300°C after radiation (Collins et al., 1978). The presence of the H3 and H4 centers was confirmed with photoluminescence (PL) spectroscopy (figure 58). The combination of all the above defects, especially the strong H1a center, indicates that the diamond was subjected to irradiation followed by annealing.

Natural near-colorless type Ia diamonds are known to be artificially irradiated to introduce blue to green color by displacing carbon atoms in the lattice to create vacancies. Annealing could be used to change the lattice defect configuration, especially GR1, to achieve a purer blue (C.M. Breeding, "A spectroscopic look at green and blue gem diamonds colored by artificial irradiation treatment," presentation at Geological Society of American 2014 annual meeting). After annealing above 500°C, the vacancies start

Figure 56. The FTIR spectrum of the 0.36 ct irradiated diamond revealed the sample was type IaAB, with absorptions at 1282 cm^{-1} (A-aggregated nitrogen) and 1175 cm^{-1} (B-aggregated nitrogen). The H1a absorption at 1450 cm^{-1}, associated with irradiation and subsequent heating, was also detected. In addition, the spectra showed peaks at 1405, 1096, and 1010 cm^{-1}, all of which are usually seen in type Ia diamond.

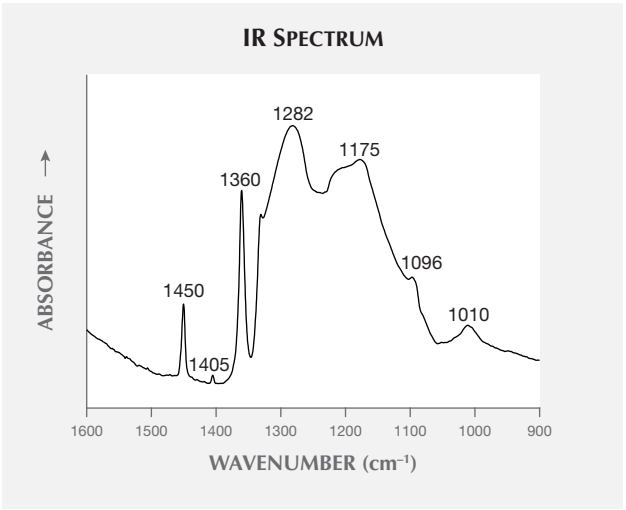

Figure 57. The UV-Vis-NIR spectrum of the 0.36 ct irradiated diamond, collected at liquid nitrogen temperature, showed a clear GR1 center defect at 741.2 nm, and weak absorption lines at 594.4 nm, 503.2 nm, and 496.2 nm.

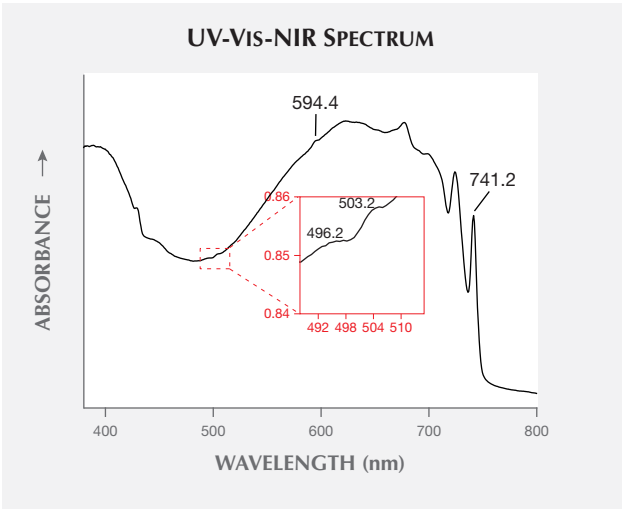

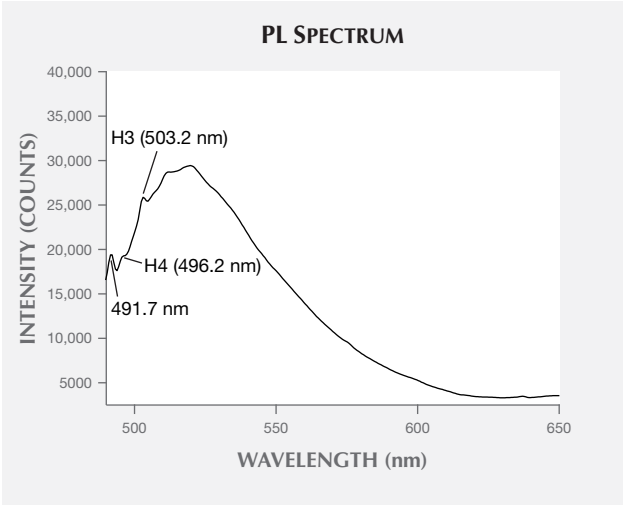

Figure 58. The PL spectrum of the sample excited with a 405 nm laser showed weak emissions at 496.2 nm (the H4 center) and 503.2 nm (the H3 center). A peak at 491.7 nm was also detected.

to migrate, and can be captured by nitrogen centers to create the H1a center (B. Dischler, *Handbook of Spectral Lines in Diamond, Volume 1: Tables and Interpretations*, Springer-Verlag, Berlin, 2012, pp. 315–316). To the best of our knowledge, this is the first diamond examined in China that has been irradiated and annealed to introduce a blue color.

Wenqing Huang, Xuguang Jin, and Wei Cai
National Center of Supervision and Inspection on Quality of Gold and Silver Products
Nanjing, China

Guanghai Shi
State Key Laboratory of Geological Processes and Mineral Resources
China University of Geosciences, Beijing

INSTRUMENTS

Universal Microscope Upgrade Kit. Israel-based GemoAid recently released the Universal Microscope Upgrade Kit (figure 59). Designed by gemologist Guy Borenstein, it offers a variety of accessories that maximize the use of a standard gemological microscope when observing unknown gems. The kit includes four mounting rings and two extension rods, which should be compatible with almost any microscope that has transmitted light capabilities. Also included are two polarizing filters, a blue filter, a yellow filter, a diffuser plate, and an immersion cell. The product, which retails for US$130, also includes a one-year warranty from the date of purchase.

The combination of components allows the microscope to act as a polariscope for making critical optical observations of gemstones and their inclusions. The colored filters and diffuser plate can also facilitate observation of subtle color zoning features such as curved color bands in yellow flame-fusion sapphires, which would be diagnostic of their manmade origin and difficult to resolve without a blue filter.

The unit examined by the author was found to be a little loose where the metal rod attaches to the mounting ring. The author also found the immersion cell to be too tall, making it difficult to manipulate small stones with tweezers—which is quite critical in immersion microscopy—but certainly the larger cell will accommodate larger stones and perhaps rough crystals.

Overall, the quality and price of the upgrade kit are well matched. It is of great value to the serious gemologist.

Nathan Renfro
GIA, Carlsbad

CONFERENCE REPORTS

Fourth International Diamond School. At the end of January 2018, some 92 attendees and 18 teachers gathered once again in the picturesque northern Italian town of Brixen-Bressanone for the fourth International Diamond School (IDS), themed "Diamonds: Geology, Gemology, and Exploration."

As in previous years, the school was underwritten by the Gemological Institute of America (GIA) in addition to the Deep Carbon Observatory (DCO), the Society of Italian Mineralogical (SIMP), and the University of Padua. Profes-

Figure 59. GemoAid's new Universal Microscope Upgrade Kit converts a gemological microscope into a polariscope, while the colored filters and diffuser plate are useful in observing subtle color zoning features. Photo by Kevin Schumacher.

Figure 60. During the Fourth International Diamond School, Pierre Cartigny delivers a presentation on stable isotopes with support from organizer Fabrizio Nestola. Photo by Marco Cuman.

sor **Fabrizio Nestola** (University of Padua) served as local organizer extraordinaire and was assisted on the organizing committee by four of the presenters: **Matteo Alvaro**, **Graham Pearson**, **Steven Shirey**, and **Wuyi Wang**.

The academic activities took place in a well-appointed auditorium owned by the University of Padua, while meals and social activities were held in the sixteenth-century Hotel Elephant—so named because the original building saw the arrival of an elephant from Ceylon—a gift to the Austrian royal family that caused a sensation and inspired artists and poets.

For the first three days, the school provided a general overview of the recent advances in diamond research, focusing specifically on the geology, exploration, and gemology of diamond from leading scientists in their fields. A brief summary of their talks follows.

Jeffrey Harris (University of Glasgow, UK) gave a very interesting overview of the history of gem diamonds from the sixth century (AD) onward. The modern era, leading directly to today's active mines, began in the 1870s in South Africa with the discovery of rich placer deposits. This period was followed by recognition of kimberlite as the diamond host rock and the battle between Barnato and Rhodes for supremacy over the kimberlite pipes in the Kimberly area.

John Armstrong (Karowe Mine, Lucara Diamond, Botswana) is the world's expert on how to extract (and not break!) very large diamonds. He outlined automated methods such as X-ray transmission to detect low-nitrogen stones and crushing methods that use the host kimberlite itself to minimize breakage.

Herman Grütter and **Jennifer Pell** (Peregrine Diamonds, Vancouver) spoke via Skype about microdiamond size frequency distributions (SFDs) and their practical use in macrograde forecasting to predict whether it will be economically worthwhile to mine a kimberlite. Each large sample of diamondiferous kimberlite dissolved by caustic fusion has its own microdiamond distribution in a plot of diamond grade (diamonds per ton) versus diamond size (carat weight). This negative correlation can be shown to merge with the same macrodiamond distribution for mines, which becomes the basis for the forecast. The challenge is that not all localities follow this relationship.

In a second Skype talk, Grütter spoke about pyroxene thermobarometry and a xenocryst-based approach. Using single clinopyroxenes from concentrates and indicator minerals, exploration major tectonothermal events in the mantle lithosphere are revealed. Because it takes some 800 million years for the lithosphere to equilibrate thermally, large clinopyroxene data sets can reveal heretofore unknown C-O-H flux fronts and mantle plumes.

Bruce Kjarsgaard (Geological Survey of Canada) discussed experimental constraints on kimberlite origin, ascent, and eruption. His talk focused on kimberlite mineralogy and isotopic compositions for kimberlite origin and experimental petrology for ascent and eruption. One of the basic questions still unanswered is whether kimberlite magmas are initially carbonatitic melts or some form of transitional melt.

Nikolay Sobolev (V.S. Sobolev Institute of Geology and Mineralogy, Novosibirsk, Russia) spoke about inclusions in Siberian diamonds and their polycrystalline aggregates and specific features of orogenic diamonds from Kazakhstan. His talk offered a useful review of inclusion types.

Making and stabilizing the deep diamond-bearing roots of the continents was the subject of a cutting-edge review by **D. Graham Pearson** (University of Alberta, Canada). Rheology turns out to be more important than buoyancy in preserving continental roots, and this stiffness makes them essentially plume-erosion proof. Lateral compression serves as a means to accumulate residues of any origin and form thick depleted lithosphere of more depleted composition. The process also accounts for late Archean intracrustal differentiation. A good modern analog to Archean craton formation may be seen in the new continent of Zealandia.

Thomas Stachel (University of Alberta) covered the entire subject of diamond formation in the earth's mantle. The newest thinking on diamond formation places less emphasis on solid-solid reactions or host-rock buffering and more emphasis on the diamond-forming fluids themselves. Critical factors include temperature change, reduction of CO_2, and presence of organic species including methane.

Oded Navon (The Hebrew University of Jerusalem) addressed diamond-forming fluids. He made the important points that there is a huge diversity of diamond-forming fluids by major and trace element composition and that the gem fluids are little different from those for fibrous diamonds.

Steven Shirey provided a framework with which to categorize diamond ages that can be used to establish meaningful age uncertainties with his talk. Since diamond ages rely on mineral inclusions for dating, debate over the years has been focused on whether these inclusions are protoge-

netic (existing before encapsulation) or syngenetic (simultaneous growth of the diamond and the inclusion). It is clear that many inclusions are mineralogically protogenetic while being geologically syngenetic.

Matteo Alvaro (University of Pavia, Italy) detailed new approaches to in-situ crystallographic study of mineral inclusions in diamond. Interestingly, mechanical re-orientation is a feature of the encapsulation of many silicate inclusions.

Pierre Cartigny (Institut de Physique du Globe de Paris; figure 60) discussed stable isotopes and diamonds in a talk that argued for massive carbon recycling into the mantle and considered the fractionation effects that occur between C, N, and the various kinds of fluids and sources from which well-studied diamond suites have come.

Diamond gemology and advanced technologies to replace visual observations were discussed by **Wuyi Wang** (GIA, New York). The talk covered GIA's research role in the $80 billion diamond trade and its assessment of color, cut, clarity, and carat weight. Dr. Wang also discussed GIA's internships and fellowships for research scientists.

Christopher M. Breeding (GIA, Carlsbad, California) covered the ever growing field of diamond defects and the identification of color treatment. While sophisticated analytical techniques allow GIA to associate color and treatment with lattice-scale mechanisms in diamond, each color requires considerable research analysis to pin down its defect mechanism.

Ulrika D'Haenens-Johansson (GIA, New York) addressed the synthesis of manmade gem diamonds and their detection. Diamonds grown by the two main methods—high-pressure, high-temperature (HPHT) growth and chemical vapor deposition (CVD)—currently can be detected chiefly from their isotopic composition and the N content of their starting compounds.

In her review of advances in in-situ isotope measurement in diamond and their inclusions, **Emilie Thomassot** (CNRS, Nancy, France) went over many of the theoretical and practical considerations affecting the accuracy and precision of ion microprobe measurements for stable isotopes, especially sulfur.

Steven Reddy (Western Australian School of Mines at Curtin University) described an exciting new direction in his talk on atom probe microscopy and its potential applications to diamond research. With this instrument, the analytical specimen is prepared in the shape of a needle and atoms from it are directed into a time-of-flight (TOF) mass spectrometer. One can retrieve the exact position of the atoms in the structure and even measure their isotopic composition. The potential is there to look at very tiny inclusions in diamond in this manner.

Dan Howell (University of Padua, Italy) covered the major uncertainties of Fourier-transform infrared (FTIR) studies of diamonds and how to overcome them. This basic technique, applicable nondestructively to any diamond, remains one of the most important ways to characterize specific diamonds and their integrated thermal history.

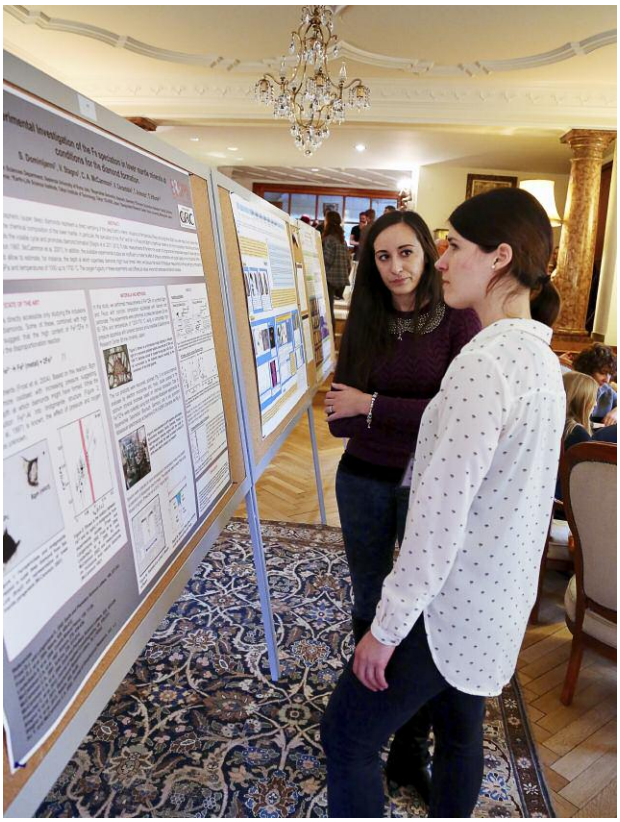

Figure 61. International Diamond School attendees discuss recent research. Photo by Marco Cuman.

Following the tradition of previous years, the International Diamond School went beyond these formal lectures (figure 61) to include practical sessions focused on microscopic observations of a complete inclusion-bearing diamond collection on the fourth day. The collection was made available to the IDS by Professor Jeffrey Harris, with microscopes provided by Zeiss and a micro-Raman spectrometer provided by Horiba Scientific.

The fifth day was devoted to 15-minute talks by students and early-career researchers providing the latest snapshot of their most recent work.

The Fourth International Diamond School was a fantastic opportunity to learn, exchange ideas, and inspire career choices. GIA's financial support reduced costs for students, and its sharing of expertise in diamond spectroscopy, diamond treatment, substitution and defect mechanisms, and grading gave the IDS an invaluable industry connection. GIA researchers were active participants throughout the week and inspired the students with their practical experience in the real world of gem diamonds.

The organizers and supporters were especially pleased with the diversity this year. The school had 110 participants from 13 different countries (Canada, Italy, Germany, France, the UK, Austria, the Netherlands, the United States, Russia, Israel, South Africa, Ireland, and Australia). There was a nearly even mix of undergraduate students,

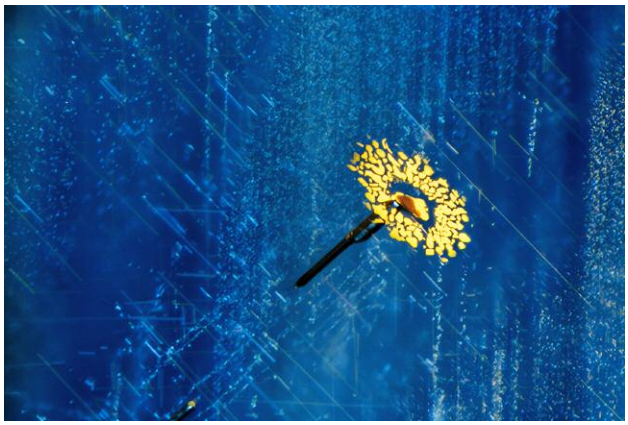

Figure 62. This inclusion scene showing a growth blockage and thin-film rosette within a Sri Lankan sapphire was enhanced by modified Rheinberg illumination to resemble a flower in a rainstorm. The image won the Internal and Overall categories in Gem-A's annual photography competition and earned Jonathan Muyal the Photographer of the Year award. Field of view 1.34 mm.

Figure 63. Muyal also won Gem-A's Humanity in Gems category with this photo of a miner after finishing for the day at a sapphire deposit near Ilakaka, Madagascar.

Ph.D. students, academic seniors, and industry figures. There was also a nearly equal gender balance, with 45 women and 47 men.

Steven Shirey
Carnegie Institution for Science
Washington, DC

ANNOUNCEMENTS

Gerd Dreher (1939–2018). The gem world mourns the loss of master carver Gerd Dreher of Idar-Oberstein, Germany. Dreher was legendary for his lifelike and meticulously detailed carvings of flora and fauna. Dreher and his family, which has worked with gem materials for 13 generations, were profiled in the Winter 2017 issue (pp. 404–422).

Jonathan Muyal named Gem-A's Photographer of the Year. Thanks to a stunning photomicrograph revealing the inclusion scene of a Sri Lankan sapphire, Carlsbad staff gemologist and *G&G* contributor Jonathan Muyal has been named Gem-A's 2017 Gemstone Photographer of the Year. The winning shot—which also took top honors in the competition's Internal category, dedicated to photomicrography—shows a growth blockage resulting in an elongate tube terminating in a rosette-like thin-film fluid inclusion. By applying modified Rheinberg illumination with blue and yellow filters, Muyal achieved the appearance of a flower caught in a rainstorm (figure 62). The image was the subject of a Fall 2017 Micro-World entry (p. 371).

Muyal was also the winner of the Humanity in Gems category, which focuses on scenes of people mining, dealing, or otherwise working with gemstones. Muyal's photo shows a Malagasy miner who has finished a day's work at a sapphire deposit near Ilakaka (figure 63).

The Photographer of the Year competition is open to all Gem-A members and students.

For More Coverage of Tucson 2018

Watch exclusive videos from the gem shows, featuring interviews and insider insight, visit www.gia.edu/gems-gemology/spring-2018-gemnews-tucson-overview or scan the QR code on the right.

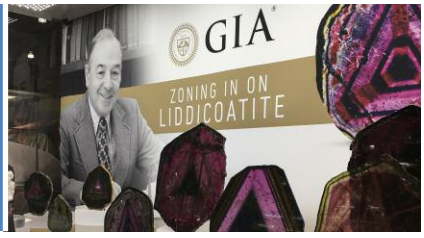

INTERNATIONAL GIA GEMOLOGICAL SYMPOSIUM

CALL FOR ABSTRACTS

2018 GIA Symposium Research Track

GIA® is accepting abstract submissions for oral and poster presentations through June 1.
Visit symposium.gia.edu and click on Research.

New Challenges. Creating Opportunities.

October 7 – 9, 2018 • Carlsbad, California

GIA®

Travel Grants Available for Eligible Presenters.
symposium.GIA.edu